

**The IMF of the massive star-forming
region NGC 3603 from NIR
adaptive optics observations**

DISSERTATION

der Fakultät für Physik
der Ludwig-Maximilians-Universität München
zur Erlangung des Grades
Doktor der Naturwissenschaften
Dr. rer. nat.

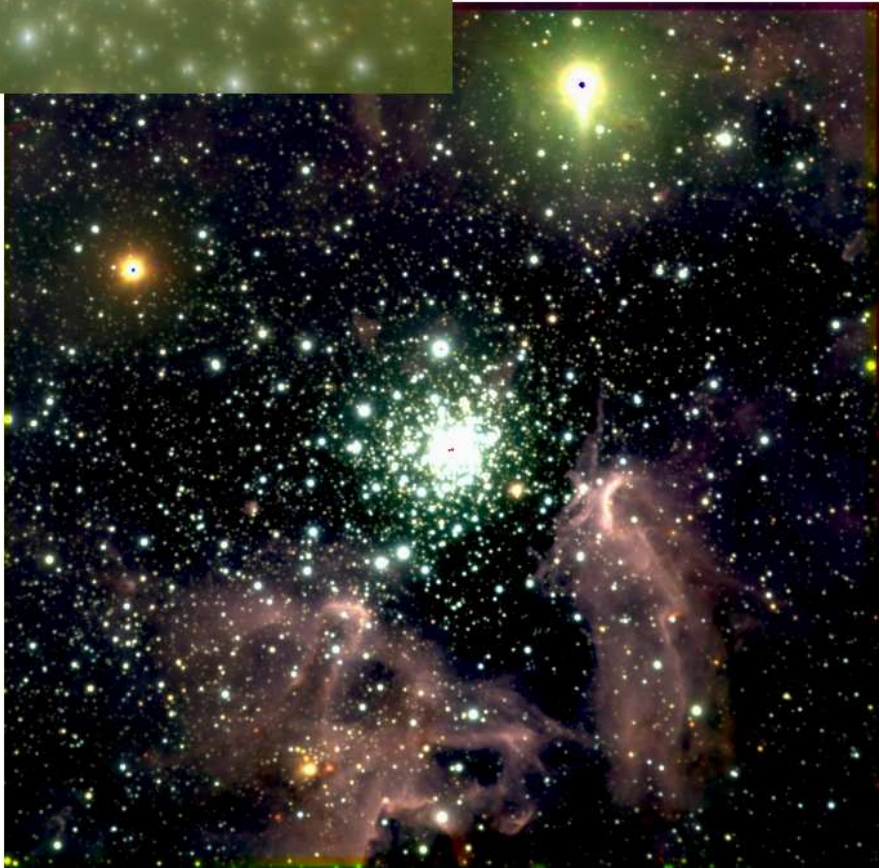
vorgelegt von
Yohei Harayama
aus Osaka, Japan

München, den 31. January 2007

1. Gutachter: Prof. Dr. Reinhard Genzel

2. Gutachter: Prof. Dr. Adalbert Pauldrach

Tag der mündlichen Prüfung: 6 Juli 2007



Cover page: The giant HII region NGC 3603 and its central starburst cluster. The images show the wide field $3'.0 \times 3'.0$ VLT/ISAAC observations and a $30'' \times 30''$ zoom to its central starburst cluster with the adaptive optics VLT/NACO. North is up and east is to the left.

Zusammenfassung

Wir untersuchen die anfängliche Massenfunktion (initial mass function, IMF) von NGC 3603, einem der massereichsten galaktischen Sternentstehungsgebiete, um eine fundamentale Frage der gegenwärtigen Astrophysik zu beantworten: ist die IMF universell, oder ist sie variabel?

Unter Verwendung von tiefen, räumlich hochaufgelösten Bilddaten, die mit dem mit adaptiver Optik ausgestatteten Kamerasystem NAOS-CONICA am VLT der ESO gewonnen wurden, ist es uns gelungen die im Haufenkern angesiedelte Population massearmer Sterne bis herab zu etwa $0.4 M_{\odot}$ (entsprechend einer Vollständigkeit von 50 %) zu untersuchen. Basierend auf JHKs-Farb-Helligkeits- und Zweifarben-Diagrammen ermitteln wir ein durchschnittliches Alter von 0.7 Myr für die Vorhauptreihensterne und eine Obergrenze von ~ 2.5 Myr für die Hauptreihensterne. Wir finden eine mittlere Vordergrundextinktion von $A_V = 4.5 \pm 0.5$ mag mit einem radialen Anstieg um $\Delta A_V \sim 2.0$ mag zu größeren Radien ($r \lesssim 50''$). Aus der im $K_S - L'$ vs. $J - H$ Zweifarben-Diagramm erkennbaren infraroten Exzessemission ermitteln wir einen Anteil von Sternen mit Scheiben von etwa 25 % für Sterne mit $M \geq 0.9 M_{\odot}$ im Haufenzentrum ($r < 10''$).

Wir bestimmen die K_S -Band Leuchtkraftfunktion (LF) für alle simultan in den Bändern J , H und K_S detektierten Sterne, wobei Vorder- und Hintergrundsterne ausgeschlossen und die Unvollständigkeit korrigiert werden. Die LF folgt einem Potenzgesetz mit einem Exponenten $\alpha \sim 0.27$ und zeigt weder einen Umschwung noch einen Einbruch innerhalb der Detektionsschwelle. Die IMF wird für Sterne innerhalb $r \leq 110''$ durch ein einzelnes Potenzgesetz mit Exponent $\Gamma \sim -0.74$ für Massen im Bereich $0.4 - 20 M_{\odot}$ gut beschrieben. Dies ist deutlich flacher als eine Salpeter-artige IMF ($\Gamma = -1.35$). Der Exponent der IMF sinkt von $\Gamma \sim -0.31$ für Radien $r \leq 5''$ auf $\Gamma \sim -0.86$ im Bereich $30'' < r \leq 110''$. Dieser Abfall des IMF-Exponenten tritt im Wesentlichen in den inneren $r \lesssim 30''$ des Feldes auf, was auf eine Massentrennung im Zentrum des Sternentstehungsgebietes hinweist.

Aus der Analyse des radialen Massedichteprofiles erhalten wir einen Haufenkernradius von $\sim 4''.8$ (~ 0.14 pc) sowie eine Untergrenze von $\sim 110''$ (~ 3.2 pc) für den Gezeitenradius. Wir bestimmen die Obergrenze des Gezeitenradius zu $r \sim 1260''$ (~ 37 pc). Basierend auf der deprojezierten Sterndichteverteilung schätzen wir die Gesamtmasse sowie den Halb-Masse-Radius von NGC 3603 ab zu $1.0 - 1.6 \times 10^4 M_{\odot}$ bzw. $25'' - 50''$ ($\sim 0.7 - 1.5$ pc). Als Kernradius ergibt sich ein Wert von $\geq 6 \times 10^4 M_{\odot} \text{ pc}^{-3}$.

Die Halb-Masse-Relaxationszeit liegt für Sterne mit einer typischen Masse von $1 M_{\odot}$ im Bereich 10 – 40 Myr, woraus sich schließen läßt dass Sterne mittlerer und geringer Masse noch nicht nennenswert von der dynamischen Relaxation des Haufens betroffen sind. Die Relaxationszeiten für Sterne hoher Masse sind wahrscheinlich viel geringer und vergleichbar mit dem Alter des Haufens. Daher können wir nicht entscheiden ob die Massentrennung der massereichen Sterne primordial angelegt oder ein Ergebnis dynamischer Evolution ist. Unsere Beobachtungen decken mindestens ~ 67 % der Sterne mittlerer und geringer Masse in NGC 3603 ab, wobei die Sterne außerhalb des Beobachtungsbereiches die IMF um nicht mehr als $\Delta\Gamma \leq 0.16$ steiler werden lassen können. Da die IMF außerhalb eines Bereiches $r \gtrsim 30''$ nahezu konstant verläuft, gehen wir davon aus dass unsere IMF die gesamte Sternentstehungsregion NGC 3603 korrekt beschreibt.

Desweiteren untersuchen wir ausgiebig die systematischen Unsicherheiten in unserer Bestimmung der IMF. Unter Berücksichtigung der systematischen Fehler erhalten wir für NGC 3603 einen Exponenten von $\Gamma = -0.74^{+0.62}_{-0.47}$. Unser Ergebnis unterstützt somit die Hypothese kopflastiger IMFs in Sternentstehungsgebieten, insbesondere im Zusammenhang mit Untersuchungen vergleichbarer Objekte wie dem Archeshaufen oder dem Sternhaufen im Galaktischen Zentrum.

Abstract

We study the initial mass function (IMF) of NGC 3603, one of the most massive galactic star-forming regions, to answer a fundamental question in current astrophysics - is the IMF universal, or does it vary?

Using our very deep high angular resolution images obtained with the NAOS-CONICA adaptive optics system at the VLT/ESO, we have successfully revealed the low-mass stellar population in the cluster core down to about $0.4 M_{\odot}$ (50 % completeness limit). Based on the $JHK_S L'$ color-magnitude and color-color diagrams, we first derive an average age 0.7 Myr for the pre-main sequence stars, and an upper limit of ~ 2.5 Myr for the main sequence stars. We find an average foreground extinction of $A_V = 4.5 \pm 0.5$ mag, with a radial increase of $\Delta A_V \sim 2.0$ mag towards larger radii ($r \lesssim 50''$). From the infrared excess emission identified in the $K_S - L'$ vs $J - H$ color-color diagram, we measure a disk fraction of ~ 25 % for stars with $M \geq 0.9 M_{\odot}$ in the cluster center ($r \leq 10''$).

Applying a field star rejection and correcting for incompleteness, we derive the K_S -band luminosity function (LF) for stars simultaneously detected in the JHK_S -bands. The LF follows a power-law with an index of $\alpha \sim 0.27$, and shows no turnover or truncation within the detection limit. The IMF for stars within $r \leq 110''$ is reasonably fitted by a single power-law with index $\Gamma \sim -0.74$ in the mass range of $0.4 - 20 M_{\odot}$. This is substantially flatter than the Salpeter-like IMF ($\Gamma = -1.35$). The IMF power-law index decreases from $\Gamma \sim -0.31$ at $r \leq 5''$ to $\Gamma \sim -0.86$ at $30'' < r \leq 110''$. This radial steepening of the IMF mainly occurs in the inner $r \lesssim 30''$ field, indicating mass segregation at the very center of the starburst cluster.

Analyzing the radial mass density profile, we derive a cluster core radius of $\sim 4''.8$ (~ 0.14 pc), and a lower limit of $\sim 110''$ (~ 3.2 pc) for the cluster size. We also derive an upper limit of $r \sim 1260''$ (~ 37 pc) for the cluster size adopting an estimate of the tidal radius of the cluster. Based on the de-projected stellar density distribution, we estimate the total mass and the half-mass radius of NGC 3603 to be about $1.0 - 1.6 \times 10^4 M_{\odot}$ and $25'' - 50''$ ($\sim 0.7 - 1.5$ pc), respectively. The derived core radius is $\geq 6 \times 10^4 M_{\odot} \text{ pc}^{-3}$.

The estimate of the half-mass relaxation time for stars with a typical mass of $1 M_{\odot}$ is $10 - 40$ Myr, suggesting that the intermediate- and low-mass stars have not yet been affected significantly by the dynamical relaxation in the cluster. The relaxation time for the high-mass stars is expected to be much smaller, and is comparable to the age of the cluster. We can thus not conclude if the mass segregation of the high-mass stars is primordial or caused by dynamical evolution. Our observation covers at least ~ 67 % of intermediate- and low-mass stars in NGC 3603, and the stars residing outside the observed field can merely steepen the IMF by $\Delta\Gamma \leq 0.16$. Therefore, because of the almost constant IMF beyond a radius $r \gtrsim 30''$, we are confident that our IMF adequately describes the whole NGC 3603 starburst cluster.

We also thoroughly analyze the systematic uncertainties in our IMF determination. We conclude that the power-law index of NGC 3603 including the systematic uncertainties is $\Gamma = -0.74_{-0.47}^{+0.62}$. Our result thus supports the hypothesis of a top-heavy IMF in starbursts, especially in combination with other studies of similar clusters such as the

Arches cluster and the Galactic Center cluster.

Contents

1	Introduction	1
2	The Initial Mass Function	5
2.1	A brief history of the IMF, and open questions	5
2.2	The IMF of young star-forming regions	8
3	NGC 3603 and the central starburst cluster HD 97950	11
3.1	A Galactic template for extragalactic starbursts	11
3.2	Summary of earlier studies of NGC 3603	12
3.2.1	Early studies	12
3.2.2	Various other studies	14
3.2.3	Recent star count studies	14
4	Observations	17
4.1	Adaptive optics observations	17
4.1.1	Atmospheric turbulence	17
4.1.2	Principle of adaptive optics technique	19
4.1.3	Strehl ratio	21
4.1.4	Anisoplanatism	23
4.2	Observations of NGC 3603 with NAOS-CONICA	25
5	Data reduction	29
5.1	NAOS-CONICA data	29
5.1.1	JHK_S -band data	29
5.1.2	L' -band data	31
5.2	ISAAC data	32
6	Photometry	35
6.1	NAOS-CONICA data	35
6.1.1	JHK_S -band data	35
6.1.2	L' -band data	36
6.2	ISAAC data	37
6.3	Additional calibration with respect to anisoplanatism	38
6.4	Photometric uncertainties	39
6.5	Photometry list	41

7	Completeness and detection limits	47
7.1	Incompleteness correction	47
7.2	Detection limits	51
8	Color-magnitude diagrams and color-color diagrams	53
8.1	Fundamental properties of NGC 3603	53
8.1.1	Distance	54
8.1.2	Age	54
8.1.3	Interstellar extinction	62
8.2	Color-Color Diagrams	64
8.2.1	Radial variation in the CCD	64
8.2.2	CCD of the central region	66
8.2.3	$K_S - L'$ vs $J - H$ diagram of the central region	66
9	Cluster membership	75
10	Luminosity functions of NGC 3603	79
10.1	Introduction to the luminosity function	79
10.2	LF of NGC 3603	80
10.2.1	Combination of NACO and ISAAC data	80
10.2.2	The observed LF	81
10.2.3	The field star LF	81
10.2.4	The cluster star LF	83
11	Initial mass functions of NGC 3603	89
11.1	IMF determination	89
11.2	Radial variation of the IMF	90
11.3	Comparison with previous studies	94
12	Mass segregation in NGC 3603	99
12.1	Radial mass density profile	99
12.2	Total mass of NGC 3603	101
12.2.1	Size of NGC 3603	101
12.2.2	Deprojection of the surface mass density distribution	103
12.3	Dynamical evolutionary status	105
13	Systematic uncertainties of the IMF determination	107
13.1	Age	108
13.2	Distance	109
13.3	Foreground extinction	111
13.4	Theoretical model dependence	112
13.5	Metallicity	114
13.6	Individual extinction	114
13.7	Incompleteness correction	115
13.8	Unresolved binary systems	116
13.8.1	Unresolved binary fraction from the observed CMD	118
13.8.2	Systematic error of the IMF from unresolved binaries	119
13.9	The stellar mass outside the observed field of view	123
13.10	Error combination	124

14 Discussion	125
15 Summary and concluding remarks	131
A Photometry list	135
Bibliography	139

Chapter 1

Introduction

Massive star-forming HII regions in the Milky Way and starbursts in local galaxies are of great interest in present day astrophysics. Because of their proximity, and thanks to the development of current powerful Adaptive Optics (AO) assisted ground-based and space-based telescopes, the detection of not only the integrated light from such populations but also spectrophotometry of their resolved components have become available. Therefore, it is now possible to reveal detailed properties of individual components of stellar populations. For example, one can derive the chemical composition of the stellar photospheres, presence of circumstellar disks and gas-dust envelopes, frequency of binary/multiple systems, and the influence of massive stars on their surroundings. Those small scale phenomena are the building blocks of larger scale phenomena, such as dynamical and chemical evolution of clusters, and eventually, the formation and evolution of galaxies.

Hence, studies of resolvable massive star-forming regions in the Milky Way and Large Magellanic Cloud - *galactic templates* of starbursts - are of critical importance to understand distant starburst galaxies, for which only integrated properties are available. Locally, such starburst templates are mainly massive star clusters. One can list, for example, NGC 3603 in the Carina spiral arm, the Arches, Quintuplet and central clusters in the Galactic Center, and Westerlund 1 (see, e.g. Clark et al., 2005) in the Milky Way. The Trapezium cluster in the Orion Nebula Cluster and the massive star cluster R136 in 30 Doradus in the Large Magellanic Cloud are also typical examples of the starburst templates.

One of the most interesting properties of massive star-forming regions which are not fully understood is the stellar Initial Mass Function (IMF). The IMF is the function giving the number of stars per uniform mass interval, or logarithmic mass interval, in a population at the time of its formation. In practice, it is expressed by $\xi(\mathcal{M}) = dN/d\mathcal{M}$, where N is the number of stars of mass \mathcal{M} .

As the life of a star is essentially determined by its mass, the evolution and fate of a cluster depends on its stellar content. In particular, the chemical enrichment of the ISM, the feedback effects of massive stars and supernovae, the recycling process of material are affected by the ratio of high to low-mass stars.

Since the pioneering work by E. Salpeter in 1955, which led to a standard picture of the IMF, the so-called *Salpeter IMF* ($dN/d\log \mathcal{M} \propto \mathcal{M}^\Gamma$ with $\Gamma = -1.35$), numerous efforts have been made to understand the IMF of many types of stellar populations such as field populations, stellar associations, open and globular clusters, and galaxies. In spite of the large number of studies, a fundamental question is still unanswered. Is the IMF

universal, or does it depend on environmental effects? The currently accepted picture is that the mass distribution exhibits a power-law feature with Salpeter-like slope index from the high-mass end down to $\sim 1 M_{\odot}$, and then shows a slight flattening towards the subsolar mass regime. The distribution starts to decline in the substellar mass range. Several models have so far been proposed for the standard IMF - for example, a lognormal distribution (Miller & Scalo, 1979; Scalo, 1986), a segmented power-law distribution (Scalo, 1998; Kroupa, 2001), and a combination of both (Chabrier, 2003).

In contrast to the evidence of the almost universal IMF, ample observational evidence of the variability of the IMF in a wide variety of populations has also been reported. The variations are mainly in the power-law index, and in the characteristic masses such as the one at which the single power-law breaks, and the one at which the distribution peaks towards lower-mass. For example, intense star-forming regions and starbursts tend to show slightly shallower mass distributions than the Salpeter IMF over the whole observable mass spectrum. These so-called *top-heavy* IMFs indicate fewer low-mass stars than in field populations. This suggests possible feedback effects of high-mass stars on the formation of low-mass stars under intense star-forming environments or effects of dynamical evolution of the population.

Despite many recent studies which have attempted to provide constraints on the IMF in massive star clusters, it is still unclear if the observed IMF variations are true intrinsic variations, or are merely false fluctuations due to either observational errors and uncertainties in theory used in the analysis. Since the IMF study is of a statistical nature, examples have to be collected from various types of objects at various wavelengths.

Therefore, in order to obtain new insights into the IMF of intense starburst environment, and to address the question of the IMF variability, we study the IMF of the massive star-forming HII region NGC 3603. This work is based on our near-infrared observations using the adaptive optics system NAOS-CONICA mounted at the VLT/ESO. Among a wide variety of observational techniques from X-ray to radio wavelengths, near-infrared observations have some great advantages. For example, they are much less affected by the interstellar extinction than those in the optical, and several atmospheric windows in the region make it possible to utilize the ground-based large telescopes. Combined with the AO technique, near-infrared observations provide high spatial resolution observations of young massive clusters. Since NGC 3603 is one of the closest massive star-forming regions located in the Sagittarius-Carina arm at a distance of $d \sim 6$ kpc, it is a suitable target to study the characteristics of the IMF of starbursts.

Our main goal in the present study is to derive the IMF of young and massive star-forming clusters to approach the question of the IMF variability in starburst environments. Based on unprecedented resolution observations of the central starburst cluster in NGC 3603 obtained by the VLT/NACO as well as a wider field with the VLT/ISAAC, we construct the IMF of NGC 3603. We then compare it with the IMF of other populations.

The outline of the present report is the following. In Chap. 2. We first present the fundamental knowledge about the IMF of stellar populations, and our correct understandings and open issues with respect to the IMF including various types of populations. Next we present properties of NGC 3603 and a summary of previous studies in Chap. 3. In Chap. 4 we introduce fundamental knowledge about adaptive optics observations, and then detailed information about our observations of NGC 3603 with VLT/NACO. We explain our technical details for the data reductions in Chap. 5, and then for the PSF photometry in Chap. 6. Investigations of completeness and detection

limits of the observed data, and subsequent technique of incompleteness correction are described in Chap. 7. In Chap. 8 we present our analysis of fundamental properties of NGC 3603, such as distance, age, interstellar extinction, and disk fraction via color-magnitude and color-color diagrams. We then introduce our technique for the selection of cluster members in Chap. 9 as a preparatory step for the following constructions of the luminosity function in Chap. 10 and IMF of the cluster in Chap. 11. In Chap. 12 we present our investigation of the evolutionary status of NGC 3603 and discuss about the nature of mass segregation in NGC 3603. Potential systematic uncertainties in our IMF derivation are carefully investigated one by one in Chap. 13. In Chap. 14 we then discuss the resulting IMF of NGC 3603 in comparisons with other young star-forming clusters. We present the summary of this study with primary findings, and concluding remarks in Chap. 15.

Chapter 2

The Initial Mass Function

In this chapter, we introduce the fundamental properties of the Initial Mass Function (IMF). We first give the definition of the IMF, outline its importance for many aspects of modern astrophysics, and review earlier studies. We then summarize the current status of the IMF measurements in a variety of stellar populations, and point out the open questions. This leads us to the advantages of studying the IMF in nearby young and massive star-forming regions.

2.1 A brief history of the IMF, and open questions

As the evolution of a star is primarily a function of its mass, the spectrum of stellar masses, i.e., the Mass Function (MF), determines predominantly the evolution of stellar populations such as associations, open and globular clusters, and galaxies.

The masses of stars range from 0.08 times of the mass of our Sun (denoted by M_{\odot}) for the least massive stars to more than $100 M_{\odot}$ for the most massive stars. The smallest mass is defined by the hydrogen burning limit, which is required for a protostar to start its life as a star by generating energy in its core through burning four hydrogen nuclei into one helium nucleus, releasing energy corresponding to the loss of mass in the reactants based on the Einstein's relation $\Delta E = \Delta mc^2$. The lifetime of stars decreases rapidly with increasing stellar mass. Low-mass stars, e.g. the Sun, live for about 10 billion years slowly consuming their material for the nuclear fusion, whereas high-mass stars live only for about a few Myr, finishing their life by catastrophic events such as supernovae explosions.

Owing to this strong dependence of the stellar lifetime on mass, the evolution of a stellar population is predominantly determined by the distribution of stellar masses of its components. Accordingly, the MF, i.e. the number of stars per unit mass interval in a given volume of space, is an essential quantity in the study of stellar populations. In particular, the Initial Mass Function (IMF) - the mass distribution at the time of birth of the population - is of extreme importance to understand stellar populations. In case of a stellar population where the majority of stars formed in a single starburst event, which is most likely the case of young stellar populations such as open clusters, the IMF predominantly determines the path of evolution and the fate of the population. Combined with the star formation rate and the stellar evolution, the IMF allows us to predict the evolution and fate of clusters and galaxies.

The IMF is defined as the number of stars born per logarithmic mass interval, and

thus it is expressed as

$$\xi(\log \mathcal{M}) = \frac{dN}{d \log \mathcal{M}}. \quad (2.1)$$

The concept of the IMF was first presented by E. Salpeter in 1955. Based on the study of the luminosity function of main-sequence stars in the solar neighborhood, he calculated the star formation rate as a function of stellar mass, that is the IMF. He found that in a mass range of about $1 - 10 M_{\odot}$ the IMF is well fitted by a power-law which increases towards lower stellar masses, and thus can be described by

$$\frac{dN}{d \log \mathcal{M}} \propto \mathcal{M}^{\Gamma} \quad (2.2)$$

with a power-law index of $\Gamma \sim -1.35$. This power-law IMF with index $\Gamma \sim -1.35$ is called *Salpeter IMF*. The equivalent term *field IMF* is used for the IMF of stars which are not belonging to any specific groups or aggregations.

An alternative expression commonly used to characterize the mass distribution is the number of stars per unit mass interval,

$$\xi(\mathcal{M}) = \frac{dN}{d\mathcal{M}} = \frac{1}{\mathcal{M}(\ln 10)} \xi(\log \mathcal{M}) \quad (2.3)$$

and thus, $dN/d\mathcal{M} \propto \mathcal{M}^{\gamma}$ with $\gamma = \Gamma - 1$. As the power-law IMF is linear in the $\log N - \log \mathcal{M}$ diagram, its slope (power-law index) provides an intuitive comparison of the mass distributions of different stellar populations, and has been subject of many studies.

The IMF is related to many other fundamental astrophysical processes such as the core contraction in molecular clouds, the formation of stars and planetary systems, and the formation and evolution of clusters. It has broad implications in modern astrophysics from the study of the first stars (Pop III stars) and galaxies in the early universe to that of the recycling of interstellar material and the formations of next generation stars, which has been repeated in the universe since the big bang.

Therefore a large number of studies have aimed at deriving the IMF for various stellar populations, covering the whole stellar mass range from very massive stars down to substellar brown dwarfs.

Several fundamental properties of the IMF have been established for all stellar populations. It is currently accepted that the IMF follows a Salpeter-like power-law in the high- to intermediate-mass range ($M \gtrsim 1 M_{\odot}$). It becomes flatter towards subsolar masses and peaks at a characteristic mass of several tenths of a solar mass. Many studies have found the distribution to then decline towards the brown dwarf mass range. Therefore several analytical expressions have been proposed for the IMF. The widely used form of the IMF is the broken or segmented power-law distribution (Scalo, 1998; Kroupa, 2001, 2002).

For example, Scalo (1998) compiles a large number of IMF studies of star clusters and associations in the Milky Way, and the Large Magellanic Cloud (LMC). Although he finds a substantial scatter of the power-law index for masses above $1 M_{\odot}$, Scalo (1998) concludes a three-segment power-law with $\Gamma = -0.2 \pm 0.3$ for $0.1 - 1 M_{\odot}$, -1.7 ± 0.5

for $1 - 10 M_{\odot}$, and -1.3 ± 0.5 for $10 - 100 M_{\odot}$, in which the IMF is the steepest in the intermediate-mass range.

The second expression commonly used for the IMF is a log-normal or Gaussian distribution. It was proposed by Miller & Scalo (1979) on the basis of the study of the solar neighborhood, and the IMF is expressed as

$$\xi(\log \mathcal{M}) = \frac{A}{\sqrt{2\pi}\sigma} \exp \left[-\frac{(\log \mathcal{M} - \log \mathcal{M}_{mean})^2}{2\sigma^2} \right] \quad (2.4)$$

where \mathcal{M}_{mean} and σ^2 are the mean logarithmic mass and variance, respectively. For typical stellar populations, the authors derive the following formula

$$\frac{d \log \xi(\log \mathcal{M})}{d \log \mathcal{M}} = -(1 + \log \mathcal{M}). \quad (2.5)$$

This log-normal IMF can be fitted with a segmented power-law with $\Gamma = -1.0$ for the mass range of $0.1 - 1 M_{\odot}$, -1.9 for $1 - 10 M_{\odot}$, and -2.6 for $10 - 50 M_{\odot}$.

Also the combination of the power-law and the log-normal distribution can be found in literature. Analyzing the IMF in various stellar populations in the Galaxy such as the disk, spheroid, young, and globular clusters, Chabrier (2003) derive an IMF which can be described by a power-law at ($M \gtrsim 1 M_{\odot}$) and by a log-normal distribution below. The critical mass at around $1 M_{\odot}$ is thought to be linked to the local thermal Jeans mass in the parent molecular cloud.

Since these standard representations of the IMF fit reasonably well the various types of stellar populations from the field stars to star clusters, the idea of the *universality* of the IMF was born. These standard IMFs have been commonly applied with slight variations in many fields of astronomy, for example in modeling the formation and evolution of galaxies.

Is the IMF universal?

Despite the numerous studies deriving the IMF for various stellar populations, one major question is still open: Is the IMF universal, or does it vary with environmental conditions such as the density, velocity fields, chemical composition, and tidal forces in the natal molecular clouds? A universal IMF would basically suggests a universal star formation mechanism in the universe. However, it is somewhat intuitive that different physical conditions can lead to different star formation processes, and consequently, some variability in the IMF. Indeed, there is growing evidence that the IMF varies among different stellar populations. There are significant variations in the power-law index, and the characteristic masses, at which the distribution shows the peak or at which the power-law breaks. A typical example of an IMF which does not follow the Salpeter distribution is the so-called *top-heavy* IMF in starburst galaxies and young, massive star-forming regions (see Sect. 2.2).

However, the available studies are not yet conclusive to answer the question whether the IMF is variable or universal. For that we need to clarify, for at least some stellar populations, if the observed IMFs are without any doubt different from the Salpeter-type IMF, or if they can simply be accommodated by the combined effects of observational, theoretical and statistical uncertainties? Many studies have addressed this question. For

example, Scalo (1998) and Scalo (2005) report a substantial spread in the IMF power-law index among the Galactic field and star clusters. On the other hand, Kroupa (2001) concludes that the so-far observed scatter in IMF power-law index can be explained by the intrinsic uncertainties such as Poisson noise, dynamical evolution, and unresolved binaries.

In summary, we have not yet been able to draw an amicable conclusion with respect to the IMF variability. To answer the question whether the IMF is universal or not, it is necessary to accumulate more measurements of the IMF for various stellar populations such as field main-sequence stars, old globular clusters, intermediate-age open clusters and associations, and young star-forming HII regions, including the careful consideration and proper treatment of potential uncertainties.

2.2 The IMF of young star-forming regions

Young star-forming regions offer a unique opportunity to measure the IMF over a large stellar mass range, because the short lived high-mass stars are still alive, and because the dynamical evolution is still moderate. In contrast, the stellar mass distribution of a relatively old population differs from the *initial* MF, and it is commonly called the Present Day Mass Function (PDMF).

To then trace the observed PDMF back to its origin, i.e. the IMF, is by no means straightforward. For example, the ongoing stellar evolution depletes the high-mass stars because of their shorter life, and the dynamical evolution depletes the low-mass stars through evaporation. To reconstruct the IMF from the PDMF, we need to know accurately the stellar evolution, the star formation rate, and the dynamical evolution.

However, if one observes a newly born stellar population, the evolutionary effects are supposed to be moderate, and we can directly derive the IMF without the uncertainties associated with the complicated evolution. The other advantage of measuring the IMF in young star-forming regions is that in this case all stars have a common distance, metallicity, and age, which allows a rather direct mass determination using theoretical isochrones.

Therefore young star-forming regions in the Milky Way and in the Magellanic Clouds have been extensively studied in the past decades. Compared to extragalactic starbursts (e.g. M82), those so-called *nearby starburst templates* are close enough to resolve the individual stars with current ground-based telescopes and the space-based facilities. In particular the invention of adaptive optics, the start of operation of 8-m class telescopes, and the availability of large, highly sensitive infrared detector arrays have boosted the observation of these regions. We are now able to observe in great detail various star-forming clusters in the Galactic disk and in nearby molecular clouds, in which the high line-of-sight extinction prohibits the observation at optical wavelengths.

These clusters include, for example, the Arches cluster (Figer et al., 1999; Stolte et al., 2005; Kim et al., 2006), the Quintuplet cluster (Figer et al., 1999), NGC 3603 (Eisenhauer et al., 1998; Sung & Bessell, 2004; Stolte et al., 2006), the R136 cluster (Brandl et al., 1996; Massey & Hunter, 1998; Sirianni et al., 2000), and NGC 3576 (Figueroa et al., 2002). For more nearby (but less massive) star-forming regions the IMF has been measured even down to the brown dwarf mass regime, for example, in the Trapezium cluster in the ONC (Hillenbrand & Carpenter, 2000; Muench et al., 2002; Briceño et al., 2002), the Pleiades cluster (Bouvier et al., 1998), the Taurus cluster (Briceño et al., 2002), and the IC 348 cluster (Preibisch et al., 2003; Luhman et al., 2003).

These studies have shown a substantial variations in the IMF, and most noticeably a top-heavy IMF among the most massive starburst clusters. Our detailed study of NGC 3603 will add with unprecedented accuracy further evidence for such a top-heavy IMF, and thus strengthens the case of a variable IMF.

Chapter 3

NGC 3603 and the central starburst cluster HD 97950

In this chapter we introduce the giant HII region NGC 3603 and its central stellar cluster, and we give a short chronological summary of previous studies.

3.1 A Galactic template for extragalactic starbursts

NGC 3603 is one of the most luminous, optically visible HII regions in the Milky Way (Goss & Radhakrishnan, 1969). Because of its global properties such as $L(\text{H}\alpha) \sim 1.5 \times 10^{39}$ ergs s^{-1} (Kennicutt, 1984) and the total mass of molecular clouds $\sim 4 \times 10^5 M_{\odot}$ (Grabelsky et al., 1988), NGC 3603 is considered as a potential Galactic template of extragalactic regions (Nürnberg & Stanke, 2003). Its total bolometric luminosity is as large as $10^7 L_{\odot}$, two orders of magnitude larger than the Orion Nebula Cluster, and just an order of magnitude smaller than another well known starburst template R136 - the central star-forming cluster in the 30 Dor giant HII region in the Large Magellanic Cloud. In particular, the young starburst cluster located in the northern part of the gigantic HII complex including HD 97950 - a very compact system with plenty of high-mass components (Walborn, 1973) - at its center, is one of the most massive and the densest star-forming region known in the Galaxy.

The starburst cluster with the Trapezium-like system HD 97950 consists of three WNL stars, six O3 stars, and many other late O- and B-type stars (Moffat, 1983; Clayton, 1986; Moffat et al., 1994; Drissen et al., 1995; Hofmann et al., 1995; Crowther & Dessart, 1998), providing most of the ionizing radiation in the giant HII region NGC 3603. Thus it shows remarkable similarities with the starburst template R136. In the Milky Way, NGC 3603 is located towards the tangential point of the Sagittarius-Carina arm ($l \sim 291^{\circ}.6$, $b \sim -0^{\circ}.5$). Its distance from the Sun has been estimated in many earlier works by means of both photometric and kinematic analysis (Sher, 1965; Goss & Radhakrishnan, 1969; van den Bergh, 1978; Melnick & Grosbøl, 1982), and the currently accepted value is about 7 ± 1 kpc (Moffat, 1983; Melnick et al., 1989; Crowther & Dessart, 1998; Eisenhauer et al., 1998; De Pree et al., 1999; Pandey et al., 2000; Nürnberg et al., 2002; Stolte et al., 2004; Sung & Bessell, 2004).

Owing to its uniqueness in terms of the intrinsic properties such as the proximity, relatively low visual extinction of only $A_V = 4 - 5$ mag, and the extreme compactness and brightness, NGC 3603 is one of the most suitable Galactic templates of starburst

phenomena in distant galaxies. Therefore, since its discovery more than a century ago, NGC 3603 has been intensively studied in many groups.

3.2 Summary of earlier studies of NGC 3603

To date, NGC 3603 has been studied by means of photometric and spectroscopic observations in all available channels from X-ray to radio wavelengths with various ground-based instruments and the space-based telescope such as the HST. We therefore present a summary of the earlier studies.

3.2.1 Early studies

The first attempt to resolve the stellar components of HD 97950 was performed by van den Bos (1928), and the first photometric study of NGC 3603 was reported by Sher (1965), who derived the first estimate of the cluster’s distance (much smaller than the currently accepted value) and the foreground extinction ($A_V \sim 4.26$ mag). Goss & Radhakrishnan (1969) analyzed radio continuum data of the giant HII region, and derived the cluster’s dynamical distance $d \sim 8.4$ kpc. Later, van den Bergh (1978) derived a cluster’s kinematic distance of $7.2^{+0.8}_{-1.0}$ kpc based on their *UBV* photometric study. The latter two values are close to what is currently accepted. Walborn (1973) firstly suggested the similarity of HD 97950 and R136a in 30 Dor, and suggested that HD 97950 (as well as R 136) may be a Trapezium-like system with a Wolf-Rayet component.

Following those earlier studies, the stellar content as well as the structural properties of the cluster started to be revealed intensively through many observations. Based on a spectral observation, Moffat (1983) probed the stellar content of the central cluster, and identified 12 O and B stars and a WN6 spectral feature in HD 97950 with a distance estimate $d \sim 7 \pm 0.5$ kpc. Using speckle interferometry data, Hofmann & Weigelt (1986) resolved for the first time the central core with $0''.1$ resolution, finding four distinct components A1, A2, A3, and B, and derived visible photometry for the sources. From *UBV* CCD photometry combining optical spectral information, Melnick et al. (1989) investigated fundamental properties of the cluster such as the distance (7.2 kpc), interstellar extinction ($E(B - V) = 1.44$ for $r < 50''$), and age (2 – 3 Myr). In addition, several star formation events instead of one coeval formation in the cluster was suggested.

As for properties of one of giant HII regions, Kennicutt (1984) derived $L(H_\alpha) \sim 1.5 \times 10^{39}$ ergs s^{-1} , $M(H^+) \sim 4 \times 10^4 M_\odot$, and $M_{star} \sim 5 \times 10^3 M_\odot$ based on the H_α and radio continuum data. Balick et al. (1980) investigated the cluster’s structural and kinematical morphology based on their radio observation. They found a gas- and dust-free cavity ($r \sim 0.6$ pc) created by strong stellar winds from the resident massive stars around the cluster center, surrounded by a highly ionized dense core ($n_e \gtrsim 1800$ cm^{-3}) and a faint outer halo ($n_e \lesssim 100$ cm^{-3} at $r \leq 50$ pc). The presence of this wind-driven “stellar bubble” has been supported by recent studies. From H_α and [NII] lines study Clayton (1986) found a large-scale motion with velocity variations of up to 150 $km s^{-1}$, which was probably due to supernovae explosions before the cluster formation, as well as several shell-like structures caused by the WR stars’ activities.

In the middle 90’s high-resolution observations of NGC 3603 became available thanks to the application of the adaptive optics technique for large ground-based telescopes as well as to the appearance of the space-based facilities such as the Hubble Space Telescope (HST). In particular, the characteristics of the massive components such as WR stars

and OB stars at the very center of the cluster became a target of intense studies in those high-resolution observations.

First, performing an optical HST observation, Moffat et al. (1994) revealed a remarkable similarity between the properties of bright components in HD 97950 and those in R136. As an example of spectroscopic observations using HST, Drissen et al. (1995) resolved HD 97950 into 3 WN6+abs, 6 O3 stars, and many other O stars in a volume less than a cubic light year. They concluded that those members would provide about 80 % of the Lyman continuum radiation which are necessary to create the HII region. In this study the massive WR star B was suggested to be a binary system, as suggested earlier (Moffat & Niemela, 1984; Moffat, 1985). Then Crowther & Dessart (1998) performed quantitative analysis of the WR stars in HD 97950 as well as R136 using HST spectroscopic data, and concluded that the WR stars, which amount to ~ 10 % of the massive stellar population, provided ~ 20 % of the total ionizing flux in the core ($r < 0.5$ pc), and ~ 60 % of the total kinetic energy released into the surrounding interstellar medium (ISM). They derived a photometric distance of ~ 10 kpc.

From their analysis of hydrogen and helium lines of the three WR stars in HD 97950 based on HST observations, Schmutz & Drissen (1999) found that these WR stars were hydrogen rich, and their components showed H/He ratios close to solar value, indicating that these stars were still in an early evolutionary stage. They also suggested that the initial mass of the component B could be in excess of $120 M_{\odot}$. It is then a candidate to be the most massive star in the Milky Way, unless it is a binary system as has indeed been suggested by (Moffat & Niemela, 1984; Moffat, 1985; Drissen et al., 1995). Moffat et al. (2004) analyzed HST/NICMOS data in order to investigate the variability among the stellar components, and found a half a dozen variable candidates. One of the most brightest components in the very center - A1 - could be an eclipsing binary composed of a $30 - 90 M_{\odot}$ H-rich WR star (WN6ha) and a $25 - 50 M_{\odot}$ O-type star.

In addition to observations in the visible to radio wavelengths, the cluster became a subject of X-ray observations. Based on a *Chandra* X-ray satellite observation complemented by centimeter-wavelength radio imaging and HST optical observations, Moffat et al. (2002) studied the multi-wavelength properties of the bright WR and early O-type members in the central cluster. They found several hundred X-ray point sources with greater frequency towards the cluster center, 40 of them having optical counterparts. The large number of X-ray sources with no obvious optical counterparts were found, and those source might be low-mass pre-main sequence stars or other types of high X-ray flux objects. They also detected anomalous brightness of the three WR stars in the X-ray band, suggesting that those sources, in fact, could be very luminous main sequence stars with strong wind-produced emission lines. Most of the centimeter radio emission were found to arise from peripheral regions of the current star formation, and showed no correlation with X-rays.

Other studies with respect to the cluster's fundamental properties after the late 90's are following. De Pree et al. (1999) found $d \sim 6.1 \pm 0.6$ kpc as the cluster's kinematic distance, and a sign of sequential star formation in the cluster based on their radio lines and continuum data observed by the Australia Telescope Compact Array. From a study of *UBVRI* CCD photometry and $H\alpha$ data, Pandey et al. (2000) derived properties such as a distance of 6.3 ± 0.6 kpc by means of isochrone fitting, a mean age of ≤ 1 Myr with a slight spread of several Myr, and a mean extinction of $E(B - V) = 1.48 \pm 0.21$ with a spatial variation along the radial distance from the cluster center. Based on multi-wavelength investigations including optical imaging, *JHK*-bands

imaging and spectroscopy, Tapia et al. (2001) found populations of massive objects with large infrared excess emissions at the south of the central star-forming cluster. Those populations appeared to be younger than that in the central cluster, providing evidence for a continuous star formation from north to south over the past 3 – 6 Myr.

3.2.2 Various other studies

Not only the central starburst cluster, but also other objects have been studied because of the diverse characteristics of this massive star-forming HII complex. Performing optical photometric and spectroscopic observations, Brandner et al. (1997) studied the nature of the B1.5 supergiant Sher 25 located $\sim 22''$ north of HD 97950. They found a ring-shaped nebulous feature with a diameter of ~ 0.4 pc and a bipolar outflow signature centered on the star. This leads to the conclusion that it is indeed a member of the cluster, and a highly evolved star in a red supergiant stage. Using optical HST/WFPC and NIR VLT/ISAAC observations, Brandner et al. (2000) reported the discovery of three proplyd-like sources in the gaseous nebulae in the giant HII region. They appeared to be dynamically dominated by the star-forming cluster. Based on radiation hydrodynamical simulations of a star-disk-envelope system, they suggested that proplyds and circumstellar disks around young stars were common in NGC 3603.

Based on large scale CS (2 - 1) and CS (3 - 2) mapping observations at millimeter wavelengths, Nürnbergger et al. (2002) investigated the spatial distribution and kinematic structure of the dense gas in the giant molecular cloud. They identified 13 molecular clumps within the sampling field, and derived the cluster's kinematic distance of 7.7 ± 0.2 kpc. Based on observed associations of the molecular clumps with near- and mid-IR sources and other maser sources, they suggested the presence of still ongoing star formation in NGC 3603.

Nürnbergger & Stanke (2003) investigated the cluster population at $11.9 \mu\text{m}$ and $18 \mu\text{m}$ using TIMMI 2 mounted on the ESO 3.6-m telescope. They detected mid-IR emissions from the three WR stars in HD 97950, implying a presence of dust productions in circumstellar envelopes. In the diffused emissions, they found many structural phenomena such as pillars, shocks, and ionization fronts, indicating significant influence of massive stars in the cluster. From detections of distinct mid-IR emissions from IRS 9A-C in the highly reddened object IRS 9 located $\sim 1'$ south-east from the OB cluster center, Nürnbergger (2003) concluded that IRS 9A-C represented a sparse association of high-mass protostars. From their surface stellar density analysis, they also found an elongated stellar distribution in the cluster with an enhancement towards the SE-E direction from the cluster center, and suggested that this would be due to tidal interactions with either the Galactic Center or the nearby Carina arm.

3.2.3 Recent star count studies

The luminosity and mass functions of NGC 3603 have also been the topic of a number of studies. The first attempt to derive the IMF of NGC 3603 was done using the HST observations (Moffat et al., 1994), yielding a power-law slope of $\Gamma = -1.4$ for the massive members ($30 - 60 M_{\odot}$). From diffraction-limited speckle masking observations, Hofmann et al. (1995) derived a fairly steep IMF ($\Gamma = -1.59$) after a cluster age estimate of ~ 3.2 Myr through the isochrone fitting. They mentioned that HD 97950 has a high number ratio of WN to OB stars compared to cores of other extragalactic HII regions,

indicating an instantaneous burst of star formation as its origin. The total mass of OB stars in HD 97950 was estimated to be $\sim 1000 M_{\odot}$.

Eisenhauer et al. (1998) studied the stellar population and the IMF of the central cluster HD 97950 from NIR diffraction-limited observations obtained by the AO-system ADONIS at the ESO 3.6-m telescope. They revealed the presence of low-mass PMS population down to $\sim 1 M_{\odot}$ in the violent star-forming cluster, and estimated the cluster's age to be $0.3 - 1$ Myr. The IMF they derived showed a fairly flat slope with $\Gamma = -0.73$ ($1 M_{\odot} < M < 30 M_{\odot}$). No turnover or truncation were found in the IMF.

Sagar et al. (2001) derived cluster properties and MFs of NGC 3603 in the framework of a photometric study of seven southern open clusters based on their seeing limited *UBVRI* CCD photometric observations with the 1-m Elizabeth Telescope at the South African Astronomical Observatory. They derived an IMF with a power-law index of $\Gamma \sim -0.85$ ($7 - 75 M_{\odot}$). In addition, they concluded that, above $1 M_{\odot}$, MF slopes of star clusters younger than 500 Myr (equivalent to IMF) in the solar neighborhood had no dependence on the Galactic longitude, Galactocentric distance, and cluster age, and those were in agreement with the Salpeter IMF all within a 1σ error (scatter of $\sigma_{\Gamma} = 0.3$ around Salpeter value).

Nürnberg & Petr-Gotzens (2002) presented high-resolution NIR observations with the VLT/ISAAC at ESO for a region more extended towards the south of the central cluster than the field analyzed in Brandl et al. (1999). Based on the radial stellar density profile from the K_S -band photometry, the authors determined a cluster radius of $\sim 2'.5$. A constructed K_S -band luminosity function showed similar properties to those in Brandl et al. (1999). As for the cluster's IMF, Miller-Scalo type IMF (Miller & Scalo, 1979) for intermediate- and low-mass components of the cluster, and a Salpeter IMF (Salpeter, 1955) for the high-mass components were inferred.

Based on ground-based optical data coupled with HST optical and *Chandra* X-ray archival data sets, Sung & Bessell (2004) investigated the stellar population and IMF of the cluster. Analyzing optical CMDs from the *UBVRI* and H_{α} photometry, they confirmed the presence of low-mass PMS population, which were earlier found in the NIR studies, in the optical regime too. They supported a suggestion by that the diffused X-ray emissions near the cluster center could originate from low-mass PMS stars (Moffat et al., 2002). They also derived a cluster's age of 1 ± 1 Myr and a distance of 6.9 ± 0.6 kpc, as well as a radial variation in the interstellar reddening, which showed the lowest value and an increase towards outer regions. They then derived a moderately flat IMF with a power-law index of $\Gamma = -0.9$ for a whole region, and a gradual steepening towards the outer regions ($\Gamma = -0.5$ at $r \leq 0'.1$, -0.8 at $r = 0'.1 - 0'.2$, -1.2 at $r \geq 0'.2$). From the surface density profile of bright members with X-ray counterparts, they also derived the radius of NGC 3603 to be $\sim 2'$, slightly smaller than the estimate in the NIR ($r \sim 2'.5$) by Nürnberg & Petr-Gotzens (2002). They also suggested that halo populations in the cluster had an older age ~ 5 Myr, supporting the sequential star formation in the cluster (see also Melnick et al., 1989).

A detailed study based on high resolution NIR photometric observations with VLT/ISAAC were presented in a series of articles. First, Brandl et al. (1999) reported results of photometric analysis, and they reveal the PMS population with stellar masses down to $\sim 0.1 M_{\odot}$ and derived $0.3 - 1$ Myr as the age of the population. Stolte et al. (2004) studied the characteristics of the stellar population using the ISAAC *JHKL*-bands photometric observations as well as H_{α} observations with HST/WFPC2. They derived a cluster distance of 6.0 ± 0.3 kpc and interstellar extinction of $A_V = 4.5 \pm 0.6$ mag for the PMS stars

in the cluster center. They found a secondary sequence in the CMD, which was thought to be a sequence of equal-mass binaries, and a consequent unresolved binary fraction of 30 %. Analyzing the L -band excess emission, they estimate the disk fraction of ~ 20 % at the cluster center (with radial increase towards outer region up to 40 %), which is much lower than one seen in the Trapezium cluster, suggesting the presence of strong impacts on low-mass star formation in the dense star-forming cluster. Stolte et al. (2006) derived the cluster's PDMF with applying different treatments of field star population, individual dereddening, incompleteness, and a potential binary contribution. The resultant PDMF for the region of $7'' < r < 65''$ showed a power-law slope of $\Gamma = -0.91 \pm 0.15$ within a mass range of $0.4 - 20 M_{\odot}$. They found radial variations in terms of the fraction of high- to low-mass stars, characteristic mass at a given radius, and a depletion of massive stars at the high-mass end of the MF, but not in terms of the power-law slope of MFs. They propose to use these three parameters for comparisons of MF characteristics in different populations rather than the frequently applied power-law slope of the MF. Comparing their results with other local starburst clusters, they suggests that a strong mass segregation appears to be present in high-mass component in the cluster core, but the low-mass population appears to have a constant shape, indicating the role of primordial segregation to some extent in the cluster in addition to a possible strong effect of dynamical evolution.

Chapter 4

Observations

In this section, we first present some basic knowledge about the adaptive optics technique in the context of its principle and the pros and cons on practical applications for astronomical observations. We subsequently present detailed information about our near-infrared observations of NGC 3603 performed with the adaptive optics assisted NAOS-CONICA at the ESO VLT.

4.1 Adaptive optics observations

4.1.1 Atmospheric turbulence

In the long history of astronomical observations, the resolution of observations performed by any telescopes had been primarily limited by the atmosphere of the Earth, i.e, dominant effect of the atmospheric turbulence on the light passing through the atmosphere. As long as the telescope is ground-based, this limitation had been thought to be inevitable. The invention of the Adaptive Optics (AO) technique, however, has enabled us to overcome this limitation and to pursue better resolution performance, which is then a function of the size of telescope.

In an ideal case, the resolution of an optical system theoretically is determined by the diffraction, i.e., *diffraction-limited* resolution, and it is represented by an angle derived by the following relation

$$\theta = 1.22 \frac{\lambda}{D} \quad (4.1)$$

where λ is the observing wavelength and D is the diameter of the pupil of the system, e.g., primary mirror in the case of large reflecting telescopes, and the unit is *radian*. The larger the primary mirror of telescope is, the better the resolution is. For example, an 8-m telescope has the diffraction limited resolution of $\sim 0''.069$ in *K*-band ($2.2 \mu\text{m}$). In this ideal diffraction-limit case, the light of an object collected by the telescope is then focused onto the detector as an intensity profile called *Airy function* or *Airy pattern*. The resolution determined by Eq. 4.1 corresponds to an angular distance between the central peak and the center of the first dark ring on the Airy pattern. The Airy pattern is described by

$$P_0(\vec{\alpha}) = \frac{\pi D^2}{4\lambda^2} \left[\frac{2J_1(\pi D|\vec{\alpha}|/\lambda)}{\pi D|\vec{\alpha}|/\lambda} \right]^2 \quad (4.2)$$

where $P_0(\vec{\alpha})$ is the light intensity of a point source in the focal plane, as a function of angular coordinate $\vec{\alpha}$, and J_1 is the Bessel function.

In reality, however, the ideal resolution can not be achieved as long as the observation is performed from the ground because of the presence of the Earth's atmosphere. Since the atmosphere on the sky is neither steady nor flowing homogeneously but is, in fact, moving complicatedly and generating turbulence randomly, the light of observing objects is inevitably affected by the turbulence before it reaches the telescope. Hence in this so-called *seeing-limited* observation, the images of objects appear with a resolution (*FWHM*) described by a relation

$$\theta \approx \frac{\lambda}{r_0} \quad (4.3)$$

where r_0 is a characteristic length, called the coherence length. This is the limiting size of an aperture of the atmosphere over which the lightwave can keep the coherence all the way from the source to the receiver (strictly, there is about one radian of rms of the phase aberration on the lightwave), and is often referred to as *Fried's parameter*, or a *seeing cell size*.

Since this parameter scales by the wavelength as $\lambda^{6/5}$, the seeing-limited resolution has only a weak ($\lambda^{-1/5}$) dependence on wavelength. The value varies from a few meters under very good seeing conditions at infrared to a few centimeters under difficult seeing at visible. The typical value at $2.2 \mu\text{m}$, for example, is about 60 cm. The *correlation time* τ_0 of the turbulence is dependent mainly on the wind speed V in the atmosphere and, assuming $V = 10 \text{ m/s}$ typically, the correlation time is on the order of $r_0/V = 60 \text{ ms}$ at $2.2 \mu\text{m}$. Thus the r_0 and τ_0 are critical parameters in observations. The larger they are, the more stable the atmosphere is, and the better the observational performance. An image of astronomical objects obtained with an exposure time of $\leq \tau_0$ is called a short-exposure image, and the atmospheric turbulence is regarded as *frozen*. One obtained with a longer exposure time is then called a long-exposure image.

Both the diffraction- and seeing-limited resolutions as a consequence of the presence of the atmospheric turbulence are schematically shown in Fig. 4.1. Under the presence of the atmospheric turbulence, a short-exposure imaging of a point source profiles in a collection of a diffraction-limited small spot called *speckle* with $FWHM \sim \lambda/D$ on the focal plane. And in the long-exposure imaging, the speckle profiles are superposed, resulting in the blurred seeing-limited intensity profile.

As explained above, even in case of observations with a telescope whose aperture is much larger than the coherence length on the sky, the resolution is constrained by this parameter and any better resolution can not be attained. A possible means to avoid the influence of the atmospheric turbulence would be to directly go out of the atmosphere and observe in space like the HST. Space facilities, however, are extremely costly to construct and to operate, and it generally costs an order of magnitude higher than ground-based facilities. In addition, to build and launch much larger telescope would confront exponential increase of difficulties in terms of the cost as well as technical issues. Therefore a way which has been commonly applied to reduce the atmospheric blurring effect as much as possible is to carry out the observation at locations as high altitude as possible, normally on tops of mountains. The effect of atmospheric turbulence on the observing light, in fact, physically means the effect of a local variation of refractivity of the atmosphere on the electromagnetic wave. The air has an index of refraction near 1.0, which is close to a vacuum, but not exactly 1.0, and the index is not uniform in the air due to its dependency on the temperature, pressure, and density. Therefore the light from stars passing through the air is distorted due to the variation of the refractive index. Since the density of the air decays exponentially with height and the degree of

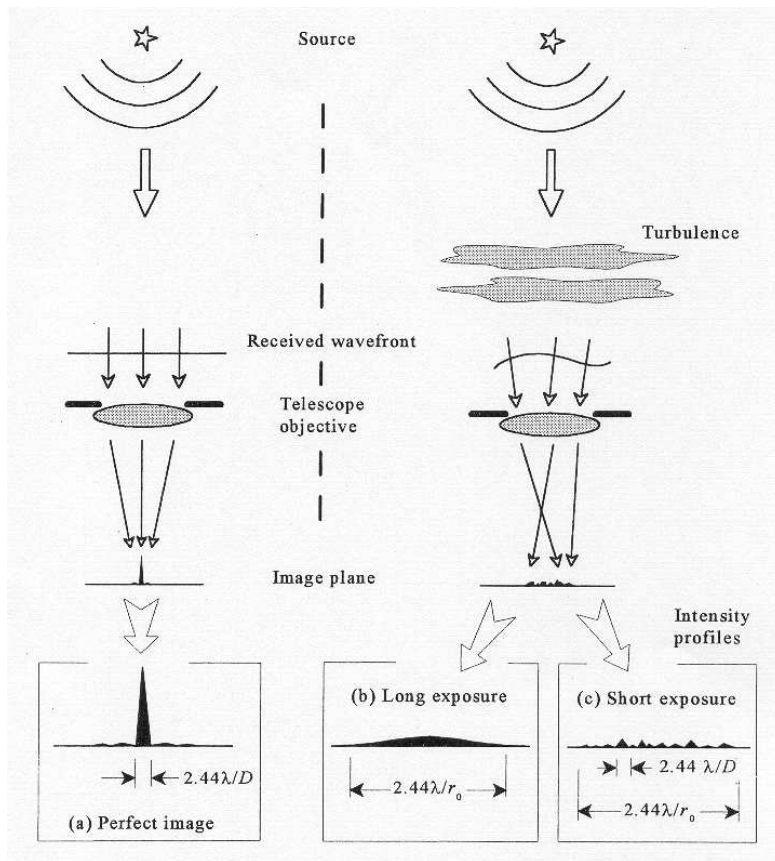


Figure 4.1: **Schematic picture of the influence of the atmospheric turbulence on the resolution of a point source image.** In the ideal case without the atmospheric turbulence, the wavefront of light emitted from a point source located far enough to be a plane wave is not disordered so that it reproduces the diffraction-limited intensity profile (*left*). Under the presence of atmospheric turbulence, however, the wavefront is perturbed, and a point source results in a blurred seeing-limited intensity profile (*right*). (from Hardy 1998)

temperature fluctuation of the air decreases with height too, the effect of the atmosphere generally decreases with height, leading peaks of mountains to being common locations of present-day astronomical observatories. Even in case of observations with such high altitude facilities, the seeing-limited resolution seems to have stabilized around $1''$ down to $\sim 0''.5$ at the best, and this is still an order of magnitude larger than that of the diffraction-limited case.

4.1.2 Principle of adaptive optics technique

In order to utilize the advantages of modern 8-m class large telescopes in terms of not only the light collecting power but also the spacial resolution, the adaptive optics technique has been developed. By performing a real-time compensation procedure, an AO system enable us to overcome the seeing-limited resolution imposed by the turbulent atmosphere, and to achieve higher resolution performance approaching the ideal diffraction-limited resolution. In fact, the AO is useful for compensating a wide variety of aberrations, not

just that imposed by the atmosphere but also one originated in optical components on the instrumental side.

The basic principle of AO is schematically shown in Fig. 4.2. An AO system consists of three principal elements, which are the crux of all modern AO systems. These are a wavefront sensor (WFS), a deformable mirror (DM), and a real-time computer unit. The whole system contains also various optical components to guide the incoming beam, as well as science instruments such as camera, which provides the output data. The light collected by the telescope is guided to the WFS experiencing reflections in the DM located in between, and the WFS measures the deviation of the wavefront from the ideal case. Utilizing the information from the WFS, the real-time control system then operates a set of actuators under the DM so as to compensate for the distortion and to flatten the wavefront interactively in the closed-loop real-time process. The most basic AO systems uses a light from ideally a point source to probe the shape of the wavefront, and the brightness of this so-called *reference* or *guide star*/source is one of the most important factors on the wavefront correction performance. As shown in the basic principle, the AO technique is achievable only if the atmospheric turbulence is *frozen* in time by the speed of the real-time process. A typical time scale of the whole process (signal readout of the WFS, the calculation of the wavefront correction, and the adjustment of the actuators below the DM etc.) is a few milliseconds. As this is an order of magnitude shorter than the correlation time τ_0 (a time scale of the change of the wavefront aberration) of a few tens of milliseconds, the AO compensation system is sensitive enough and fast enough to keep up with the changing atmosphere. In other words, this *an order of milliseconds operation* is the essential requirement for the realization of the AO concept and, thanks to developments of the computing technology, it became available as a strong tool in the current ground-based astronomical observations.

A type of WFS used in the NAOS, for example, is called Shack-Hartmann WFS. It consists of a lenslet array and corresponding detectors onto which beams split by the subapertures in the lenslet focus as spots. From the information of an offset of the spot position relative to the predictable position in case of the ideal wavefront on each detector, the tilt of the wavefront in the subaperture can be deduced. Then, based on the integrated information of all subapertures, the real-time computer decodes the distortion of the wavefront in the entire observing aperture, constructs appropriate movements of the actuators, and performs the deformation of the DM for the wavefront compensation in the closed-loop process. As the specifications of NAOS, it has two WFSs - one operates in the visible and one in the near-infrared - and both sensors use a 14×14 lenslet array with 144 valid subapertures as the best setup. 185 actuators at the DM are operated irrespective of the selection of the sensors.

The performance of AO system depends on many factors. From an instrumental point of view, it depends on the number of lenslets in the lenslet array, the number of actuators under the DM, and the response time of the process. In the design of an AO system, the Fried's parameter r_0 in the range of targeting wavelength is an essential input. Since this parameter basically means a seeing cell size, it practically determines, on the plane of the telescope, the number of apertures which have to be adjusted for the wavefront correction. Subsequently, configurations, such as the number of the lenslets at the WFS, the number of the actuators under the DM, determine the physical sizes of these components and other specifications. As shown in the relation $r_0 \sim \lambda^{6/5}$, the shorter the target wavelengths is, the smaller the r_0 is, yielding the complexity on the construction of the AO system due to the necessity of higher number

of the controlling subapertures for achieving reasonable correction performance. Since the number of operating subapertures increases radically towards shorter wavelengths, it is still not possible to construct an AO system which has a capability of the theoretically ideal correction in the visible regime. The NAOS, for example, is designed to be able to achieve an effective wavefront correction down to around H -band, and the correction performance somewhat degrades towards shorter wavelength such as J -band and some narrow band filters.

Note that, however, the wavefront sensor does not necessarily operate at the same wavelength as the camera, which forms the image, does. Even in cases of near-infrared imaging, visible wavefront sensors have been used to date in most AO facilities in the world. This is because of the fact that currently standard infrared detectors are not sensitive enough to produce sufficient signals against generally large noises in such a short-time readout process for the wavefront correction. The visible detectors, on the other hand, are capable of detecting the flux and feeding the signals powerful enough to be applied to the wavefront correction technique. Although the coherence length in the visible regime is much smaller than in the near-infrared, i.e., the wavefront aberration due to the atmospheric turbulence shows a finer feature in the visible than in the near-infrared, the finer feature in the visible essentially matches that in near-infrared if its lower frequency component are considered. Therefore, even without the capability of the theoretically ideal correction, the best correction in the visible can reproduce the best correction for the near-infrared imaging. The NAOS, exceptionally, provides the infrared wavefront sensor as well, and this allows us to perform observations under which no visible reference source is available. This is sometimes the case in observations of highly dusty regions in the Galactic disk within which the extinction is too high for the visible light to be observable from the Sun. In the observations of the Galactic Center, for example, the infrared wavefront sensor at the NAOS enable us to use a near-infrared source at the very center as the reference source, being a strong tool.

Once an AO system is constructed, the AO performance then, of course, depend on observational conditions. From an observational point of view, the performance depends on the observing conditions such as the seeing, the brightness and morphology of the reference source, and the angular separation of the reference source and the object of interest. The seeing is primarily governed by the coherence length r_0 and the coherence time, and the airmass - a measure of the height of atmosphere through which an observation is being made. The airmass is often approximated by $AM = \sec(ZA)$ where ZA is the zenith distance. The beam from the reference source should be bright enough to illuminate all the subapertures on the lenslet and to focus onto the detectors with sufficient S/N ratio in the WFS. The beam from the reference source should also be in, or as close as possible to, the direction of the object being observed in order to minimize the difference on the wavefront aberration between the both passes. In other words, both beams ideally should pass through a part of the atmosphere of approximately uniform characteristics.

4.1.3 Strehl ratio

One of the main characteristic parameters of image quality in AO-assisted observations is the Strehl ratio.

Under perfect conditions, a light from a single star collected by a telescope is focused onto the detector as the Airy pattern, i.e., the diffraction-limited image in accordance

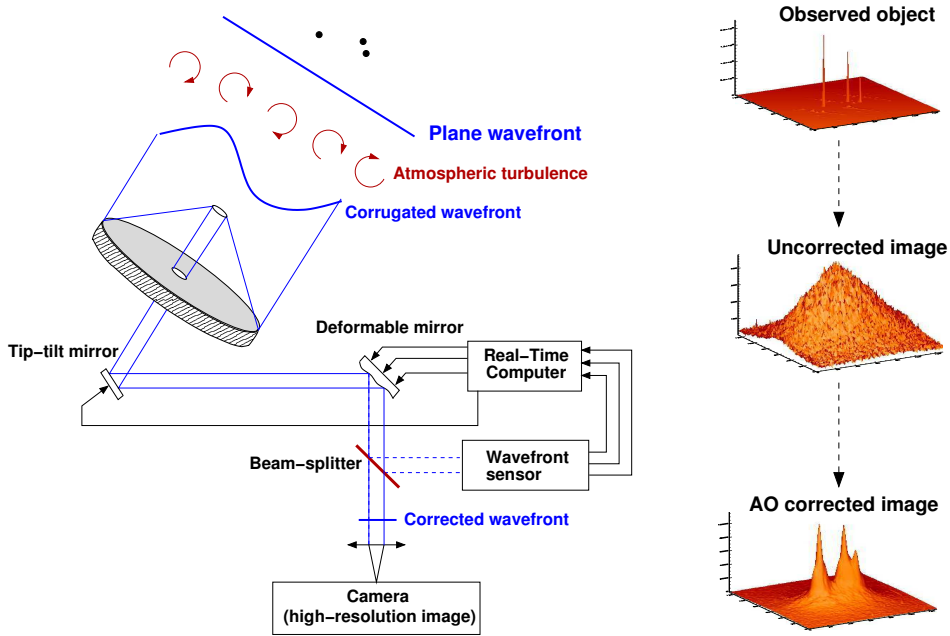


Figure 4.2: **Schematic picture of the principle of the adaptive optics observations.** *Left:* The principle of the AO technique is illustrated. A light from stars, whose wavefront is distorted by the turbulence of atmosphere, reaches the AO unit through the telescope. The wavefront sensor measures the distortion of the wavefront, and the deformable mirror controlled by the real-time computer compensates the distortion interactively. Since the time scale of the correction is much shorter than that of the atmospheric turbulence, the AO system can sufficiently reconstruct the undeformed wavefront. *Right:* Simulated profiles of point sources with and without the AO-correction on the detection are shown. (from ESO NAOS-CONICA user manual)

with the wave nature of light. The more light the optics system brings to the Airy disk (central disk of the Airy pattern), the sharper the image is. The Strehl ratio is a ratio of the amount of light contained within the Airy disk to the theoretical maximum amount of light that would have been collected within the disk in the ideal diffraction-limited case without the atmospheric influence. Therefore, in a simple representation, the Strehl ratio is described by

$$S = P(0)/P_0(0) \quad (4.4)$$

that is, the central intensity of observed PSF compared to the central intensity of the Airy function. Thus the diffraction-limited image has the highest Strehl ratio, but the ratio is always less than 1 in real observations, because any residuals of wavefront aberration after the compensation by the AO can not be zero.

For small arbitrary phase aberrations, the Strehl ratio is related to the variance of phase aberration σ_ϕ by $S \simeq 1 - \sigma_\phi^2$ (in case of a system of $S \geq 0.8$). The phase aberration of a random Gaussian process such as that given by the atmospheric turbulence, however, is much larger, and the Strehl ratio is described by

$$S \simeq e^{-\sigma_\phi^2}. \quad (4.5)$$

This is the case of systems of $S > 0.1$. As shown in the relation, the Strehl ratio is strongly related to the phase aberration, and the peak intensity rapidly decrease as the quality of correction goes down. Consequently, the AO technique becomes much more difficult as the wavelength goes down. If a rms residual of wavefront error after the AO correction is s in nm, then $\sigma_\phi = 2\pi s/\lambda$ can be applied to the previous equation, and we obtain

$$S \simeq e^{-(2\pi s/\lambda)^2}. \quad (4.6)$$

The Strehl ratio depends on the wavelength, and decreases towards shorter wavelength. In AO-assisted NIR observations, if the observing conditions is fairly well with respect to the seeing, and the brightness and location of the AO reference source, the resulting Strehl ratio in K -band ($2.2 \mu\text{m}$) is typically larger than 30 % (0.3) and that in J -band is as high as about 10 %.

4.1.4 Anisoplanatism

While the AO technique provide us with an order of magnitude better resolution than that of the seeing-limited observations, there are several particular limitations in its applications. One of the limitations is the fact that the capability of the wavefront correction is limited to imaging of only relatively small field of view.

To perform a reasonable wavefront correction, it is important that the light beam from the reference star should travel through a part of the atmospheric turbulence with as similar characteristics as possible to a part the light from the objects of interest does. If both beams travel through exactly the same path in the air (*on-axis* case), the correction performance is optimum, and it goes down as the angle between the beams increases in case of the *off-axis*. This effect is called *anisoplanatism*. A correction is valid if the displacement of both light beams in the turbulence is no more than the coherence length r_0 . If the mean height of the characteristic turbulent layer in the atmosphere is \bar{h} , then the maximum size of corrected field of view around the reference star is given by the so-called *isoplanatic angle* determined by

$$\theta_0 = 0.31 \frac{r_0}{\bar{h}}. \quad (4.7)$$

In definition the mean-square wavefront within the isoplanatic patch is smaller than 1 rad^2 . The wavefront error due to the anisoplanatism for an angular distance θ is obtained by

$$\sigma_{iso}^2 = \theta/\theta_0. \quad (4.8)$$

This phenomenon is very troublesome for the AO technique, because it limits the distance between the guide star and science targets. Thus it is quite often the case in observations that there is no suitable reference star available near the objects of interest. Hence applications of artificial laser guide stars have become available such as the PARSEC project at ESO VLT (Rabien et al., 2004).

Since the effect of the anisoplanatism is present in our NAOS-CONICA data to some extent, we have had some difficulties in our PSF photometry. As the AO reference

source is the multiple brightest components located at the center of the starburst cluster, the effect becomes larger with increasing radial distance from the center. The further a source is, the more elongated PSF it has. Moreover, there is a particular direction (which is the northwest - southeast direction in the FOV and possibly be the wind direction at the observation) along which the effect is so strong that the photometry performance would be somewhat inaccurate. Concretely, in case of an elongated source, a non-variable PSF photometry yields multiple detections (mainly three) for the source, and thus the resultant flux is slightly underestimated since only the central detections remains and minor detections at both sides are rejected after the source selection.

In order to deal with the photometric uncertainty imposed by the anisoplanatism, we will perform a variable photometric calibration for the NACO photometry later (see Sect. 6.3). However, in order to avoid the effect as much as we can, we set $r = 13''$ as the maximum radius for the NACO field. Applying some typical values at the ESO Paranal site into the characteristic parameters in Eq. 4.7, we could derive a crude estimate of the isoplanatic angle θ_0 . First using a typical seeing of $0''.85$ in visible (0.5 nm), we derive the coherence length r_0 of 0.36, 0.51 and 0.72 m in J , H and K_S -bands, respectively. Adopting a typical turbulence characteristic altitude of $\bar{h} = 3$ km above the Paranal site, we then derive the isoplanatic angle of $7''.7$, $10''.9$ and $15''.3$ in JHK_S -bands, respectively. Thus, theoretically speaking, the field selection criterion of the NACO field with $r \leq 13''$ would be considered to be safe in K_S -band, but some degree of the anisoplanatic effect is expected in the J -band photometry. But this estimate is fairly dependent on the adopted conditions, and probably be too simplified.

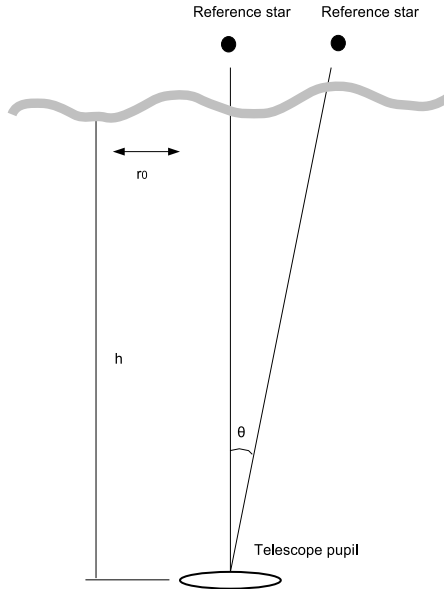


Figure 4.3: Schematic showing of the isoplanatic angle.

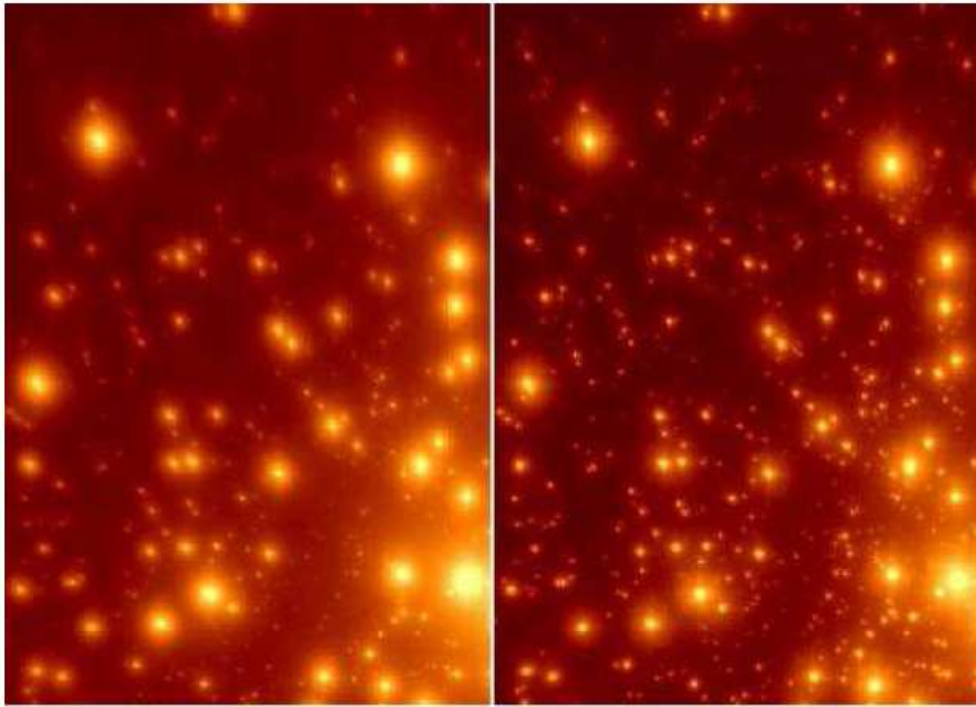


Figure 4.4: **Anisoplanatism observed in the NACO frames.** The images show the north-east part in the central starburst cluster of NGC 3603 in the J (left) and K_S (right) mosaic frames. Since the AO reference source is located at the center of the cluster (lower right in the frames), the anisoplanatic effect is discernible as the PSF elongation with respect to radial direction. Moreover, the elongation is stronger in the J -band than in the K_S -band because of the wavelength dependency of the anisoplanatism. For the sake of visibility, stellar flux are enhanced in logarithmic scale.

4.2 Observations of NGC 3603 with NAOS-CONICA

Observations were carried out in two periods, on 18-21 March 2003 and 14-16 February 2005, using the adaptive optics system NAOS-CONICA at the Very Large Telescope (VLT) at the European Southern Observatory (ESO) on Paranal, Chile. Note that, in the present study, the data obtained in the 2nd observing run has been used mostly in the following analysis. The data from the 1st run has been used so far for the estimate of statistical uncertainties in our PSF photometry (Sect. 6.4). NAOS-CONICA consists of a high-resolution near-infrared imager and a spectrograph (CONICA) and the Nasmyth Adaptive Optics system (NAOS) mounted at the Nasmyth focus of the VLT UT4. The NAOS is equipped with both visible and infrared wavefront sensors. It contains five dichroics, which split the light from the telescope to the CONICA and the wavefront sensors. The CONICA is capable of imaging, long slit spectroscopy, coronagraphic, and polarimetric observations. It has an Aladdin 1024×1024 pixel InSb array detector, and a variety of filters and pixel-scale selections. The central starburst cluster including the high-mass stellar complex HD 97950 in NGC 3603 (RA = $11^h 15^m 05^s.90$, Dec = $-61^\circ 15' 28''.4$ (J2000)) was imaged in three bands with the NACO J ($1.27 \mu\text{m}$), H ($1.66 \mu\text{m}$), and K_S ($2.18 \mu\text{m}$) filters in both observing runs, and an additional band with the L' ($3.80 \mu\text{m}$) filter in the 2nd observing run. The visible dichroic in NAOS was selected

for all observations. There are several Wolf-Rayet stars and OB stars reside in the very center of the cluster, and this bright core of multiple stars was used for the reference source for the AO correction. The S27 camera and the L27 camera (pixel scale of ~ 27 mas) were used for JHK_S -bands and L' -band, respectively, and corresponding field of views of the both camera are about $28'' \times 28''$.

The observations were carried out under fairly good seeing conditions in the both observing runs, and the average seeing was ~ 0.7 with variations ranging from 0.5 to 1.0 during observations. Integration times of a single frame were 40 s ($20 \text{ s} \times 2$ exposures) in J and K_S -bands, and 45 s ($15 \text{ s} \times 3$ exposures) in H -band in the both runs. In the L' -band observation, a very short exposure time of 0.2 s was chosen so as to avoid saturation due to the substantially high sky background level in this wavelength, and the total integration per frame was 30 s ($0.2 \text{ s} \times 150$ exposures). Additionally, we carried out short-exposure observations in JHK_S -bands with the aim of acquisition of photometry of the brightest members, and the integration time of a single frame was 10.5 s ($0.35 \text{ s} \times 30$ exposures).

In case of ground-based observations in NIR, the sky background is fairly changeable. Therefore, in JHK_S -bands for example, it is necessary to trace the background variation on a time scale of several tens of minutes typically to achieve reliable estimates of the background variation. In L' -band observations, however, it is desirable to trace the variation on a much shorter time scale, typically on several minutes.

In case of imaging of very crowded fields such as our target NGC 3603, relatively sparse fields are needed to be imaged separately from the object fields for producing representative sky frames. In our NACO observations, the sky fields were obtained in 'Sky' mode, in which the NACO AO system does not perform the correction so as to avoid any AO-corrected sharp PSF in the frame. Applying the jittering acquisition technique, we can create reasonable sky frames through the median combination method. The jittering acquisition also helps us to minimize contaminations arising from bad pixels and flux remnants due to totally saturated bright stars for the mosaic construction. Accordingly, in the 1st run we spent about one third of the total observing time for the sky acquisitions. We imaged four distinct fields - the central core and a northern adjacent field as object fields, and two sparse sky fields located just north of the object fields ($\sim 45''$ apart from the center) - sequentially to let them form a T-shape in one observing block. In the 2nd run, we observed the cluster center and a fairly sparse sky field located $\sim 4'$ apart to the south in one sequence. Note that, in the L' -band observation, we obtained images with the nodding technique in the NACO 'FixedSkyOffset' mode, because a common chopping method by 'AutoChopNod' mode was not available at our observing run. We therefore observed the same sky field as in JHK_S bands observations. Since acquisitions in a sequence of OBJECT-SKY-SKY-OBJECT are repeated in this mode, the sky variation is traced in each OBJECT-SKY pair with the minimum overhead time.

Configurations of all observations, and observing conditions are summarized in Tab. 4.1.

Date	Pixel Scale (mas/pixel)	Filter	Dichroic	Seeing ^a (")	Airmass	DIT×NDIT ^b (s)×exposures	Number of Frames ^c	Total integration time ^d on object (s)
The 1st observing run								
19 March 2003	27.03	<i>J</i>	VIS	0.57-0.82 (0.66)	1.31-1.35	20×2	24 (12)	480
19 March 2003	27.03	<i>H</i>	VIS	0.55-0.76 (0.62)	1.28-1.31	15×3	24 (12)	540
19 March 2003	27.03	<i>K_S</i>	VIS	0.52-0.78 (0.58)	1.26-1.28	20×2	24 (12)	480
21 March 2003	27.03	<i>J</i>	VIS	0.60-0.90 (0.72)	1.47-1.55	20×2	24 (12)	480
21 March 2003	27.03	<i>H</i>	VIS	0.75-1.05 (0.87)	1.40-1.47	15×3	24 (12)	540
21 March 2003	27.03	<i>K_S</i>	VIS	0.80-1.09 (0.94)	1.35-1.40	20×2	24 (12)	480
The 2nd observing run								
15 February 2005	27.19	<i>L'</i>	VIS	0.62-1.21 (0.82)	1.78-2.25	0.2×150	60 (30)	900
15 February 2005	27.19	<i>L'</i>	VIS	0.57-0.97 (0.77)	1.49-1.76	0.2×150	60 (30)	900
15 February 2005	27.15	<i>K_S</i>	VIS	0.59-1.15 (0.74)	1.37-1.48	20×2	36 (24)	960
15 February 2005	27.15	<i>H</i>	VIS	0.56-1.19 (0.74)	1.49-1.64	15×3	36 (24)	1080
15 February 2005	27.15	<i>J</i>	VIS	0.48-0.74 (0.59)	1.24-1.29	20×2	58 (40)	1600
15 February 2005	27.15	<i>J</i>	VIS	0.52-1.18 (0.75)	1.24-1.27	20×2	36 (24)	960
15 February 2005	27.15	<i>H</i>	VIS	0.70-0.92 (0.81)	1.27-1.34	15×3	36 (24)	1080
15 February 2005	27.15	<i>K_S</i>	VIS	0.54-1.40 (0.82)	1.34-1.45	20×2	36 (24)	960
15 February 2005	27.15	<i>J</i>	VIS	0.68-1.21 (0.89)	1.46-1.51	0.35×30	24 (16)	168
15 February 2005	27.15	<i>H</i>	VIS	0.62-0.80 (0.70)	1.52-1.58	0.35×30	24 (16)	168
15 February 2005	27.15	<i>K_S</i>	VIS	0.69-0.83 (0.76)	1.58-1.64	0.35×30	24 (16)	168
16 February 2005	27.15	<i>J</i>	VIS	0.43-0.93 (0.59)	1.26-1.35	20×2	108 (72)	2880
16 February 2005	27.15	<i>J</i>	VIS	0.46-0.77 (0.57)	1.36-1.48	20×2	36 (24)	960
16 February 2005	27.19	<i>L'</i>	VIS	0.45-0.86 (0.57)	1.49-1.64	0.2×150	39 (19)	570

Table 4.1: **Summary of NGC 3603 observations with VLT NAOS-CONICA.**

^a Shown in a range of recorded variation, and a typical value in bracket.

^b DIT is the detector exposure time. NDIT is the number of exposures that were combined into single output.

^c A total number of frames in the whole sequence. Number of frames on object is shown in the bracket.

^d Given by DIT × NDIT × Number of frames on object.

Chapter 5

Data reduction

Data reductions for the observed NACO data sets, and the ISAAC data sets retrieved from the ESO archive were performed in a standard manner of NIR image reductions. The procedure basically consists of a sky-subtraction, a flat-fielding, a bad-pixel correction, and a mosaic combination as major procedures. Most of the procedures were done using the *IRAF*¹ package, *IDL*, and in part the *eclipse* package developed by ESO basically for the pipeline procedures of the VLT instruments.

5.1 NAOS-CONICA data

5.1.1 JHK_S -band data

Although the 2nd NACO data set is basically used in the following analysis in the present paper, we present explanations of the data reduction of the both two NACO data sets. The 1st data set was used in the derivation of statistical photometry errors in our JHK_S -bands PSF photometry with combining the 2nd data set. We have performed slightly different procedures between the 1st and the 2nd data sets simply because of convenience in each case, however the principal procedures were the same. We note that since the detector in the CONICA was replaced in May 2004 and some of the characteristics, e.g., gain and pixel scale were slightly changed, we corrected frames to compensate the discrepancies due to these changes.

As for the reduction of the 1st data set, we first constructed a representative sky image from sky frames obtained with the jittering method in each sky offset field. We combined the obtained sky frames in each sequence of sky acquisition on top of each other, and assigned a minimum value, in preference to a median value, of each pixel in the cube with the aim of avoiding any contamination of remnants caused by bright stars in the contributing frames. Since taking minimum values results in a slightly lower background level compared to that of a averaged sky field, we added a uniform background onto the minimum sky image. The second step is the flat-fielding. This is a correction of possible bias in flux imposed by an inhomogeneity in sensitivity among pixels across the detector. We used lamp flat frames obtained as day-time calibrations to make a representative flat image. Since several pairs of ON-OFF flat frames were available in each observing night, we used three pairs, and made an averaged frame after

¹*IRAF* is distributed by the National Optical Astronomy Observatories, which are operated by the Association of Universities for Research in Astronomy, Inc., under cooperative agreement with the National Science Foundation.

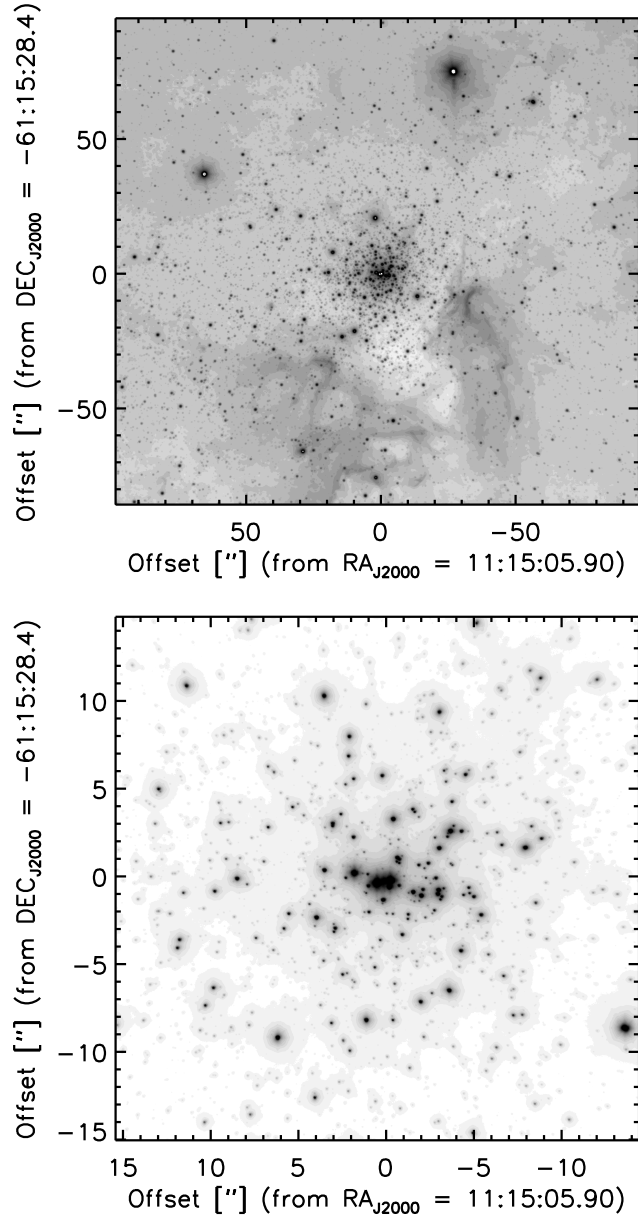


Figure 5.1: **ISAAC K_S -band mosaic of NGC 3603 and NACO K_S -band mosaic of the central starburst cluster.** Upper panel shows the wide field of approx. $3'.2 \times 3'.2$, corresponding to 5.2×5.2 pc at $d \sim 6$ kpc ($(m - M)_0 = 13.9$ mag) with the resolution of $\sim 0''.46$ ($FWHM$ of the PSF) constructed from the ISAAC K_S -band data. Lower panel shows the central field of approx. $30'' \times 30''$ (0.9×0.9 pc) with the resolution of $\sim 0''.1$ constructed from NACO K_S -band data. Note that, for this NACO mosaic, the long-exposure data set was chosen so as to cover the visibility of faint stars, therefore the bright stars in the center were saturated. Such stars are safely detected in the range of linearity in the short-exposure data set. For the sake of visibility, stellar fluxes are shown in square-root and log scales for the NACO and the ISAAC images, respectively. North is up and east is to the left in these images.

ON-OFF subtraction for each pair. We, then, divided all the sky-subtracted frames by the flat image. In the bad-pixel correction, first we created a hot-pixel map and a dead-pixel map in order to construct a representative bad-pixel map for each band. The hot-pixel map was created from several dark frames with defining a pixel of unusually high value as a hot pixel. The dead-pixel is a pixel which is not sensitive to the light, hence it is basically detectable in an ON-OFF frame. The correction was performed by the *IRAF fixpix* task. The *fixpix* replaces a bad-pixel in the bad-pixel map applying a linear interpolation along lines or columns using the surrounding pixels. The correction worked very well for the reduced frames.

Data reduction of the 2nd NACO observation data was performed in almost the same manner as the 1st data set, but several different tools were used in some procedures simply because of their handiness. As the differences, we used the *conicap* tasks, which were CONICA pipeline tasks in the *eclipse* package. In the flat-fielding, the *dark* task creates a master dark frame using dark frames taken in daytime calibrations, and then the *twflat* task creates a flat frame using the master dark frame and twilight flat images taken in the calibrations. In this procedure a bad-pixel map was also created, and subsequent bad-pixel correction was performed by the *fixpix*.

After the above basic reduction procedures, we combined the reduced frames for each data set to make a mosaic frame. We measured offsets of all contributing frames relative to an original star on the first frame in sub-pixel accuracy, and then aligned all frames. We used the *IRAF imcombine* task to combine a set of frames into a mosaic frame. This task allows us to combine frames using various algorithms and selection criteria such as average or median combination, evaluation of additive zero levels of contributing frames, rejection of anomalous pixels, and so forth. Note that we selected only frames with reasonable resolution in order to achieve the highest resolution for the mosaic frames. Consequently, typical Strehl ratios measured on individual sources around the cluster center are ~ 12 , 18 , and 32 % in JHK_S -bands mosaic frames, respectively.

5.1.2 L' -band data

The L' -band frames were reduced, in principle, in the same manner as JHK_S except the sky-subtraction procedure. The sky-subtraction was performed for each OBJECT-SKY pair obtained in the nodding mode. This is due to the fact that, in the L' -band, the fluctuation of the sky background has a much shorter time scale than those in the shorter wavelength such as JHK_S -band, hence the sky monitoring should have been done on a time scale an order of several tens of seconds. Since a slight fluctuation in background levels among frames was present in our data even after the about 30 seconds sky correction, we have adjusted the background level by adding a mean value of each frame. After the basic reduction, a mosaic frame was constructed. The resulting mosaic is presented in Fig 5.2. A typical Strehl ratio in the L' -band frame is more than 70 %.

The properties of constructed mosaic frames are summarized in Tab. 6.2. Since mosaic frames are constructed from the jittered obtained frames, total integration time varies through the field and those in the most overlapping region in the center being the longest, and otherwise become shorter towards outer region.

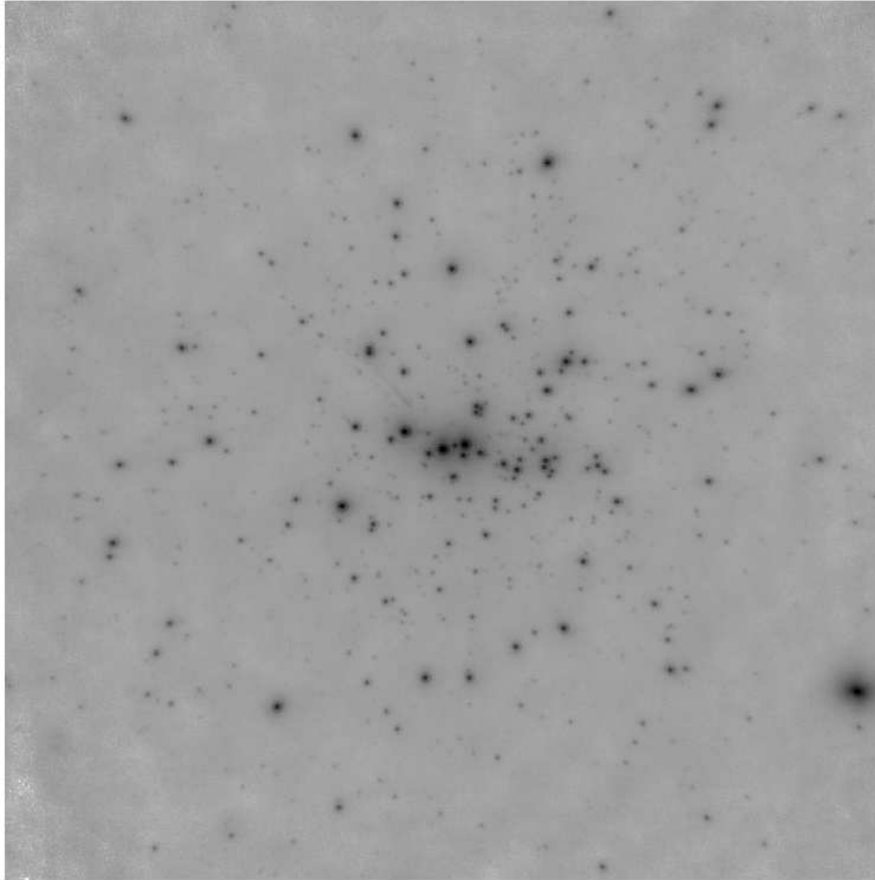


Figure 5.2: **NACO L' -band mosaic of the central starburst cluster.** The image shows the central $30'' \times 30''$ (0.9×0.9 pc) region constructed from the L' -band observation. The image is displayed with north at the top and east on the left. The stellar flux is enhanced in logarithmic scale.

5.2 ISAAC data

In addition to the high resolution NACO observation of the very center of the cluster ($\sim 15''$), we also analyzed the VLT/ISAAC - J_S ($1.24 \mu\text{m}$), H ($1.65 \mu\text{m}$), and K_S ($2.16 \mu\text{m}$) bands data sets of a wider field of view retrieved from the ESO/ST-ECF Science Archive Facility. Combining this wider picture of the massive HII complex NGC 3603 with the detailed central picture from the NACO data, we can investigate the cluster's global properties such as fore- and background contributions, distribution of the extinction. Then these analysis enable us to assess the probable existence of the mass segregation in the cluster from a radial variation of the stellar mass distributions.

The J_S , H , and K_S -bands data were obtained with the pixel scale of 0.147 arc-sec/pixel, corresponding to the field of view of about $150'' \times 150''$. The total integration time per frame is 1 min ($1.772 \text{ s} \times 34$ exposures). This was the shortest exposure time of the camera for the purpose of avoiding saturation of bright stars as much as possible. (Even with the shortest exposure, some of the brightest stars in the center are saturated and some are beyond the linearity regime, hence these stars need to be excluded from the following interpretations about the mass function).

The data reduction for $J_S H K_S$ -bands frames were done in almost the same manner as in the reductions of NACO data sets, but additionally two particular procedures - ghost removal and geometrical distortion correction - were performed. The electrical ghost induced by very bright objects in the field of view was removed by *ghost* in *isaacp* tasks in the *eclipse*. As the field of view covers a much larger area relative to the most crowded cluster core, each frame is not suffering from the crowding problem. Thus it is possible to create representative sky images in a time scale of several ten minutes from the object frames themselves with jittering method by means of the median combination. In fact there are several completely saturated sources as well as pixels of large negative values due to the saturation. Therefore we performed rejections of bright and faint values in the combination, and typically one faintest and 4 – 6 brightest pixels among a cube of 10 – 20 frames were removed. The resultant sky images showed satisfactorily smooth distributions.

Before the coordinate alignment in the mosaic frame creation, we needed to perform a correction of geometrical distortion in each frame. We ascertained that the distortion seemed to result in a mismatch of several pixels in periphery of the field. We therefore corrected the distortion using the *geotran* task in the *IRAF*². Whereas the resultant $J_S H K_S$ mosaic frames cover about $3'.4 \times 3'.4$ of the cluster field, we trimmed somewhat noisy peripheral regions off, and a field of about $3'.2 \times 3'.2$ was applied for the following PSF photometry. The NACO and ISAAC K_S -band mosaic frames used in the photometric analysis are shown in Fig. 5.1.

In each data set, after the mosaic frame constructions, an alignment of coordinates among the all bands ($J H K_S L'$ in NACO, and $J_S H K_S$ in ISAAC) in each data set was performed so that an identical star has the same coordinate in the photometry of all bands.

Properties of created mosaic frames in each observation are summarized in Tab. 6.2 together with summary of the photometry described in Chapt. 6.

²Files of the necessary parameters for the correction of the ISAAC field distortion were kindly provided by Dr. Lidman at ESO

Chapter 6

Photometry

In this chapter, we explain the flux measurements by means of the PSF photometry for the constructed NACO and ISAAC mosaic frames, and the photometric calibrations. We also present an estimate of statistical uncertainty in the photometry. We then explain our field selections criteria for the following analysis in the context of reliable photometric performance which is subject to the anisoplanatic effect and low S/N ratio at the rims of the mosaic frames. Finally, we provide a photometry list of detected stars ($m_J \leq 15.5$) in the cluster center from the NACO photometry.

6.1 NAOS-CONICA data

6.1.1 JHK_S -band data

Since the stellar distribution in the observed starburst cluster in NGC 3603 is extremely crowded, it is not possible to measure the stellar fluxes with a simple aperture photometry. We therefore have adopted the point spread function (PSF) photometry for the detection of stellar objects and the derivation of instrumental magnitudes using the *STARFINDER* package implemented in IDL (Diolaiti et al., 2000). The PSF, by definition, is a light intensity profile of a point source on the focal plane, and it is dependent on individual observational systems as well as observing conditions. The *STARFINDER* is designed to analyze AO-assisted images of highly crowded fields, which often have suffered from the blending of stellar flux. The package performs a PSF fitting technique using an empirical PSF extracted from sources of the measuring frame itself. As the AO-assisted imaging data generally show peculiar PSF, i.e., a sharply peaked core with widely extended wings, for the flux measurement, the application of the directly measured empirical PSF would be more suitable than the application of a PSF based on analytical models. A GUI package *XSTARFINDER* enables us to build the empirical PSF by selecting one or multiple sample stars on the measuring image interactively, and to execute the photometry readily. In the source detection, thresholds in unit of a Gaussian noise standard deviation calculated on the image are able to be applied for the selection of only reliable sources. We became aware of the necessity of determining an optimal threshold frame by frame rather than using a uniform value for reasonable detections. Thus we chose a threshold for each mosaic frame separately based on the impression on the detection quality so as to achieve an optimal detection.

After the flux measurements, we combined the photometry lists of J , H , and K_S -bands in order to identify sources which were detected in all three bands simultaneously.

The source detection is primarily limited by the J -band data, i.e., the J -band photometry has the lowest number of detections, which is due to a combined effect of the lowest correction performance at shorter wavelength in AO-observations and our shortest total integration time in this band. While the K_S photometry has the largest number of detections. Hence the K_S and H lists were first combined together, and subsequently, J list was combined with the HK_S list. The tolerance of offsets for an identical detection was carefully determined so as to avoid miss combinations but to identify as many stars as possible. Consequently, a source which coincided in all three bands within ≤ 70 mas was regarded as a JHK_S detected source. This three bands combining procedure provides us with an effective means of selecting only reliable sources, and of excluding spurious detections, which are inevitably present to some degree in each photometry result. Such a spurious detection, which is mostly located at regions such as the outskirts of a bright source and a nebulous emission region, is not likely to coincide in all the three bands within the tolerance. The photometric calibrations of the measured instrumental magnitudes were then performed using final photometry lists of the ISAAC data set as the photometric standards. The procedures of photometry and calibrations of the ISAAC data are explained in Sect. 6.2.

After performing the flux measurements, three-bands combinations, and photometric calibrations all in the same manner, the long- and short-exposure photometry lists were combined together so as to make a final photometry list of the NACO data. Note that in case of the long-exposure photometry, we regarded 13 mag as the brightest limit of a magnitude range safely within the detector non-linearity for all three bands. In the combination we therefore used sources brighter than 13 mag in the short-exposure list, and sources fainter than 13 mag in the long-exposure list in each band. Note that in case of sources which are identical in both lists in the range of 13 – 15 mag, we adopted each average value. As a consequence, the final combined list contains 1543 JHK_S detected stars in the entire field. Note that source selections, e.g., radial selection, will be applied in the following statistical analysis such as investigations of the luminosity functions and mass functions of the population.

The summary of the PSF photometry is shown in Tab. 6.2, and the results of the source identification are summarized in Tab. 6.1. As mentioned above, since the spacial resolution varies across the field of view with respect to its distance to the AO reference source, the $FWHM$ of the constructed PSF used in the photometry is shown in Tab. 6.2 as a representative resolution of each observation. For instance, the $FWHM$ of J , H , and K_S PSFs in the 2nd NACO data are about $0.''15$, $0.''11$, and $0.''10$, respectively.

6.1.2 L' -band data

In addition to the photometry of the JHK_S mosaics and the three bands combinations, we also performed the photometry and subsequent list combination for the L' -band mosaic frame. The photometry was done in the same manner as the JHK_S photometry. As for photometric calibrations, we used a set of observations of a standard star obtained during the observing run. The photometric standard is the source HD 38921 in the UKIRT standards list observed with the Mauna Kea $JHKL'M'$ system (Leggett et al., 2003). Note that any transformation of filter systems has not been performed.

We note that in the computation of a zero-point performing an aperture photometry for the standard source, we employed an aperture diameter of $\sim 1''.7$. Although this value was not enough to encompass all the extended skirt of the PSF of the standard

source, this was based on the size of PSF frame used in the PSF photometry which was restricted by the crowding.

Since we only used the set of frames of the single standard star, we would think that the calibration is very limited. Although this calibration based on only one set of standard frames is a potential uncertainty, we regard this photometry as still valuable for the purpose of our study such as examining evolutionary stage of the cluster members, i.e., presence of disks and circumstellar material on the basis of color-color diagram investigations. After the calibration, the L' -band sources was combined to the JHK_S combined final list, and consequently, 676 sources were identified as $JHK_S L'$ detected sources.

6.2 ISAAC data

As for the NACO data, the photometry of the ISAAC data was also performed by means of the PSF photometry using *XSTARFINDER*. As we prefer to make the source detection as accurate as possible rather than to pursue the number of detections, we set the thresholds of detections with careful inspections. Therefore we adopted slightly high values for each of the $J_S H K_S$ mosaic frames separately, and this could cause somewhat conservative detections of faint sources. Apart from the innermost part of up to $r \sim 30''$, where the crowding effect is thought to limit the source detection, the source detection is limited simply by the S/N ratio in most parts of the ISAAC field. Our estimates of these detection limits in the outer regions are presented in the Sect. 7.2.

Then, the photometry results in J_S , H , and K_S -bands were combined together in the same manner as the NACO data. The tolerance of offsets in cross identifications was ~ 0.3 arcsec. The number of the $J_S H K_S$ identified sources is presented in Tab. 6.1. Note that, even with the shortest exposure, some fraction of the brightest stars in the field are saturated and some are over the linear regime. Therefore those saturated sources have to be excluded from the output list for further analysis. The linearity breaks in all bands are located at 11 – 12 mag (after calibrations described below). Some of them are expected to be excluded in this three bands cross identification owing to the less accurate astrometry in the PSF photometry, and hence we have not performed any exclusion of potentially saturated sources. Although we expect that the number of such sources is fairly small, we adopt only the magnitude range down to 12 mag in the future assessments of the LF and IMF.

As for the photometric calibration, we first performed a calibration using frames of standard stars obtained during or close to the observing run and reduced in the same manner as the science frames. From all available data sets of 6 standard stars in the LCO/Palomar NICMOS photometric standards system (Persson et al., 1998), the average zeropoints of the J , H , K_S lists were derived. Note that, although we have not performed any airmass corrections of the standard frames, the effect is expected to be negligible considering the fact that the airmass differences among the frames are likely smoothed over to some extent by the averaging effect. We have not performed any corrections of the atmospheric extinction at the ESO Paranal site. We note that the standard frames were obtained in the ISAAC J_S filter, whereas the standard system provide the J -band magnitude as the reference. In order to deal with this non-negligible effect, a correction of the measured J_S magnitude was performed with respect to a color term factor provided in the ISAAC documentation. Since effects of the filter dependency in H , and K_S -bands are thought to be negligible, we have not performed any correction

6.3. Additional calibration with respect to anisoplanatism

Observations	Combined bands	Number of stars
1st NACO obs.	JHK_S	896
2nd NACO obs.	JHK_S	1472
	$JHK_S L'$	615
Short exposure	JHK_S	274
Final list (Long + Short)	JHK_S	1543
	$JHK_S L'$	676
ISAAC archive	$J_s H K_s$	8410

Table 6.1: **Multi-bands combination of photometry results.** Photometry results were combined together in each observation, and only stars identified simultaneously in JHK_S and $JHK_S L'$ are used as the detected star. The long and short combined lists (1543 JHK_S sources, 676 $JHK_S L'$ sources) from NACO, and the list of 8410 $J_s H K_s$ sources from ISAAC are used in the following analysis.

for these bands. With the aim of cross-checking the calibrations based on the standard star frames, we also performed a calibration using ~ 60 identical sources with high photometric reliability in the Two Micron All Sky Survey (2MASS)¹ catalogue, and the resultant zeropoints showed fairly close values to those derived in the standard star calibration with a dispersion of zeropoints of ≤ 0.04 mag. Here we note that, using these calibrated ISAAC photometry lists, we performed the calibrations of the short- and long-exposure NACO photometry lists presented in Sect. 6.1.

The following analysis of the cluster’s radial stellar density profile, LF, and IMF involve the combination of both NACO and ISAAC photometry. Considering somewhat moderate photometric accuracy in our PSF photometry, we expected that possible effects of the different filter systems between the two instruments are insignificant, and the calibrated ISAAC and NACO photometry can be reasonably combined together without any corrections. We therefore have not performed any corrections between them for the following analysis. For the sake of simplicity, hereafter we use J -band for the color term corrected ISAAC J_S -band photometry.

Photometry results are summarized in Tab. 6.2 together with properties of each mosaic frame, and the combinations of the photometry are summarized in Tab. 6.1.

6.3 Additional calibration with respect to anisoplanatism

In addition to the photometric calibration of NACO lists using the calibrated ISAAC lists, we performed a calibration of the NACO lists with respect to the anisoplanatic effect in the outer field.

As described in Sect. 4.1.4, a potential difficulty in the PSF photometry is the anisoplanatism, i.e., a spatial variation of the PSF, and in fact our NACO data show this effect even after the field selection with $r \leq 13''$. By checking the performance of the measurement during the PSF photometry, we obtained an impression that the anisoplanatic effect is particularly noticeable along the NW-SE direction in outer region in the NACO field. Therefore measured fluxes of some fraction of sources in the outer region may be underestimated because of their multiple detection against the elongated PSF.

¹Two Micron All Sky Survey, which is a joint project of the University of Massachusetts and the Infrared Processing and Analysis Center/California Institute of Technology, funded by the National Aeronautics and Space Administration and the National Science Foundation.

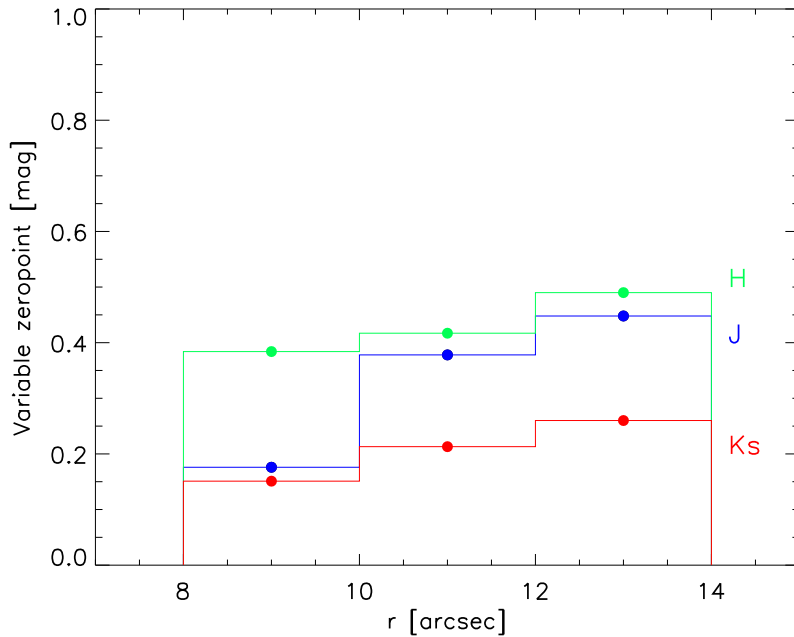


Figure 6.1: **Corrections of the anisoplanatic effect for the NACO photometry.** Offsets of magnitudes between the NACO and the ISAAC caused by the anisoplanatic effect is shown as a function of distance from the cluster center. In each annulus with a step of $1''$ within the outer NACO field ($r > 7''$), sources which coincide in both NACO and ISAAC photometry lists were used to derive an average $m_{NACO} - m_{ISAAC}$ offset. Sources in these outer regions in the uniformly calibrated NACO photometry lists were then calibrated with respect to the variable zeropoint in each band.

In order to deal with the anisoplanatic effect in the NACO photometry lists, we performed an additional photometric calibration by again using the ISAAC photometry lists. In each annulus with a step of $2''$ at $8'' < r \leq 14''$, we identified sources which coincide in both NACO and ISAAC lists, and computed a typical offset of $m_{NACO} - m_{ISAAC}$ magnitudes. The offsets as a function of the distance from the cluster center are shown in Fig. 6.1. A radial trend was observed in each band, which was a gradual increase of the offset with increasing radial distance. Subsequently, we performed a correction of photometry of sources in the NACO list using those variable zeropoints in each binned annulus. Note that, in this procedure, we used the values of average offsets in each bin instead of applying any analytical functions. Although the offset due to the anisoplanatic effect is expected to vary exponentially, we corrected the photometry by a step function considering the fact that the derived offsets mainly start to appear in the bin ($8'' < r \leq 10''$). Therefore sources in the inner regions were not corrected.

6.4 Photometric uncertainties

To estimate potential statistical photometric uncertainty of our PSF photometry, we derive the scatter in the flux measurement as a function of magnitude using the NACO 1st and 2nd data sets. Photometry of both data sets were carried out in the same manner, and so were the calibrations using the ISAAC photometry. Consequently the

Band	Number of frames ^a	Total integration time ^b at the center (s)	<i>FWHM</i> of PSF ^c ($''$)	Detection thresholds ^d in photometry (σ)	Number of detected sources ^e
NAOS-CONICA mosaics from the 1st run					
<i>J</i>	11	440	0.15	7	1807
<i>H</i>	17	765	0.13	7	3163
<i>K_S</i>	16	640	0.096	7	3688
NAOS-CONICA mosaics from the 2nd run					
<i>J</i>	127	5080	0.15	15	2589
<i>H</i>	36	1620	0.11	10	4228
<i>K_S</i>	39	1560	0.098	7	4269
<i>L'</i>	73	2190	0.12	4	1216
Short exposure					
<i>J</i>	15	157.5	0.16	11	480
<i>H</i>	15	157.5	0.12	10	1620
<i>K_S</i>	16	168	0.11	7	1677
ISAAC mosaics from the ESO archive					
<i>J_S</i>	36	2160	0.47	17	10106
<i>H</i>	59	3540	0.49	11	14089
<i>K_S</i>	58	3480	0.46	8	16105

Table 6.2: **Summary of mosaic frame properties.**

- ^a Total number of contributing frames to the final mosaic frames after frame selection with respect to the spatial resolution.
- ^b Total integration time of the most overlapping central region where all frames are contributing. This decreases towards outer regions from the center.
- ^c *FWHM* of the PSF extracted empirically from the mosaic frame and used in the flux measurement.
- ^d Detection threshold applied in the photometry in *XSTARFINDER* in unit of noise standard deviation calculated from the measuring mosaic frame.
- ^e Number of candidate sources detected in the PSF photometry.

estimate of the photometric error here does not provide any insight into a systematic uncertainty encompassed in our PSF photometry, however, provides an estimate of the statistical uncertainty in terms of repeatability of our PSF photometry.

The uncertainty for each band was derived as follows: 1) photometry results of the 1st and 2nd data were combined together to identify sources which coincide in the innermost $r \leq 13''$. Within a reasonable magnitude range in an $(m - \Delta m)$ plane for each band, a systematic offset between the two data set was determined, and subsequently one data was aligned to the other so as to cancel the systematic offset. 2) a standard deviation from the bias-corrected two magnitudes was derived for each identified source, 3) the standard deviations were binned along the magnitude (on the $\sigma - m$ plane), and a median value in each magnitude bin was derived as a typical value of the bin, and 4) a curve was fitted onto the median points and the curve represents the statistical uncertainty of the photometry. The results of the measurement are shown in Fig. 6.2. The reasonable magnitude ranges used for the curve fit are indicated by vertical dotted lines. The deviations out of the sampling magnitude ranges are most likely caused by differences of the linearity and the detection limits among both data sets. Standard deviations determined by the curve are then used as photometric errors in the following analysis, e.g., the CMD and CCD investigations in Chap. 8.

As mentioned above, the error estimate above shows merely a statistical uncertainty and the real photometric error would consist of systematic uncertainties as well. The corrected offsets in step 1 are likely to arise from the photometry calibrations, and these amount to ~ 0.09 mag in J - as well as H -band, and ~ 0.04 in K_S -band. A possible systematic which could be present but not corrected in our procedures is the uncertainty in the flux measurement in the PSF photometry, which is a function of the measured magnitude and is normally getting larger with increasing magnitudes. Since we have not performed an estimate of this type of systematic error yet, the presented statistical error would be a lower limit of the error associated with the photometry in this work. However this statistical error can be reasonably regarded as an indication of the scatter of the stellar distribution in the following investigations of cluster's fundamental properties mainly based on the CMDs and CCDs. Since we have only one data set on L' -band, inhibiting us from applying the same method on JHK_S data sets, we have not performed any estimate of photometric uncertainty for the L' -band data.

6.5 Photometry list

We construct a photometry list of $JHK_S(L')$ -bands detected sources of $m_J < 15.5$ mag in the innermost $r \leq 13''$ region (diameter of ~ 0.75 pc at $d \sim 6$ kpc) from the NACO data. This list encompasses all sources within the magnitude range on the projected plane, and any rejections of field stars have not been performed. The m_J threshold corresponds to ~ 95 % completeness (see Fig. 7.2). The assessment of incompleteness correction and the results will be presented in Sect. 7.1.

The photometry list of 256 detected sources is presented in Appendix A. Each source has an ID number, a coordinate, JHK_S magnitudes, and a L' magnitude in case of a source detected in the all four bands. The sources are aligned according to increasing m_J . The coordinates of the sources are indicated in their offsets from the cluster center (RA = $11^h 15^m 05^s .90$, Dec = $-61^\circ 15' 28'' .4$ (J2000)). Note that these equatorial coordinates are instrument-provided values, i.e., coordinates recorded in the FITS header information. To determine the center of the cluster, we computed a geometric center of the projected

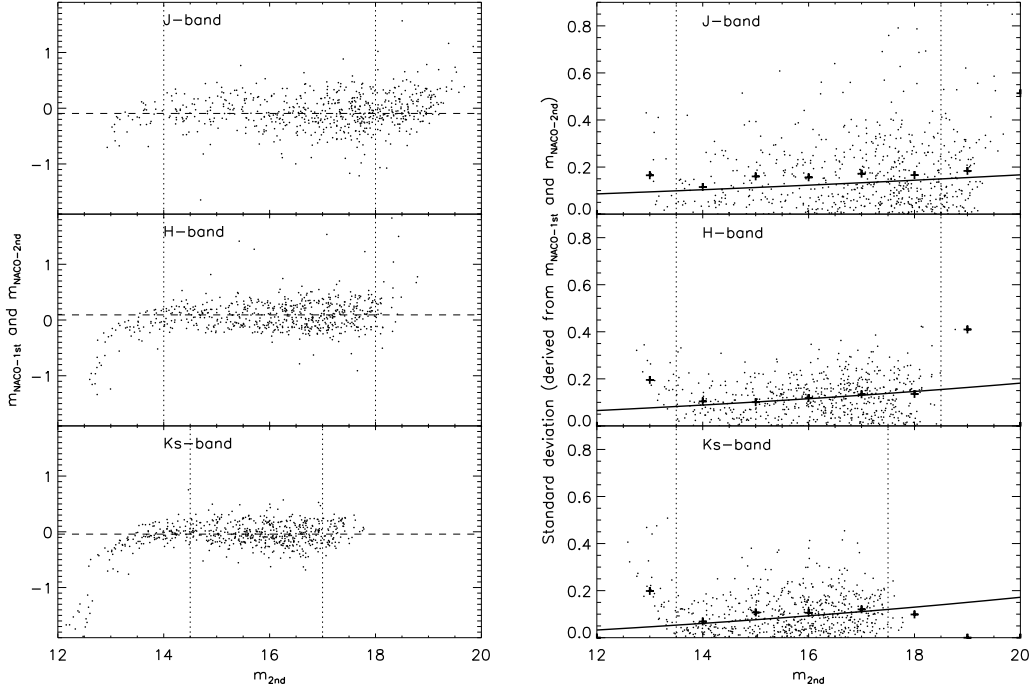


Figure 6.2: **Statistical errors in the photometry based on the NACO 1st and 2nd data sets.** *Left* panels: Differences of measured J , H , and K_S magnitudes of sources which coincide in the NACO 1st and 2nd data sets in $r \leq 13''$ are plotted in panels from top to bottom. Within a reasonable magnitude range indicated by two vertical dotted lines, an offset shown by the horizontal dashed line was determined as a systematic offset among the two data sets, and subsequently corrected for the following derivation of standard errors. *Right* panels: Estimates of statistical photometric errors. In each panel, individual points represent standard deviations calculated from bias-corrected magnitude differences of the coincide sources. In each band, plus symbols denote median values of standard deviations in magnitude bins and a solid curve illustrates a best-fit second-order polynomial curve onto the median points. The fit was performed within a reliable magnitude range, and the curve was used for deriving photometric errors as a function of magnitude in the analysis of CMDs and CCDs.

surface stellar density distribution. We note that the quality of the measured magnitudes in the PSF photometry provided in this list is considered to have moderate accuracy. Moreover, since the photometric calibration of the L' -band photometry was done by merely one data set of a single standard star, the presented L' -band magnitude has to be considered as a roughly-calibrated magnitude list. The spectral types are adopted from Crowther & Dessart (1998) (Tab. 8 therein), which consists of their stellar spectral types combined with those originated from Moffat (1983) and Drissen et al. (1995).

In case of sources which are identical or likely to be counterparts to objects in other studies, the designations or IDs as well as the corresponding references are presented. We perform identifications of sources with the HST optical detections presented in Moffat et al. (1994) (MDS94), with the ground-based mid-infrared detections in Nürnberger & Stanke (2003) (NS03), and with the optical detections (brighter than $V = 14$ mag) from the HST data set in Sung & Bessell (2004) (SB04). The identifications of sources are done by means of an eye inspection after making maps of the source lists in the references with the same scale as our NACO map. We obtain an impression that there seems to be some degree of position mismatches across fields among the maps due perhaps to differences of instrumental properties such as resolutions, sizes of field of view, and geometric distortions. Thus we use the eye inspection rather than applying any solid criteria, e.g., a tolerant distance of a coincidence in the cross identifications. As for designations of the counterparts, the source IDs in Melnick et al. (1989) (MTT) as well as the letters A1-3 to F (van den Bos, 1928; Hofmann & Weigelt, 1986) are simply adopted from Moffat et al. (1994).

Additionally, the X-ray counterparts obtained by the *Chandra* satellite in Moffat et al. (2002) are also indicated. We simply adopt the MDS94 sources with X-ray counterparts presented in the reference (Fig. 2 therein). Only bright WR and early O-type stars with X-ray counterparts are presented and, since the authors suggested that many detected X-ray sources might be low-mass PMS members, much more sources in our NACO list are expected to have X-ray counterparts. Since no list of X-ray detections were available, we are not able to perform an identification. As for the identification with the mid-infrared sources, since the spatial scale of our NACO near-infrared data is much smaller than that of the referring data in Nürnberger & Stanke (2003), a single mid-infrared source could be superposed with several near-infrared sources. In such a case, only a source which would have a dominant flux contribution at least in the near-infrared is presented. As mentioned above, since the cross-check was done simply by an eye inspection, the results of our mid-infrared counterpart identification should be considered to be a crude estimate.

In addition to the photometry list, we construct maps of the astrometry of the detected sources. The maps are shown in Fig. 6.3 and Fig. 6.4. Thanks to the unprecedented level of high resolution by the AO-assisted NACO system, we could identify objects in the highly crowded starburst cluster center, and perform the photometry from the brightest to the faintest stars. For the sake of visual clarity in the crowded core, a close-up map of the central region of $r \leq 5''$ is presented in Fig. 6.4. The numbers of sources in the plot are identical to the ID numbers in the photometry list in Appendix A.

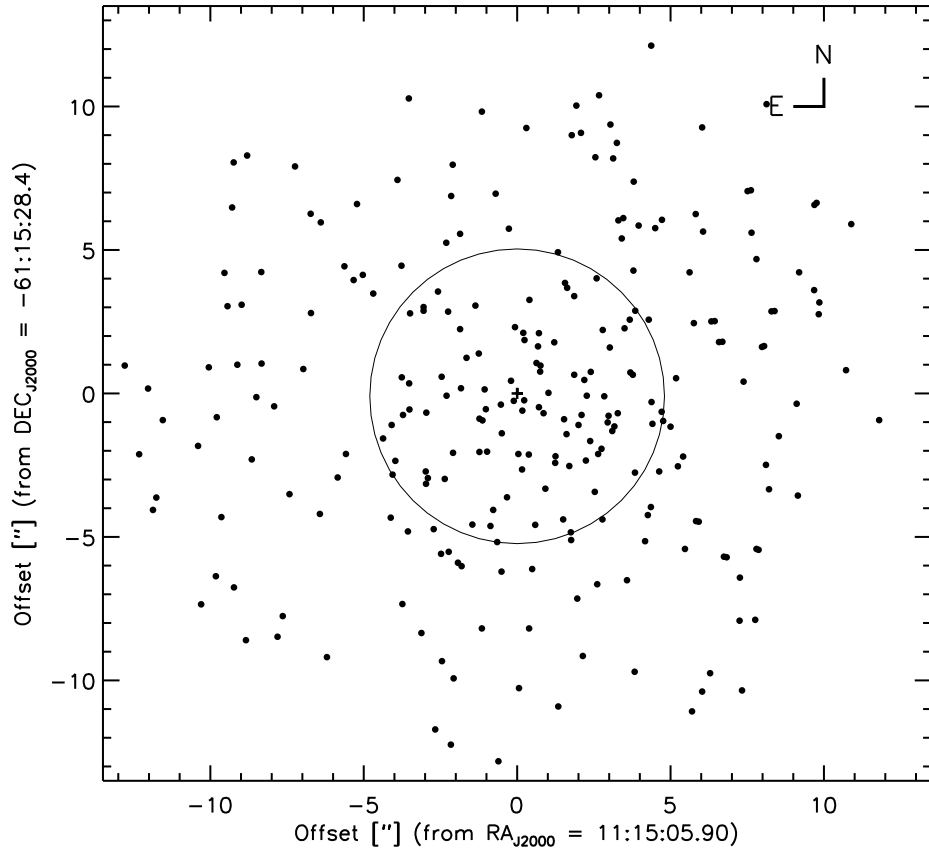


Figure 6.3: **Overview of a $26'' \times 26''$ (0.76×0.76 pc) astrometry map of the central cluster in NGC 3603.** The map contains 256 JHK_S detected sources brighter than $m_J = 15.5$ mag ($\sim 95\%$ completeness) in the central region $r \leq 13''$. A plus symbol indicates the determined center of the cluster. Offsets of sources from the center are listed in the photometry list in Appendix A. A circle indicates a close-up field of the central part of $r \leq 5''$ presented in Fig. 6.4. North is up and east is to the left.

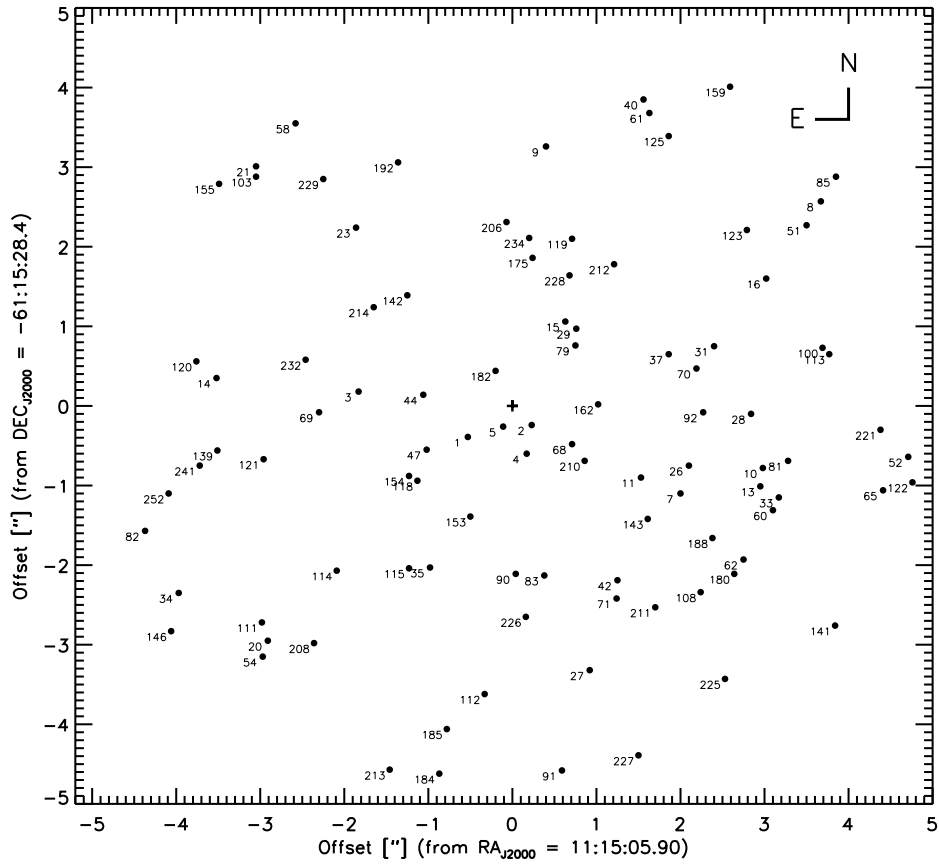


Figure 6.4: A close-up $10'' \times 10''$ (0.29×0.29 pc) field of the astrometry map shown in Fig. 6.3. This field contains sources in the innermost $r \leq 5''$. The source numbers in the photometry list (in Appendix A) are shown.

Chapter 7

Completeness and detection limits

In this chapter we investigate the effects of completeness and detection limits in our data. Two factors possibly affect the detections of sources: one is the crowding effect and the other is simply the sensitivity limit. In the crowded central cluster region in the NACO frame as well as the innermost region (up to $r \sim 30''$) in the ISAAC frame, the source detection is predominantly limited by the crowding effect of the highly concentrated stellar distribution, and hence an incompleteness correction is necessary for deriving LF and IMF of the cluster. In relatively sparse outer region in the ISAAC frame, the crowding is unimportant, and the S/N ratio simply determines the source detection. Therefore we first explain our incompleteness corrections which will be applied to the central field in the NACO frame as well as to the innermost ISAAC field. We then explain how we derive the sensitivity limit in the outer ISAAC field in each band by means of an artificial source detection analysis.

7.1 Incompleteness correction

We performed an incompleteness correction for our photometry results in order to provide more reliable quantitative assessments of the cluster LF and IMF. In this section we explain the procedure of the incompleteness correction we have applied in the present work.

Even in the case of our high spatial resolution imaging data from the NACO AO observations, the central region of HD 97950 shows an extremely crowded stellar distribution. The blending effect of bright sources to surrounding faint sources have made it difficult to detect faint sources in our study, which is essentially aiming to uncover stars as faint as ~ 20 mag in the JHK_S -bands. Therefore we should take into account the fact that a substantial fraction of faint sources are embedded in fluxes of bright sources and hence not detected in the raw outputs of our PSF photometry. Even in case of the wider field ISAAC data, these missing detections of faint sources in particular in the central part of the cluster need to be corrected. We have therefore performed an incompleteness correction for both the NACO and ISAAC photometry results.

In the reporting study we have employed the empirical method first introduced by Eisenhauer et al. (1998) for the ADONIS observation of NGC 3603, instead of the commonly applied statistical approach on the basis of recovery test of artificially added

7.1. Incompleteness correction

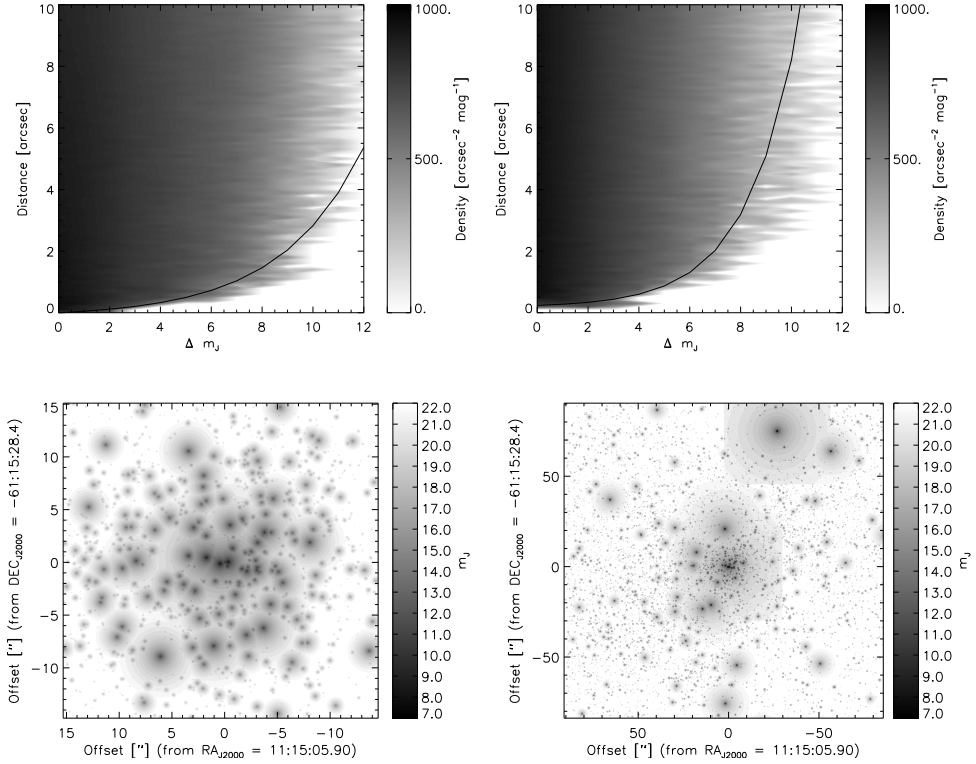


Figure 7.1: **Critical distance curve and the blending map derived from J-band photometry** (*left* panels are from NACO, and *right* panels are from ISAAC). *Upper* panels: a plot shows the scaled distribution $F(\Delta m_J, d)$ and the critical distance determined based on a curve fit to half the point of the converging density (which appears towards further distance) at each Δm bin (see description in the text). The color bar illustrates the density (frequency scaled by areas) in log scale, thus the darker color corresponds to a higher probability to detect a star. *Lower* panels: a plot illustrates the blending map coupled with the color bar of limiting magnitude constructed from each critical distance and J -band photometry of JHK_S detected sources.

sources in the photometry through Monte Carlo simulations. In our empirical method we used the measured data themselves, i.e., the spatial distribution and measured photometry of the observed sources to predict the probability of missing sources across the fields. In this idea of incompleteness correction, several basic assumptions are required.

i) The probability of the detection of a source with a given magnitude is uniform across the whole field of use irrespective of the difference in the stellar density distribution.

ii) Every object has a circular area around itself over which any sources fainter than Δm mag relative to the object can not be detected, and the size of this circular area depends on the difference in brightness Δm and is determined by the corresponding critical distance $d(\Delta m)$.

iii) At any point in the field, the blending effect is dominated only by the single brightest neighboring star, and the other neighboring stars do not contribute to the blending.

The technique of this incompleteness correction mainly consists of three steps. These are 1) the derivation of the *critical distance* using the obtained photometry, 2) the construction of the *blending map* using the critical distance and the photometry, and 3) the computation of the *incompleteness correction factor* based on the blending map.

1) Derivation of the critical distance

The critical distance $d(\Delta m)$ around a star of mag m_1 is the distance below which a star of mag $m_2 = m_1 + \Delta m$ can not be detected because of blending or crowding effects. To derive the critical distance, we first computed a distribution function $f(\Delta m, d)$ using the photometry of the JHK_S detected sources. For this we used J -band magnitude considering the fact that the detections of sources in our AO-assisted NACO as well as the diffraction-limited ISAAC observations are limited by J -band detections. This f illustrates how often two stars with a difference in magnitudes Δm and a relative distance d are found in the observation. Scaling f by the corresponding sampling annulus, the density distribution $F(\Delta m, d)$ should converge to a certain value towards large radii because stars do not blend with each other any more. No pairs of stars with distances smaller than the critical distance should be detected. Then from the decay of the distribution at small separations, a representative curve for defining the critical distance can be derived. The scaled distributions F and determined critical distance curves for the NACO and ISAAC data are shown in Fig. 7.1 (upper panels). Each curve was determined by a curve fit onto points at which the frequency distribution has *half* the value of the converged plateau towards the larger distance. Here we note that, although the ISAAC observations showed an expected distribution $F(\Delta m, d)$, the NACO data showed a slightly different characteristic in its distribution. Instead of showing the flat plateau, the $F(\Delta m, d)$ up to a certain Δm showed gradual decreasing slopes towards large d . This is probably due to the intrinsic characteristic of crowding. The stellar density distribution of the NACO field shows a gradient with a peak at the center and a decline towards the outer part even within the NACO central field. However, the determination of the critical distance curve with a careful eye inspection yielded a reasonable curve. We note that besides the critical distance from taking half of the value of the converged plateau in the frequency distribution, we create another critical curve by taking 2/3

of the value of the converged plateau. This selection therefore provides a somewhat *larger correction* option in the sense that it creates slightly stronger incompleteness correction factor. We construct this option too in order to investigate an uncertainty of the incompleteness correction on the IMF slope. We will discuss about this in Sect. 13.7.

2) Construction of the blending map

Applying the derived critical distances $F(\Delta m, d)$ back into the photometry, specifically, the J -band magnitudes and the coordinates of the sources, we can then make a map, over which all detected sources have the concentric circular areas of the blending effect around themselves. For this we binned the J -band magnitude with a bin size of 0.5 mag from 7.5 to 22 magnitude. Fig. 7.1 (right) show the constructed blending maps from the NACO and ISAAC data. We note that the saturation limit of the ISAAC data is ~ 12 mag in J -band, therefore the photometry of stars whose magnitudes are similar to or lower than this limit would be less accurate, and consequently the affecting area around such stars would be somewhat underestimated. As for very bright stars ($m_J \leq 10$), we employed magnitudes from the 2MASS database. Note that we needed to apply some simplifications so as to make our adopting method fit to the obtained data reasonably. One of the simplifications is that we set a limit of magnitude for bright stars at 7.5 mag in J -band. Therefore, although the 2MASS magnitudes are adopted for stars of $m_J \leq 10$, the brightest value is set at 7.5 mag. This is due to the fact that the brightest sources in the NACO data, in which there are no saturated sources, is $m_J \sim 7.5$ mag. Only one star brighter than 7.5 mag exists in our wider ISAAC field. Another simplification is that we set the maximum of magnitude difference at $\Delta m = 12$ mag within the magnitude range of 7.5 – 21.5 mag. The reason is the fact that, owing to the exponential increase on the critical distance curve at larger Δm , a critical distance of a very bright star towards the limiting magnitude could be determined unreasonably large. Thus it does not represent the real incompleteness effect on our frames. Because of this cut-off, as can be seen on the blending map of the ISAAC in Fig. 7.1, a bright star located at the north-west and the central core consists of many bright stars have square-shaped affecting areas instead of circular one.

3) Computation of the incompleteness correction factors

Using the constructed blending maps, we then calculated the *completeness fractions* for each magnitude bin. A completeness fraction of a magnitude bin is given by measuring a reciprocal proportion of the area over which a source with a given magnitude is detectable to the total area of the investigated field on the blending map. Therefore it is described as $\frac{A_{total} - A_m}{A_{total}}$, where A_m is a sum of the prohibited areas for the given magnitude and A_{total} is the total area. Then the *incompleteness correction factors* are given by taking the inverse of the corresponding completeness fractions, and are assigned to each source in the photometry as a weight for number counting in the following statistical analysis.

The incompleteness effect is not uniform but is strongly dependent on the stellar density across the projected field, and it is predominantly associated with the radial distance from the cluster center. The completeness is the lowest at the cluster center due to the heaviest concentration of stars, and it becomes higher towards outer regions.

This variation, therefore, has to be taken into account in the derivation of correction factors, and hence we applied the variable correction factors in the analysis of the radial density profile, LF, and IMF instead of applying a global correction factor. In case of the LF and IMF, the incompleteness correction factors are calculated from concentric annuli with a width of $2''$ for the inner part ($r \leq 13''$) of the NACO field and $10''$ for the outer part ($13'' < r \leq 110''$) of the ISAAC field so as to take into account the spatial variation, as well as to somewhat smooth out possible local effects. We note that, in the derivation of correction factors, some sources, especially, those in the central region would have very high weights due to the exponential feature of the critical distance curve, and some have no weight because of the possible presence of sources which were indeed detected in the photometry but are not supposed to be, according to the critical curve. In order to accomplish realistic incompleteness corrections, we therefore set a maximum weight at 10 corresponding to corrections of populations up to 10 % completeness limit.

To illustrate the radial variation or trend of the completeness, we calculated completeness fractions from four distinct regions with increasing radius from the cluster center (Fig. 7.2). As shown in the figure, the inner part of the field has the lower completeness due to the higher density of stars. Note that, in this empirical method, the observed data itself was used for the derivation of completeness fractions and corresponding correction factors, therefore some local effects can appear in case of taking a small step (e.g., $1''$) for the width of sampling annuli. However, normally it is considered that the variation of completeness in the stellar cluster is a function of radial distance from the cluster center, and it changes smoothly towards the outskirts.

7.2 Detection limits

In the wider ISAAC field of view, the incompleteness is present in the innermost part of up to $r \sim 30''$. But the source detection in the rest of the field is limited simply by the detector noise. In order to investigate faint- and low-mass ends of the luminosity functions and mass functions of the cluster, our actual detection limits by the sensitivity need to be assessed. We therefore performed tests of artificial source detections using a sample region in the ISAAC field. The sample region is located in the north-eastern part of the field, and is sufficiently apart from the central cluster to be sparse. In each band we constructed a stellar PSF by sampling several bright and isolated stars, and placed 30 artificial stars made from the PSF with a fixed magnitude randomly into the sample frame. We added the artificial stars with varying stellar magnitude in a step of 0.2 mag between 18 and 21 mag, and performed the PSF photometry with the *XSTARFINDER*. Note that the number of artificial sources corresponds to about 2 – 3 % of total number of detections in the original frames in all *JHK_S*-bands experiments. We used a single set of 30 coordinates, which was randomly generated, to all frames.

The resultant recovery rates as a function of apparent magnitude are shown in Fig. 7.3. Defining a 50 % recovery rate as a detection limit, the limits are about 20.5, 19.8, and 19.7 mag in *J*, *H*, and *K_S*-bands, respectively.

In this seeing-limited ISAAC observations, the *J*-band detection limit shows the deepest apparent magnitude among the three bands. However, considering the typical *J* – *K_S* color of ~ 1.8 for low-mass PMS stars, it is indicated that the *J*-band photometry in fact limits our source detections in the ISAAC data as the case in the AO-assisted NACO data.

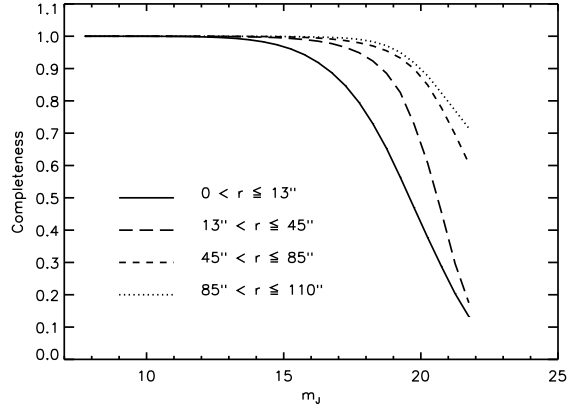


Figure 7.2: **Completeness fractions.** Curves show the completeness fractions as a function of the observed J -band magnitude. To illustrate its variations depending on the distance from the cluster center, completeness fraction curves calculated from four distinct radial regions are shown. Using the blending maps of NACO and ISAAC, a completeness fraction for each distinct region in the magnitude range of 7.5 – 21.5 mag with a bin size of 0.5 is determined by measuring the ratio of the observable- to total-areas within the investigated area. Then corresponding correction factors are used for the correction of number counting in the radial profile, LF, and IMF constructions.

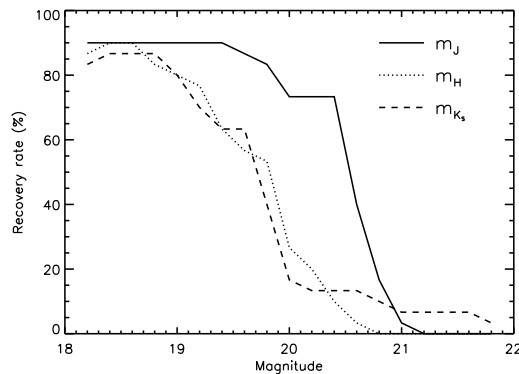


Figure 7.3: **Detection limits in outer regions in the ISAAC field.** Recovery rates as functions of magnitudes in the artificial star experiments are shown. A solid, dotted, and dashed lines indicate the rates in J , H , and K_S -bands, respectively.

Chapter 8

Color-magnitude diagrams and color-color diagrams

Color-Magnitude Diagrams (CMDs) and Color-Color Diagrams (CCDs) are the standard diagnostic tools to investigate stellar populations of star cluster like NGC 3603. The comparisons of the magnitudes and colors of the observed stars with stellar evolutionary models provide a large variety of information about the cluster, for example, its distance, age, and the interstellar extinction towards the cluster. The colors and magnitudes provide also information about the individual stars, allowing to probe the membership, the evolutionary status, and the individual extinction and infrared excess emissions from circumstellar dust and disks.

8.1 Fundamental properties of NGC 3603

We have investigated the fundamental properties of NGC 3603 by building the CMDs and CCDs of the central field of the cluster from the NACO data, and a wider field from the ISAAC data. This allows us in particular to prove for radial variations in the stellar population.

In comparison, the NACO observations offer a variety of advantages over the ISAAC observations. First, the NACO observations includes images with short and long exposure times. The combined data covers a wide range of the stellar fluxes from the brightest stars of magnitudes of $m_J \sim 8$ mag to the faintest detected stars of ~ 20.5 mag. Specifically the photometry of the bright MS population therefore helps us to measure the interstellar extinction to the cluster. Second, the high spatial resolution of the NACO data reduces the uncertainty from potential binaries which are less resolved in the seeing-limited ISAAC data. Third, the innermost field suffers less from nebulae emission, which is mainly located towards the south-west region from the central cluster (see Fig. 5.1). And forth, the central field with its much higher stellar density is statistically less affected by contamination from field stars. All that leads to significantly lower scatters in the CMDs and CCDs.

Since the young star-forming region NGC 3603 hosts a large population of low-mass PMS stars together with a MS population of more massive stars (plus possibly an earlier generation), there is a substantial fraction of stars on the PMS-MS transition region in the CMD. In this transition region the isochrones of stars lie roughly horizontal in the CMD. The apparent magnitude of the features allows us to assess the cluster's age and

distance by means of isochrone fitting. The following sections outline this analysis and present the results.

8.1.1 Distance

Many earlier studies have addressed the distance of NGC 3603 (Moffat, 1983; Melnick et al., 1989; Crowther & Dessart, 1998; Eisenhauer et al., 1998; De Pree et al., 1999; Pandey et al., 2000; Nürnberger et al., 2002; Stolte et al., 2004; Sung & Bessell, 2004). The currently accepted value from these photometric and kinematic studies is about 6 – 8 kpc.

From their *UBV* photometry investigation Melnick et al. (1989) derived 7.2 kpc, whereas Pandey et al. (2000) derived 6.3 ± 0.6 kpc from their optical photometric study. In the most recent optical analysis Sung & Bessell (2004) derived 6.9 ± 0.6 kpc, fitting the observed cluster sequence including its PMS population in the CMD. Based on NIR photometry, Stolte et al. (2004) derived the distance as well as the foreground extinction focusing on the PMS-MS transition region. Our study is based on the same ISAAC observation data used in this article. The authors derived a distance modulus of $(m - M)_0 = 13.9$ mag corresponding to $d = 6.0 \pm 0.3$ kpc. Their photometric distance is quite similar to the kinematic distance of 6.1 ± 0.6 reported by De Pree et al. (1999) based on the radio continuum surveys, and is slightly smaller than another kinematical distance estimate of 7.7 ± 0.2 kpc in the recent work by Nürnberger et al. (2002).

Our infrared photometry can not constrain the distance any better without having any knowledge about the spectral type of the cluster’s components. The complexity is as follow: the distance determination can in principle be performed fitting an isochrone to the PMS-MS transition region and the PMS turn-off in the CMD. The shape and location of the isochrones in fact depend on the age, distance, and foreground extinction.

However, the dependency on age and distance is strongly degenerate: An older stellar population at smaller distance exhibits the PMS-MS turnover at similar magnitude as a more distant younger cluster. The subtle difference in the detailed shape of the transition, for example the slope and change in color, is hardly detectable within the photometric uncertainties. We therefore adopt $(m - M)_0 = 13.9$ mag throughout the following analysis, and strict ourselves to a consistency check.

Assuming a 2.5 Myr isochrone from the Geneva stellar evolutionary models (Lejeune & Schaerer, 2001) for the MS population and a 0.7 Myr PMS isochrone created from the PMS models from Palla & Stahler (1999) (see Sect. 8.1.2), and applying our best estimate of the interstellar extinction $A_V = 4.5$ mag (see Sect. 8.1.3), the adopted distance modulus of 13.9 mag provides a reasonable match with the observed CMD. The error is estimated to ± 0.3 mag in distance modulus from a visual inspection. This corresponds to a distance $d \sim 6.0 \pm 0.8$ kpc.

8.1.2 Age

The age of NGC 3603 has been estimated to be from several tenths Myr to about 3 Myr. The age estimates are derived from fitting isochrones to the observed CMD, and by analyzing the spectra of the most massive stars in the cluster. The estimate of the age based on the isochrone fitting technique has been performed in many studies (Eisenhauer et al., 1998; Brandl et al., 1999; Pandey et al., 2000; Sagar et al., 2001; Stolte et al., 2004; Sung & Bessell, 2004). The age estimated from the PMS population is slightly smaller than the results from the MS population, but overall the age has been estimated to be within 0.3 – 1 Myr.

In particular, the age has been deduced from the evolutionary status of the massive stars. The presence of Wolf-Rayet (WR) stars and early O-type stars in the cluster indicates that the cluster is not more than several million years old. The presence of WR stars and numerous OB-type stars in a volume of less than a cubic light year in the starburst cluster has been suggested by (Walborn, 1973; Moffat, 1983, 1985). Based on spectroscopy and photometry taken with the HST, the three brightest members designated A1, B, C in the highly luminous central component HD 97950 have been classified to be WN6ha stars, leading to the cluster age of ≤ 2.5 Myr (Moffat et al., 1994; Drissen et al., 1995; Crowther & Dessart, 1998).

Based on the isochrone fitting of the $(J_S - K_S, J_S)$ CMD, and taking into account a potential age spread on the PMS-MS transition, an observed binary sequence, and the age constraints from the massive stars, Stolte et al. (2004) suggest 1 Myr as a common age for the MS and PMS populations. In this scenario the starburst cluster in NGC 3603 is formed in a single star formation event. Also Sung & Bessell (2004) derive an age of $1 (\pm 1)$ Myr, fitting isochrones to the optical CMD from the HST observations.

In this study we present an age estimate from fitting isochrones to the NIR CMD of the central $r \leq 13''$ field. In particular we focus on the shape of the CMD in the PMS-MS transition region to derive the age of the PMS population, as well as on the most massive stars for the age estimate of the MS population.

Fig. 8.1 shows the $(J - K_S, J)$ CMD of the 1158 JHK_S detected stars in the central region ($r \leq 13''$) of the NACO data. In order to fully cover the observed mass range from high-mass MS stars of several tens of solar masses down to low-mass PMS stars with masses close to the hydrogen burning limit, we have used three stellar evolutionary models. The MS population is covered by the Geneva stellar evolution models (Lejeune & Schaerer, 2001). For PMS population we use two models for two mass ranges. For the high-mass PMS population we use the isochrones from Palla & Stahler (1999), and for the low-mass PMS population we employ the isochrones from Baraffe et al. (1998). Hereafter we designate those models as LS01, PS99, and BCAH98, respectively. The blue, green, and red curves illustrate the MS isochrones from LS01, the PMS isochrones from PS99, and the low-mass PMS isochrones from BCAH98, respectively. The age of the isochrones is coded in brightness. Note that the offset between the measured distribution and the isochrones is dependent on the adopted distance and interstellar extinction. Here we apply the best estimates of the distance modulus of $(m - M)_0 = 13.9$ mag and a global extinction of $A_V = 4.5$ mag. This extinction is derived from the isochrone fitting presented in the next sections applying an extinction law from Rieke & Lebofsky (1985).

We have assumed a solar metallicity for all isochrones. Considering the similar Galactocentric distances of NGC 3603 and the Sun in the Milky Way in which the metallicity shows the centric gradient feature, the assumption is expected to be reasonable (see e.g. Rudolph et al., 2006). The uncertainties in the IMF determination from this assumption is discussed in Sect. 13.5.

First we compare the PMS population with the PS99 isochrones. Taking into account the age constraint of ≤ 3 Myr arose from the presence of the most massive O3 stars in this starburst cluster, we restrict the comparison to the 0.3, 0.5, 1, and 3 Myr isochrones.

Focusing on the offset between the isochrones and the observed stellar distribution in the PMS-MS transition region (approx. $0.7 < J - K_S < 1.4$, and $14 < J < 16$ mag), we can exclude an age of 3 Myr fairly convincingly. Also the 0.3 Myr isochrone is slightly offset from the center of the somewhat scattered stellar distribution in the

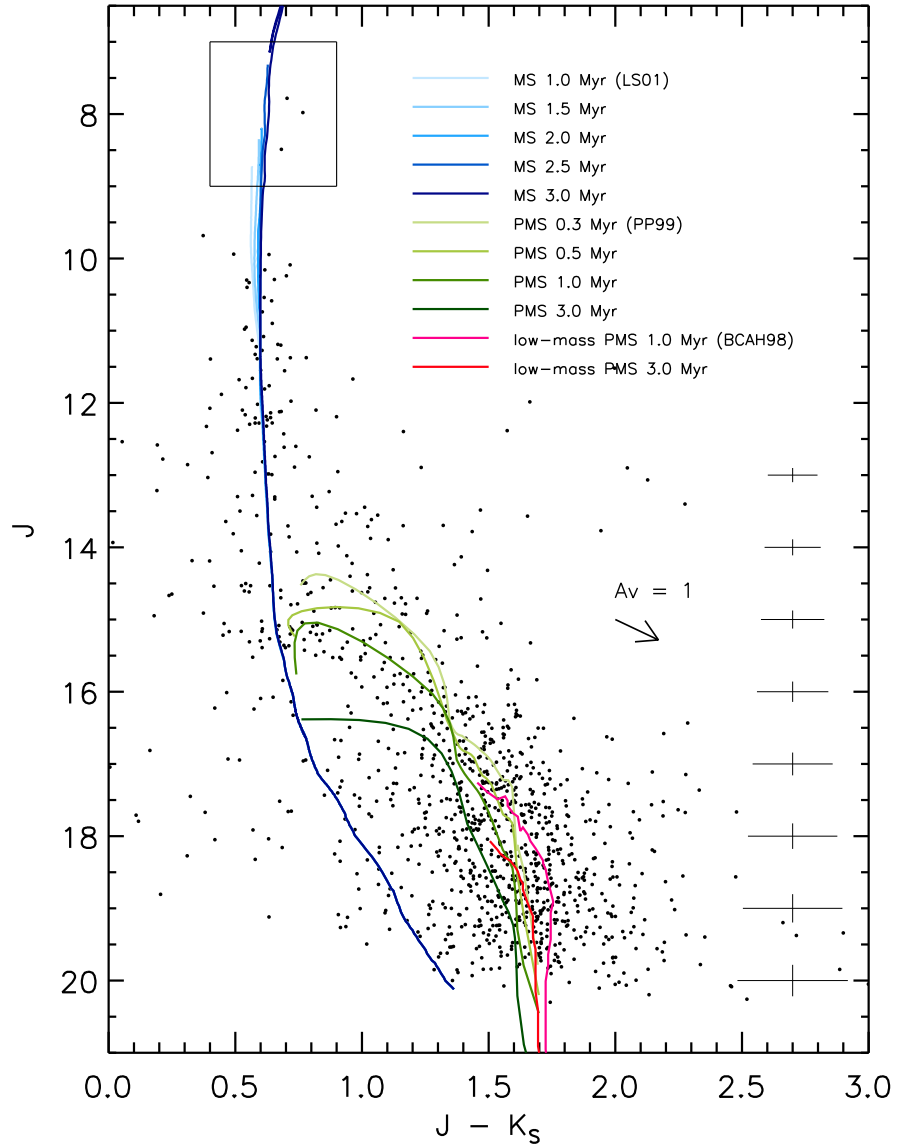


Figure 8.1: **Color-magnitude diagram of NGC 3603.** The plot shows $J - K_S$ colors and J magnitudes of the 1158 JHK_S detected sources in the inner region ($r \leq 13''$) of the NACO observations. Curves in blue, green, and red are the MS isochrones from the Geneva stellar evolutionary models (Lejeune & Schaerer, 2001), the PMS isochrones from Palla & Stahler (1999), and the Low-mass PMS isochrones from Baraffe et al. (1998), respectively. The brightness of the curves indicate the age of the isochrone. The isochrones are plotted after corrections with respect to a distance modulus of $(m - M)_0 = 13.9$ mag and average interstellar extinction of $A_V = 4.5$ mag. An arrow illustrates the reddening for an extinction of $A_V = 1$ mag. The error bars on the right side give the statistical errors (see Sect. 6.4). The errors in the color are computed from a quadratic sum of the J and K_S magnitudes for a typical color of $J - K_S = 1.5$ mag. The box indicates a zoom on the three brightest stars shown in Fig. 8.2.

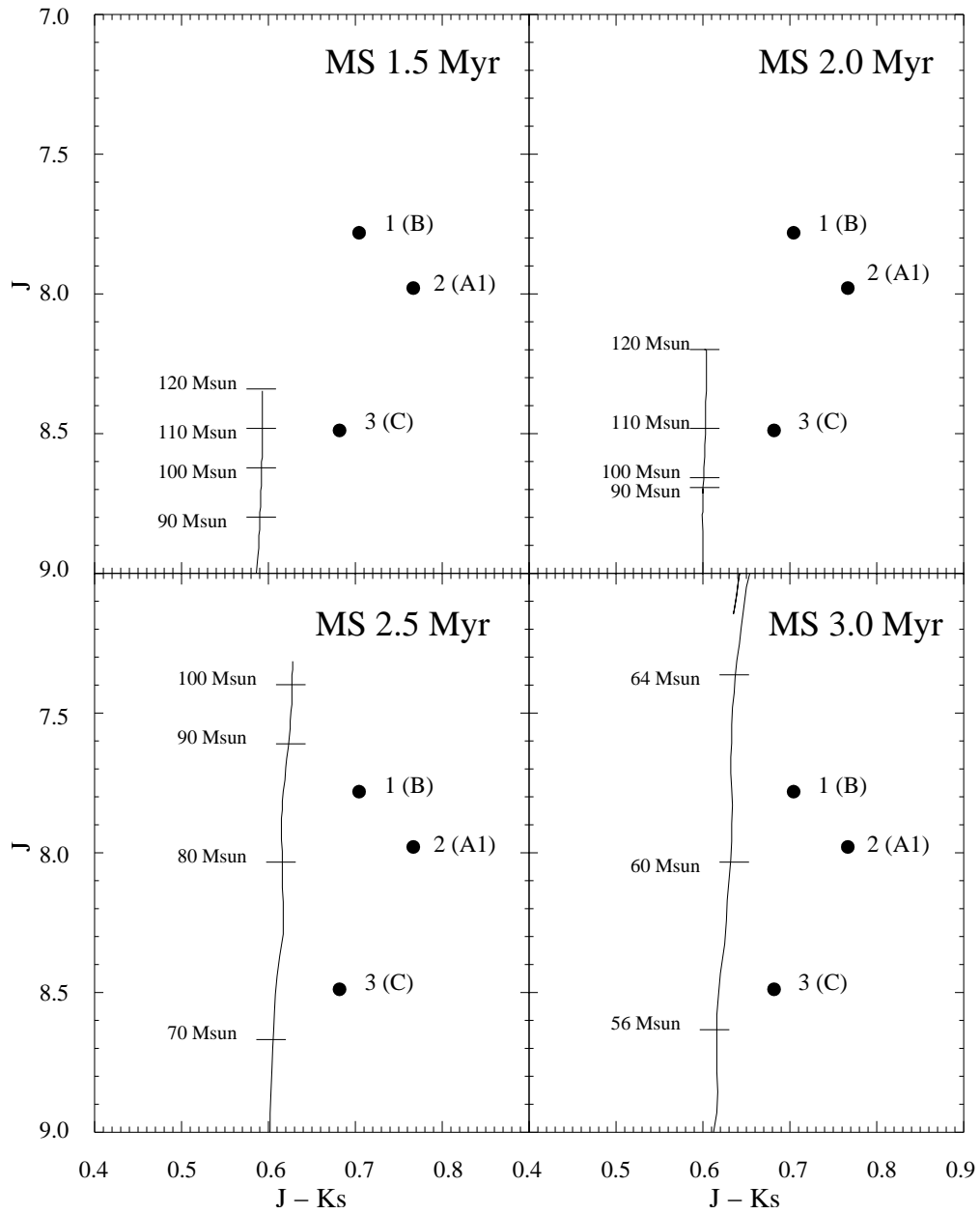


Figure 8.2: **CMD of the brightest stars.** The panels show the 1.5, 2, 2.5, and 3 Myr LS01 isochrones together with the three brightest WR stars 1 (B), 2 (A1), and 3 (C). The designated source numbers correspond to the photometry list presented in Appendix A. Stellar initial masses are indicated along the isochrones.

PMS-MS transition. The other two isochrones - 0.5, and 1 Myr isochrones - fit the PMS-MS transition region reasonably, thus choosing between the 0.5 and 1 Myr is not easy. Therefore we argue that the best-fit age is between 0.5 and 1 Myr, and in the following we use a 0.7 Myr isochrone constructed from a linear interpolation of these two isochrones.

In the recent study using the ISAAC data set by Stolte et al. (2004), the authors suggested a possible presence of a sequence of equal-mass binaries, which stretches along the MS and PMS-MS transition regions. This leads to the interpretation that the star formation history in NGC 3603 is consistent with a single star formation event ~ 1 Myr ago (see also discussions in Sect. 13.8). While we have found no obvious secondary sequence but a scattered distribution in the PMS-MS transition region. This scatter appears to be larger than the error bars, which are derived from the statistical error estimate in Sect. 6.4. The difference could be due to a combination of photometric and other uncertainties such as field star contamination and potential individual extinctions. However, the scatter is due to the photometric uncertainty to some extent, and also could be due to an intrinsic age spread of the PMS populations of about several hundred thousand years. Alternatively, this could reflect a possible variation in the time necessary for the core formation and the subsequent contraction phases in the protostar evolution before the main PMS evolutionary phase. The zeropoint in the PS99 PMS models is defined to be the birthline, which is the point at which the protostellar accretion process ceases, and the quasi-static contraction phase starts so that the object becomes visible (Stahler, 1983). Hence, even in case of a single event triggering the star formation in the molecular cloud, the age estimate based on the PS99 PMS models will vary from star to star, because the time required to form the protostellar core and to finish its accretion to reach the birthline varies with the local physical conditions. Assuming a typical mass accretion rate of $10^{-5} M_{\odot} \text{ yr}^{-1}$ (Stahler et al., 1980), the pre-birthline contraction phase lasts for several 10^5 yr for a star with several M_{\odot} star. This could result in the apparent scatter in the CMD even for a single star-forming event. Moreover, collapse and accretion processes in the protostar formation are not fully understood, causing a significant uncertainty in the birth line. Therefore it is difficult to discuss an age spread in a young stellar population whose age is ≤ 1 Myr, for which the age discrepancy between the available PMS evolutionary models becomes larger partly due to dependence of the initial conditions (e.g., discussions in Tout et al., 1999; Baraffe et al., 2002).

Taking into account these uncertainties, we summarize that the age of the PMS population is around 0.5 – 1.0 Myr based on the application of the PS99 isochrone, and assume an average age of 0.7 Myr for the luminosity-mass conversion in the following determination of the IMF. For the low-mass PMS stars with a mass less than $1.2 M_{\odot}$, we apply the 1 Myr isochrone from the BCAH98 model. Unfortunately there are no isochrone available for stars with such low-masses and age of less than 1 Myr. However, the 1 Myr BCAH98 isochrone nicely fits the observed CMD, and the 1 Myr is still consistent with our estimate of 0.5 – 1.0 Myr. We thus expect only little impact from the slight deviation from our best age estimate of 0.7 Myr.

Finally, we compare the MS population with the LS01 isochrones. We put a particular focus on the locations of the three bright members 1 (A1), 2 (B), and 3 (C) in the CMD. Since the presence of massive stars such as WR and early O-type stars confine the age of the population within a few million years (e.g., Meynet & Maeder (2003) for time scales of high-mass stellar evolution with rotation), we compare the observed

magnitudes and colors with the 1, 1.5, 2, 2.5, and 3 Myr isochrones from the LS01 evolutionary models.

As can be seen in Fig. 8.1, all LS01 isochrones follow almost the same track up to $m_J \sim 11$ mag, and then start to show slight divergences in the horizontal direction at higher luminosities. However, those variations are within our errors in the $J - K_S$ color. The only age indication from the isochrones is the luminosity of the most massive stars.

Fig. 8.2 shows the CMD of the three brightest stars together with the 1.5, 2, 2.5, and 3 Myr LS01 isochrones. In order to determine the age of the high-mass MS stars, we need to assume initial masses of the stars. As mentioned above, the three brightest stars are classified as WN6h+abs stars based on the HST spectroscopic observations by Crowther & Dessart (1998), and the authors derived the current masses of about $60 - 100 M_\odot$. The likely initial masses of the WN stars is expected to be $\geq 120 M_\odot$.

We therefore assume initial masses of the WN stars to be about $80 - 120 M_\odot$ (this is deduced from a plot of stellar luminosities and surface hydrogen mass fractions combining a theoretical tracks in Crowther & Dessart (1998)). Taking into account these initial masses, we can see in Fig. 8.2 that both 2.0 and 2.5 Myr isochrones produce reasonable matches over the bright components. Although the 2 Myr isochrone can not be clearly excluded, the best match for all three stars is the 2.5 Myr. We therefore adopt the 2.5 Myr isochrone for the subsequent construction of the single isochrone for the luminosity-mass conversion. We note, however, that this age estimate should be treated with caution because the mass determination of the WR stars and other O-type stars in NGC 3603 is affected by potential observational and theoretical uncertainties.

It is worth mentioning that potential binary/multiple systems in the three WN6 stars would be insignificant in our age estimate. In a study based on J -band light curves using HST NICMOS data, Moffat et al. (2004) suggested that one of the two outstandingly bright stars A1 is possibly an eclipsing binary system with a $30 - 90 M_\odot$ H-rich WR component (WN6ha) and a $25 - 50 M_\odot$ O star companion. However, the rest of the bright members, B and C did not show variabilities in their detection level. Although B, indeed, has been suggested to be a binary system (found in Moffat & Niemela (1984), confirmed in mof85 and supported in Drissen et al. (1995)), no sign of binarity was found in this variability study in Moffat et al. (2004). Even though the source B is assumed to be a binary system, Crowther & Dessart (1998) derived the contribution from the companion, which is assumed to be a O3-5V star, of ~ 0.1 mag, being a negligible contribution.

One potential uncertainty is the still unclear nature of the three WN6 stars in HD 97950. For example, strong hydrogen absorption features have been detected in their spectra, leading to the hypothesis that they are more likely hydrogen-rich, extremely luminous main sequence stars that have not evolved but have mimicked WR features with generating strong, hot stellar winds (Drissen et al. (1995); see also Schmutz & Drissen (1999); Moffat et al. (2002) about a discussion of those objects' anomalous brightness in X-ray). Walborn et al. (2002) reported that they identified two O2 - O3.5 III(f*) stars - spectral types introduced in the article - in the core. The O2 star is thought to be a star in an immediate pre-WN evolutionary state. Therefore, if those sources are indeed such very luminous main sequence stars, the cluster's age would be smaller than our estimate. It could be about 1 Myr, allowing an interpretation of a single star-forming event for both the low-mass PMS and high-mass MS stellar population.

If our age estimate from the isochrone fitting holds, we would be confronted with a puzzling inconsistency or a real age spread among the $0.5 - 1$ Myr old PMS population

and the 2 – 2.5 Myr MS population. One possible explanation for the age spread is that, several massive stars first formed in the center of the natal molecular cloud, and subsequently the strong winds and radiation from those massive stars have triggered a second generation of low-mass stars. Therefore it would be possible that this extreme starburst cluster has undergone star formation over several million years.

In addition to this hypothesis of a somewhat extended star formation in the cluster center, previous studies have been suggesting sequential star formation throughout the giant HII region. Sher 25 (Sher, 1965; Moffat, 1983), for example, has turned out to be an evolved post-red supergiant with hour glass shaped nebula, which is excited by the HD 97950 stars (Brandner et al., 1997). These BSGs have an age of typically 10 Myr. Therefore if these stars indeed physically belong to NGC 3603, there should be at least two distinct episodes of star formation in NGC 3603 separated by about 10 Myr. However, we note that, whether or not Sher 25 is a cluster member is not clear yet (Crowther et al., 2007). Other studies have been suggesting sequential and ongoing star formation from north to south (Melnick et al., 1989; Hofmann et al., 1995; De Pree et al., 1999; Tapia et al., 2001; Nürnberger et al., 2002; Sung & Bessell, 2004).

Therefore we have to keep it in mind that some fraction of stars in the observed population could be sources which formed in earlier epochs. However, the high-mass stars which formed for example 10 Myr ago would have exploded in a supernova. Therefore most of the observed high-mass stars can safely be considered to be part of several Myr old population of the cluster center.

Because of their very long contraction time-scales, the low-mass stars can not be in the main sequence stage yet. For example, $2 M_{\odot}$ low-mass stars do not reach the ZAMS stage as readily seen in Fig. 8.1, in which the 3 Myr PMS isochrone is still located on the PMS population. This is supported by the fact that almost no stars have been detected in the low-mass MS regime in optical observations (Sung & Bessell, 2004; Grebel, 2004). Applying a field star correction, Sung & Bessell (2004) found no MS population for $M \lesssim \sim 4 M_{\odot}$ in their optical observation (see Fig. 7 and related analysis therein). The absence of low-mass MS stars is also reported in Grebel (2004) who derived the IMF and mass segregation of NGC 3603 from HST optical observations. This indicates the fact that most of the stars detected in the cluster are thought to belong to the several Myr old population.

Therefore the main objective of our study - the measurement of the IMF and its interpretation - is not significantly affected by this possible mixture of stellar generations.

In summary, combining the isochrone fitting to the PMS and MS population, we conclude that NGC 3603 has undergone a somewhat extended star formation history, and, on the basis of the application of PS99 isochrone we estimate that the PMS population predominantly formed 0.5–1.0 Myr ago. As mentioned above this somewhat depends on the isochrone models of use, our estimate is consistent with determinations in the recent studies (Eisenhauer et al., 1998; Stolte et al., 2004; Sung & Bessell, 2004). As for the MS population, although we apply the 2.5 Myr isochrone, this determination is based merely on the isochrone fitting to the three WN stars and hence is still uncertain. We therefore conclude 2.5 Myr as an upper limit of the age of the cluster population.

A further discussion about potential mechanisms for the sequential star formation history is beyond the scope of our investigation. The impact of the age uncertainties on the derived IMF will be discussed in detail in Sect. 13.1.

Luminosity to mass conversion

In order to construct the IMF, the stellar masses have to be derived from the obtained photometry. We have adopted a method in which a mass of a single source is directly derived from its observed JHK_S magnitudes using the best-fit isochrones from the previous section. For that we have created a single luminosity-mass conversion relation by connecting the three isochrones for the various mass ranges. The isochrone was created from the 2.5 Myr LS01 isochrone for the MS population down to $\sim 4 M_\odot$, the 0.7 Myr PS99 isochrone for the PMS population from $\sim 4 M_\odot$ down to $\sim 1.2 M_\odot$, and the 1 Myr BCAH98 isochrone for the even lower-mass PMS population. Among currently available PMS evolutionary models, the BCAH98 model has been reported to have the best consistency with dynamical mass determination for stellar mass below $1.2 M_\odot$ (Hillenbrand & White, 2004).

Fig. 8.3 shows the (Stellar mass - M_J) relation for the combined isochrone. The turnover around $2 - 4 M_\odot$ is originating from the PMS evolution. According to a study of the protostellar evolution by Iben (1965), the radiative tracks of PMS stars ($\geq 1 M_\odot$) show a luminosity maximum associated with the occurrence of ignitions of some of the CNO-cycle reactions at the end of the contraction phase just before reaching the main sequence. In particular stars with $M \geq 1.25 M_\odot$ show double luminosity maxima and minima, which also become noticeable in the HD diagram, just before beginning the hydrogen burning.

Note that, since there are indeed several evolutionary models from different groups that can be used in the mass determination, we estimate the potential influence of the selection among currently available models on our derivation of the IMF of NGC 3603 in Sect. 13.4.

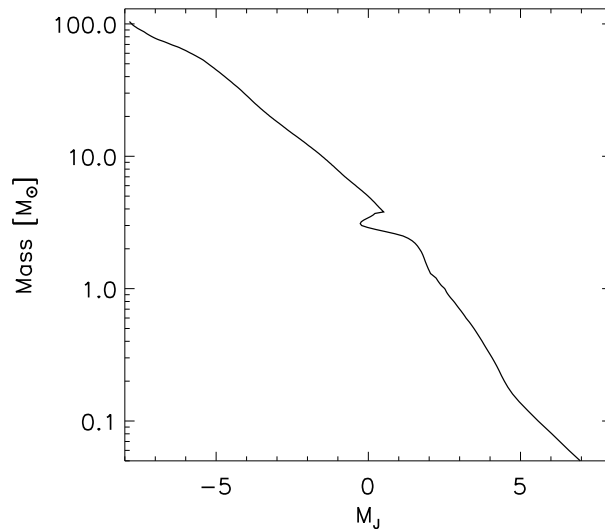


Figure 8.3: **Combined luminosity-mass conversion relation constructed from the best-fit isochrones.** The relation was created from the 2.5 Myr LS01 isochrone for the MS population down to $\sim 4 M_\odot$, the 0.7 Myr PS99 isochrone for the PMS population from $\sim 4 M_\odot$ down to $\sim 1.2 M_\odot$, and the 1 Myr BCAH98 isochrone for the PMS stars with even lower-masses.

8.1.3 Interstellar extinction

The line-of-sight interstellar extinction towards NGC 3603 has been estimated in previous studies. The average value is around $E(B - V) = 1.44$ mag (Moffat, 1983; Melnick et al., 1989; Crowther & Dessart, 1998; Pandey et al., 2000; Sagar et al., 2001; Sung & Bessell, 2004; Stolte et al., 2004), with only little variation. As for the distance and age, the interstellar extinction can be determined from the isochrone fitting to the observed CMDs. Here we present an analysis of the NACO observations for the cluster center with $r \leq 13''$.

As mentioned above, the determinations of the distance, age, and extinction on CMDs are dependent each other. The extinction estimate, however, is *to some extent* independent thanks to the fact that, in the $(J - K_S, J)$ diagram, the reddening vector, i.e., the direction of the shifting adjustment of isochrones, is almost horizontal, and that the MS isochrone for intermediate to bright stars stretches almost vertically. The interstellar extinction can thus be determined to some extent independently from the distance determination, which is done by shifting the isochrone vertically.

Fig. 8.4 shows the $(J - K_S, J)$ CMD of the central cluster ($r \leq 13''$) with the combined isochrone from Sect. 8.1.2. We adopted the best estimate of the distance modulus of $(m - M)_0 = 13.9$ mag. The three curves illustrate the isochrone shifted by a visual extinctions of $A_V = 4.0, 4.5, 5.0$ mag. The visible extinction was converted to the near-infrared extinction using the reddening law by Rieke & Lebofsky (1985). The isochrone with a shift of $A_V = 4.5$ mag matches best the MS distribution for intermediate to high-mass stars. Also the PMS population of the central cluster ($r \leq 13''$) is well fitted with the extinction of $A_V = 4.5$ mag (corresponding to $E(B - V) = 1.45$). Including the uncertainties from the photometric calibration we estimate the error in the visual extinction ± 0.5 mag. For comparison, Stolte et al. (2004) derived an extinction of $A_V = 4.0$ mag (average within their fit ranging 3.5 – 4.5 mag) for the MS population, and $A_V = 4.5$ mag for the PMS population.

Radial variations in CMD

In order to explore a possible radial variation of the interstellar extinction, we also constructed CMDs for different radii from the wider ISAAC field (see Fig. 8.5). We divided the ISAAC field into four distinct annuli of $7'' < r \leq 30''$, $30'' < r \leq 55''$, $55'' < r \leq 80''$, and $80'' < r \leq 110''$. The stellar population in the innermost ISAAC annulus reasonably resembles the central field from the NACO observations, and the combined isochrone fits reasonably well the entire mass range from the bright MS stars to faint PMS stars. Towards larger radii ($r \geq 30''$), however, we find two profound differences in the CMDs: an increasing redwards shift of the stellar distribution relative to the isochrone, and an increasing scatter of the color distribution. This trend is seen up to the $55'' < r \leq 80''$ annulus, at which point the reddening and scatter stay constant. At larger radii of $80'' < r \leq 110''$ the distribution does not significantly change any more. The most outer region appears to have a similar offset and scatter as the $55'' < r \leq 80''$ annulus. These differences could be the consequence of a combination of additional extinction and excess emission from dust envelopes and circumstellar disks. Both effects make a source redder in $J - K_S$.

The radial trend, i.e., the increased number of reddened sources and the larger scatter in color can be explained by the winds and radiation from the central high-mass stars which create a cavity in the interstellar matter. Moreover, the strong winds and

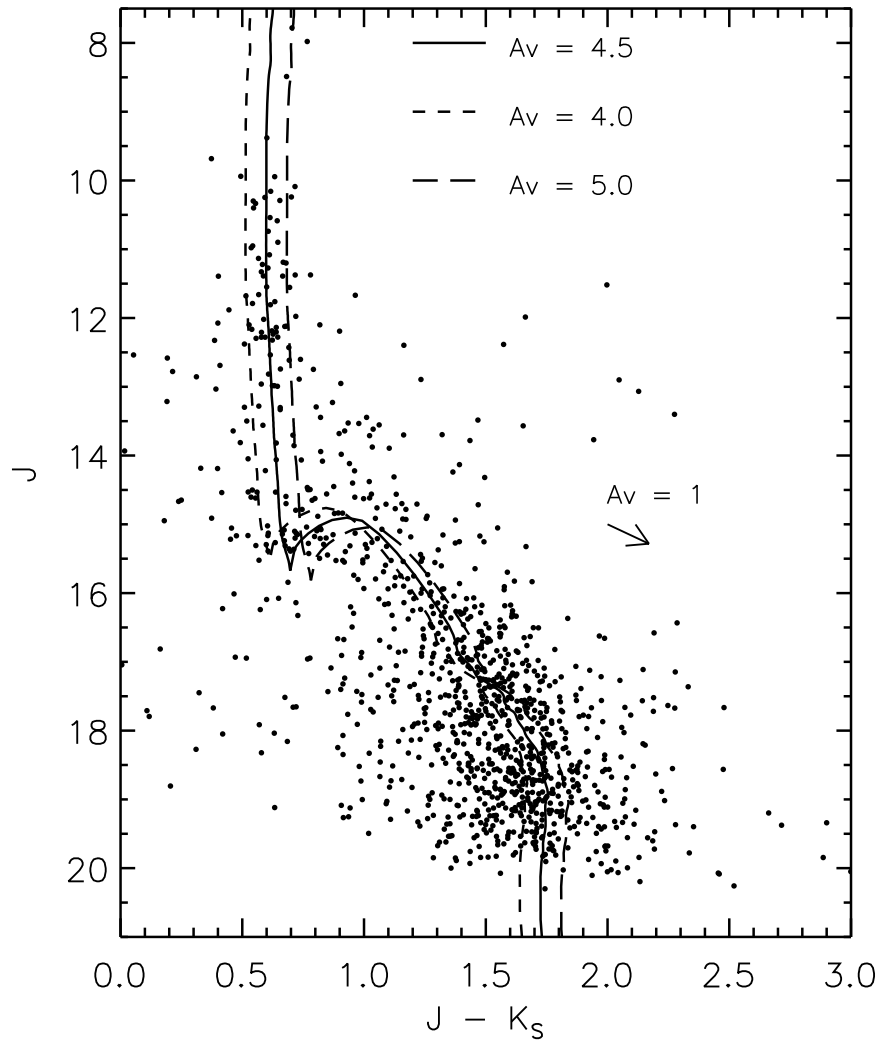


Figure 8.4: **CMD of the cluster center with the combined isochrone.** The 1158 JHK_S detected sources in the innermost region ($r \leq 13''$) are plotted together with the combined isochrone created by connecting the three best-fit isochrones from Sect. 8.1.2. These stars are the same as in Fig. 8.1. The isochrone is shifted by the distance modulus of $(m - M)_0 = 13.9$ mag. The figure shows the isochrones for three different interstellar extinctions of $A_V = 4.0, 4.5, 5.0$ mag using Rieke & Lebofsky (1985) extinction law. An arrow illustrates the reddening vector for an extinction of $A_V = 1$ mag.

radiation may have also blown away the local dust envelopes and circumstellar disks, again resulting in a smaller extinction and less infrared excess towards the center.

Also previous studies have reported a radial trend of the interstellar extinction in NGC 3603 (Melnick et al., 1989; Pandey et al., 2000; Sung & Bessell, 2004). Sung & Bessell (2004) for example found a radial increase of the interstellar extinction, with a minimum of $E(B - V) = 1.25$ mag at the core ($r \leq 0'.2$), and an increase up to 1.8 mag or even higher at larger radii. This also supports the hypothesis of a cavity in the cluster center where the radiation pressure and stellar winds from the massive stars have driven most of the gas and dust away (Frogel et al., 1977; Balick et al., 1980; Clayton, 1986). Another support for this scenario comes from the presence of pillar-like nebulae in southeast and west of the cluster pointing towards the cluster center

However, the color-magnitude diagram does not allow to distinguish between dust extinction and infrared excess from hot dust. This distinction can be made from the color-color diagram, which is analyzed in Sect. 8.2.

8.2 Color-Color Diagrams

In addition to the color-magnitude diagram, color-color diagrams (CCDs) are also powerful tools to analyze various aspects of a stellar population. In particular they allow to distinguish between the interstellar extinction and infrared excess emissions. The reason is that two effects lead to shifts in different directions in the CCD. Another advantage is that CCDs are not relying on any distance estimate. Thus a more reliable determination of the interstellar extinction can be performed. Because the various types of PMS and proto-stars have considerable excess emissions, the CCDs also allow us to distinguish between various stellar types, for example, weak-line T-Tauri stars, classical T-Tauri stars and Herbig AeBe stars (Lada & Adams, 1992).

8.2.1 Radial variation in the CCD

In order to assess in more detail the radial variations of the stellar population, we constructed $H - K_S$ vs $J - H$ CCDs for the same four concentric annuli as in the analysis of the CMD (Sect. 8.1.3). The inner and outer radii for the annuli are $r = 7'', 30'', 55'', 80'',$ and $110''$. The CCDs are shown in Fig. 8.6.

The figures show the colors of the stellar distribution after dereddening with the average interstellar extinction of $A_V = 4.5$ mag. The red curve shows the loci of empirical main-sequence stars from Bessell & Brett (1988). The solid black line shows the colors from the excess emission from circumstellar disks around classical T-Tauri stars (Meyer et al., 1997). The dashed lines originated from the MS locus illustrate the dust reddening band of the MS population. Blue dots are stars which are classified as non-cluster members based on the color-cut criteria - our cluster member selection explained in Chap. 9.

There is a noticeable radial trend in the colors of the stellar population: we find an increased number of stars shifted in the direction of the dust reddening vector with increasing distance from the cluster center. This increase in extinction is very prominent when comparing the $7'' < r \leq 30''$ and $30'' < r \leq 55''$ annuli. This trend slightly continues in the next annulus. Not further change is noticeable beyond $r \sim 80''$. The best estimate, by eye, of the radial increase in extinction is $\Delta A_V \sim 2.0$ mag as the maximum at the outermost region. This finding supports the hypothesis that the massive OB

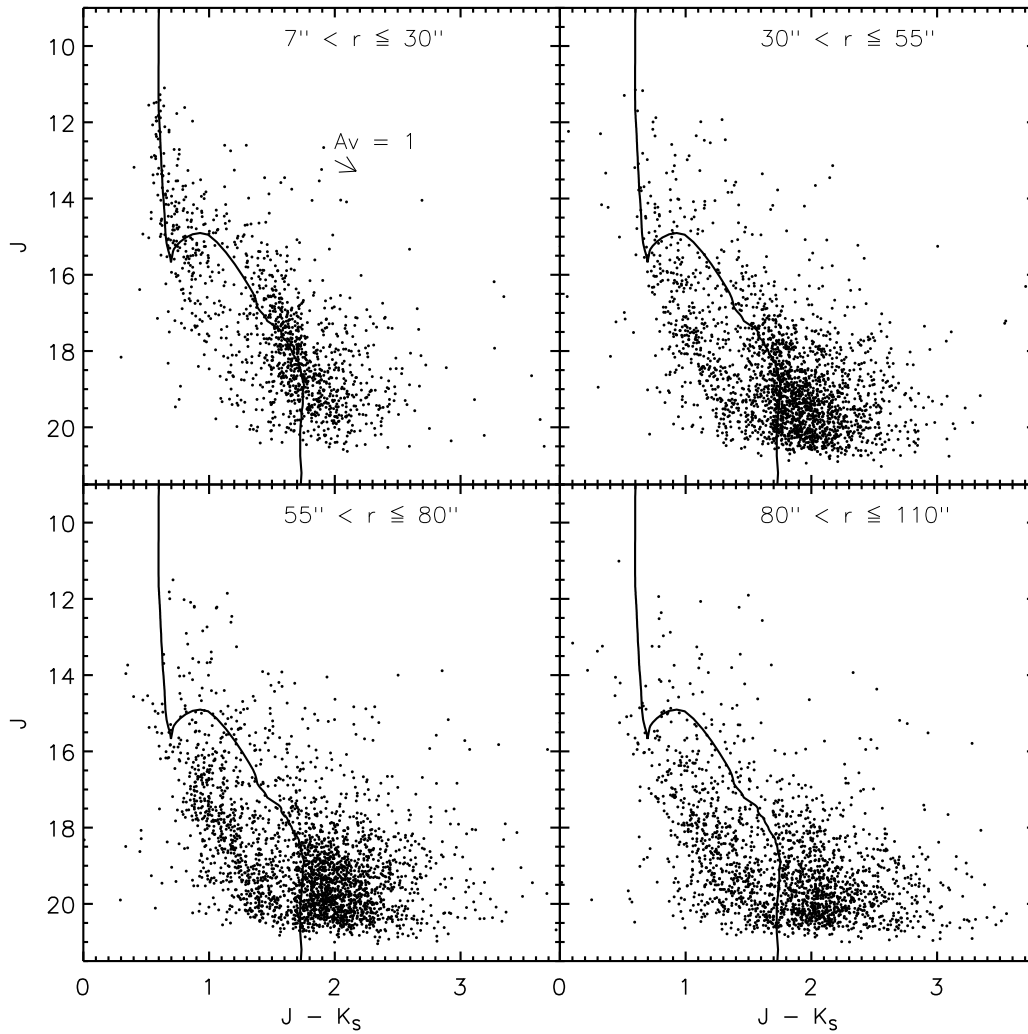


Figure 8.5: **Radial variations in the CMD.** CMDs from four radial regions with radii $7'' < r \leq 30''$, $30'' < r \leq 55''$, $55'' < r \leq 80''$, and $80'' < r \leq 110''$. The solid curve shows the combined isochrone derived in the previous section.

stars in the cluster core have blown a bubble of $r \sim 0'.2$ in the interstellar medium (e.g., Balick et al. (1980). See Sect. 8.1.3).

In contrast to the radial increase in the dust extinction, we have not recognized any profound trend in the infrared excess emissions, which would basically shift the stars more horizontally in the $H - K_S$ vs $J - H$ CCD. There is a slight increase of the scatter in the excess direction between the innermost region and the second region. The scatter then stays about constant at larger radii $r \geq 30''$. This indicates that there is a certain degree of increase in the disk fraction within $\sim 0'.2$. This trend has already been reported by Stolte et al. (2004), who explored the same ISAAC data set. We will discuss the excess emission and the consequent disk fraction in the central cluster using the NACO L' -band data in the following section.

8.2.2 CCD of the central region

In addition to the CCDs of the outer regions in the cluster ($r \geq 7''$) from the ISAAC data, we construct the CCD of the central part of the starburst cluster using the NACO data. The resulting CCD is shown in Fig. 8.7.

As one can see, there is a slight scatter in the distribution, in particular, the low-mass stars scatter along a direction almost perpendicular to the reddening direction. The reason for this scatter are residual photometric errors from the anisoplanatism, even after the additional photometry correction described in Sect. 6.3. To illustrate the effect of anisoplanatism on the CCD, we also show the CCD from the NACO observations without the additional correction (lower panel in Fig. 8.7). Comparing the two plots, one notices that the additional correction moves the centroid of the low-mass members towards the upper left. There is a sign of a slight over-correction in the sense that the stars are now somewhat too far to the upper left side of the MS loci, however, the corrected data match much better the colors of MS stars.

The distribution does not show a significant scatter towards the reddening direction. Therefore assuming an average extinction of $A_V = 4.5$ mag is indeed a good approximation to derive the absolute luminosities and the masses of the individual stars in the central cluster. This lack of individual extinction in the very center of the cluster supports the finding from the ISAAC data (see Sect. 8.2.1), and strengthens the hypothesis of a wind and radiation-driven cavity surrounding the high-mass stars.

Because of the scatter from the photometric uncertainties, we can not distinguish PMS stars with and without an infrared excess emission, which is indicative of a circumstellar disk, from the $H - K_S$ vs $J - H$ CCD. We will therefore analyze the NACO L' -band data to detect stars with infrared excess emission, then to derive the disk fraction in the following section.

As for the presence of sources which are fairly apart from the main distribution, i.e., those with ($J - H \leq 0$ and $H - K_S \geq 1$), we attribute them to relatively large errors. However, the number of such sources is quite low and statistically negligible for the constructions of the luminosity and mass functions. We have thus not exclude these sources from the following analysis.

8.2.3 $K_S - L'$ vs $J - H$ diagram of the central region

The CCD with near-infrared $JHKL$ -bands photometry is a commonly used tool to identify stars with excess emissions originated from protoplanetary disks and surrounding

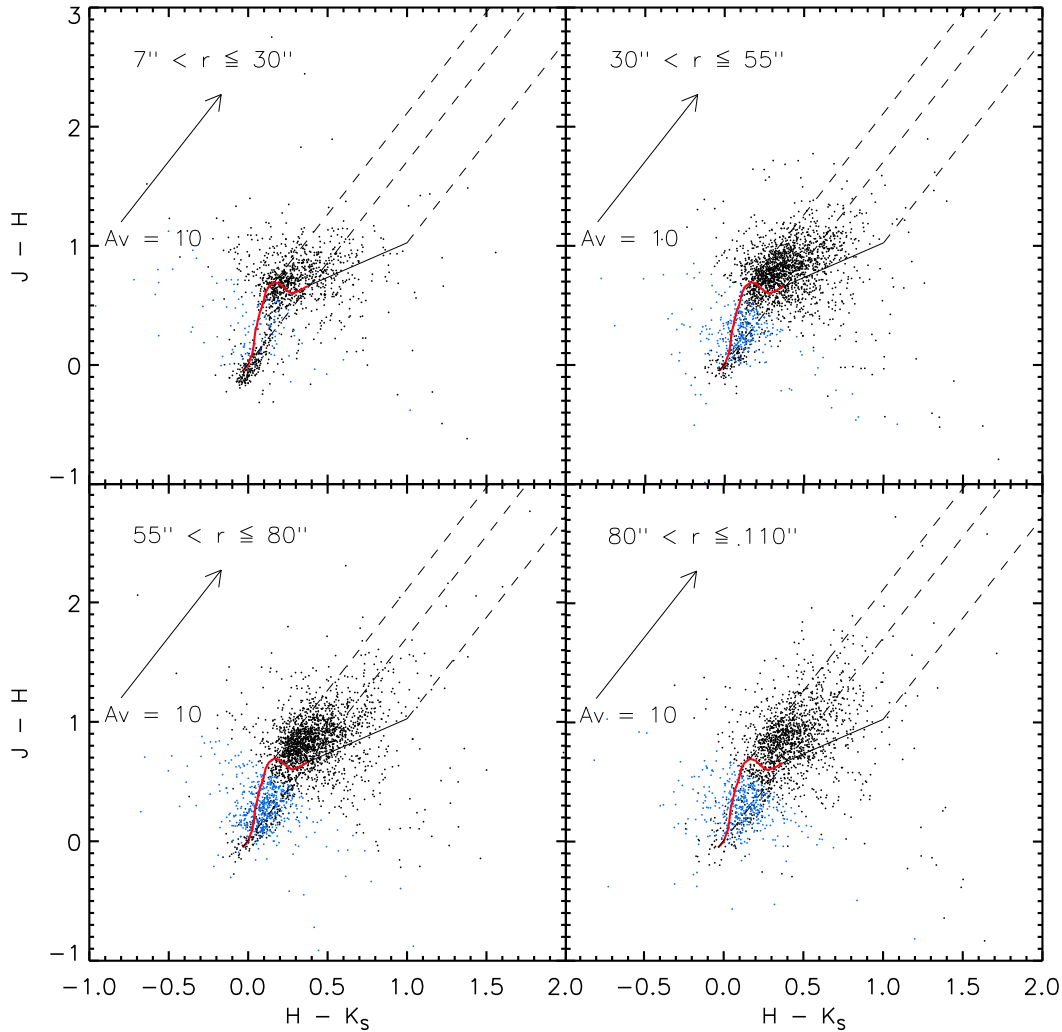


Figure 8.6: **Radial variations in the CCD.** The panels show the $H - K_S$ vs $J - H$ CCDs for four annuli with radius $7'' < r \leq 30''$, $30'' < r \leq 55''$, $55'' < r \leq 80''$, and $80'' < r \leq 110''$. The MS (from Bessell & Brett (1988)) is shown in a solid red curve. The black solid line indicates the locus of colors of classical T-Tauri stars with infrared excess emissions (from Meyer et al. (1997)). The three dashed parallel lines show the reddening bands for massive O-type stars, M-type stars, and classical T-Tauri stars with maximum infrared excess. Blue dots are stars which are classified as non-cluster members according to our selection criterion introduced in Chap. 9.

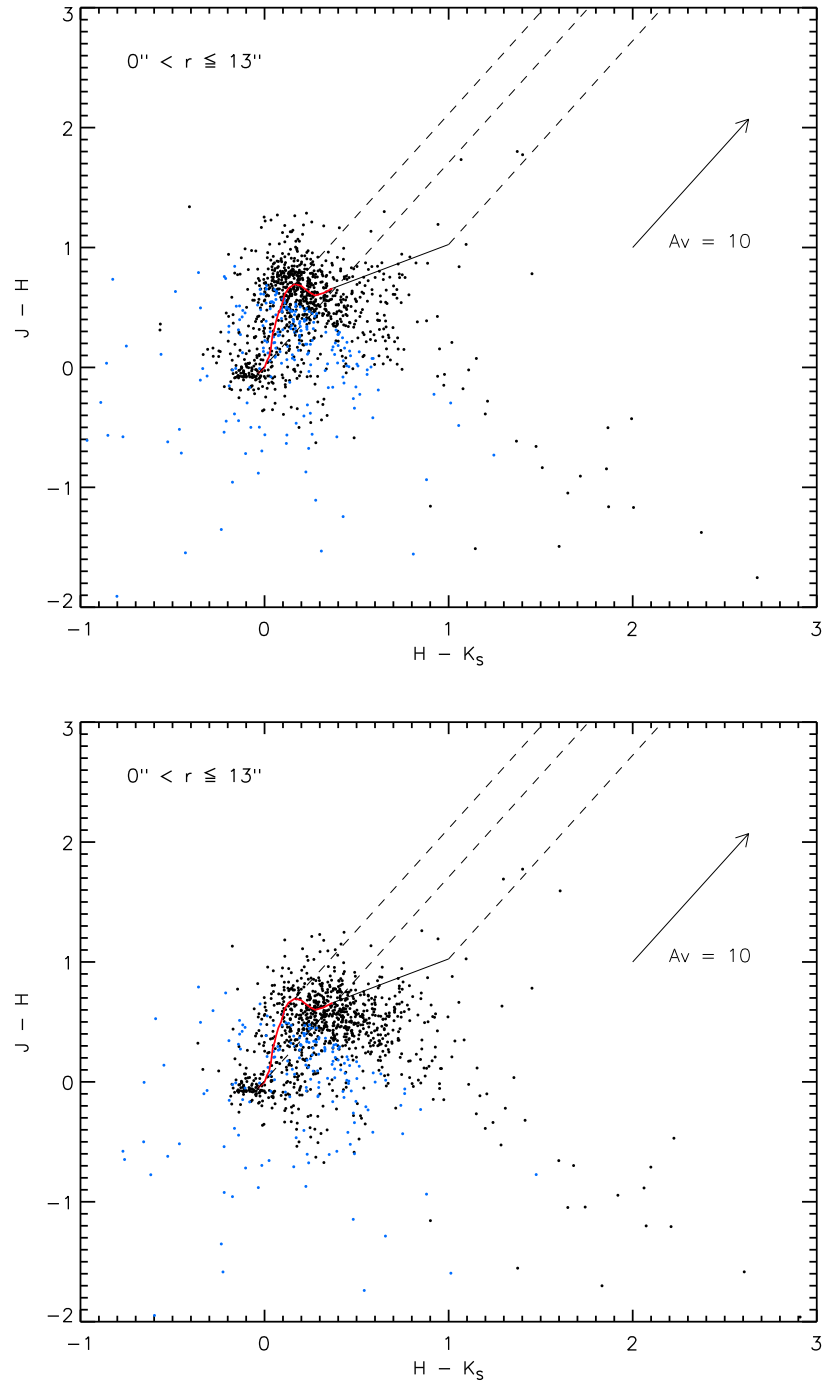


Figure 8.7: **Color-color diagram of the cluster center.** *Upper panel:* $H - K_S$ vs $J - H$ color-color diagram from the NACO observations for the cluster center ($r \leq 13''$). As in Fig. 8.6, the red curve, the black solid line, and the dashed lines show the colors of MS stars, the loci of classical T-Tauri stars, and their reddening bands, respectively. The blue dots are non-cluster members selected on the basis of our color-cut (see Chap. 9). *Lower panel:* CCD without the additional correction of the effect of anisoplanatism.

dust envelopes in young stellar populations (Lada & Adams, 1992). The L -band observation, in particular, is an effective tool to identify the infrared excess emission arose from circumstellar disks (Kenyon & Hartmann, 1995; Lada et al., 2000). Here we construct the $K_S - L'$ vs $J - H$ diagram for the central region ($r \leq 10''$) with the aim of examining the fraction of infrared-excess stars associated with circumstellar disks, i.e., disk fraction.

The analysis of the $K_S - L'$ vs $J - H$ CCD has several advantages to reveal disk populations with excess emissions, both from an observational and theoretical point of views. Intrinsic properties of the excess emissions from the disk make an excess emission at NIR a reliable disk diagnostic (Haisch et al., 2000; Wood et al., 2002), at least for populations of age younger than a few Myr. Wood et al. (2002) for example examined simulated spectral density distributions (SEDs) and colors over a wide range of disk masses, showing that the SED is most sensitive to the disk mass in longer wavelengths and, as the disk mass decreases, the excess emission from the disk decreases rapidly at longer wavelengths than at short wavelengths. Hence the disk stays optically thick, to radiation from the host star, much longer at NIR than at the far-IR, millimeter and further. Therefore the NIR observations are suitable for detecting the disk populations. Within our NIR observations, however, it is not feasible to derive the disk fraction from $H - K_S$ vs $J - H$ CCD because of the relatively large scatter due to photometric errors as can be seen in the $H - K_S$ vs $J - H$ diagram in Fig. 8.7. Therefore we investigate the $K_S - L'$ color excess so as to detect stars with circumstellar disks. There are indeed several advantages of use of the L -band observations for identification of the disk population. Since the K -band excess emission from a star with a disk substantially depends on parameters such as the disk inclination, accretion rate, and presence and size of inner holes, not all the stars in a young cluster have detectable excess emission in a JHK CCD (Lada & Adams, 1992; Meyer et al., 1997; Hillenbrand et al., 1998). Another point is that a K -band excess emission can have other origins such as extended emission from reflection nebulae (e.g. Haisch et al., 2000). There is indeed ample evidence of the suitability of L -band application for the excess investigations as tracer of circumstellar disks in study of star-forming regions such as Taurus-Auriga molecular cloud (Kenyon & Hartmann, 1995), Trapezium cluster (Lada et al., 2000), Chamaeleon I dark cloud (Kenyon & Gómez, 2001), 30 Dor (Maercker & Burton, 2005), and NGC 3576 (Maercker et al., 2006). Therefore the $K - L$ color of a star is a robust indicator for the presence of a circumstellar disk.

The derived $K_S - L'$ vs $J - H$ diagram is presented in Fig. 8.8. Note that although we have performed the additional photometric calibration for the JHK_S -bands photometry regarding to the anisoplanatic effect, we have not performed it for the L' -band photometry because of the absence of the ISAAC L' -band data. We therefore restrict the analysis to stars in the innermost $r \leq 10''$ field so as to avoid the uncertainty to some extent in this investigation. We also exclude sources which have unexpectedly blue ($J - H$) colors. The population of such sources, however, is only $\sim 3\%$ of the total sources of use, and most of them are located in a region of strong anisoplanatic effect at the north-west of the cluster center.

We have detected a total of 398 stars simultaneously in $JHK_S L'$ -bands with the given criteria in the central $r \leq 10''$ region after the color-cut. Because of the L' -band detection limit of ~ 15.8 mag (corresponding to ~ 17.7 mag in J -band), this analysis is restricted to stars more massive than $\sim 0.9 M_\odot$ (according to BCAH98 models). In order to classify stars with and without the L' -band excess emission from a circumstellar disk,

we define a threshold of $K_S - L'$ color, adopting the reddening law from Rieke & Lebofsky (1985) and a typical error bar of $K_S - L'$ color. We calculated a 1σ scatter of $K_S - L'$ color for the bulk of the PMS population that we defined stars confined in $13 < L' \leq 15.8$ mag and $-0.2 < K_S - L' \leq 0.5$ mag in the $(K_S - L', L')$ CMD. The resulting 1σ of the color is 0.14 mag.

In the figure the solid curve illustrates the empirical MS with spectral types from B8 to M0. The dashed line indicates a reddening vector which goes through the high-mass MS star (B8) in the empirical locus, the dotted line indicates the line shifted by the 1σ color of $\Delta(K_S - L') = 0.14$ redwards. All sources to the right of the dotted line are regarded as stars with L' -band excess emissions. Applying this criterion, 100 out of 398 sources are classified as infrared excess stars, corresponding to a disk fraction of ~ 25 %.

The resulting disk fraction, however, is strongly depending on the adopting selection criterion, and in particular it is quite sensitive in case of low number statistics. If we adopt a zero-threshold instead of the 1σ criterion, the disk fraction rises to ~ 36 %. If we apply a 2σ threshold, then the outcome is ~ 19 %. Therefore, considering the relatively large scatter in the $K_S - L'$ color as well as the slight systematic offset of the $K_S - L'$ color relative to the empirical MS (several tenths of a magnitude), we are not able to determine the disk fraction to better than about ± 10 %. We therefore conclude that the disk fraction for the population of $0.9 \geq M_\odot$ stars within $r \leq 10''$ is ~ 25 % with a substantial uncertainty (± 10 %).

In order to examine a possible radial variation of the disk fraction, we also derive the fractions for regions of $r \leq 5''$ and $5'' < r \leq 10''$. Both fields show very similar values ~ 25 % with a variation of less than 0.3 %. This leads to the conclusion that there is no variation in the disk fraction at least in this very center ($r \leq 10''$) of the cluster. In addition, we examine a mass dependency of the disk frequency in the cluster center, and derived the disk fraction for three distinct magnitude ranges of $J \leq 14$, $14 - 16$, and > 16 mag (limiting magnitude is ~ 18 mag), corresponding to mass ranges of $\gtrsim 3.8 M_\odot$, $\sim 1.5 - 3.8 M_\odot$, and $\lesssim 1.5 M_\odot$. The resulting disk fractions are ~ 24 , ~ 36 , and ~ 19 %, respectively, which leads to the interpretation that there is no linear correlation with stellar mass.

Comparing with literature, our result is consistent with earlier studies of NGC 3603, as well as with the general consensus on the circumstellar disk frequencies in intense star-forming regions. Based on the L' -band luminosity and the H α emission, which is an indicator of young stars with accreting disks, Stolte et al. (2004) derived 27 ± 3 % for the disk fraction with a radial increase from ~ 20 % in the inner region ($r < 20''$) to ~ 40 % in the outer regions. Our result of $\sim 25 \pm 10$ % is compatible with their results, and since our data is restricted within the innermost $10''$ region, it is also compatible with the hypothesis that the disk fraction starts to increase outside in the cluster.

It is estimated that the median lifetime of inner optically thick accretion disks, which produce near-infrared excess emissions, may be as short as 2–3 Myr (Hillenbrand, 2005). Using the $K - L'$ color, (Haisch et al., 2000, 2001a,b) have derived the disk fractions for young (NGC 2024, Trapezium, and IC 348) and intermediate-age (NGC 2264, NGC 2362, and NGC 1960) star clusters covering an age of 0.3 – 30 Myr. These papers also examined the mass dependency of the disk fractions, and the evolution and lifetimes of the circumstellar disks with the aim of drawing implications for current theories of planet formation. A clear correlation between the disk fraction and the mean age was found: 50 % of the disks in a cluster are lost in only about 3 Myr. The overall disk

lifetime in the surveyed sample is ~ 6 Myr. Based on a study of evolutionary models for protoplanetary disks, Armitage et al. (2003) reported that in young clusters up to 30 % of stars lose their disks within 1 Myr, the remainder, however, have disk lifetimes of typically in the range of 1 – 10 Myr. Considering the age of NGC 3603 ≤ 2.5 Myr, the disk fraction in the central core region is somewhat smaller than the expected value of ~ 60 % based on this correlation (see Fig. 1 in Haisch et al., 2001a). We interpret this discrepancy such that the winds and radiation from the central high-mass stars have not only created a cavity in the ISM, but have also evaporated and disrupted the circumstellar disks of nearby stars.

It is not clear whether or not the disk fraction is generally dependent on stellar masses. Analyzing NIR imaging observations of the young σ Orionis cluster (3 – 5 Myr), Oliveira et al. (2006) derived a disk frequency of 33 % for the low-mass stellar population with masses between 0.04 and $1.0 M_{\odot}$, but found no obvious mass dependence of the disk fraction within the mass range. They also found no evidence for a spatial segregation of sources with and without circumstellar disks. Based on optical and near-infrared study of a young cluster NGC 2264 in Mon OB1 association, Rebull et al. (2002) reported that there was no statistically significant variation of disk fraction on the stellar mass.

Whereas, there is evidence of a difference in the characteristics of circumstellar disks depending on the stellar mass, which implies a mass dependency of the disk fraction. Based on N-body dynamical simulations and simulations of the mass loss from the star-disk encounters, Pfalzner et al. (2006) find that in the Trapezium cluster the circumstellar disks around high-mass stars dissipate much faster than those of intermediate-mass stars. This effect is largely due to gravitational interactions. This shorter disk dissipation time scale for higher-mass stars is generally consistent with most observations. For the low-mass stars, based on a Spitzer near- and mid-infrared photometric study of the IC 348 cluster, Lada et al. (2006) recently reported a peak in the disk frequency for late K to early M spectral types, which also suggests a mass dependency of the disk fraction.

Based on the *JHKL* observations of the Trapezium cluster, Lada et al. (2000) found that the disk fraction in the young embedded cluster is relatively high, and is independent of spectral type for stars with spectral types between F-M. This suggests the probability of disk formation around a star at the time of its birth is independent of stellar mass over essentially the entire mass range down to the hydrogen burning limit. They, however, found a considerably lower disk fraction for the high-mass O, B, and A stars, and this could be due to either a lower probability for disk formation or more rapid disk dispersal times.

Note that, there is a potential uncertainty which would somewhat underestimate the disk fraction. Since there are potential star/disk systems which are detectable only at longer wavelength, e.g., at $K_S L'$ or merely L' , the use of the stars detected in *JHK_SL'*-bands simultaneously could underestimate the actual disk fraction. With the aim of obtaining an insight into a potential contribution of those stars on the disk fraction, we compute a disk fraction using also stars detected only in L' -band based on a simple assumption that stars detected only in L' -band are star/disk systems. Counting those stars as well as the *JHK_SL'* detected stars with excess derived adobe, the resulting disk fraction increases to ~ 43 %.

In summary, we observed the disk fraction of $\sim 25 \pm 10$ % for stars with $\mathcal{M} \geq 0.9 M_{\odot}$ within $r \leq 10''$. This slightly small disk fraction compared to the other young clusters can be explained by the presence of the central cavity. We have found neither radial variation of the disk fraction nor its mass dependency.

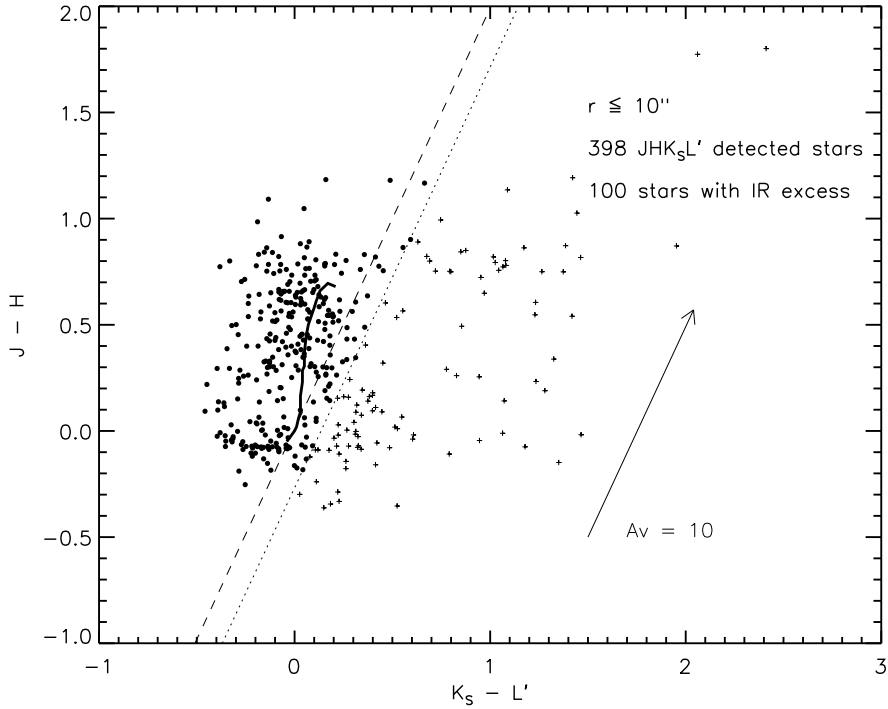


Figure 8.8: $K_S - L'$ vs $J - H$ color-color diagram of the cluster center. The figure shows all sources simultaneously detected in the $JHK_S L'$ -bands in the innermost central core region ($r \leq 10''$). The colors are dereddened using the extinction law by Rieke & Lebofsky (1985). The solid curve shows the empirical colors of MS stars from Bessell & Brett (1988) with spectral types from B8 to M0. The dashed line indicates the reddening vector passing through the B8 star on the empirical MS. The dotted line indicates the selection criterion for the disk population, which is the reddening line of the B0 star shifted by the 1σ photometric error of $\Delta(K_S - L') = 0.14$ mag. Those excess stars are shown in crosses, and in total 100 out of 398 sources are classified as stars with disk emission, corresponding to a disk fraction of $\sim 25\%$.

We note that, in case of very young clusters such as NGC 3603, it is difficult to perform more accurate determinations of these fundamental properties on the basis of photometric information alone. In the isochrone fitting, the evaluation of the suitable isochrone is considerably uncertain because of the fact that, particularly in NIR, the photometric colors of bright MS stars can not provide precise effective temperature, and observed magnitudes can not provide accurate enough stellar luminosity.

Moreover, the presence of individual extinction to some extent affects on the reliability of the isochrone fitting. Hence, for example, an information of spectral type of MS stars of $\sim 10 M_\odot$, which are young enough to be in MS regime, enables us to perform more accurate determinations of the cluster distance. As for the age estimate, a MS star of several M_\odot with an additional differential reddening could mimic a PMS star on the PMS-MS transition in the CMD. Therefore, any inputs of spectral types of stars in those mass ranges based on the extinction-free spectral information will help us to pin down the locations of those sources and subsequent selection of a suitable isochrone. Subsequently, using the more reliable distance and age estimates of the clus-

ter, the interstellar extinction can also be derived with more confidence. Therefore, for the further assessment of the cluster's fundamental properties, any information about spectral types of MS and PMS stars via spectroscopic observations are highly desired. Thus acquisition of spectral information of cluster members in such mass ranges in NGC 3603 would certainly be our next step for further investigations. In the later chapters, we therefore investigate potential impacts on the IMF characteristics by the uncertainties on the distance, selections of isochrone age, and interstellar extinction.

Chapter 9

Cluster membership

In studies of Galactic disk populations - as the case of NGC 3603 - the line-of-sight field star population can provide a non-negligible contribution, causing an error in the analysis of statistical properties such as the LF and IMF. Accordingly it is necessary to distinguish between cluster members and non-cluster members, and only use the cluster members in those analysis. In the present work, in order to construct the LF and IMF of the cluster population, we apply two different approaches for the correction of field stars. The first approach aims at measuring the density and LF of the field stars for subsequent subtraction from the measured distribution, and the second approach directly excludes non-cluster members based on their colors.

The first approach is commonly applied in the analysis of stellar clusters, and it requires the observation of a so-called control field, which is located far enough from the object of interest so as to guarantee that no cluster members are included. Since we did not observe a control field in our NACO observing runs, and because the ISAAC data set does not include such frames either, a direct measurement of the field star density is not possible. However, we can derive an upper limit for the field star density from the outermost region ($80'' < r \leq 120''$) of the ISAAC field. Another estimate is available from observations of NGC 3603 presented in Nürnbergger & Petr-Gotzens (2002) (NPG02 hereafter).

In contrast to the commonly applied statistical correction, the second approach is based on the physical properties of stars. We differentiate the likely non-cluster members from the cluster members on the basis of their locations in the CMD. We hence call this method *color-cut* hereafter. Because of the lack of a statistical estimate from a control field, we mainly apply the color-cut method for the subsequent constructions of the LF and IMF. A comparison of the three possible field population estimates - from the outermost region, from the NPG02 field KLF, and from the color-cut - is presented in the context of the LF analysis in Sect. 10.2.3. Here we explain why the color-cut is seen as the most suitable for our analysis.

Fig. 9.1 illustrates the idea of the color-cut. The best-fit combined isochrone used for the luminosity-mass conversion (shown in Fig. 8.5), is shown as a black solid curve, applying a uniform extinction of $A_V = 4.5$ mag and a distance modulus of $(m - M)_0 = 13.9$ mag ($d \sim 6$ kpc). The black dashed curve indicates the MS. The gray solid curve indicates the color-cut boundary. This boundary is created by smoothing out the turnover feature in the PMS-MS transition in the combined isochrone, and shifting this curve bluewards by $J - K_S \sim 0.26$ mag, corresponding to $A_V = 1.5$ mag. The shift is applied only in the $J - K_S$ direction i.e., no shift is performed in the vertical J direction.

The sources located on the left, blue side of the color-cut boundary are thought to be mostly fore or background stars. Therefore these sources are excluded from the following derivations of the LF and IMF.

Here we discuss the possible origin of the sources based on their locations on the CMD. Stars which are located around the MS (black dashed curve) at $m_J \geq 16$ mag and which are bluer than the color-cut could be part of the following groups: 1) background MS stars with $A_V \simeq 4.5$ mag, 2) foreground low-mass MS, 3) cluster stars formed in earlier generations.

As for the first group, they would most likely be low- and intermediate-mass MS stars with an interstellar extinction similar to those of the cluster members, but with a smaller brightness due to their larger distance compared to the cluster population. The average interstellar extinction of the cluster members and that of a background population can have similar values if we assume a pure foreground screen extinction. In this case the interstellar material such as gas and dust are existing locally along the line of sight, and hence the interstellar extinction behaves as a step function rather than a linear increase with distance. The second potential group of stars which occupy this part of the CMD are foreground low-mass stars. These stars are intrinsically redder because of their lower temperature, a reduced interstellar extinction, however, can shift them back on the blue side of our color-cut.

And thirdly, these supposedly field stars could indeed be cluster members which have formed prior to the starburst ≤ 2.5 Myr ago when the majority of the cluster members are thought to be born. Since the IMF study is the subject of single star formation process, such sources are legally rejected from our analysis. In fact, as indicated by the lack of such stars in the optical CMD as reported in previous studies, the number of stars from earlier generations is thought to be very small (see the discussion on the possible age spread in Sect. 8.1.2). This supports our assumption that most of the sources with colors and magnitudes of low-mass MS stars are background MS stars rather than low-mass MS stars from earlier generations in the cluster.

The next category of potential field stars is even bluer, and is located to the left of the gray solid/dashed curve in the CMD. Intrinsically blue stars with no or negligible dust extinction located very close to the Sun could be in this category. Moreover, some of the sources that appear to be very blue among this category could also be false detections or misidentification in the JHK_S combination procedure, although such sources are expected to be rare.

The potential limitations of this color-cut method for the field star estimate are the following points. First of all, the determination of the location of the color-cut is based on an eye inspection, therefore the correction essentially relies on this judgment. Also the photometric errors, which add to the scatter of the intermediate- and low-mass stars in the CMD, could also affect the quality of this selection. However, as shown in Fig. 8.5, there is a somewhat visible gap between the low-mass PMS population and the faint MS population, and the color-cut boundary is satisfactory separating them. The second limitation is the fact that the region redwards of the color-cut could still contain some non-cluster sources. They could be highly reddened high-mass MS stars in the background, or very red foreground stars with substantial individual dust extinction and/or infrared excess emissions from disks. However, owing to the rareness of massive field stars as well as to the possibly small number of red foreground stars, the influence of those sources on our following statistical analysis would be insignificant.

In summary, this color-cut method provides a reasonable correction for the field star

population when deriving the LF and IMF. Hence we use this technique in the following analysis.

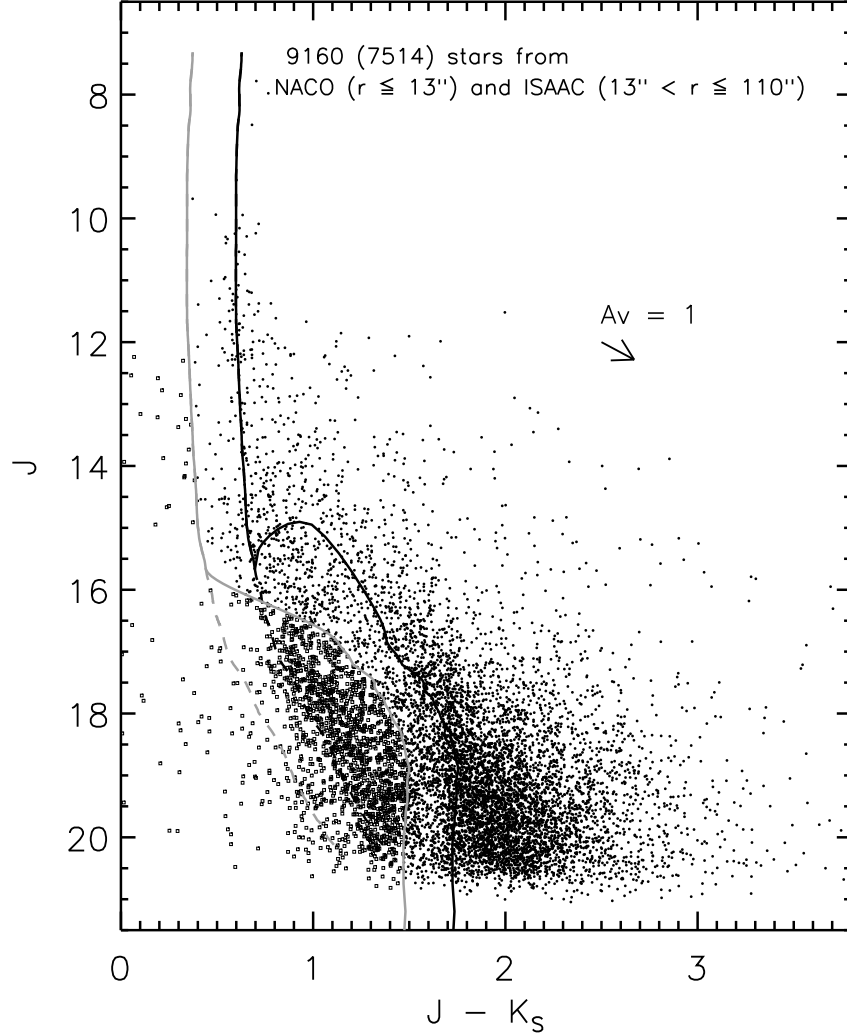


Figure 9.1: **Color-cut selection of cluster members from the CMD.** The figure shows the $(J - K_S, J)$ CMD for the 9160 JHK_S detected stars in the inner $r \leq 13''$ NACO field and the outer $13'' < r \leq 110''$ ISAAC field. The black solid curve is the combined isochrone from Sect. 8.1.2. The dashed curve illustrates a 2.5 Myr MS isochrone. For both isochrones we apply a uniform extinction of $A_V = 4.5$ mag and a distance modulus of $(m - M)_0 = 13.9$ mag ($d \sim 6$ kpc). The gray solid curve illustrates the color-cut. This curve is created by smoothing out the turnover feature in the PMS-MS transition of the combined isochrone, and it is shifted bluewards by $J - K_S \sim 0.255$ mag, corresponding to $A_V = 1.5$ mag. A source with a color bluer than this curve is regarded as a non-cluster member (square). These stars are excluded in the derivation of the LF and IMF. Applying the color-cut, we find 7514 out of 9160 stars to be cluster members.

Chapter 10

Luminosity functions of NGC 3603

10.1 Introduction to the luminosity function

In this chapter we present the derivation of the Luminosity Function (LF) of NGC 3603, and discuss the resultant LF characteristics. The LF is the distribution of measured luminosities in the stellar population, i.e., number of stars per photometric magnitude interval, hence is described as $\psi(M) = dN/dM$. The LF is one of the most important diagnostic tools in the study and comparison of star clusters, since it is not influenced by any theory-related uncertainties, but is purely an observational quantity. In contrast, the IMF in principle relies on the transformation of the observed LF using a luminosity - mass relationship, and in that sense imposes an additional assumption.

The relation between the IMF $\xi(\mathcal{M})$ and the LF $\psi(M)$ of a stellar population with a given age is

$$\psi(M) \propto \xi(\log \mathcal{M}) \frac{1}{\mathcal{M}} \frac{d\mathcal{M}}{dM} \quad (10.1)$$

The LF usually exhibits a clear decrease towards lower magnitude. In addition to the intrinsic property of star formation, higher-mass stars are born less frequently, this trend is also due to an evolutionary effect. The higher the stellar mass is, the faster its stellar evolution proceeds. Unless it is a new-born star cluster, higher-mass stars have evolved through a post main sequence stage to the end stages of their evolution such as white dwarfs, neutron stars, and black holes, resulting in the almost monotonous decrease in the LF towards higher luminosities. Based on study of field stars in the vicinity of the Sun, Salpeter (1955) was the first to present this concept, finding that the total number and mass of stars which evolved away from the main sequence was comparable with total number of white dwarfs and with the total mass of faint MS stars, respectively. However, in case of NGC 3603 the stellar population is young enough ($\tau \lesssim 3$ Myr) to provide the *initial* distribution. Therefore the LF is mostly not affected by stellar evolution, providing an empirical basis for the derivation of the *initial* mass distribution.

10.2 LF of NGC 3603

In this section we explain the procedure to derive the LF of NGC3603. We first investigate the feasibility of combining the NACO and ISAAC observations, and then present J , H , and K_S LFs from the combined data set. Secondly we compare the field star correction from the color-cut method with other estimates, e.g., the field star KLF in Nürnberg & Petr-Gotzens (2002), and the LF from the population in the outermost ISAAC field as an upper limit of the estimate of field population. Subsequently we present our best estimate of the KLF after applying the field star correction and the incompleteness correction, and then discuss its variation with distance from the cluster center.

10.2.1 Combination of NACO and ISAAC data

In this section we construct the LFs of NGC 3603 by combining the NACO and ISAAC observations. Therefore we first need to verify that this combination is feasible. Since the two data sets have different angular resolutions, limiting magnitudes, and saturation limits, we assess potential effects when combining the data in a single LF.

First, as for the limiting magnitudes, the detection of stars is basically limited by the J -band observations in both data sets. The NACO observations are limited by the J -band images because they have the lowest angular resolution and thus suffer most from crowding in the central regions. The large ISAAC field is limited by the J -band because of the larger interstellar extinction at shorter wavelengths. By chance, both NACO and ISAAC have a similar J -band limiting magnitude of about 20.5 mag (see Sect. 7.2 and the CMDs of NACO field in Fig. 8.1 and the ISAAC field in Fig. 8.5). Therefore the limiting magnitude can cause no unfavorable bias on the faint end of LFs.

Secondly, in order to investigate a possible discrepancy in the detection frequency from the different angular resolution in the data sets, we constructed the LF from an annulus at $r = 10'' - 13''$, which overlaps in the both NACO and ISAAC fields. The two LFs show a fairly similar power-law slope, but have a slight discrepancy in frequency. In the magnitude range of $m_J = 12 - 16$, over which the photometry is free of saturation and for which there is only little confusion in the ISAAC data, the difference is about 17 %.

We ascribe this discrepancy to a slightly small incompleteness correction in the ISAAC data. This is probably due to the fact that the overlapping region of $r \sim 13''$ is still too close to the cluster center for a perfect correction. However, the effect is expected to diminish quickly with increasing distance from the cluster center, and hence it is statistically insignificant for the LFs of the whole ISAAC field, which extends up to about $r \sim 110''$ (up to $\sim 120''$ towards the corners of the field).

The third potential complication in combining the NACO and ISAAC data are differences in the saturation limits. As the NACO list was created by combining long- and short-exposure time observations, all stars are within the linearity range, including the three most luminous WN stars in the cluster center. In contrast, the ISAAC list appears to have a linearity break at roughly $m \sim 12$ mag in all bands, therefore any sources which are brighter than this magnitude should be regarded as saturated sources. In addition there are few completely saturated stars which are not included in the list, because they could not be identified in the source detection. However, the impact on our LF and IMF analysis is expected to be negligible because of the rareness of such bright

stars in the outer field covered by the ISAAC data. For instance, within the region of use ($13'' < r \leq 110''$) in the ISAAC data, the number of sources whose J -band magnitude is less than 12 mag in the photometry list is about 24. The number of sources which are completely saturated and hence not in the list is about 15 based on a careful visual inspection. Thus the total of ~ 40 is negligible relative to the total number of used sources of ~ 8000 . However, in order to keep assessments on the LF as reliable as possible, the following analysis of slope variations will be restricted to the reliable magnitude range of ($m \geq 12$ mag). In conclusion, we find no fundamental problem in combining the NACO and ISAAC data, and we therefore construct LFs from both data sets, and we present interpretations based on the combined LFs in the following sections.

We note that we will again investigate a feasibility and consistency of combining the NACO and ISAAC data for the IMF construction and its interpretation in Chap. 11 based on the observed radial trend in the IMFs.

10.2.2 The observed LF

We first derived LFs for the JHK_S detected stars. Fig. 10.1 shows the J , H , and K_S LF of the 9160 stars detected within $r \leq 110''$ (1158 stars in the innermost field at $r \leq 13''$ from NACO and 8002 stars in the outer field at $13'' < r \leq 110''$ from ISAAC). Note that the K_S -band LF shows a peak at around 18 mag, and this is not caused by the detection limit in K_S -band, but by the J -band detection limit of ~ 20.5 mag in both the NACO and ISAAC data. Since low-mass PMS stars show a typical $J - K_S$ color of ~ 2 mag, the K_S -band LF derived from the JHK_S detected sources has its detection limit at around 18.5 mag.

10.2.3 The field star LF

In order to compare all available approaches for the correction of the field star population, and to decide which method is most suitable, we build K_S -band field star LFs based on those three methods. The three methods are the color-cut, using the outermost peripheral region ($80'' < r < 120''$) in our ISAAC field, and adopting the KLF from NPG02. The respective KLFs are shown in Fig. 10.2 (top).

There are several noticeable differences among them. While the outermost field KLF and the NPG02 field KLF show fairly similar shapes within the reliable magnitude range of $m_J \geq 12$ mag, there is a considerable discrepancy in their number counts. The outermost ISAAC KLF is by a factor of ~ 4 larger than the NPG02 field KLF. This discrepancy is probably due to a mixed effect of the following reasons. First, since the radius of NGC 3603 has been estimated to be larger than $2'$ (e.g., $\sim 2'$ in Sung & Bessell (2004) and $\sim 2'.5$ in NPG02), the outermost region in our ISAAC field is not far enough and is probably still populated with cluster stars. Therefore it is conceivable that there is some degree of discrepancy considering the fact that the NPG02 field KLF was constructed from a control field at $r \leq 150''$. Secondly, a different detection criteria in the two studies can to some extent contribute to the discrepancy.

Our source detection based on three photometric bands can help us to regard a detection as a true star. In contrast NPG02 identified the stars in one band only, and this would require a much larger detection threshold for a confident detection resulting in a loss of stars in the faint end of the K_S magnitude. Although this is not always the case considering the fact that our detection is limited by the J -band magnitude, this

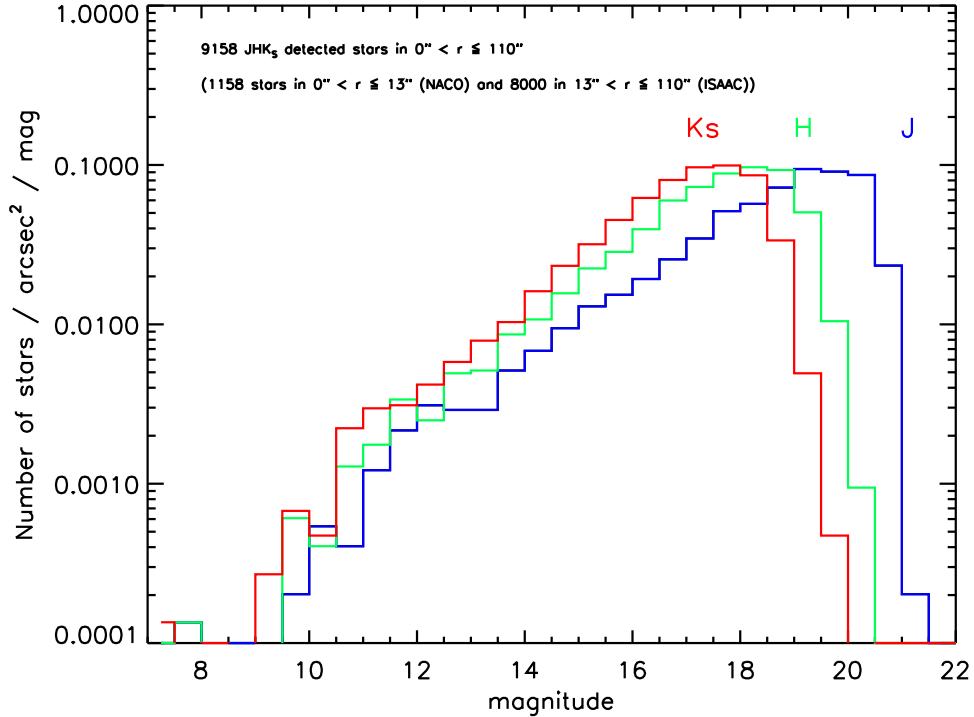


Figure 10.1: **Luminosity functions of JHK_S detected stars.** A total of 9160 stars are simultaneously detected in the three bands within $r \leq 110''$ (1158 in $r \leq 13''$ (NACO) and 8002 in $13'' < r \leq 110''$ (ISAAC)). The blue, green, and red line show the J , H , and K_S luminosity distributions, respectively. The LFs are binned in magnitude intervals of 0.5 mag.

could be a contributory factor in the discrepancy in case that the missing sources in NPG02 is substantial.

The second point which can be easily seen in the three field LFs is that, although the NPG02 field KLF and the outermost field KLF show a smooth increase from the bright to the faint domain, the color-cut field KLF shows a remarkable gap at intermediate luminosities. This is because the color-cut mainly exclude low-mass stars in the populations, as one can see in Fig. 9.1.

Another noticeable point in the figure is a cut-off at $m_{K_S} \sim 12$ mag in the color-cut field KLF. Since the outermost field LF shows number counts even in the regime of $m_{K_S} \leq 12$ mag, the cut-off can not be due to the saturation limit in ISAAC data. But, as in the case of the second point, it is a direct outcome of this color-cut technique. Our criterion in the color-cut with the $A_V = 1.5$ mag bluewards shifted isochrone does not exclude large portion of bright stars as can be seen in the CMD in Fig. 9.1. Thus this could be the case that our color-cut underestimate the high-luminosity field stars to some extent, and the true distribution of the field stars extend towards the high-luminosity end. We therefore need to exclude the high-luminosity range of $m_{K_S} \leq 12$ mag in the investigation of characteristics of the LF.

Since all three methods for measuring the field population are different in several aspects, we compare the various field star corrections by subtracting the three field KLFs

from the observed KLF (in Fig. 10.1) in order to see possible impacts on the resulting LF. The KLFs corrected by the three field KLFs are shown in Fig. 10.2 (bottom). As expected, the correction by the outermost field KLF shows a noticeably different distribution from others, because it overestimates the field star density. The two other KLFs, however, show fairly similar properties despite the large gap in the color-cut field KLF. This indicates that the difference between the color-cut and the NPG02 field KLFs is statistically insignificant. Considering the unknown uncertainties from the different observational properties between the NPG02 data and ours, we thus use the color-cut method for the field star correction in the following LF and IMF analysis.

10.2.4 The cluster star LF

We constructed the KLF of NGC 3603 applying all corrections previously mentioned, such as the field star decontamination based on the color-cut, and the incompleteness correction. Fig. 10.3 shows the KLF derived from 7514 JHK_S detected stars in $r \leq 110''$. The NACO field of $r \leq 13''$ and the ISAAC field of $13'' < r \leq 110''$ are used. A variable incompleteness correction depending on the radial distance is applied.

Here we note that, because of the highly crowded inner region and relatively sparse outer region, the variation of the incompleteness is so large across the field that determining a single representative completeness limit for the LF is not adequate. We therefore compute the 50 % completeness limits (at which 50% of the stars are detected in the images, and another 50% are added in the incompleteness correction) from two regions, an inner region at $r \leq 13''$ from the NACO field, and an adjacent outer annulus at $13'' < r \leq 30''$ from the ISAAC field. The resulting 50 % completeness limits in the both regions have coincidentally almost the same value of $m_J \sim 19.4$ mag.

From that J -band limit we obtain a K_S -band 50 % completeness limit of 17.4 mag, using the typical $J - K_S$ color of ~ 2 mag for low-mass PMS stars in NGC 3603. The 50 % completeness limit is indicated by a vertical dashed line in the figure. Note that the completeness limit is an average limit for each region. Because of the strong spatial variation of the crowding, there are also strong variations of the 50 % limit. For example, the J -band completeness limit in the innermost $r \leq 2''$ is ~ 15 mag and it increases sharply to ~ 20.5 mag at $10'' < r \leq 12''$.

At larger radii $30'' < r \leq 110''$, the detection is not limited by crowding, but simply by the noise in the images. This detection limit is derived from a Monte Carlo simulation adding artificial sources (see Sect. 7.2). The J -band limiting magnitude is ~ 20.5 mag, corresponding to a K_S -band limit of 18.5 mag (indicated by a vertical dotted line in the figure). The power-law slope is computed for the magnitude range from 12 mag up to the 50 % completeness limit of $m_{K_S} = 17.4$ mag.

The LF shows a monotonous increase towards faint magnitude with a power-law index of $\alpha = 0.27 \pm 0.01$. The nature of the flattening at the faint end of the LF at $m_{K_S} \sim 17.5 - 18$ mag is not clear. As mentioned in Sect. 7.1 on the incompleteness correction, we applied a maximum correction factor of 10, corresponding to a 10 % completeness limit. Any corrections beyond this factor is considered to be unreliable, and we can thus not conclude if the observed sign of flattening is a real feature or a result of the observational limitation.

For the sake of comparison of our LF with those in previous publications, we construct several LFs matching as good as possible the field of view.

For this comparison, we construct a KLF for the innermost $r \leq 33''$ region, applying

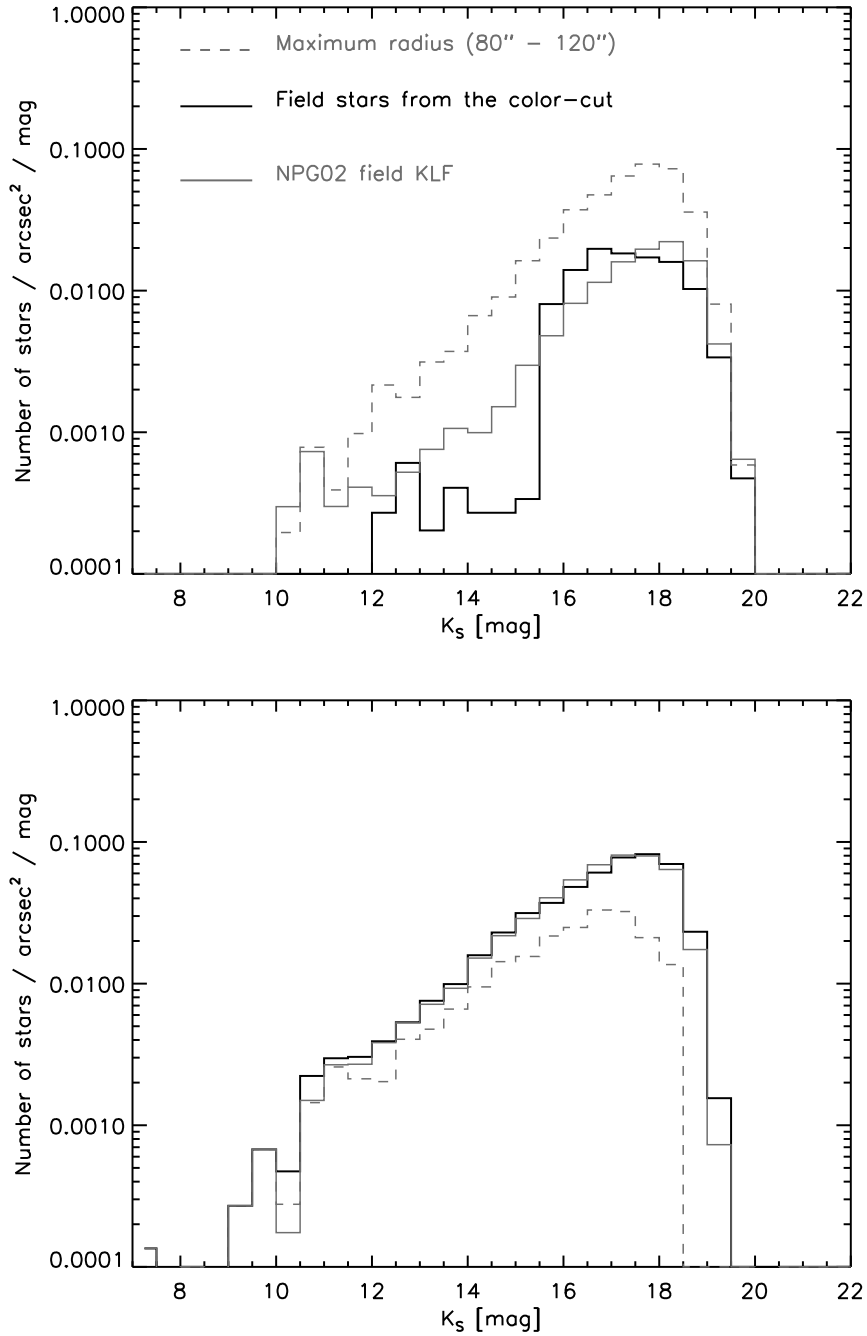


Figure 10.2: **Comparison of K_S -band LFs based on three different methods for the field star subtraction.** *Top* panel: KLFs of the field population based on three different estimates. The black solid line indicates the KLF of the field population derived by the color-cut, the gray dashed line indicates the KLF derived from the outermost region ($80'' < r \leq 120''$) of the ISAAC field, and the gray solid line indicates the KLF extracted from Nürnbergger & Petr-Gotzens (2002). *Bottom* panel: Observed LF in K_S -band (red histogram in Fig. 10.1) subtracted by the three field star KLFs from the top panel. The type and color of the lines indicate a subtraction of the according field LF in the top panel.

a field star correction derived from a population in an outer annulus of $75'' < r \leq 102''$, just like NPG02. Note that this outer annulus still contains cluster stars, and hence the derived field star population is most likely substantially overestimated. This effect is obvious from a direct comparison with the KLF derived from the $80'' < r \leq 120''$ region presented in Fig. 10.2. Fig. 10.4 shows the resulting LF. The power-law slope is derived from a fit in the range of $13 \leq m_{K_S} \leq 16$. The power-law index is $\alpha = 0.29$ for the incompleteness corrected LF (dash-dotted line in Fig. 10.4), and $\alpha = 0.26$ for the uncorrected number counts (shown as a solid line; extrapolation shown as a dashed line). The according slope in the KLF from NPG02 is $\alpha = 0.23$, fully consistent with our value ($\Delta\alpha = 0.03$). In their study the authors also performed a comparison with a KLF presented in Brandl et al. (1999) (B+99). They found the two KLFs fairly similar except for the absolute number counts (see Fig. 11 therein). A similar discrepancy is found in the number counts of our KLF and the KLF from NPG02, which is attributed to the use of a more stringent detection threshold in NPG02 (see Sect. 10.2.3). We find a slightly higher number counts ($\times \sim 1.5$) than B+99 despite the fact that our ISAAC data is the same data set as B+99. This discrepancy is clearly due to the fact that we could resolve more sources in the crowded inner field ($r \leq 13''$) with our additional NACO data, which could not be detected in the seeing limited ISAAC data.

In summary we find the slope of our LF consistent with the previous works, but our higher angular resolution NACO data reveals ~ 50 % more stars in the central $r \leq 33''$.

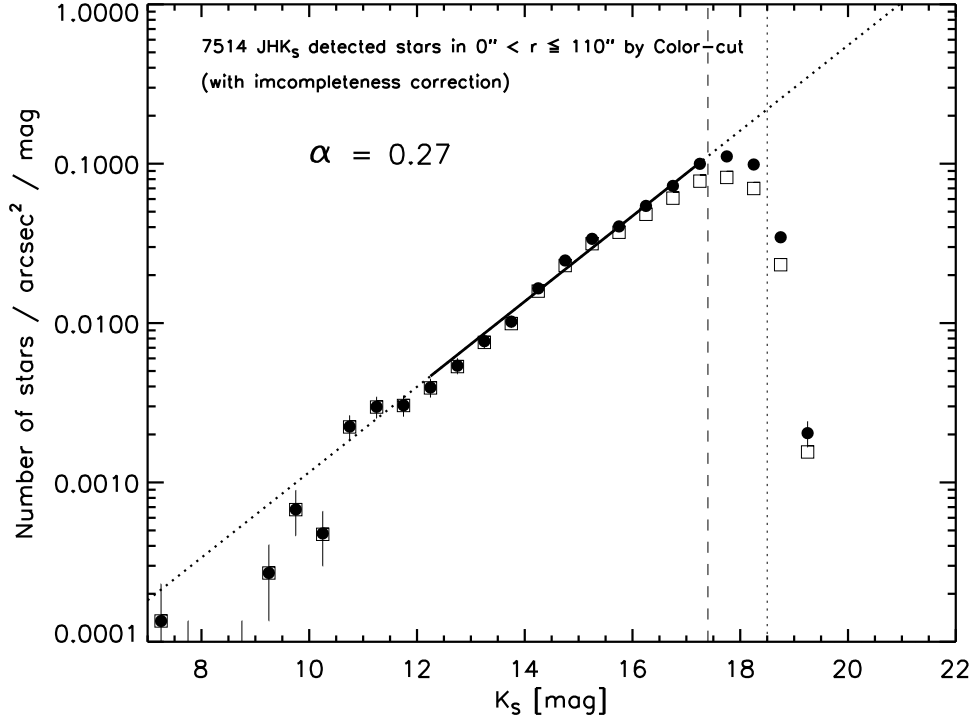


Figure 10.3: **K_S -band luminosity function of NGC 3603.** The figure shows the luminosity distribution derived from 7514 JHK_S detected stars within $r \leq 110''$ which are classified as cluster members by the color-cut. The circles and squares show the distribution with and without applying the incompleteness correction. The vertical dashed line represents the 50 % completeness limit in the inner $r \leq 13''$ part of the NACO field and the adjacent $13 < r \leq 30''$ annulus from the ISAAC field. The vertical dotted line indicates the detection limit in the outer ISAAC field derived in Sect. 7.2. The K_S -band completeness limits have been calculated from the J -band completeness limits assuming a typical $J - K_S$ color of 2 mag for low-mass PMS stars. The power-law index was measured in a magnitude range from about 12 mag up to the 50 % completeness limit of $m_{K_S} = 17.4$ mag. The solid line illustrates the best-fit power-law slope.

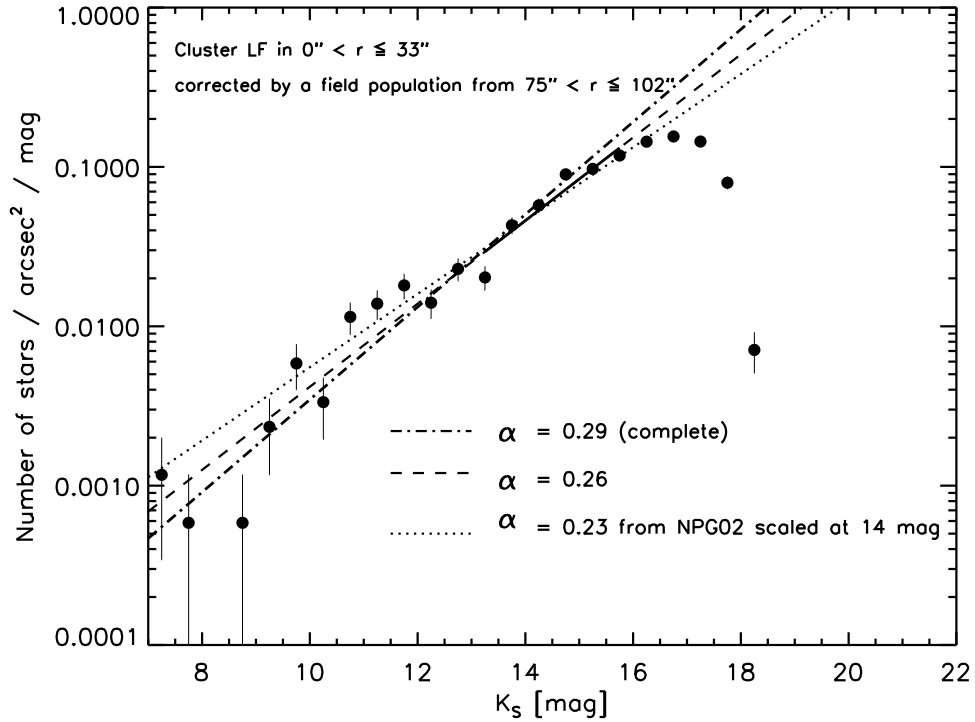


Figure 10.4: **Comparison of our KLF with previous studies.** The plot shows the KLF within $r \leq 33''$. The number counts are corrected for a field population derived from an outer ring at $77'' < r \leq 102''$. No incompleteness correction is applied to the plot. The solid line indicates a power-law fit for the range of $13 \leq m_{K_S} \leq 16$, the extrapolation is plotted as a dashed line. The dotted line indicates the best-fit power-law slope for the NPG02 KLF scaled to our number counts at 14 mag. The dash-dotted line shows the power-law slope for our incompleteness corrected number count.

Chapter 11

Initial mass functions of NGC 3603

In this chapter we present the analysis of the IMF of NGC 3603. We first explain the technique we have applied for the IMF determination. We then derive our best estimate of the IMF of NGC 3603 for the full field, and compare that with the IMFs of NGC 3603 reported in previous studies.

Subsequently we present the IMF as a function of distance from the cluster center using the NACO and ISAAC data. We investigate the observed radial trend in the IMF characteristics, and compare it with the results from other studies. In the section we also demonstrate the consistency between the IMFs derived from the NACO and ISAAC data, a prerequisite to safely interpret the observed radial variation of the IMF. The observed radial variation, which is a sign of the presence of a mass segregation, then leads us to investigate the dynamical evolutionary status of the cluster in the following chapters.

11.1 IMF determination

In our determination of the IMF we apply the preparatory treatments: the color-cut method to identify cluster members and the incompleteness correction. Note that, as demonstrated in the LF analysis in the previous chapter, combining the NACO and ISAAC data sets for a single IMF does not impose any systematic bias (see Sect. 10.2.1), and that the IMFs can be directly compared as long as the mass range is carefully chosen.

Fig. 11.1 shows the resulting IMF of the whole field out to $r \sim 110''$ (innermost $r \leq 13''$ from NACO, the outer field at $13'' < r \leq 110''$ from ISAAC). It is derived from the 7514 stars which are simultaneously detected in JHK_S and classified as cluster members based on the color-cut criterion. To compute the stellar masses, we used the combined luminosity-mass relation created from the 3 Myr MS, 0.7 Myr PMS, and 1 Myr low-mass PMS isochrones (see Sect. 8.1.2). All J , H , and K_S magnitudes were used to determine the best-fit stellar mass. The number of stars in a logarithmic mass intervals with $\Delta \log \mathcal{M} = 0.2$ were calculated. Note that we have used a double size bin at around $4 M_\odot$ to smooth out a discontinuity arose from connecting the MS and PMS isochrones.

As mentioned in Chap. 11, the IMF is generally described by a power-law for masses down to about $1 M_\odot$, then by a slightly shallower power-law below, thus it can be

described in forms such as a log-normal (Miller & Scalo, 1979), a broken power-law (e.g. Scalo, 1998; Kroupa, 2001), or a combination of both (Chabrier, 2003). Whereas in our derived IMF, there is no obvious turnover or a truncation down to our completeness limit. We thus employ merely the single power-law fit as a reasonable representation of the derived IMF. Note that, although we find a turnover at around $0.2 M_{\odot}$, we can not answer if the turnover is intrinsic to the stellar population or simply caused by the detection limit, because the 50 % detection limit of $\sim 0.15 M_{\odot}$ in the outer ISAAC field ($r > 30''$) varies substantially across the field. The slope of the power-law is derived for the mass range of $0.4 - 20 M_{\odot}$. This mass range is not affected by the saturation in the ISAAC data, and it guarantees a completeness of at least 50% even in the most crowded central region. The slope is derived from a weighted linear least-square fit, assuming a Poisson statistics for the uncertainty in the number counts.

The best-fit power-law index is $\Gamma = -0.74 (\pm 0.02)$. The error of the index is merely a formal fit error. The real errors of the index involves many other uncertainties in the entire scheme of the IMF determination, and it is expected to be larger than the present value. We will discuss in detail in the following chapter.

We have so far assumed only a uniform extinction in the luminosity-mass conversion, however, if the individual extinction is taken into account, the conversion from the luminosity to the stellar mass would yield a slightly different result. First, all sources are shifted according to the uniform extinction of $A_V = 4.5$ mag. Then, in case of the uniform extinction, their corresponding stellar masses are determined by taking the closest point from the source on the isochrone in the JHK_S magnitudes space. In case of the individual extinction, after the uniform shift, a stellar mass is determined from the intersection of the reddening vector of each star on the isochrone instead of taking the closest point.

Specifically some intermediate mass stars which are located on the PMS-MS transition region would be affected, because here the reddening vector is almost parallel to the isochrone (see the reddening vector and the PMS isochrones in the CMD of Fig. 8.1). In this case, the luminosity-mass conversion is fairly sensitive to our photometric errors. We have thus applied the uniform extinction in the IMF determination. We will discuss the impact of a potential individual reddening on the IMF characteristics in detail in Chap. 13.

In summary, we find a fairly shallow IMF ($\Gamma = -0.74$) for NGC 3603 when compared to the normal Salpeter IMF ($\Gamma = -1.35$). The detailed discussion in Chap. 13 will show if this finding is significant within the systematic uncertainties. In particular we will test if NGC 3603 as a whole has a shallow IMF, or merely the observed region within $r \leq 110''$.

11.2 Radial variation of the IMF

One of the characteristics of NGC 3603 which makes it a particularly interesting object is the high concentration of many massive OB and WR stars in the central starburst cluster (Moffat, 1983; Clayton, 1986; Drissen et al., 1995; Hofmann et al., 1995; Crowther & Dessart, 1998; Nürnberger & Stanke, 2003). This brings up the question of a possibly mass-segregated stellar distribution in the cluster. Since the richness of stellar population in our data of NGC 3603 enables us to better investigate the radial variations in cluster properties, to answer the question, we have built IMFs of seven concentric annuli with radii of $0 - 5'' - 10'' - 13''$ (from NACO) and $13'' - 30'' - 55'' - 80'' - 110''$

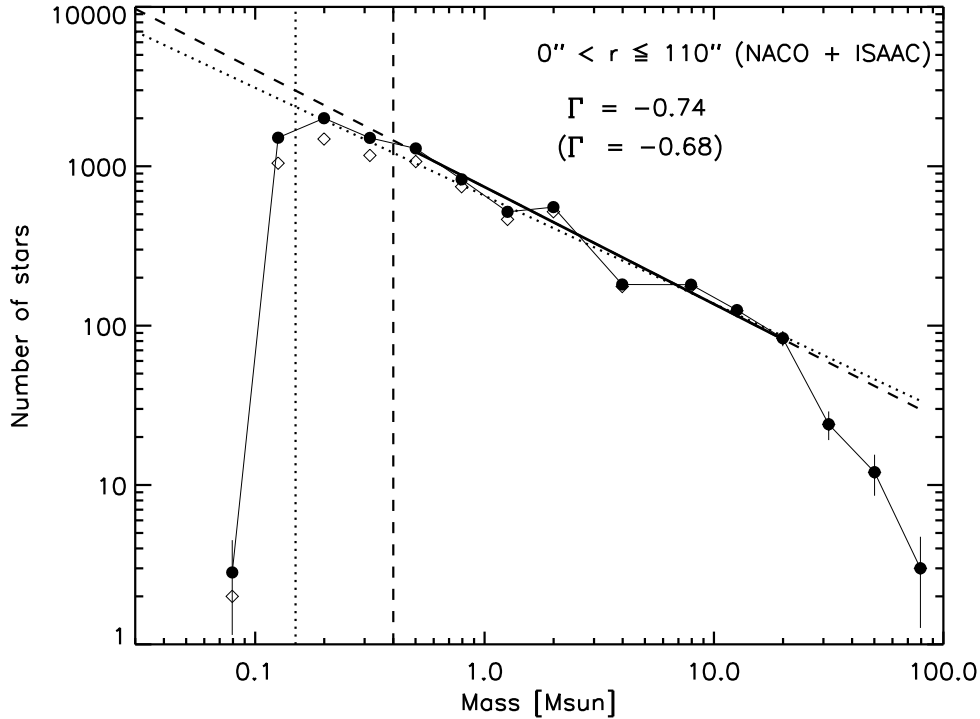


Figure 11.1: **IMF of NGC 3603.** The figure shows the IMF of the whole field extending out to $r \sim 110''$ (innermost $r \leq 13''$ from NACO, the outer field at $13'' < r \leq 110''$ from ISAAC). In this region we have identified 7514 JHK_S stars which are simultaneously detected in JHK_S and which are classified as cluster members based on the color-cut selection. Open diamonds and filled circles indicate the raw and the incompleteness corrected mass distributions, respectively. The best-fit power-law slopes are shown as a dotted and a dashed line. The fit was performed within a mass range of $0.4 - 20 M_\odot$ (shown as a solid line) determined by the detection limit for the low-mass end, and the saturation limit in the ISAAC data for the high-mass end. The vertical dashed line indicates the 50 % completeness limit within the innermost region of up to $r \sim 30''$. The vertical dotted line shows the detection limit in the ISAAC outer fields.

(from ISAAC).

The according IMFs are shown in Fig. 11.2. The symbols and lines are identical to the global IMF in Fig. 11.1. The best-fit single power-law is computed for a mass range of $0.4 - 20 M_{\odot}$ for the sake of keeping consistency across the whole field. While crowding is the dominant limitation for the detection of faint stars in the cluster center, the detection limit in the outer parts is given by the limiting magnitude. The vertical dashed lines in the first four panels ($r \leq 30''$) indicate the 50 % completeness limit from crowding, the vertical dotted lines in the other panels indicate the source detection limit derived from a Monte Carlo simulation with artificial stars.

Here we note that there is likely to be a potential application of an additional slope in a form of segmented power-law for high-mass bins in the IMFs for the inner three regions from the NACO data in which there is no saturation problem. We, however, adopt the single power-law with keeping the fitting mass range of $\leq 20 M_{\odot}$ for the consistency with the outer regions from the ISAAC data to trace the radial variation.

The IMF power-law indices for the seven annuli are $\Gamma = -0.31, -0.55, -0.72, -0.75, -0.80, -0.86, -0.83$ (with increasing radius). From these seven plots, several characteristics can be identified with respect to the radial variation of the mass distribution in this starburst cluster. First there is an obvious steepening of IMF with increasing radius up to $r \sim 30''$. The strongest change is within the innermost $r \sim 13''$. For larger radii the slope stays more or less constant around $\Gamma \sim -0.8$ (-0.86 as its maximum). The resulting power-law indices are also summarized in Tab. 11.1.

This observed variation of the slope indicates a mass-segregated stellar population. The main characteristics of this mass segregation are follows: 1) a strong concentration of high-mass stars in the very center at $r \lesssim 13''$, 2) a shallow IMF ($\Gamma \sim -0.8$) at $r \sim 30''$, 3) no evidence for further steepening at larger radii beyond $\sim 30''$.

The third point allows us to conclude that the IMF of the whole cluster (including the regions not covered by our observations) can not be steeper than a power-law with index $\Gamma \sim -0.9$. This suggests that the IMF of the entire NGC 3603 cluster is thus significantly shallower than the Salpeter IMF even if mass segregation has been occurring in the cluster.

However, to make conclusive discussions about the characteristics of the resulting IMF, in particular, with respect to its shallowness as a whole cluster, more detailed investigations into the observed mass segregation becomes necessary.

Particularly, any insights about the evolutionary status in terms of its dynamical evolution are of extreme importance for understanding the high concentration of high-mass stars at the center, and the population for the extended region in the cluster which have not covered in our observations. A detailed discussion of the mass segregation and dynamical evolution is given in later chapters.

Consistency between the NACO and ISAAC data

Since we have investigated the radial trend of the IMF using the inner regions from the NACO data and the outer regions from the ISAAC data, it is necessary to check the consistency of the two data sets.

As presented in Sect. 10.2.1, we verified that combining the two data sets in a combined LF does not cause any serious bias. Since the LF and IMF are directly linked by the luminosity-mass conversion relation, we expect that the combined IMF is also not affected by the differences between the two data sets.

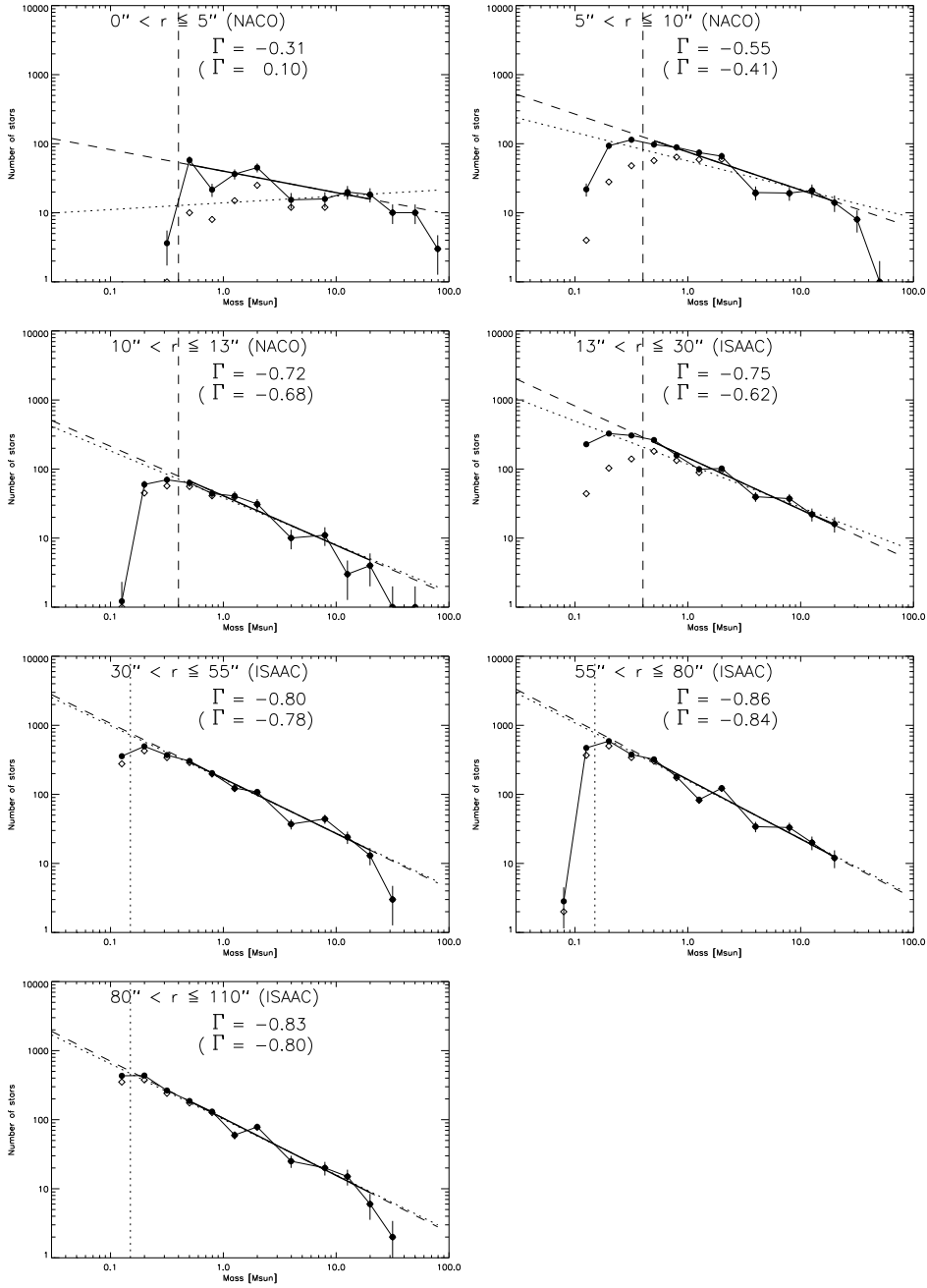


Figure 11.2: **Radial variation of the IMF.** The panels show the IMF for seven concentric annuli with increasing radius. The IMFs of the first three annuli are derived from the NACO field ($r \leq 13''$), and those of the four outer regions are derived from the ISAAC field ($13'' < r \leq 110''$). Open diamonds and filled circles show the raw and the incompleteness corrected distributions, respectively. The best-fit power-law are indicated as dotted (without incompleteness correction) and dashed (with incompleteness correction) lines. The according power-law indices are included in each panel (the numbers in brackets refer to the uncorrected IMF). The fit is performed within a mass range of $0.4 - 20 M_{\odot}$ (shown as solid lines). The vertical dashed lines in the first four IMFs ($r \leq 30''$) indicate the 50 % completeness limit from crowding. The vertical dotted lines in the other indicate the detection limit in the outer ISAAC fields.

Regions	Γ	Data
$r \leq 5''$	-0.31	NACO
$5'' < r \leq 10''$	-0.55	
$10'' < r \leq 13''$	-0.72	
$13'' < r \leq 30''$	-0.75	ISAAC
$30'' < r \leq 55''$	-0.80	
$55'' < r \leq 80''$	-0.86	
$80'' < r \leq 110''$	-0.83	

Table 11.1: **Radial variation of the IMF power-law index.**

Here, we want to ensure that combining the both data sets into a single IMF is indeed a reasonable treatment. To investigate the consistency we constructed two IMFs from NACO and ISAAC in an overlap region at $10'' < r \leq 13''$. Fig. 11.3 shows the resulting IMFs after applying the incompleteness correction for each data set. The power-law indices are derived from a fit in the mass range of $0.3 - 20 M_{\odot}$. As can be seen, the two data show quite similar distributions in the intermediate mass range (around $1.5 - 6 M_{\odot}$), however, show slight differences at the low- and high-mass ranges. There is a discernible discrepancy for low-mass stars, which are less frequently detected in the ISAAC data. There is also a slight discrepancy for high-mass stars, in which the ISAAC data has a higher frequency. Based on a careful inspection of the photometry we found that the both discrepancies are due to the severe crowding in the ISAAC field.

The low number count for low-mass population in the ISAAC data is mostly attributed to an under reconstruction of the number counts in the incompleteness correction because of the extreme crowding in the region. The high number count for high-mass stars in ISAAC is caused by a relatively less accurate photometry in this region due also to the crowding. Because of the larger pixel scale of the ISAAC data, the PSF photometry works less accurately than in the smaller pixel scale NACO data in the overlap region, and we confirmed that fluxes of some stars in the region are systematically overestimate. These effects leads to a slightly flatter slope for the mass distribution.

However, the crowding in the ISAAC field decreases dramatically for larger radii. Therefore the incompleteness causing the deficit of low-mass stars and the overestimation of the fluxes causing the high-mass shift in the ISAAC mass distribution are expected to decay rapidly. Thus those effects affect only slightly on the population in the larger annulus of $13'' < r \leq 30''$ in the ISAAC field, and are insignificant in the analysis of the IMF radial variation.

We thus conclude that, as the case of the LF, the two data sets are compatible, and their combination for analysis of the IMF radial trend is a reasonable treatment.

11.3 Comparison with previous studies

The IMF of NGC 3603 has been studied in earlier works based on both ground- and space-based observations. (Note that the IMF studies are summarize in the history of the studies of NGC 3603 in Sect. 3.2, we again summarize them below for the sake of convenience).

Moffat et al. (1994) derived the IMF of the high-mass stars from HST/PC1 observations. They found power-law index of $\Gamma = -1.4 \pm 0.6$ in a mass range of $30 - 60 M_{\odot}$.

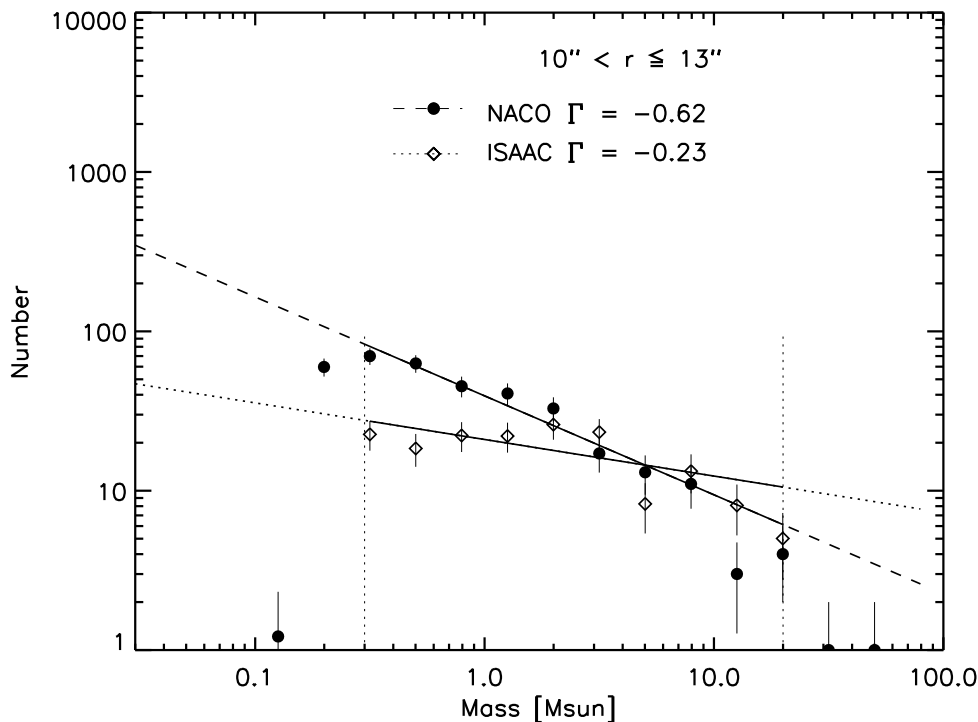


Figure 11.3: **Comparison of the IMFs from the NACO and ISAAC data.** The figure shows the IMFs for the overlap region with $10'' < r \leq 13''$. Diamond symbols show the number counts from the ISAAC observations, and filled circles show the number counts from the NACO observations. Incompleteness corrected distributions are used in the two mass functions to compensate for the crowding. The power-law slopes are fitted for a mass range of $0.3 - 20 M_{\odot}$. The limits (vertical dotted lines) of this mass range are the 50 % completeness limit of the NACO observations, and the saturation limit from the ISAAC images.

Hofmann et al. (1995) derived the IMF with a slope of $\Gamma \sim -1.59$ within a mass range of $15 - 50 M_{\odot}$ based on their diffraction-limited speckle observations. These results are consistent with the standard Salpeter IMF, however, only the high-mass stellar populations is covered in their studies. Eisenhauer et al. (1998) were the first to present high resolution near-IR observations using the adaptive optics ADONIS and the SHARPII+ camera at the ESO 3.6-m telescope. This study revealed the PMS population with masses as low as $\sim 1 M_{\odot}$ in the central starburst cluster. The IMF was found to be rather shallow with a power-law slope of $\Gamma \sim -0.73$ within a mass range of $1 - 30 M_{\odot}$, with no turnover or cut-off within that mass range.

Based on the seeing-limited *UBVRI* CCD photometric observations with the 1-m Elizabeth Telescope at the SAAO, Sagar et al. (2001) derived the MF for seven distant open star clusters, including NGC 3603. The slope of the MF is $\Gamma \sim -0.85$ within a range of $7 - 75 M_{\odot}$.

Recently, combining multi-wavelength ground-based, HST, and *Chandra* X-ray observations, Sung & Bessell (2004) derive a moderately flat IMF with a slope $\Gamma = -0.9$ over a mass range of $2.5 - 100 M_{\odot}$. The IMF shows a gradual steepening towards the outer regions ($\Gamma = -0.5$ at $r \leq 0'.1$, -0.8 at $r = 0'.1 \sim 0'.2$, -1.2 at $r \geq 0'.2$).

Based on $JHK_S L'$ photometric observations with the ISAAC at the VLT and H_α imaging from the HST/WFPC2, Stolte et al. (2006) derived the MF taking into account the field star population, individual reddening, and the potential binary contribution in the central region ($7'' < r < 65''$). The derived IMF has a power-law slope of $\Gamma \sim -0.91 \pm 0.15$ for $0.4 - 20 M_\odot$.

Comparing our results with these previous studies, we find the IMF slopes largely consistent with the results in several previous studies (Eisenhauer et al., 1998; Sagar et al., 2001; Stolte et al., 2006). Our power-law slope $\Gamma = -0.74$ for the entire field ($r \leq 110''$) is fairly similar to that from the central cluster in Eisenhauer et al. (1998) ($\Gamma \sim -0.73$). Even though we can detect much fainter stars in our new data, we still see no sign of turnover for masses as low as $\sim 0.4 M_\odot$.

Our result is also in agreement with the resulting MF of $\Gamma \sim -0.85$ ($7 - 75 M_\odot$) in Sagar et al. (2001), the authors, however, regard it as being consistent with the standard Salpeter-like IMF within errors in their derivation. In the study the authors mentioned that, above $1 M_\odot$, MF slopes of star clusters younger than 500 Myr (equivalent to IMF) in the solar neighborhood had no dependence on Galactic longitude, Galactocentric distance, and cluster age, and those were in agreement with the Salpeter IMF all within a 1σ error (scatter of $\sigma_\Gamma = 0.3$ around the Salpeter value), supporting the universality in the IMF in Galactic star-forming regions above $1 M_\odot$. As mentioned in Scalo (2005), this implies that their actual uncertainties are very large. In contrast, our interpretation of the resulting slope is a case of *flat* IMF, and this types of inconsistent interpretations among IMF studies would be discussed later in Chap. 14.

Like Sung & Bessell (2004), we find a radial variation in the IMF. However, our IMFs are somewhat flatter than their IMFs. Their IMF of the outermost region of $r > 12''$ shows a slope of $\Gamma = -1.2$, which is ~ 0.3 steeper than the IMF of their whole field ($\Gamma = -0.9$). In contrast, our IMF of the outer region ($\Gamma \sim -0.85$) is not substantially steeper than the IMF of the whole cluster ($\Gamma = -0.74$). As for the innermost region, they derived the IMF slope of $\Gamma \sim -0.5$ for $r \leq 6''$, being slightly steeper than our derivation of $\Gamma \sim -0.3$ for $r \leq 5''$. One possible reason for these differences is that Sung & Bessell (2004) include stars with masses up to $100 M_\odot$, while the saturation in the ISAAC images restricts our analysis to stars with masses $\leq 20 M_\odot$. Moreover, our mass range covers down to $0.4 M_\odot$, which is slightly lower than their low-mass coverage, contributing to the discrepancy. Therefore, a direct comparison of our IMFs with that of Sung & Bessell (2004) is not feasible.

Compared to the results in Stolte et al. (2006), our IMF shows a slightly shallower power-law slope of $\Gamma = -0.75$ for $13'' < r \leq 30''$ ($\Gamma = -0.87$ for $7'' < r \leq 33''$ in Stolte et al. (2006)). Since the same data set is used, this difference could arise from technical differences such as the field star subtraction and incompleteness correction. Indeed, we applied a slightly smaller correction than Stolte et al. (2006). Although we will present our analysis of the systematic uncertainties from the incompleteness correction in detail (Sect. 13.7), we note that a application of a stronger incompleteness correction for the IMF determination is found to steepen the power-law slope with $\Delta\Gamma \sim -0.13$. Thus some part of the slight difference in the IMF power-law index between our study and Stolte et al. (2006) would likely be explained by the difference of the correction rates.

While Stolte et al. (2006) claim no significant variation in power-law slope of the IMF, but talk of a depletion of the high-mass tail of the stellar mass distribution with increasing radial distance, we see a strong variation with radial distance over the whole

$0.4 - 20 M_{\odot}$ range from $\Gamma \sim -0.31$ for $r \leq 5''$ to $\Gamma \sim -0.85$ for $r \leq 110''$. The reason for this discrepancy is that Stolte et al. (2006) could not probe the central $r \leq 7''$ because of crowding, while our high resolution NACO observations resolve the central cluster even at $r \leq 5''$. The most part of the variation of the IMF slope, which is a steepening from $\Gamma \sim -0.3$ to -0.7 , occurs within the innermost $13''$ region in the cluster core.

In summary, our resultant IMF of NGC 3603, which has successfully revealed population in the central core with the mass range from the most massive stars down to $\sim 0.4 M_{\odot}$ within 50 % completeness, is in agreement with the previous studies by Eisenhauer et al. (1998), Sagar et al. (2001), and Stolte et al. (2006). This supports our hypothesis that the IMF of NGC 3603 is substantially flatter than the Salpeter IMF, and is an evidence of a top-heavy IMF in the star-forming environment.

However, for more detailed discussion of the resulting IMFs, we need to be more confident in our IMF determination. As will be discussed in Chap. 14, Kroupa (2001) reported that the potential effect of the uncertainties such as Poisson noise, dynamical evolution, and unresolved binary systems are large enough to reproduce the so far observed examples of the IMF variation. Thus, in order to approach the question - if our resulting IMF is indeed evidence of non-universal IMF, or is a case of the universal IMF within the errors - it is necessary to investigate the reliability of our IMF determination. Therefore, we investigate the systematic uncertainties of our IMF derivation in the following chapter.

Chapter 12

Mass segregation in NGC 3603

In this chapter we discuss the observed mass segregation in NGC 3603.

The mass segregation in a stellar cluster can potentially lead to a systematic error in the IMF determination *if the observations do not cover the entire cluster*. Such a mass segregation is observed in NGC 3603. The observed mass function shows a radial steepening from the cluster center to the outermost field up to $r = 110''$ (Sect. 11.2). The radial variation of the mass function power-law index mainly occurs within the innermost $13''$ of the cluster, where it decreases from $\Gamma \sim -0.3$ at $r \leq 5''$ to $\Gamma \sim -0.7$ at $r \leq 13''$. The high-mass stars are more concentrated towards the cluster center than the intermediate- and low-mass stars. We therefore have to investigate if the observed mass segregation can explain why the IMF of NGC 3603 appears to be significantly shallower than the Salpeter IMF.

For that, we need to know if the mass segregation in NGC 3603 is primordial or if it is caused by dynamical evolution, or if it is a mixture of both. A primordial mass segregation would result from the fragmentation of the parent molecular cloud in the early stage of star formation. Higher-mass stars tend to form near the bottom of the gravitational potential due to the richer supply with molecular gas (e.g. Bonnell et al., 1997), and subsequently remain near the cluster center.

The dynamical mass segregation, on the other hand, results from the tendency of the stellar cluster to reach an energy equipartition between the stars with different masses. The high-mass stars lose their kinetic energy through stellar encounters and preferentially sink towards the center of the cluster, while the low-mass stars attain high velocities and expand their orbits towards the outskirts of the cluster.

Below we investigate the dynamical mass segregation of the cluster. For that we first derive the global cluster properties such as its size, the total mass, the core radius, and the half-mass radius. These quantities then allow us to estimate the relaxation time of the cluster, and to conclude on the origin of the observed mass segregation.

12.1 Radial mass density profile

To determine the global properties of the cluster, we measure the projected radial mass density distribution and fit analytical models to the profile.

In a first step we fit the observed surface density using the standard empirical formula by King (1962). In this model, three quantities are used to parameterize the radial mass density profile. The first quantity is the core radius r_c , at which the surface mass density

has fallen to half of its central value. The second quantity is the tidal radius r_t , at which tidal forces from the host galaxy remove stars from the gravitationally bound star cluster and, consequently, the surface mass density becomes zero (in our case approaches the density of the background population). The third parameter is the central surface mass density. This King model is commonly used to describe the radial stellar density and brightness density profiles of globular clusters and old galactic clusters, and it is described as

$$f(r) = k \left[\frac{1}{\sqrt{1 + (r/r_c)^2}} - \frac{1}{\sqrt{1 + (r_t/r_c)^2}} \right]^2 \quad (12.1)$$

where $f(r)$ is the surface mass density as a function of the projected distance r from the cluster center. k is a normalization factor, which is approximately the central mass density, r_c is the core radius, and r_t is the tidal radius. Because our color selection may not reject all field stars, we modify the King model Eq. 12.1 by adding a constant term so that the profile converges to the background level at the tidal radius. For comparison, we also fit a modified power-law used by Elson, Fall, & Freeman (1987; hereafter EFF) in their study of the radial surface brightness profiles of young clusters in the LMC. They find that the young LMC clusters do not appear to be tidally truncated even at radii of several hundred arcsec, indicating that these clusters likely extend beyond their Roche limits as a result of dynamical interactions. The EFF model is described as

$$f(r) = f_0 \left(1 + \frac{r^2}{a^2} \right)^{-\gamma/2} \quad (12.2)$$

where f_0 is the central surface mass density, a is a measure of the core radius, and γ is the power-law index at large radii. The parameter a is related to the core radius r_c of the equivalent King model (Eq. 12.1) by $r_c = a(2^{2/\gamma} - 1)^{1/2}$.

Fig. 12.1 shows the radial mass density profile of NGC 3603 for stars within the mass range of $0.5\text{--}2.5 M_\odot$. The mass density of the innermost field ($r \leq 13''$) is measured from our NACO data using $1''$ wide concentric annuli, and the outer field ($13'' < r \leq 110''$) is measured from the ISAAC data with $8''$ wide annuli. We have applied the same field star rejection by the color-cut method and the same incompleteness correction as for the IMF. The best-fit King model and EFF model are shown in the plot. Here we note that we use the barycentre as determined from the observed projected stellar density distribution as the center of the cluster. This barycentre is located in the middle of the two brightest stars at the cluster core.

We find a decrease of density in the innermost $r \lesssim 2''$, which may not be real but caused by the blending from the bright central stars. We have therefore omitted this region in the model fit. Except for this very center, the incompleteness is not significant for the considered mass range of $0.5\text{--}2.5 M_\odot$, which corresponds to a K_S -band magnitude of about 15–17 mag. We select this mass range considering the following aspects. In case of a cluster with a mass segregated population, the shape of the mass density profile and consequently its characteristic radii depend on the considered mass range. Since the main goal of this chapter is to determine how many intermediate- and low-mass stars potentially reside outside the observed field of view, we chose the upper-mass limit of $2.5 M_\odot$. The lower-mass limit of $0.5 M_\odot$ is set by more than 50 % completeness of our data set.

From the fit of the King model we derive a core radius of $r_c \sim 4''.8$ (~ 0.14 pc at $d \sim 6$ kpc). The best-fit EFF model shows a fairly similar core radius of $r_c \sim 4''.7$. Because the best fit power-law index is $\gamma = 1.97$, the EFF profile is essentially identical to the King model with $r_t \rightarrow \infty$. For comparison, Grebel (2004) report a core radius of ~ 0.25 pc based on HST observations, and NPG02 report $\sim 23''$ (~ 0.66 pc at our estimate of $d \sim 6$ kpc) as an upper limit. Sung & Bessell (2004) derive about $3''$ from the optical data.

We can not directly deduce the tidal radius from our measurement. The observed stellar surface density is still decreasing at the maximum observed distance from the cluster center ($r \lesssim 110''$). The King model can satisfactory fit our observations for any tidal radius $r > 110''$. This difficulty is also expected from the fact that the EFF model, which does not take into account a tidal radius, fits our mass density profile equally good to the King model. Since we need to estimate the cluster size for deriving the total mass, half-mass radius, and relaxation time of the cluster, we will discuss other constrains for the tidal radius and the cluster size in the following section.

12.2 Total mass of NGC 3603

In this section we estimate the total mass and the half-mass radius of NGC 3603 using the radial mass density profile.

12.2.1 Size of NGC 3603

In order to derive the total mass of the cluster by integrating the radial mass density profile, the size of the cluster has to be known. As discussed in Sect. 12.1, fitting a King model to the measured radial mass density profile can not realistically constrain the cluster's tidal radius if it is outside the observed field.

In the following we will first summarize the results from previous, larger field observations, and then independently derive an upper limit combining the measured density profile and the Galactic tidal field.

Several previous studies report the size of NGC 3603, however, using substantially different definitions. For example, Nürnbergger & Petr-Gotzens (2002) give $r = 150'' \pm 15''$ as the radius where the stellar density falls below 3σ of the background variation. They also give a tidal radius $r_t \sim 1300''$ from the best-fit King model, but as in our study, the extrapolation beyond the observed field of view does not allow a reliable determination. Similarly, Sung & Bessell (2004) report a cluster radius of $2'$ based on the density profile of the bright stars identified in their optical and X-ray observations. The tidal radius derived from their King model fitting is $r_t \sim 900''$.

Following these two studies, we subsequently adopt a cluster size of $r \sim 150''$ to derive the cluster mass and half-mass radius. In addition, we give upper and lower limits to properly estimate the uncertainties in these quantities. Since the radial mass density profile decreases steadily within our observed field, the cluster certainly extends beyond this limit. We therefore can give a conservative lower limit of $r = 110''$ for the cluster size. The upper limit of the cluster size is calculated in a self-consistent way from the Galactic rotation curve and the measured density profile. This estimate is self-consistent in the sense that the tidal radius derived from the Galactic potential is a function of the total cluster mass, which itself is calculated from integrating the cluster mass density profile up to this tidal radius.

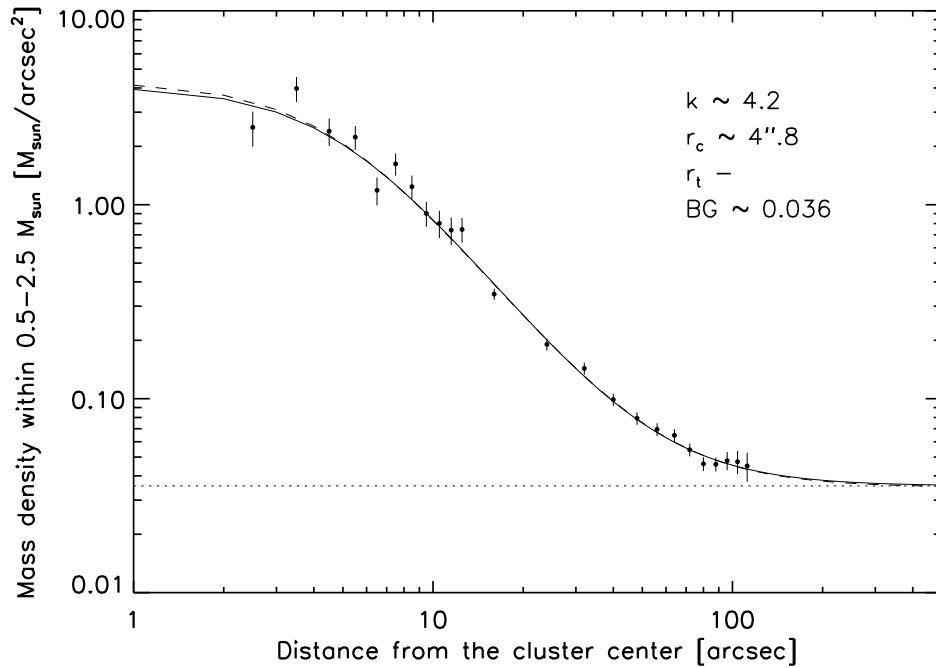


Figure 12.1: **Projected radial mass density profile of NGC 3603 for intermediate- and low-mass stars.** The surface mass density is plotted against the projected distance from the cluster center. Only stars within a mass range of $0.5 - 2.5 M_{\odot}$ are taken into account. We have applied the same color-cut for the field star rejection and the incompleteness correction as for the IMF determination. The error bars are based on an uncertainty from the Poisson statistics. The solid curve shows the best-fit King model. The horizontal dotted line shows the background stellar surface density derived from the fit. The dashed curve shows the best-fit EFF model.

The tidal radius r_t depends on the mass of the cluster M_c , the mass of the Milky Way inside the orbit of the cluster M_g , and the radius of the orbit R_g (assuming the cluster follows a circular orbit in the Milky Way). Treating the cluster and the Milky Way (partial mass) as a simple two-body system, the tidal radius is given by

$$r_t = R_g \left(\frac{M_c}{2M_g} \right)^{1/3}. \quad (12.3)$$

In the study of the Pleiades cluster Pinfield et al. (1998) give an approximate expression for the tidal radius of the cluster:

$$r_t = \left[\frac{GM_c}{2(A-B)^2} \right]^{1/3} = 1.46M_c^{1/3} \quad (12.4)$$

where $(A - B)$ is the difference of the Oort constants, describing the differential rotation of the Galaxy in the solar neighborhood, from Kerr & Lynden-Bell (1986). Since the Galactocentric distance of NGC 3603 is similar to that of the Sun, we adopt this relation for our estimate.

Using Eq. 12.4 and the total mass calculated from the mass density profile (which will be explained in the following part), we can iteratively determine a self-consistent tidal radius. We start with an initial guess of r_t to get a first estimate of the total mass by integrating the best-fit King model up to this tidal radius. Equation 12.4 then gives an improved estimate for r_t . This procedure is repeated until the tidal radius converges to a self-consistent value. As a result we derive $r_t \sim 1260''$. This value is used as the upper limit of the cluster size.

12.2.2 Deprojection of the surface mass density distribution

The calculation of the total mass of the cluster is done in the following way: 1) deprojection of the surface mass density profile into a volume density, 2) integration of the volume mass density from the cluster center up to the cluster radius, and 3) scaling the stellar mass from the mass range ($0.5 - 2.5 M_\odot$) used for measuring the cluster profile to the full stellar mass range (assuming $0.1 - 100 M_\odot$) using the IMF.

In a spherical system, the surface mass density $f(R)$ is related to the volume mass density $m(r)$ by the Abel integral

$$f(R) = 2 \int_R^\infty \frac{rm(r)dr}{\sqrt{r^2 - R^2}}. \quad (12.5)$$

Inverting this equation gives the volume mass density

$$m(r) = -\frac{1}{\pi} \int_r^\infty \frac{df(R)}{dR} \frac{dR}{\sqrt{R^2 - r^2}} \quad (12.6)$$

where r and R are the spatial and the projected radii, respectively. The enclosed mass in a sphere of radius r is then obtained by integrating Eq. 12.6.

$$M(r) = 4\pi \int_0^r m(x)x^2 dx. \quad (12.7)$$

It is worth mentioning that the total mass from integrating the profiles up to the cluster radius is the same when using the surface density and the volume density. However, there is a difference when integrating the enclosed mass within a certain radius

which is smaller than the cluster size. The integration of the surface mass density profile $M(R) = 2\pi \int_0^R f(x)xdx$ gives an enclosed mass in a cylinder of radius R , which is larger than according enclosed mass in a sphere. For example, we would overestimate the enclosed mass in a sphere by $\sim 7\%$ and $\sim 9\%$ for the cluster radius of $r = 150''$ and its lower limit ($r = 110''$), respectively, when simply integrating the surface density profile. This effect becomes large and yields non-negligible errors when calculating the half-mass radius and the core mass density (see below). We will therefore use the volume density distribution derived from the deprojection of the best-fit King model with the tidal radius of $r_t = 1260''$.

First we derive the upper limit of the total mass M_{total} and half-mass radius r_{hm} of NGC 3603 from the upper limit of the tidal radius $r_t = 1260''$. Integration of the de-projected King model up to this tidal radius gives a total mass of approx. $2520 M_\odot$ for the stars within the range of $0.5 - 2.5 M_\odot$ used in the radial density profile. Assuming a power-law IMF with $\Gamma = -0.74$ over a stellar mass range of $0.1 - 100 M_\odot$, we then get a total stellar mass of $M_{total} \sim 16000 M_\odot$. The half-mass radius of NGC 3603 is $r_{hm} \sim 52''$ (~ 0.7 pc at 6 kpc). As we have measured the radial mass density profile for stars with masses of $0.5 - 2.5 M_\odot$, this half-mass radius applies only to stars in this mass range, and does not take into account any mass segregation.

In the same way we derive the total mass and half-mass radius using the best-guess and lower limit of the cluster radius. For the best-guess radius of $r = 150''$, we derive $M_{total} \sim 11800 M_\odot$ and $r_{hm} \sim 30''$. For the lower limit $r = 110''$, we derived $M_{total} \sim 10700 M_\odot$ and $r_{hm} \sim 25''$.

To get a hand on the uncertainty of the derived total mass, we analyze the propagation of potential systematic errors in the IMF power-law index ($\Gamma = -0.74$) and the stellar mass range of the cluster ($0.1 - 100 M_\odot$). For that we restrict ourselves to the case of the best-guess of the cluster size $r = 150''$.

We first check the uncertainty resulting from the assumed IMF power-law index. Since our goal is to estimate the total stellar mass outside the observed field of view $r \geq 110''$, it may be more suitable to use the IMF of the outermost ISAAC fields instead of the average IMF ($\Gamma = -0.74$). The IMFs of the outermost two annuli have similar power-law indices $\Gamma = -0.83$ and -0.86 (Fig. 11.2). We therefore adopt $\Gamma = -0.85$. In this case we derive a total cluster mass of approx. $9700 M_\odot$, i.e., $\sim 18\%$ less than for the average IMF. Next we test the stellar mass range. If we assume a slightly wider mass range of $0.01 - 120 M_\odot$ instead of $0.1 - 100 M_\odot$, we derive a total mass of approx. $13500 M_\odot$, $\sim 15\%$ increase in the total mass. Taking into account the lower and upper limits for the cluster radius ($r \sim 110''$ to $\sim 1260''$) and the errors from the IMF slope and the stellar mass range, we estimate the total mass of NGC 3603 to be $1.0 - 1.6 \times 10^4 M_\odot$, and the half-mass radius to be about $25 - 50''$ ($0.7 - 1.5$ pc at $d = 6$ kpc).

From the de-projected best-fit King model with the core radius of $r \sim 5''$ we can also derive the central mass density. It is $\sim 6 \times 10^4 M_\odot \text{pc}^{-3}$. As the high-mass stars are more concentrated towards the cluster center compared to the stars used in the measurement of the density profile ($0.5 - 2.5 M_\odot$), the above central mass density is a lower-limit. It is worth mentioning that the core density measured directly from the surface density profile (without de-projection) would give a factor of ~ 2 larger value (approx. $1.2 \times 10^5 M_\odot \text{pc}^{-3}$).

12.3 Dynamical evolutionary status

To answer the question if the observed mass segregation in NGC 3603 has a dynamical origin or a primordial origin, or a combination of the both, we estimate the *relaxation time* of the cluster from its total mass and half-mass radius.

The relaxation time is the time over which stars have slowly wandered away from their initial orbits by experiencing gravitational encounters, and at which they have lost their memory of their original kinetic energy. Through a myriad of gravitational encounters, the stars exchange their kinetic energy and smooth out the energetic differences. Thus higher-mass stars slow down and concentrate towards the cluster center, while lower-mass stars gain kinetic energy and expand their orbits towards the outskirts of the cluster. Consequently the system gradually approaches equipartition, resulting in a stratified mass distribution in radial direction.

Because the relaxation time depends on the stellar density, it is a function of radial distance from the cluster center, and varies by several orders of magnitude across the cluster. While the inner parts relax most quickly, the outer parts take much longer to relax. The relaxation time also depends on the stellar mass. Higher-mass stars relax more quickly than lower-mass stars.

In our study we restrict ourselves to the *average* relaxation time of the cluster. Following Binney & Tremaine (1987), the median relaxation time t_{relax} of a stellar population is given by

$$t_{relax} = \frac{6.5 \times 10^8}{\ln(0.4N)} \left(\frac{M}{10^5 M_\odot} \right)^{\frac{1}{2}} \left(\frac{1M_\odot}{m_\star} \right) \left(\frac{r_{ch}}{1pc} \right)^{\frac{3}{2}} \text{ yr} \quad (12.8)$$

where M is a total mass within the characteristic radius r_{ch} , m_\star is the characteristic stellar mass, and N is a total number of stars in the cluster. Usually the half-mass radius r_{hm} is taken as the characteristic radius (e.g., Portegies Zwart et al., 2002). The according *half-mass relaxation time* is then a good estimate for the dynamical time scale of the whole cluster.

Here we estimate the relaxation time for the two extreme cases of upper and lower limits of the total mass and half-mass radius. For the upper limit half-mass radius $r_{hm} = 50''$, a total mass of $\sim 8000 M_\odot$ within the half-mass radius (i.e., half of the upper limit cluster's total mass $\sim 16000 M_\odot$), a characteristic stellar mass of $1 M_\odot$, and a total of approx. 16000 stars, we get a half-mass relaxation time of ~ 39 Myr. As a lower limit we derive a relaxation time of ~ 11 Myr using $r_{hm} = 25''$, a total half-mass of $\sim 5400 M_\odot$, and $N \sim 10000$. Taking into account the uncertainty in the number of stars, the half-mass relaxation time could vary by about 5 to 10 %. In any case it is safe to say that the dynamical time scale for stars with masses around $1 M_\odot$ is of the order of ten million years. This is about an order of magnitude larger than the age of the intermediate- and low-mass stars in the cluster, which is less than ~ 1 Myr. The intermediate- and low-mass stars ($\lesssim 2 M_\odot$) are still young enough such that the dynamical evolution has not yet changed substantially their initial kinetic energy.

As the dynamical time scale is inversely proportional to the stellar mass, the high-mass stellar population of NGC 3603 is expected to have a much shorter relaxation time. The smaller half-mass radius of the massive stars further decreases the relaxation time proportionally to the power of 1.5 (see Eq. 12.8). For example, if we simply apply the lower limit of $r_{hm} = 25''$ which is derived based on the $\lesssim 2 M_\odot$ stars, we obtain a rough estimate of the relaxation time of about 1 Myr for stars typically $10 M_\odot$. We therefore

conclude that the massive stars in the central cluster in NGC 3603 have a dynamical time scale which is an order of magnitude smaller than that of the solar mass stars, and therefore comparable to the cluster age. Thus we can not conclude if the observed mass segregation is dynamical or primordial.

Similar dynamical state is seen in other young stellar populations. For example, the young ONC ($\lesssim 1$ Myr) has been reported to show a mass segregation. Here the higher-mass stars are preferentially located in the cluster center due to primordial effects. But like in NGC 3603, there is no evidence of mass segregation for stars below $1 - 2 M_{\odot}$ (Hillenbrand et al., 1998).

Chapter 13

Systematic uncertainties of the IMF determination

There are several systematic uncertainties which could potentially affect the derived characteristics of the IMF. A first class of such uncertainties could arise from the determinations of the age, distance, and foreground extinction of the cluster. Since these parameters are derived from the analysis of the CMDs and CCDs, these uncertainties implicitly include the systematic errors from the PSF photometry.

The selection of stellar evolutionary model among various available choices is also subject to an uncertainty, and once a set of evolutionary model is chosen, the metallicity selection is also a potential uncertainty.

From a technical point of view, our incompleteness correction based on the empirical approach, and the treatment of the field population based on the color-cut method are possible uncertainties in the IMF derivation. Moreover, since our observations up to $r = 110''$ cover a partial of the whole cluster, the stellar mass outside the observed field of view has to be considered.

As for the intrinsic properties of the cluster, the presence of variable extinction and infrared excess, and the unresolved binary/multiple systems could also affect the derived IMF characteristics. In the following we demonstrate how those uncertainties could alter the derived IMF, and in particular, how the index of the power-law slope could vary by scrutinizing these uncertainties one by one.

For the examination of uncertainties due to age, distance, foreground extinction, metallicity, evolutionary model, and the stellar mass outside the observed field, we construct a simplified two mass bins IMF in each case. Here we count only the stars in two mass ranges, $1.7 - 2.6 M_{\odot}$ and $8 - 19 M_{\odot}$ as low- and high-mass bins, respectively. This allows us to examine the mass distribution in a simple and consistent way. Computing the power-law index from the number counts in the two bins, we can examine the potential change of the index due to each of the uncertainties. We have selected the $1.7 - 2.6 M_{\odot}$ and $8 - 19 M_{\odot}$ mass bins, because these mass ranges do not suffer from the detector saturation in the ISAAC observation, and are also almost free from incompleteness even in the highly crowded central cluster in the NACO field. Another simplification is that we use only the J -band magnitude for the luminosity-mass conversion, in contrast of using all three JHK_S -bands for the best estimate of the IMF in Chap. 11.

For deriving uncertainties in the IMF determination from the individual extinction,

the incompleteness correction, and the unresolved binary population, we follow the technique of determination of the best IMF using all three JHK_S -bands, but here with different assumptions. The purpose of this exercise is to derive the systematic error of the IMF power-law index for each uncertainty. Since some of the errors have asymmetric distributions, we then give the median and the upper and lower limits from each measurement.

After analyzing the individual systematic uncertainties, we combine all resulting errors by a technique of asymmetric error propagation to obtain the best estimate of the power-law index including the combined systematic error. Together with the analysis of the dynamical evolution of the cluster, this will allow us to discuss the IMF in the context of the claim of a universal IMF.

13.1 Age

In this section we analyze the systematic error in the IMF from the uncertainties in the age selection based on the isochrone fitting. As presented in Sect. 8.1.2, we have used the 2.5 Myr LS01 isochrone for the MS population and the 0.7 Myr PS99 isochrone for the PMS population. This selection is in agreement with the current age estimate of $\lesssim 3$ Myr in literature. In order to safely cover the uncertainties in the age estimate, we study the effect of a selection among the 0.2, 1, 2.5 and 5 Myr MS isochrones (LS01) for the high-mass bin, and the 0.3, 0.7, 1, and 1.5 Myr PMS isochrones (PS99) for the low-mass bin.

By counting the number of stars in the $1.7 - 2.6 M_\odot$ and $8 - 19 M_\odot$ mass bins, we compute the IMF power-law indices for all possible combinations of the MS and PMS isochrones. We summarize the results in Tab. 13.1.

There are several points to highlight from the result. First, there is a correlation between the age and the resulting power-law index. If the age of the MS isochrone is fixed to 2.5 Myr, a younger age of the PMS isochrone results in a shallower IMF slope. In contrast, in case of a fixed PMS isochrone age, a younger age of the MS isochrone results in a steeper slope of the IMF. This outcome can be explained by re-writing the definition for the IMF $\xi(\mathcal{M})$ using the mass-luminosity(magnitude) relationship:

$$\xi(\log \mathcal{M}) \propto \psi(M) \times \mathcal{M} \times \frac{d\mathcal{M}^{-1}}{dM} \quad (13.1)$$

(from Eq. 10.1), where the last term is the derivative of a mass-magnitude relation. When plotting the mass-magnitude diagram ($\log \mathcal{M} - M_J$) of the various isochrones (Fig. 8.3), a younger age shows a steeper profile. As a result, a given mass range (e.g., the examined two mass bins $1.7 - 2.6 M_\odot$ and $8 - 19 M_\odot$) covers a narrower magnitude range for younger isochrones, i.e., larger derivatives, resulting in smaller number counts. This leads to the observed correlation between the age and the power-law slope.

The other point is the fact that the biggest change of the IMF power-law index originates from the selection of the PMS isochrone (as can be seen in the upper part of the table). This is due to the fact that the mass-magnitude relation of PMS stars is more sensitive to the age variation, i.e., the change of the derivative $d\mathcal{M}/dM$ is stronger, than that of the $8 - 19 M_\odot$ MS stars. We derive the most extreme change for the youngest 0.3 Myr PMS isochrone, because it shows the steepest mass-magnitude profile within the examined mass range (i.e., the largest $d\mathcal{M}/dm$), resulting in a substantially lower number counts, and thus a shallow IMF.

We note that the IMF power-law index derived from the two mass bins is only little different from fitting the complete IMF. For our best age estimate (2.5 Myr MS and 0.7 Myr PMS) the index from the simple two mass bins analysis gives $\Gamma = -0.82$ in comparison to $\Gamma = -0.74$ for the thorough analysis. This slight discrepancy arises from two technical reasons. The first is a different mass range for the power-law fit: we have used the mass range of $0.4 - 20 M_{\odot}$ for the best IMF, while the power-law index of the simple method is derived from a narrower range ($1.7 - 19 M_{\odot}$). The other aspect is that the simple two mass bins method uses solely the J -band magnitude, while the thorough analysis takes advantage of all three JHK_S -bands.

As a result, we find that the age uncertainty leads to a systematic uncertainty in the IMF power-law index of $\Delta\Gamma = +0.60$ and -0.41 . We note that the IMF could become even shallower by the selection of an even younger age (< 0.3 Myr) for the PMS population, but that any age selections can steepen the power-law slope by merely $\Delta\Gamma \sim 0.4$.

We note that the systematic error in the above analysis provides the upper and lower limits, but that the realistic uncertainty is expected to be much smaller. Fig. 13.1 shows the CMD of the NACO fields with the four tested PMS isochrones. As can be seen, the 0.7 Myr and the 1.0 Myr isochrones reasonably fit the PMS-MS transition region as well as the MS turn-on point at about $J = 15.2$ mag and $J - K_S = 0.7$ mag. However, the 1.5 Myr isochrone clearly fails to fit the MS turn-on point, and the 0.3 Myr isochrone fails to reproduce the bulk of the population in the PMS-MS transition region.

Age of isochrone (Myr)		Γ
High-mass bin (MS)	Low-mass bin (PMS)	
0.2	0.3	-0.35
1.0	0.3	-0.34
2.5	0.3	-0.30
5.0	0.3	-0.28
0.2	0.7	-0.87
1.0	0.7	-0.86
2.5	0.7	-0.82
5.0	0.7	-0.80
0.2	1.0	-1.10
1.0	1.0	-1.09
2.5	1.0	-1.05
5.0	1.0	-1.03
0.2	1.5	-1.28
1.0	1.5	-1.27
2.5	1.5	-1.23
5.0	1.5	-1.21

Table 13.1: Variation of the power-law index due to age.

13.2 Distance

Here we examine the potential influence of a systematic error in the distance of NGC 3603 on the IMF measurement. Earlier studies have measured the distance to be within $6 - 8$ kpc, and $d \sim 6$ kpc yields a reasonable fit in our isochrone fitting in the CMD. We therefore study distances of 5, 6, 7, and 8 kpc (they correspond to distance moduli of

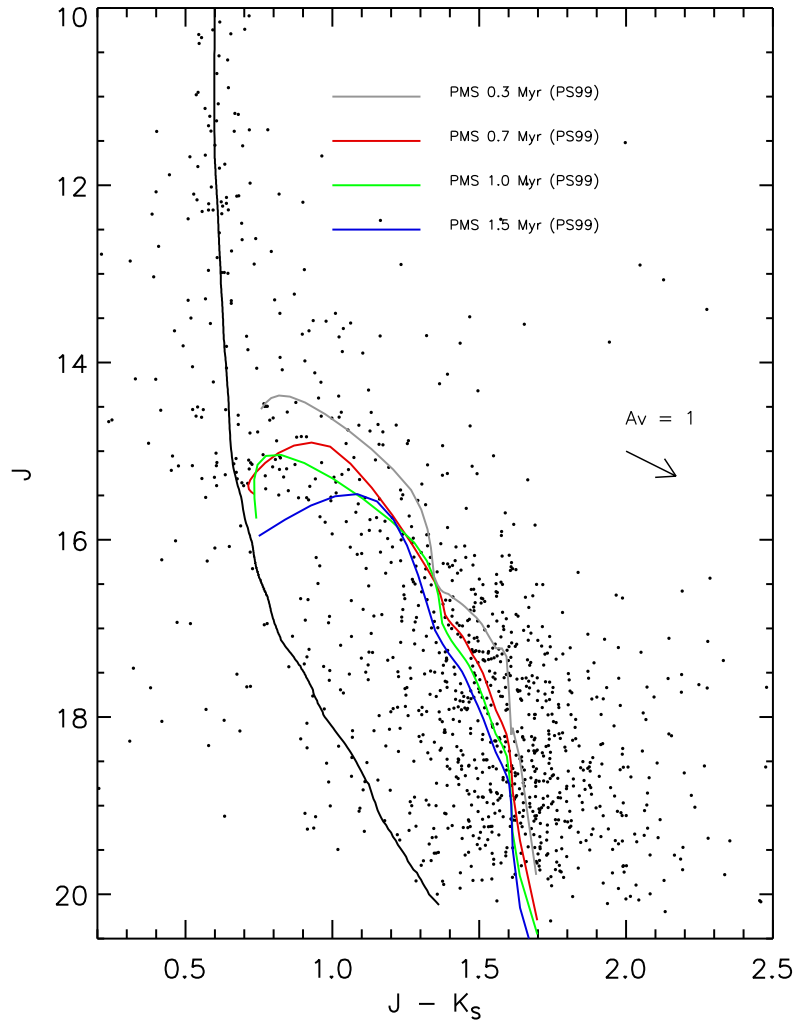


Figure 13.1: **PMS isochrones (PS99) in the $(J - K_S, J)$ CMD.** The $(J - K_S, J)$ CMD from the NACO is shown with the PMS isochrones for an age of 0.3, 0.7, 1.0, and 1.5 Myr. The 0.7 and 1.0 Myr isochrones reasonably fit the PMS-MS transition region, and the MS turn-on point at about $J = 15.2$ mag and $J - K_S = 0.7$ mag. However, there is a void in the stellar distribution at the MS turn-on of the 1.5 Myr isochrone, which let us reject the according isochrone for the IMF determination.

$(m - M)_0 = 13.49, 13.89, 14.22,$ and 14.51 mag respectively) to see the resulting change of the IMF slope. Note that we do not adjust the color-cut for the rejection of field stars, but only change the distance to calculate the apparent magnitude-mass conversion.

We summarize the resulting power-law indices in Tab. 13.2. The indices are fairly insensitive to distance changes. We derive a negligible variation of $\Delta\Gamma = \pm 0.01$. The small variation of the index is expected from the fact that a change in distance simultaneously shifts both low- and high-mass magnitude ranges, and thus does not yield any significant differences in the ratio of the high- to low-mass counts.

Distance (kpc)	Γ
5.0	-0.85
6.0	-0.84
7.0	-0.86
8.0	-0.85

Table 13.2: Variation of the power-law index due to distance.

13.3 Foreground extinction

Here we analyze the systematic error in the IMF slope resulting from the uncertainty in the foreground extinction. As described in Sect. 8.1.3, our best estimate of the interstellar extinction towards NGC 3603 is $A_V = 4.5 \pm 0.5$ mag, consistent with the earlier studies.

Considering the observed radial increase of the foreground extinction of $\Delta A_V \sim 2.0$ mag from the cluster center to the outermost ISAAC fields in Sect. 8.2.1, we apply three different values $A_V = 4.0, 4.5, 6.5$ mag to derive the uncertainty in the IMF slope. The according isochrones are shown in the CMD of Fig. 8.4. Like for the analysis of the systematic error from the age uncertainty, we do not adjust the color-cut for the rejection of field stars.

We summarize the resulting power-law indices of the IMF in Tab. 13.3. The slope does not show any trend, and is fairly insensitive to the adopted foreground extinction with $\Delta\Gamma = {}_{-0.01}^{+0.02}$. Note that the slight difference between the power-law index derived from the simple two mass bins method ($\Gamma = -0.83$ for $A_V = 4.5$ mag) and that of the IMF determination in Sect. 11.1 ($\Gamma = -0.74$) arises from the difference in the mass range for the slope fitting.

A_V (mag)	Γ
4.0	-0.86
4.5	-0.83
6.5	-0.86

Table 13.3: Variation of the power-law index by foreground extinction.

13.4 Theoretical model dependence

In this section, we investigate the systematic error from the selection of a specific stellar evolutionary model on our IMF determination. For that we use several currently available MS and PMS evolutionary models to derive the number counts for the low- and high-mass bins, and calculate the change in the power-law index of the resulting IMF.

For the $8 - 19 M_{\odot}$ high-mass bin, in addition to the 2.5 Myr MS isochrone in the Geneva model (LS01), we alternatively apply a solar metallicity isochrone of the Padova evolutionary model computed with the 2MASS filter system (Bertelli et al., 1994; Girardi et al., 2000; Bonatto et al., 2004). Since the available isochrone set starts from 4 Myr, we use the youngest 4 Myr isochrone here. For the $1.7 - 2.6 M_{\odot}$ low-mass bin we apply the PS99 set, a PMS model published by Siess et al. (2000) (designate as SDF00), and the Y^2 isochrones based on the revised Yale models (Yi et al., 2001; Demarque et al., 2004, and references therein). It is well known that the various available PMS evolutionary models result in considerable discrepancies in the age estimate of a star cluster, in particular, for a very young age (less than a few Myr). The reason for this discrepancy are different initial conditions used in the models (Tout et al., 1999; Baraffe et al., 2002). There are also discrepancies when deriving stellar masses from the various currently available models. Hillenbrand & White (2004) report the comparison of PMS models with dynamically derived stellar masses. They find that the BCAH98 model shows the most reasonable match for stars below $1.2 M_{\odot}$. This supports our use of the 1 Myr BCAH98 isochrone below $1.2 M_{\odot}$ (in Sect. 8.1.2). As a reminder, we estimated the age of the more massive PMS population in NGC 3603 to be $0.5 - 1.0$ Myr and its average to be 0.7 Myr on the basis of the application of the PS99 PMS isochrones (see detail in Sect. 8.1.2). However, for the analysis of the model dependency of the IMF it is necessary to individually select the best-fit age for each PMS model instead of simply applying 0.7 Myr. Thus we first performed an isochrone selection from the $(J - K_S, J)$ CMD.

As a result, we select the 1.5 Myr SDF00 isochrone and the 1.5 Myr Y^2 isochrone for the PMS. For illustration we show a $(J - K_S, J)$ CMD for the innermost $r \leq 13''$ NACO region with various candidate isochrones in Fig. 13.2. As can be seen, the 2.5 Myr LS01 (Geneva) and 4 Myr Padova NS isochrones, show only a slight difference in the $J - K_S$ color at $m_J \leq 14$ mag, while the three PMS isochrones show noticeable offsets. Compared to the 0.7 Myr PS99 isochrone, the 1.5 Myr Y^2 isochrone is slightly bluer for $J \gtrsim 16$, but fits still reasonably well the bulk of the PMS population. The 1.5 Myr SDF00 isochrone resembles well the 0.7 Myr PS99 PMS isochrone except for a slight offset at the PMS-MS transition region. As mentioned in Siess et al. (2000), the SDF00 model generally yields a somewhat younger age estimate for a given luminosity compared to other PMS models in literature.

The resulting IMF slope indices are summarized in Tab. 13.4. The power-law indices show a slightly asymmetric distribution with $\Delta\Gamma = \begin{smallmatrix} +0.07 \\ -0.13 \end{smallmatrix}$. We also checked the IMF power-law index for the 4 Myr LS01 Geneva isochrone. The difference from the slope using the 2.5 Myr is fairly small (~ 0.02). This supports the feasibility of the use of the youngest 4 Myr Padova isochrone in this investigation.

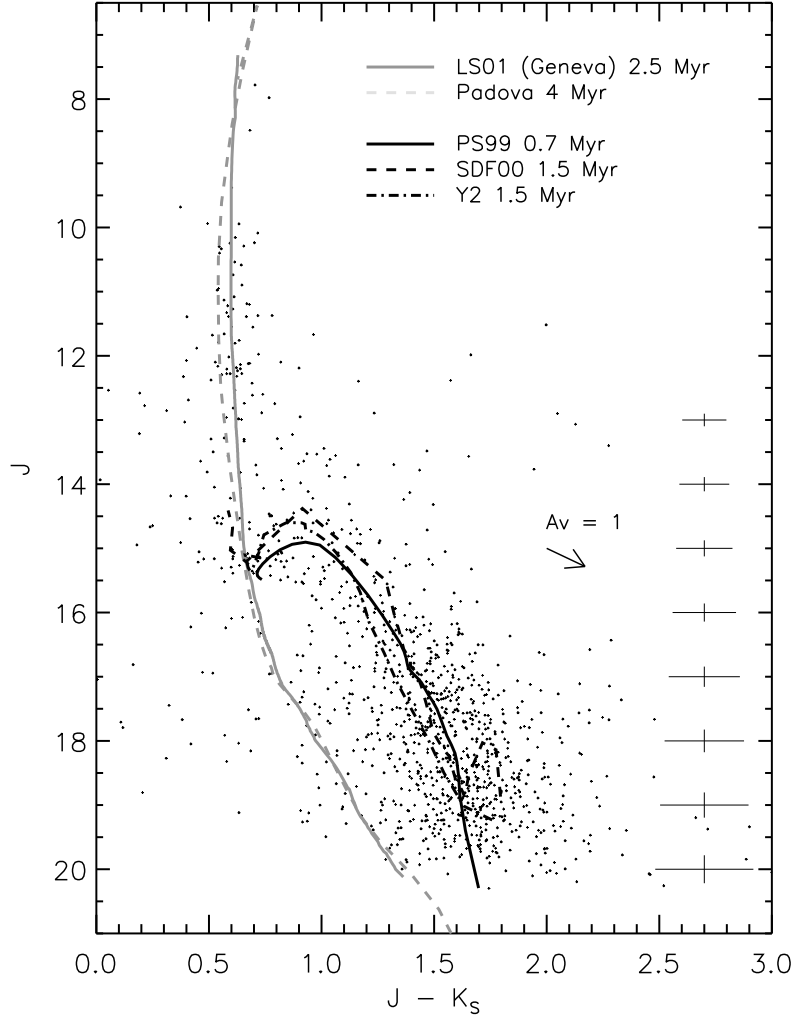


Figure 13.2: $(J - K_S, J)$ CMD with the candidate isochrones. The plus symbols show 1158 stars detected in the innermost $r \leq 10''$ region from the NACO data after dereddening by the average extinction $A_V = 4.5$ mag (no rejection of field stars is applied). The gray lines show the 2.5 Myr LS01 isochrone (solid) and the 4 Myr Padova isochrone (dashed). The black lines show the 0.7 Myr PS99 isochrone (solid), the 1.5 Myr SDF00 isochrone (dashed), and the 1 Myr Y^2 isochrone (dash-dotted), respectively. The arrow shows a $A_V = 1$ mag reddening, and the statistical error is indicated with crosses on the right side.

Isochrone model		Γ
High-mass bin (MS)	Low-mass bin (PMS)	
LS01 (Geneva) 2.5 Myr	PS99 0.7 Myr	-0.82
	SDF00 1.5 Myr	-0.75
	Y ² 1.5 Myr	-0.95
Padova 4 Myr	PS99 0.7 Myr	-0.83
	SDF00 1.5 Myr	-0.76
	Y ² 1.5 Myr	-0.95

Table 13.4: **Variation of the power-law index due to the selection of stellar evolutionary models.**

13.5 Metallicity

Here we derive the systematic error of the IMF slope resulting from the uncertainty in the metallicity of the stars in NGC 3603. Following the technique described in the previous sections, we simplify the analysis by measuring the power-law index from two mass ranges at $1.7 - 2.6 M_{\odot}$ and $8 - 19 M_{\odot}$. We have so far adopted a solar metallicity $Z = 0.02$ for deriving the IMF. This assumption is justified because the Galactocentric distance of NGC 3603 is similar to that of the Sun, so that the radial gradient of the metallicity in the Milky Way does not need to be taken into account (see e.g. Rudolph et al., 2006). To derive the systematic error in the IMF from the uncertainty in the metallicity, we re-analyze the data using a half-solar, solar, and twice-solar metallicity. Since no isochrones with different metallicities are available in the PS99 set, we employ the 1.5 Myr SDF00 PMS models (see Sect. 13.4) with $z = 0.01, 0.02,$ and 0.04 for the low-mass stars ($1.7 - 2.6 M_{\odot}$). For the high-mass stars ($8 - 19 M_{\odot}$) we use 2.5 Myr LS01 MS isochrones with $z = 0.008, 0.02,$ and 0.04 . The resulting power-law indices are summarized in Tab. 13.5. The application of the solar and twice-solar metallicity yield almost the same value. A major difference is seen for the half-solar metallicity, which is steepening the IMF by $\Delta\Gamma \sim -0.13$. Note that, although we confirmed that there were clear correlations between the metallicity and the number counts in the both low- and high-mass bins, no trend eventually was seen in the slope index from the three values.

Metallicity	Γ
1/2 solar ($z=0.008$ for MS and 0.01 for PMS)	-0.88
1 solar ($z=0.02$ for MS and PMS)	-0.75
2 solar ($z=0.04$ for MS and PMS)	-0.76

Table 13.5: **Variation of the power-law index by metallicity.**

13.6 Individual extinction

In this section we analyze the systematic error in the IMF resulting from a potential individual extinction varying from star to star. We have so far applied a uniform foreground extinction of $A_V = 4.5$ mag in the conversion from the observed luminosities to stellar masses. However, potential local variations such as from circumstellar gas and

dust, and larger scale variations on the size scale of the cluster could affect the derived stellar masses to some degree. In fact we find a radial variation of the interstellar extinction of $\Delta A_V \sim 2.0$ mag from the cluster center towards the outer regions ($r \lesssim 1'$) (see Sect. 8.2.1). In order to derive the impact of this systematic uncertainty, we construct the IMF of NGC 3603 with and without the treatment of a variable extinction. To account for the individual extinction we shift the stars along the reddening direction (from Rieke & Lebofsky (1985)) in the JHK_S magnitudes space as close as possible to the isochrone, rather than picking the closest points on the isochrone for a fixed average extinction. Note that, we use a slightly modified isochrone for this analysis in which the PMS-MS of the mass-luminosity relation is smoothed to avoid potential multiple solutions for the stellar mass. This isochrone is shown in the CMD in Fig. 13.3.

The resulting IMFs are shown in Fig. 13.4. The treatment of the variable extinction flattens the IMF slope by $\Delta\Gamma \sim +0.15$. The slight difference between the IMF power-law index $\Gamma = -0.71$ for the case of a uniform extinction derived here, and the previously quoted value $\Gamma = -0.74$ (Fig. 11.1) is caused by smoothing the PMS-MS transition of the isochrone. The reason of the change of the IMF slope is the almost parallel alignment of the reddening direction and the PMS-MS transition region in the smoothly connected isochrone. Because of this alignment, sources in the scattered PMS-MS region are dereddened to the intermediate-mass MS (Fig. 13.3), which causes an artificial bump at around $5 M_\odot$ and results in a slightly flatter IMF slope within $0.4 - 20 M_\odot$ (upper panel in Fig. 13.4). As the change of the power-law slope is mostly arose from this local feature, the real impact of the presence of the individual extinction on the IMF slope is expected to be even smaller.

13.7 Incompleteness correction

For the best estimate of the IMF we have applied an incompleteness correction based on the observed magnitude-difference versus separation distribution (Sect. 7.1). Here we evaluate the potential influence of a non-perfect incompleteness correction on the IMF by considering two extreme cases: one is without the incompleteness correction, the other is an over-correction. The first case has already been analyzed in Fig. 11.1, the power-law index being $\Gamma = -0.68$. This means that without the incompleteness correction the IMF would come out shallower by $\Delta\Gamma \sim +0.06$. For the second case, we prepared a *larger correction* option in the computation of the incompleteness correction factor (see detailed explanation in Sect. 7.1). The correction factor is larger than that used for the best IMF. Using the same technique but this larger correction factor, we constructed the IMF.

The resulting power-law index of the IMF with the larger incompleteness correction is $\Gamma \sim -0.87$, steepening the IMF by $\Delta\Gamma \sim -0.13$ compared to the normal incompleteness correction. In summary we derive $\Delta\Gamma = {}^{+0.06}_{-0.13}$ in our incompleteness correction.

Here we note that a correction by simply a factor of 2 of the normal correction in each mass bin steepens the IMF power-law index by $\Delta\Gamma \sim -0.04$. This change is smaller than that derived in the test by the larger correction.

As mentioned in Sect. 11.3, we have notice that there is a slight difference between our incompleteness correction and that in the study by Stolte et al. (2006). Considering the potential error $\Delta\Gamma \sim -0.13$ in the present analysis, the difference between two studies, in which our resulting IMFs shows slightly flatter power-law slopes than theirs, would likely be explained by the difference in the correction rates.

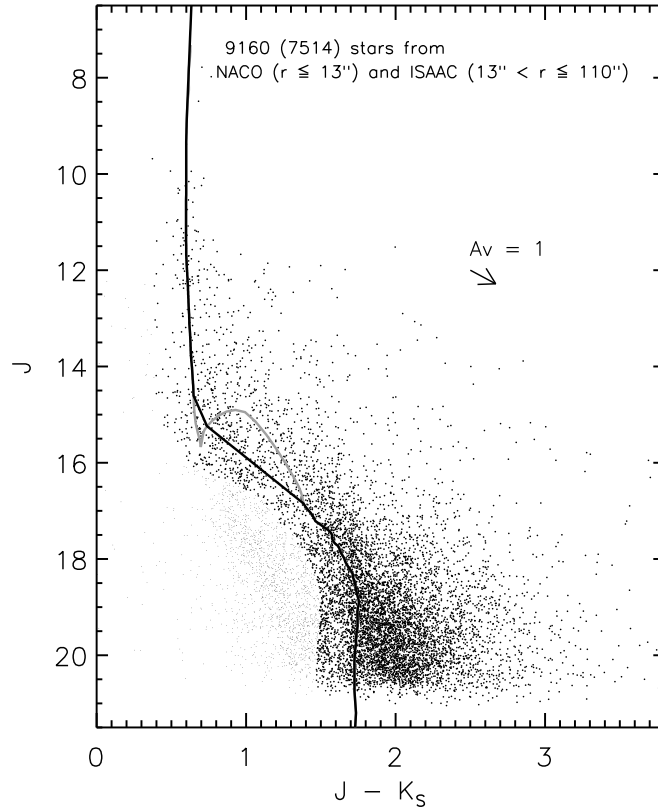


Figure 13.3: **Individual extinction correction using a smoothed PMS-MS transition isochrone.** The $(J - K_S, J)$ CMD of 9160 stars in the NACO and ISAAC data are shown with the smoothly connected isochrone (black solid line). The gray solid line is the not-smoothed isochrone used in the luminosity-mass conversion for the best estimate of the IMF. The non-cluster members based on the color-cut are differentiated by smaller filled circles.

13.8 Unresolved binary systems

Here we analyze the systematic error of the IMF power-law index caused by the potential presence of unresolved binary (multiple) systems.

Such unresolved binaries (or higher-order multiple systems) have been identified as an important uncertainty in the IMF determination (Kroupa, 2001, 2002; Malkov & Zinnecker, 2001). Any unresolved source composed of two or more stars mimics a slightly brighter single star in the photometry, resulting in an underestimate (overestimate) of the low-mass (high-mass) population. A mass function derived from a population with unresolved systems, the so-called *system mass function*, thus shows a slightly larger power-law index than the actual stellar mass function, and an appropriate treatment of the unresolved sources will steepen the derived IMF. Kroupa (2001) derives that the correction of the power-law index for the unresolved binaries can be substantial, up to $\Delta\Gamma \sim -0.5$ for stars with $\leq 1 M_{\odot}$.

In this section we first present our estimate of the binary fraction based on the analysis of the $(J - K_S, J)$ CMD. In a second step we then model the impact of the

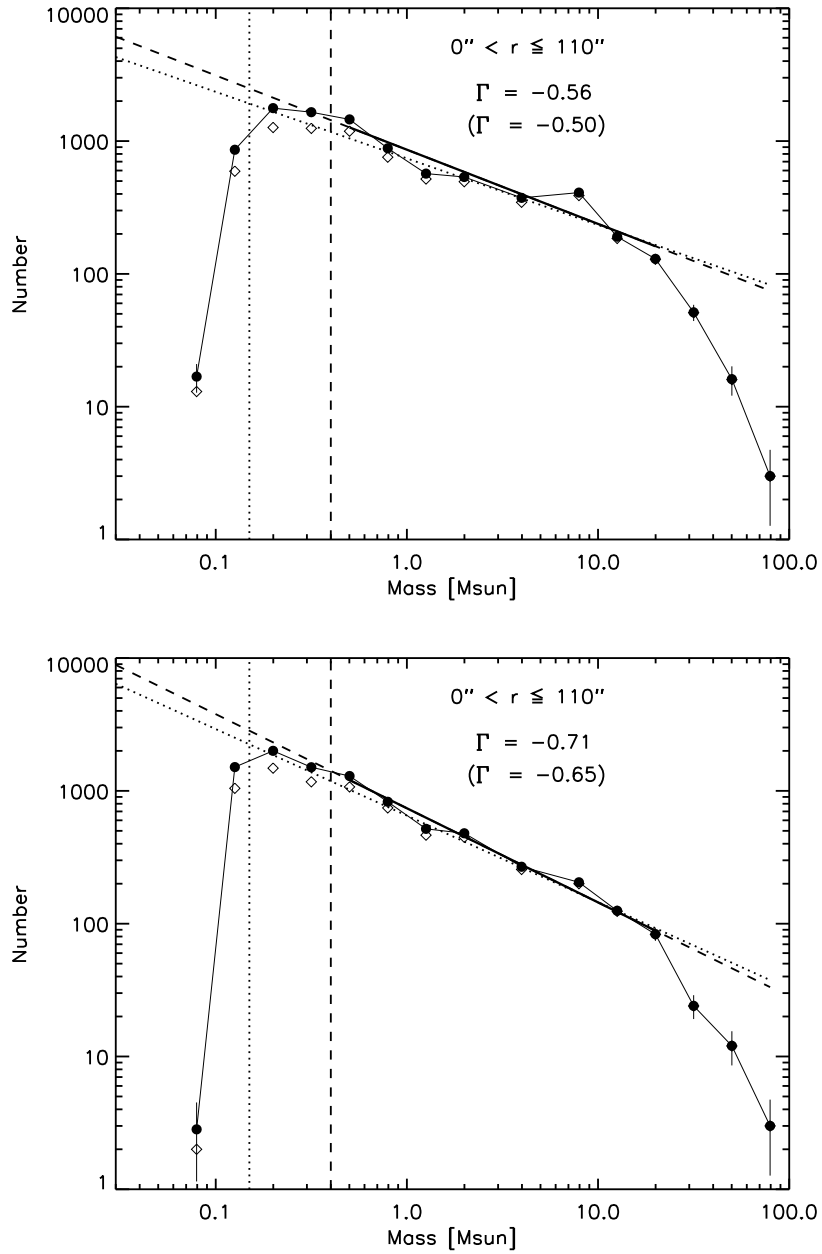


Figure 13.4: **Effect of the individual extinction on the IMF.** The figures show the IMF considering a varying individual extinction (top) and the IMF for an average foreground extinction (bottom).

unresolved binaries on the IMF by applying the well known binary distribution from the Orion Nebula Cluster (ONC).

13.8.1 Unresolved binary fraction from the observed CMD

Several studies have already reported the potential bias from unresolved binaries on the IMF of Galactic young star clusters. For example, Figer et al. (1999) derived a significantly flat IMF with $\Gamma \sim -0.65$ for the Arches cluster in the Galactic Center, for which a binary fraction of unity would steepen the IMF by $\Delta\Gamma \sim -0.3$.

Stolte et al. (2004, 2006) report the presence of a secondary sequence in NGC 3603, which shows up in their $(J - K_S, J)$ CMD towards the bright red side of the MS above the PMS-MS transition region. They interpret this secondary sequence as equal-mass binary stars, formed together with the other PMS stars in a single star formation epoch ~ 1 Myr ago. Stolte et al. (2004, 2006) find no IR excess emission for the stars of this secondary sequence in their L -band analysis, but rather find an anti-correlation between those sources and H- α emission stars. This suggests that secondary sequence is not caused by the contribution from circumstellar disks, but by unresolved binaries. From the total number of stars on the secondary sequence and the stars in the MS and PMS-MS transition region, Stolte et al. (2004, 2006) derive a fraction of unresolved binaries of 30 % in the central cluster. From the typical offset of the secondary sequence of $\Delta J = -0.75$ mag (= factor 2) they argue that most of the candidates are likely to be close to equal-mass binary systems. Using the unresolved binary fraction of 30 % and assuming equal-mass components, the authors apply a binary correction in the IMF determination, steepening the power-law by $\Delta\Gamma \sim -0.06$.

In contrast to Stolte et al. (2004, 2006) we have not found a distinct secondary sequence, but merely a scattered distribution towards the red of the MS and to the top of the PMS-MS transition region. Therefore we think it is not feasible to confidently distinguish potential unresolved binaries (which can have non-uniform mass-ratio) from reddened MS stars or younger PMS stars. Such an age spread in NGC 3603 has been suggested before also by several studies (Melnick et al., 1989; Eisenhauer et al., 1998; Brandl et al., 1999; Pandey et al., 2000). Our analysis favors an ongoing or several distinct epochs of star formation over the past 0.5 – 1 Myr for the PMS population, and $\lesssim 2.5$ Myr for the MS population (see discussions in Sect. 8.1.2).

While it is difficult to obtain a reliable estimate of the fraction of unresolved binaries in our data, we can give an rough estimate by counting sources located in the upper part of the PMS-MS transition in the $(J - K_S, J)$ CMD. The selection criterion for potential binaries is illustrated in the CMD for the innermost NACO field ($r \leq 13''$) in Fig. 13.5. The location of the binary band is defined by the following idea: in case of an equal-mass system, the real magnitude of the two stars is 0.75 mag larger (i.e., fainter) than the system magnitude. Giving a ± 0.3 mag as an example of the width of the binary band in the J magnitude, the limits of the binary band are set by shifting the isochrone by -1.05 and -0.45 mag.

From the total of 204 sources (including 18 non-cluster members based on the color-cut) in the NACO field with $r \leq 13''$ and with a J -band magnitude $m_J = 13 - 16$ mag, we find 27 stars within the binary band, corresponding to a binary fraction of ~ 13 % (Fig. 13.5 top). The same experiment for the outer ISAAC field $13'' < r \leq 110''$ yields a similar value of ~ 17 % as 96 binary candidates are found among 577 sources in the magnitude range (Fig. 13.5 bottom).

However, since the definition of the binary band is based on the assumption of equal-mass components and the typical uncertainty of ± 0.3 mag, the true number is subject to large uncertainties. For example, if we adopt a magnitude range of $\Delta m_J = 0.75 \pm 0.4$ mag to define the binary band, the resulting unresolved binary fraction increases to ~ 21 % for the NACO field and ~ 22 % for the ISAAC field.

In our J -band NACO photometry, which constrains the three-bands source detection, the minimum angular separation for which we can resolve equal brightness binaries is about 80 mas, corresponding to a projected separation of ~ 490 AU at the distance of 6 kpc. Therefore we can assume that the NACO data has resolved all equal-mass binaries with a projected separation of more than 490 AU. Because of the poorer angular resolution of the ISAAC data, the according projected separation for which binaries can be resolved is ~ 2200 AU (370 mas).

Here we note that the potential unresolved binaries in our data also include multiple sources from projection effects, i.e., optical binaries. We can estimate the fraction of optical binaries from the source density in our field. Calculating the ratio of the area for which the detection of multiple source is prevented by stars ($= [\text{number of stars}] \times \pi \times [\text{angular resolution}]^2$) and the total area of the field. We derive a likelihood for optical binaries of about 6 and 9 % for the NACO and ISAAC data, respectively.

13.8.2 Systematic error of the IMF from unresolved binaries

As outlined above, we can not reliably identify and measure the mass-ratio of unresolved sources from our data, but can only give a rough estimate for the equal-mass binary candidates in the PMS-MS transition region.

In order to quantify the systematic error of the IMF from such unresolved binaries, we choose to simulate the effect adopting the measured binary distribution in more nearby resolved stellar population. The binary fraction is a function of various parameters such as the stellar mass (spectral type), mass ratio ($q = m_2/m_1$), separation (orbital period) between the components, and environments (e.g., fields or star-forming regions). Here we first summarize the various measurements of the binary distribution as of today.

Binary fraction of high- and low-mass stars in the ONC

The binary fraction of the Orion Nebula Cluster including the Trapezium cluster is among the best studied and, because of the similarities in terms of age and high-mass stellar content with NGC 3603, it is the best suited for our purpose to study the impact on the IMF. We note that although some binary/multiple surveys mentioned below differentiate between binary and higher-order systems, we do not follow this distinction but simply use the term *binary fraction*.

Prosser et al. (1994), for example, derived a binary fraction of ~ 12 % for a projected linear separation of 26 – 440 AU in the Trapezium cluster, and Petr et al. (1998) derived a binary fraction of $\sim 9.5 \pm 4.5$ % for 63 – 225 AU for stars with masses down to $\sim 0.04 M_\odot$ (~ 6 % for low-mass stars less massive than $1.5 M_\odot$). Other studies have reported similar binary fractions such as 14 % for projected separation of 138 – 828 AU (Padgett et al., 1997) and 2 % for 132 – 264 AU (Simon et al., 1999). Combining their new observations with the results from Petr et al. (1998), Köhler et al. (2006) derive a binary fraction of $\sim 14 \pm 7$ % and $\sim 23 \pm 10$ % for stars with $M > 2 M_\odot$ in the periphery and central core, respectively, and $\sim 4.8 \pm 1.8$ % and $\sim 3.6 \pm 3.2$ % for stars with $M = 0.1 - 2 M_\odot$ for a projected separation of 60 – 500 AU. The higher binary fraction

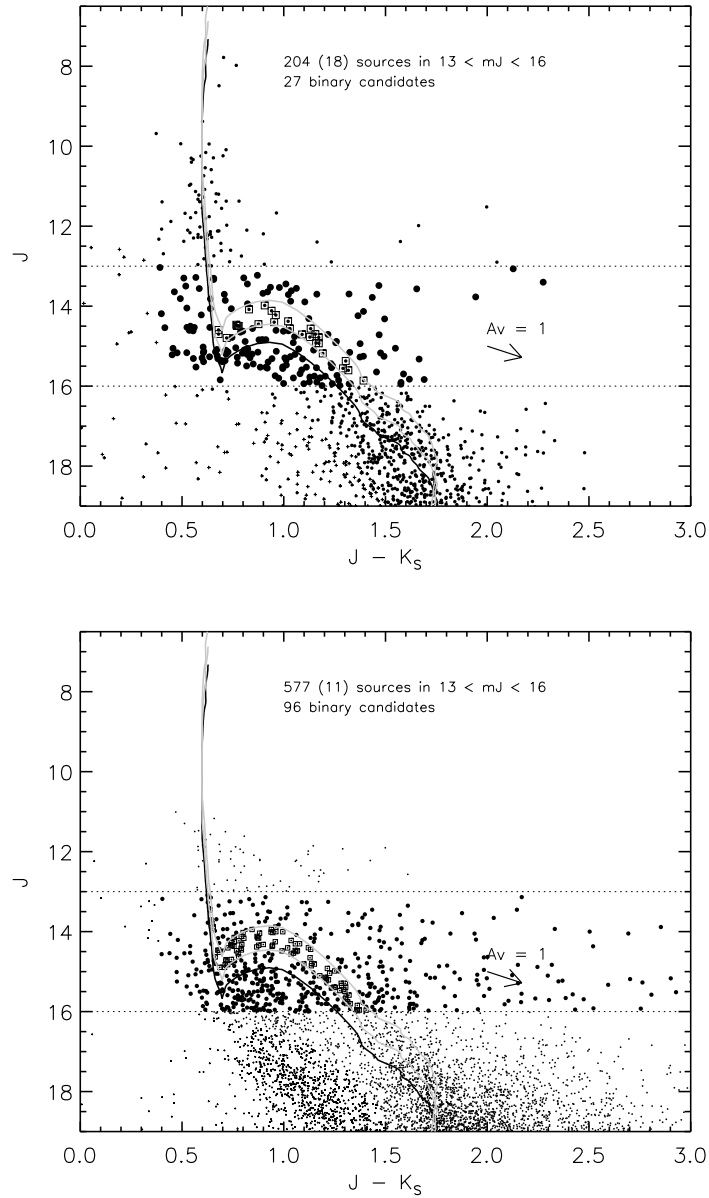


Figure 13.5: **Unresolved binary candidates in the CMD.** The figure show the $(J - K_S, J)$ CMD for stars from the inner field ($r \leq 13''$) in the NACO data (top) and for stars from the outer field of $13'' < r \leq 110''$ in the ISAAC data (bottom). The analysis is restricted to J -band magnitude range $m_J = 13 - 16$ mag (indicated by horizontal dotted lines). Sources located in the area of the binary band (gray solid curves) and within the above mentioned magnitude range are regarded to be unresolved binary candidates. Non-cluster members based on the color-cut are shown in plus symbols. In total 186 cluster members (large dots) plus 18 non-cluster members are identified in the magnitude range. 27 sources are located within the binary band (dot plus square), corresponding to a binary fraction of $\sim 13\%$. In the CMD for the outer ISAAC field, 566 cluster members plus 11 non-cluster members are detected, and 96 sources of them are found to be binary candidates. The resulting binary fraction is $\sim 17\%$.

for high-mass stars in the ONC is consistent with earlier results from Preibisch et al. (1999).

Binary fraction of other young stellar clusters

Binary surveys of other young stellar clusters have also been reported. For example the binary fraction of the young stellar cluster IC 348 is reported to be 19 ± 5 % for a physical separation of 40 – 3200 AU (Duchêne et al., 1999). The binary fraction of the young embedded star-forming region NGC 2024 is $\sim 7 \pm 3$ % for a projected separation range of 145 – 950 AU (Beck et al., 2003), and $\sim 3 \pm 2$ % for a projected separation of 184 – 460 AU (Liu et al., 2003).

Binary fraction of field stars

The binary fraction surveys of young star-forming clusters are largely in agreement with that of field low- and intermediate-mass MS population. Duquennoy & Mayor (1991) report a binary fraction of about 50–60 % for G-type stars, and Fischer & Marcy (1992); Reid & Gizis (1997) report a binary fraction of about 30 – 40 % for M-type stars. Lada (2006) compiles several studies of the binary fraction of late type stars, and shows that there is a trend with the spectral type ranging from ~ 60 % for G-type stars down to ~ 30 % for M-type stars and even lower for the L- and T-dwarfs.

Taking into account the conversion from the absolute distance to the projected separation, Köhler et al. (2006) find the binary fraction in the ONC in agreement with the field MS binary fraction except for low-mass stars, where the binary fraction in the ONC is slightly lower (~ 4 %) than in the field (~ 9 %) in Duquennoy & Mayor (1991).

Because of the similar age and high-mass stellar content of the ONC and NGC 3603, and taking advantage of the fact that the binary fraction of the ONC has been measured for a projected separation of about 60 – 500 AU which almost perfectly matches the separation which can not be resolved in our NACO data ($\lesssim 490$ AU), we adopt the binary fraction of the ONC from Köhler et al. (2006) in the following analysis. In order to simplify our analysis, we do not take into account the various dependencies of the binary fraction presented by Köhler et al. (2006), but adopt typical values of ~ 5 % for low-mass stars ($0.1 - 2 M_{\odot}$) and ~ 15 % for intermediate- to high-mass stars ($> 2 M_{\odot}$). To also cover the various other estimates of the binary fraction in young stellar clusters, and to estimate the *upper limit* of the potential impact of unresolved binaries on the IMF determination, we also analyze the case for a two times larger binary fraction, i.e., ~ 10 % for $0.1 - 2 M_{\odot}$ and ~ 30 % for $> 2 M_{\odot}$.

Binary fraction as a function of separation

As mentioned above, the angular resolution of our NACO and ISAAC data correspond to minimum detectable binary separations of ~ 490 AU and ~ 2200 AU, respectively, and hence we expect that the fraction of unresolved sources in the ISAAC data would be somewhat larger than that of the NACO data. In their binary analysis of nearby solar-type stars, Duquennoy & Mayor (1991) show that the orbital period follows a lognormal distribution. Using this distribution, Köhler (2001) derives the distribution for the projected separation, which follows the form

$$f(x) \propto \exp\left[-\frac{1}{2}(x - \bar{x})^2/\sigma^2\right] \quad (13.2)$$

where x is the logarithm of the projected separation in AU with $\bar{x} = 1.44$ and $\sigma = 1.55$ (see Fig. 6 in the reference). Integrating this distribution up to the minimum separations resolvable in our NACO (~ 490 AU) and ISAAC (~ 2200 AU) data, we can estimate that about 79 % of all binaries are unresolved in the NACO data, and about 89 % are unresolved in the ISAAC data. As difference between the two cases is rather small compared to the uncertainty in the binary fractions in the ONC and other young stellar clusters, we ignore the difference in angular resolution in the NACO and ISAAC data in the following experiment.

Binary fraction as a function of mass ratio

Many binary survey have aimed at deriving the mass ratio distribution for various types of stellar populations such as field stars, star-forming clusters, and associations. The mass ratio distribution, in fact, has shown various forms in these studies. For example, the binary survey among nearby M-dwarfs by Reid & Gizis (1997) shows evidence for preferential formation of nearly equal-mass binary systems, i.e., a peak at $q \sim 1$. In contrast, there are ample studies that show mass ratio distributions favoring non-equal-mass binary systems. For example, Duquennoy & Mayor (1991) derive a mass ratio distribution which peaks near $q = 0.2 - 0.3$ for solar-type field stars, Fischer & Marcy (1992) derive a peak at $0.4 - 0.6$ and $0.6 - 0.8$, respectively, for the field G- and M-dwarf binaries. Duchêne et al. (1999) find a distribution peaking at $q = 0.5 - 0.75$ for binaries with a primary mass of $\leq 1 M_{\odot}$ in the young star cluster IC 348. For other clusters the mass ratio distribution can be fitted by an inverse power-law $f(q) \propto q^{-\Gamma}$. The power-law index is found to be $\Gamma = 0.33 - 0.5$ for binaries with B- and A-type stars in the nearby OB association Sco OB2 (Shatsky & Tokovinin, 2002; Kouwenhoven et al., 2005). The binary survey of the Hyades cluster by Patience et al. (1998) yielded a distribution with $\Gamma = 1.3$.

Thus it is not straightforward to assume a unique mass ratio distribution, and we study only two cases, one which favors equal-mass binaries, and a second case for which most binaries are of non-equal-mass. Moreover, we allow only two values of the mass ratio instead of a continuous distribution. In the first model, which favors equal-mass binaries, 75 % of the unresolved binary systems have a mass ratio of $q = 1$ and 25 % have $q = 0.4$ and. In the second model, which favors non-equal-mass binaries, 25 % of the population have $q = 1$ and 75 % have $q = 0.4$.

Simulation of the unresolved binary correction

By using the ONC binary fractions of 5 % and 15 % for $M \leq 2 M_{\odot}$ and $M > 2 M_{\odot}$ respectively, as well as binary fractions of 10 % and 30 % as an upper limit, and the two cases of the mass ratio distribution favoring either equal-mass or non-equal-mass systems, we study the potential influence of the unresolved binaries on our IMF determination.

Since the IMF slope is varying with the radial distance from the cluster center, we perform the simulation separately for the IMF of innermost NACO field ($r \leq 13''$) and the outer ISAAC field ($13'' < r \leq 110''$), and then combine the corrected mass distributions. The IMF of the inner NACO field (938 stars) has a power-law index $\Gamma = -0.50$, and that of the outer ISAAC field (6576 stars) has a $\Gamma = -0.77$ (after applying the color-cut selection and the incompleteness correction).

In detail we perform the simulation as follows: first we generate a set of binaries for each mass bin according to the number counts and the assumed binary fraction

($M \leq 2 M_{\odot}$ and $M > 2 M_{\odot}$). We then split those systems according to the mass ratio distribution (two cases), subtract the system from the original mass bin, and add the split masses to the corresponding mass bins. Finally we combine the two resolved NACO and ISAAC mass distributions into a single IMF, and compute the power-law index within the mass range of $0.4 - 20 M_{\odot}$. The results of these simulations are summarized in Tab. 13.6.

The power-law index of the IMF becomes slightly steeper by $\Delta\Gamma \sim -0.02$. Even assuming twice the binary fraction of the ONC, the IMF steepens by only $\Delta\Gamma \sim -0.04$. The two cases of the different mass ratios (favoring equal-mass and non-equal-mass binaries, respectively) yield almost identical power-law indices.

In summary, we conclude that the systematic error in the IMF power-law index from the presence of unresolved binaries is $\Delta\Gamma \lesssim -0.04$.

Binary fraction (no correction)	Mass ratio ^[a]	Γ_{NACO}	Γ_{ISAAC}	Γ_{all}
ONC – 5 % ($\leq 2 M_{\odot}$) ^[b] 15 % ($> 2 M_{\odot}$)	equal-mass	-0.52	-0.79	-0.73
	non-equal-mass	-0.52	-0.77	-0.73
ONC×2 – 10 % ($\leq 2 M_{\odot}$) 30 % ($> 2 M_{\odot}$)	equal-mass	-0.54	-0.82	-0.75
	non-equal-mass	-0.53	-0.81	-0.74

Table 13.6: **Variation of the power-law index by unresolved binary correction.**

^[a] In the *equal-mass* case, 75 % of the binaries have $q = 1$ and 25 % of them have $q = 0.4$. In the *non-equal-mass* case, 25 % of them have $q = 1$ and 75 % have $q = 0.4$.

^[b] Binary fractions in the Orion Nebula Cluster in Köhler et al. (2006).

13.9 The stellar mass outside the observed field of view

In this section we estimate how many intermediate- and low-mass cluster stars reside outside the observed field of view, and how much these unseen stars can steepen the IMF.

In case of mass segregation, observations which do not cover the full cluster may underestimate the contribution of the stars outside the field. In earlier sections we have outlined that the high-mass stars in NGC 3603 appear to be strongly concentrated towards the cluster center. In contrast, the intermediate- and low-mass stars in the cluster appear neither dynamically nor primordially mass-segregated at this stage, and extend beyond the observed field of $r \leq 110''$. Therefore we need to quantify how much these intermediate- and low-mass stars outside the field of view can change the IMF.

To estimate the fraction of intermediate- and low-mass stars potentially missed in our observations, we use the de-projected mass density distribution from Sect. 12.2. Integrating the volume mass density of the stars within the mass range of $0.5 - 2.5 M_{\odot}$ up to the observation limit $r = 110''$, we find that our observations cover more than 90

% of these stars if the cluster radius is $r = 150''$, and still $\sim 67\%$ when using the upper limit tidal radius of $r_t = 1260''$. Qualitatively we conclude that our data indeed covers the majority of the cluster mass, and that the observed IMF is thus representative for the whole cluster.

To quantify how much the intermediate- and low-mass stars outside our field of view can change the IMF power-law index, we simply add the maximum missing mass 33 % to the number counts of the low-mass bin ($1.7 - 2.6 M_\odot$) in the simplified two mass bins IMF. As a result, the power-law index decreases from $\Gamma = -0.82$ to -0.98 , that is, a steepening of the IMF with $\Delta\Gamma \sim -0.16$.

13.10 Error combination

After analyzing the individual systematic errors in Sect. 13.1 to Sect. 13.9, we finally combine them into a single systematic error for the power-law index in our IMF determination. The various systematic errors are summarized in Tab. 13.7.

To combine those asymmetric errors, we apply the method by Barlow (2003) as implemented in the program from <http://www.slac.stanford.edu/~barlow/java/statistics1.html>. The program constructs, for each set of positive and negative errors, an asymmetric distribution consisting of two half-Gaussian distributions, and then convolves these distributions to derive a combined asymmetric error. We note that in this combination we also add the fitting error ± 0.02 in the power-law index calculation. The resulting combined error is $\Delta\Gamma = {}^{+0.62}_{-0.47}$. For comparison, the simple quadratic sum of the positive and negative errors yields fairly similar values of $+0.63$ and -0.50 , respectively.

In summary, we conclude that the IMF power-law index of NGC 3603 in the field $r \leq 110''$ for the mass range $0.4 - 20 M_\odot$ including all systematic errors is $\Gamma = -0.74^{+0.62}_{-0.47}$. Considering a Gaussian probability distribution with the above 1σ errors, we calculate the probability that the IMF of NGC 3603 is as steep as the Salpeter IMF, resulting in $Pr(\Gamma \leq -1.35) \sim 0.1$, i.e., about 10 %. This leads us to interpret that the IMF of NGC 3603 is distinguishably flatter than the standard field star IMF.

Parameters	Errors
Age	+0.60, -0.41
Distance	± 0.01
Foreground extinction	+0.02, -0.01
Evolutionary model	+0.07, -0.13
Metallicity	-0.13
Individual extinction	+0.15
Incompleteness correction	+0.06, -0.13
Unresolved binary	-0.04
Stellar mass outside the FOV	-0.16
Combined	+0.62, -0.47

Table 13.7: Summary of the error estimates and the combination.

Chapter 14

Discussion

In this chapter we discuss the IMF of NGC 3603, in particular, focusing on the question: is the IMF of NGC 3603 an example for top-heavy IMF in starbursts?

The IMF of NGC 3603 within a radius $r \leq 110''$ is well described by a single power-law with index $\Gamma = -0.74$ in the mass range of $0.4 - 20 M_{\odot}$ with a systematic uncertainty of $\Delta\Gamma = {}^{+0.62}_{-0.47}$. This IMF is slightly flatter but still consistent with previous studies, for example, $\Gamma \sim -0.73$ for the mass range of $1 - 30 M_{\odot}$ within a radius $r \lesssim 13''$ in Eisenhauer et al. (1998), $\Gamma = -0.9 \pm 0.1$ for $1 - 100 M_{\odot}$ within $r \lesssim 20''$ in Sung & Bessell (2004), and $\Gamma = -0.91 \pm 0.15$ for $0.4 - 20 M_{\odot}$ within $7'' < r \leq 65''$ in Stolte et al. (2006) (see details in Sect. 11.3). In summary, these results suggest that the IMF of NGC 3603 is somewhat flatter than the Salpeter-like field IMF with a power-law index $\Gamma \sim -1.35$.

IMF in various stellar populations

There is growing evidence that the IMF varies between different stellar populations (e.g., Scalo, 2005), and in particular for a top-heavy IMF in the nearby starburst clusters. Here we summarize some recent IMF studies of young stellar populations.

Several stellar clusters have been suggested to have a somewhat flat IMF. For example, the Arches cluster near the Galactic Center shows a comparatively shallow IMF with $\Gamma = -0.6$ to -1.1 for the high-mass regime (Figer et al., 1999; Stolte et al., 2005; Kim et al., 2006). The Quintuplet cluster - another massive young cluster near the Galactic Center - has also been suggested to have a mass distribution potentially flatter than the standard field IMF (Figer et al., 1999).

Other stellar clusters show standard Salpeter-like mass functions, but there are substantial differences between various studies. For example, the power-law index of the IMF of the massive star cluster R136 located at the center of 30 Doradus has been reported to be $\Gamma \sim -1.0$ to -1.6 (Hunter et al., 1996; Brandl et al., 1996; Massey & Hunter, 1998), and even substantially flatter for solar-mass stars (Sirianni et al., 2000). There are also many other open clusters with a Salpeter-like IMF, for example, the double cluster h and χ Persi with the power-law indices of $\Gamma \sim -1.3$ (Slesnick et al., 2002), NGC 1960 (M36) and NGC 2194 with $\Gamma \sim -1.2$ to -1.3 (Sanner et al., 2000). Recently, the IMF of the Galactic massive cluster Westerlund 2 was measured to have a power-law index of $\Gamma \sim -1.2$ (Ascenso et al., 2007).

Yet other clusters have IMFs which are slightly steeper than the Salpeter IMF, for example, NGC 2422 with $\Gamma \sim -2.0$ ($0.9 - 2.5 M_{\odot}$) (Prisinzano et al., 2003), NGC 3576 with $\Gamma = -1.62$ ($> 3 M_{\odot}$) (Figueroa et al., 2002), the Sco OB2 association with

$\Gamma = -1.9$ (Brown, 1998).

The IMF in more nearby star-forming regions has been measured down to the brown dwarf mass regime. It seems that the variations in the IMF power-law index and in the characteristic mass become even larger towards very low stellar masses.

The IMF of the Trapezium cluster in the Orion nebula shows a broken power-law with a secondary peak around several tens of Jupiter masses. Muench et al. (2002) derive the IMF of the Trapezium cluster covering stars from massive OB stars down to stars near the Deuterium burning limit using their K -band luminosity function. The resulting IMF is Salpeter-like down to $\sim 0.6 M_{\odot}$, followed by a broad peak around $\sim 0.1 M_{\odot}$. It then declines towards the substellar regime, and increases rapidly towards the secondary peak in the very low-mass domain.

Bouvier et al. (1998) derive the IMF of the low-mass stars and brown dwarfs in the Pleiades cluster, which is well fit by the log-normal IMF of Miller & Scalo (1979), but with a slight excess from the log-normal distribution in the substellar regime. The low-mass IMF in the Taurus star-forming region is similar to the Trapezium, with the exception of a significant deficit of brown dwarfs, and Briceño et al. (2002) argue that this can be explained by its lower density, leading to a larger minimum Jeans mass when compared to the Trapezium cluster. Such a brown dwarf deficit has also been observed in the embedded cluster IC 348. Using deep NIR observations, Preibisch et al. (2003) find that the stellar IMF of IC 348 follows the field star IMF, but that the brown dwarfs are deficient by a factor of 2-3 compared to the Trapezium cluster. In a similar study, Luhman et al. (2003) conclude that the IMF of IC 348 also has a different characteristic mass than the Taurus IMF. Wilking et al. (2004) measure the stellar mass distribution of the NGC 1333 molecular cloud. They find that the mass distribution is consistent with the field IMF in the stellar regime ($> 0.1 M_{\odot}$), but that the very low- and substellar-domain within $0.04 - 1 M_{\odot}$ is dominated by low-mass stars rather than brown dwarfs.

In summary, there are moderate variations in the IMF of intermediate- to high-mass stars among young stellar clusters, and substantial variations at very low- and substellar masses.

Universal or variable IMF?

The question which arises here is - is the observed IMF variation a true deviation from the Salpeter IMF? Or can the variation be explained by systematic uncertainties in the measurements?

Kroupa (2001), for example, argues that the so-far observed IMF variations are caused by the combined effects of observational, theoretical and statistical uncertainties. Prior to Kroupa (2001), Scalo (1998) summarized the state of the IMF research compiling the IMFs of many clusters and associations in the Milky Way and the LMC. Although no systematic trend is seen, there is a substantial scatter of at least unity (± 0.5) in the (Γ vs stellar mass) plot, indicative of IMF variations (Fig. 5 in the reference). The large uncertainties prevent the author from giving any conclusive statement about a varying IMF. As an average IMF, Scalo (1998) proposes a three-segment power-law IMF with the index $\Gamma = -0.2 \pm 0.3$ for the mass range of $0.1 - 1 M_{\odot}$, $\Gamma = -1.7 \pm 0.5$ for $1 - 10 M_{\odot}$, and $\Gamma = -1.3 \pm 0.5$ for $10 - 100 M_{\odot}$. Here the IMF is steepest in the intermediate-mass range.

In his subsequent work, Kroupa (2001) defines the Galactic field IMF adding the results from local star-counts to the compilation of the MF power-law indices in Scalo

(1998). The author presents his analysis in the form of a so-called alpha plot, plotting the power-law index $\alpha = 1 - \Gamma$ against the average stellar mass of the IMF (Fig. 1 in the reference). Assuming the defined average IMF, the author investigates the uncertainty inherent in any observational estimate of the IMF through N -body model calculations. The author concludes that no true variations can be detected within the *fundamental limit* of uncertainties of a universal IMF, and that this universal IMF can be described by segmented power-law with index of $\Gamma = 0.7 \pm 0.7$ for $0.01 - 0.08 M_{\odot}$, $\Gamma = -0.8 \pm 0.5$ for $0.08 - 0.5 M_{\odot}$, $\Gamma = -1.7 \pm 0.3$ for $0.5 - 1 M_{\odot}$, and $\Gamma = -1.3 \pm 0.7$ for $> 1 M_{\odot}$.

In his latest review Scalo (2005) again summarizes the current IMF estimates from field star counts and from observations of open clusters in the Milky Way. He finds that the variation of the IMF power-law index among the various field star studies within a mass range of $1 - 15 M_{\odot}$ is not negligible, and that the variation among the cluster IMFs is considerable. These variations might be accommodated by the combined effects of various study-specific uncertainties. In fact, many such uncertainties could arise from the observational and technical differences (e.g., data acquisition, data reduction, field correction, completeness correction, unresolved binaries) among the various studies. Therefore it is conceivable to find some variations in the IMF measurements. However, there are also IMF variations when observing, analyzing, and interpreting the data of several clusters in the same manner - for example, Phelps & Janes (1993) derive the IMFs of eight young open clusters in a consistent way. Although the average value of the power-law index $\Gamma = -1.4 \pm 0.13$ is in agreement with the Salpeter IMF, two of the clusters show considerable stronger deviations with $\Gamma \sim -1.8$ (NGC 581) and $\Gamma \sim -1.1$ (NGC 663). Scalo (2005) mentions that these observed variations in cluster IMFs might still be explained by the uncertainties and, if it is the case, then the cluster data are consistent with a universal IMF but with *sizeable* variations, preventing us from determining an average IMF or Γ .

We measure the IMF of NGC 3603 to have a power-law index of $\Gamma = -0.74_{-0.47}^{+0.62}$. How does this result fit with the fundamental limit in Kroupa (2001)? The author explains the observed scatter is mainly by the following three uncertainties: 1) Poisson noise due to the finite number of stars, 2) the dynamical evolution of the star cluster, i.e, the preferential diffusion of low-mass stars outwards and the concentration of high-mass stars in the center, and 3) unresolved binaries.

In our determination of the IMF of NGC 3603, the Poisson noise is taken into account when fitting the power-law. The resulting uncertainty is only $\Delta\Gamma \sim \pm 0.02$. This comparably small error is not surprising given that we have detected approx. 10000 stars in our observations.

As for the unresolved binaries, Kroupa (2001) derives that the correction for unresolved binaries will typically steepen the IMF power-law index by $0.5 \lesssim \Delta\Gamma \lesssim 0.8$ for stars with masses within $0.08 - 1 M_{\odot}$ but it does not change significantly for stars with $\gtrsim 1 M_{\odot}$. Our simulation of the potential impact of unresolved binaries on the IMF for the $0.4 - 20 M_{\odot}$ mass range yields $\Delta\Gamma \sim -0.04$ (see Sect. 13.8). Since the mass range is different in our analysis and the simulation of Kroupa (2001), it should not directly be compared. However, it is worth mentioning that there is a difference in the adopted binary frequencies. Based on the studies of the ONC, we assume a binary frequency of 15 and 30 % (as an upper limit) for $0.1 - 2 M_{\odot}$ and $\gtrsim 2 M_{\odot}$, respectively, while Kroupa (2001) adopts a binary fraction of 100 % for $\gtrsim 3 M_{\odot}$ i.e., each massive star has a companion. By comparison, the correction of unresolved binaries in Stolte et al. (2006) steepens, by $\Delta\Gamma \sim -0.06$, the IMF for stars within $0.4 - 20 M_{\odot}$ in the field

$7'' < r < 33''$.

As discussed in Sect. 12, we estimate that the dynamical evolution in NGC 3603 is expected to be insignificant for the intermediate- and low-mass stars, and thus do not affect significantly the determination of the IMF from the field covering up to $r \leq 110''$. This is supported by the fact that the IMF does not steepen significantly beyond $r \gtrsim 30''$.

We conclude that, irrespective of the three main uncertainties hold liable for the observed IMF variation by Kroupa (2001), the IMF of NGC 3603 is flatter than the Salpeter IMF, but still within the fundamental limit in Kroupa (2001). Therefore, as long as the intrinsic uncertainty by Kroupa (2001) accommodates an IMF with a power-law index of $\Gamma = -0.74$, we are not yet able to give a conclusive answer to the question whether or not the flat IMF of NGC 3603 is a true deviation from the standard Salpeter-type IMF.

Is the IMF top-heavy in young and massive starburst clusters?

The above IMF studies suggest that the IMF is almost universal in many different star-forming environments, but still with non-negligible variations in the power-law index. Although there is no clear systematic trends in these variations, there is some evidence that these variations are related to the stellar *density*. Compared to the field IMF, the IMF for intermediate- and high-mass stars tends to be slightly steeper in sparsely populated star-forming regions, while it is sometimes slightly flatter in very dense star clusters.

Among the best-studied young and massive star-forming clusters, we find NGC 3603, the Arches cluster, and the Galactic Center cluster with a slightly flatter, top-heavy IMF. The Arches cluster - one of the most massive star-forming clusters near the Galactic Center - shows a considerably shallow IMF. Figer et al. (1999) derive an IMF power-law index of $\Gamma \sim -0.65$ for stellar masses down to $10 M_{\odot}$. Stolte et al. (2005) find the PDMF to have a power-law index of $\Gamma = -0.86$ for a mass range of $6 - 60 M_{\odot}$. Kim et al. (2006) recently derive the PDMF with a power-law index of $\Gamma \sim -0.91$ for $1.3 - 50 M_{\odot}$. Using numerical simulations, these authors also correct for the dynamical evolution of the cluster, and trace back the IMF to have a power-law index $\Gamma \sim -1.0$ to -1.1 . Interestingly, their PDMF has a flatter slope ($\Gamma = -0.71$) if only high-mass stars are considered ($5 - 50 M_{\odot}$).

Also the young stellar population in the Galactic Center exhibits a top-heavy IMF. From the observed *K*-band LF of the high-mass stars orbiting the central massive black hole in two counter-rotating disks, Paumard et al. (2006) conclude that the IMF is likely substantially flatter (by 1–1.5 dex) than the Salpeter IMF. However, these stars probably have formed in very dense gas disks rather than in a self-contracting cloud, and thus a direct comparison with NGC 3603 and other clusters is problematic.

In contrast, the IMF of R136 in 30 Doradus is only marginally different from a Salpeter-like IMF, even though there is a considerable variation among different studies. For example, Brandl et al. (1996) derive IMFs with power-law indices of $\Gamma = -1.3$ at $r \leq 0.4$ pc, and $\Gamma = -2.2$ at $r > 0.8$ pc, and find an average IMF with $\Gamma = -1.6$ for the high-mass stellar population. Hunter et al. (1996) derive the IMFs for five concentric annuli for which the power-law index ranges from $\Gamma \sim -0.8$ at $0.11 - 0.34$ pc ($5 - 15 M_{\odot}$) to $\Gamma \sim -1.0$ at $1.14 - 4.47$ pc ($2.8 - 15 M_{\odot}$). Massey & Hunter (1998) measure the IMF with $\Gamma = -1.3$ to -1.4 for $2.8 - 120 M_{\odot}$. These authors also update the IMFs of three concentric annuli in Hunter et al. (1996), and give $\Gamma \sim -1.0$ at $0.11 - 0.34$ pc, $\Gamma \sim -0.7$ at $0.34 - 0.46$ pc, and $\Gamma \sim -1.1$ at $0.46 - 0.69$ pc. In contrast, based on HST optical

data, Sirianni et al. (2000) derive a broken power-law IMF with the index of $\Gamma = -1.28$ for $2.1 - 6.5 M_{\odot}$ and $\Gamma = -0.27$ for $1.35 - 2.1 M_{\odot}$, indicating a substantially flat IMF for the whole stellar mass range. Although there is ample evidence for a flattening IMF at subsolar masses (Scalo, 1998; Kroupa, 2001), the observed flattening at such high-masses of $\sim 2 M_{\odot}$ in this study is somewhat peculiar.

A common characteristic of NGC 3603, the Arches cluster, and the Galactic Center cluster is the high central mass density. As shown in Sect. 12.2, the core mass density of NGC 3603 is at least $\sim 6 \times 10^4 M_{\odot} \text{ pc}^{-3}$. Note that this value is derived from the volume mass density profile, and the central density directly measured from the surface density (as sometimes given in literature for other clusters) is a factor of ~ 2 larger, i.e., $\sim 1.2 \times 10^5 M_{\odot} \text{ pc}^{-3}$. The Arches cluster has a total mass of $\sim 1 \times 10^4 M_{\odot}$ similar to that of NGC 3603, and its core mass density is about $3 \times 10^5 M_{\odot} \text{ pc}^{-3}$, several times larger than NGC 3603 (Figer et al., 1999; Stolte, 2003). The stellar density in the core of the GC cluster is expected to be much higher due to the presence of the central massive black hole. For example the stellar density in the central arcsecond of the GC is estimated to be $> 3 \times 10^7 M_{\odot} \text{ pc}^{-3}$ (Genzel et al., 2003).

Here we note that, in fact, the R136 cluster also has a central mass density which is comparable to NGC 3603 and the Arches cluster. The total mass of the R136 cluster is estimated to be $2-3 \times 10^4 M_{\odot}$ (Hunter et al., 1995; Brandl et al., 1996; Mackey & Gilmore, 2003), slightly larger but still comparable to that of NGC 3603. Hosting more than 50 O3-type, WN6, and O/WN6 transition stars (Massey & Hunter, 1998), the central mass density is estimated to be $\sim 5.5 \times 10^4 M_{\odot} \text{ pc}^{-3}$ from stars $\geq 2.8 M_{\odot}$ within $r \leq 0.11 \text{ pc}$, and could be about three times larger with considering stars down to $0.1 M_{\odot}$ (Hunter et al., 1995). Mackey & Gilmore (2003) estimate the central mass density within $r_c \leq 0.32 \text{ pc}$ to be about $3 \times 10^4 M_{\odot} \text{ pc}^{-3}$. Therefore more study would be required to address the reason why, despite the high central density, the R136 cluster has shown the Salpeter-like IMF but with a substantial variation.

On the other hand, the central mass densities in the other Galactic or Local group young stellar clusters are about an order of magnitude smaller than those in NGC 3603 and the Arches cluster. The ONC, for example, has a core radius of $\sim 0.2 \text{ pc}$, which is similar to NGC 3603, but has an order of magnitude smaller total mass of $\sim 10^3 M_{\odot}$. The ONC has thus also an order of magnitude smaller central mass density of $2 \times 10^4 M_{\odot} \text{ pc}^{-3}$ (Hillenbrand & Hartmann, 1998). As mentioned above, the IMF of the Trapezium cluster in the ONC - in contrast to NGC 3603 and the Arches cluster - follows the Salpeter IMF above a solar mass (Muench et al., 2002).

Therefore, although with low statistical significance, the variations of the IMF could be linked to the stellar density of the population. In particular the most massive starburst clusters like NGC 3603 and the Arches cluster with their dense central regions tend to have a distinguishably flatter IMF compared to the standard Salpeter-like IMF.

Chapter 15

Summary and concluding remarks

Our study is aiming at a fundamental question of current star formation research: is the IMF universal, or does it vary with environment? To answer this question, we measured the IMF of NGC 3603 - one of the most massive galactic star-forming regions - from our near-infrared observations with the NAOS-CONICA (NACO) adaptive optics camera at the VLT/ESO. Our very deep, high angular resolution data show unprecedented details of the stellar population in NGC 3603, and we could successfully reveal stars in the dense cluster core covering the mass range from the most massive stars down to $\sim 0.4 M_{\odot}$. In the following we summarize the main results from our study.

NIR imaging, photometry and astrometry

Using the adaptive optics $JHK_S L'$ -band images obtained with NACO and the wider field seeing limited JHK_S images from VLT/ISAAC, we derive magnitudes and positions of almost 10000 stars in NGC 3603.

The typical Strehl ratios in the NACO data are about 12, 18, and 32 % in the JHK_S -bands, respectively, and more than 70 % in L' -band. Because of the low Strehl ratio in J -band, this band limits our ability to detect stars simultaneously in all three JHK_S -bands of the NACO observations. The 50 % completeness limit in the NACO J -band images is ~ 19.5 mag, corresponding to $m_{K_S} \sim 17.5$ mag for stars with the typical color of $J - K_S \sim 2$ mag. The detection limits of the seeing limited ISAAC mosaics are about 20.5, 19.8, and 19.7 mag in JHK_S -bands.

The brightest 256 in the NACO images of the inner $r \leq 13''$ (corresponding to a diameter of ~ 0.75 pc at $d \sim 6$ kpc) were cross identified with potential counterparts in previous studies, and are explicitly listed in Appendix A.

Age, foreground extinction, and disk fraction of NGC 3603

Using the stellar evolution models of Lejeune & Schaerer (2001), Palla & Stahler (1999), and Baraffe et al. (1998), we could derive the age and foreground extinction from the CMDs and CCDs.

The age of the PMS stars is about 0.5 – 1.0 Myr. The upper limit for the age of the MS stars is about 2.5 Myr. This may suggest a slight age spread in the cluster. We further derived an average foreground extinction of $A_V = 4.5 \pm 0.5$ mag. This foreground extinction is not uniform, but increases by $\Delta A_V \sim 2.0$ mag towards larger radii ($r \gtrsim 55''$).

Analyzing the $K_S - L'$ vs $J - H$ CCD, we derived a circumstellar disk fraction of $\sim 25 \pm 10$ % for stars with a mass $\mathcal{M} \geq 0.9 M_\odot$ in the central cluster ($r \leq 10''$).

IMF of NGC 3603 and its radial variation

After rejecting the field stars (based on their location in the CMD), we find a total of 7514 stars within $r \leq 110''$. The completeness corrected K -band LF follows a power-law $dN/dM \propto M^\alpha$ with index $\alpha \sim 0.27$, and is in agreement with earlier studies. No turnover or truncation is found within the detection limit of $m_{K_S} \sim 17.5$ mag.

The IMF is derived from simultaneously fitting the JHK_S magnitudes of the stars using the model isochrones from Lejeune & Schaerer (2001), Palla & Stahler (1999), and Baraffe et al. (1998). Within the mass range of $0.4 - 20 M_\odot$ the resulting IMF is well described by a single power-law with a power-law index $\Gamma \sim -0.74$. Compared to earlier studies, our IMF is slightly shallower, suggesting a top-heavy IMF rather than normal Salpeter IMF ($\Gamma = -1.35$).

We also measured the IMF for seven concentric annuli and found the power-law index decreasing from $\Gamma \sim -0.31$ at ($r \leq 5''$) to $\Gamma \sim -0.86$ at $30'' < r \leq 110''$), i.e., the IMF steepens towards larger radii. The radial change mainly occurs in the inner $r \lesssim 30''$, pointing towards mass segregation in the very center of the cluster. No significant variation of the IMF is found for larger radii ($r \sim 30'' - 110''$).

Size, mass, and dynamical status of NGC 3603

Fitting a King model to the radial density profile of stars with a mass of $0.5 - 2.5 M_\odot$ (corresponding to a K_S -band magnitude of about $15 - 17$ mag), we derived a core radius of $\sim 4''.8$ (~ 0.14 pc at $d \sim 6$ kpc). As the radial density decreases even at the limits of our field of view, we can give a firm lower limit of $r = 110''$ (~ 3.2 pc) for the cluster size. We also derive an upper limit of $r = 1260''$ (~ 37 pc) for the cluster size adopting an estimate of the tidal radius of the cluster based on the Galactic rotation curve and the measured density profile.

The de-projected King model allowed us to extrapolate to the total mass of NGC 3603. Assuming a single power-law IMF with index $\Gamma = -0.74$ within the mass range of $0.1 - 100 M_\odot$, we found a total mass of about $1.0 - 1.6 \times 10^4 M_\odot$. The half-mass radius is found to be within $25'' - 50''$ ($0.7 - 1.5$ pc). The derived core mass density of the cluster is $\geq 6 \times 10^4 M_\odot \text{ pc}^{-3}$.

From the half-mass radius and the total number of stars we could calculate a half-mass relaxation time of approx. $10 - 40$ Myr for stars with a typical mass of $1 M_\odot$. This time scale is an order of magnitude larger than the age of the PMS population in the cluster ($\lesssim 1$ Myr). This implies that the intermediate- and low-mass stars have not yet experienced significant dynamical relaxation. However, the relaxation time of the high-mass stars is expected to be an order of magnitude shorter, and is comparable to the cluster age. We could thus not conclude if the observed mass segregation of the high-mass stars is caused by dynamical evolution or if it is primordial.

We compute that our images with a maximum radius of $r = 110''$ cover at least ~ 67 % of intermediate- and low-mass stars of NGC 3603. The stars outside the observed field can not steepen the IMF by more than $\Delta\Gamma \lesssim 0.16$. Considering also the fact that the IMF does not significantly change beyond $r \gtrsim 30''$, we conclude that the observed IMF is representative for the whole NGC 3603 stellar cluster, irrespective of the mass

segregation in the very center.

Systematic uncertainties of the IMF

We thoroughly analyzed the systematic errors in the IMF determination. In particular we derived the errors from the uncertainties in the age, distance, foreground extinction, stellar evolution models, metallicity, incompleteness correction, individual extinction, unresolved binaries, and the stellar mass outside the observed field.

Combining all systematic errors we derived a power-law index of $\Gamma = -0.74^{+0.62}_{-0.47}$ in the mass range ($0.4 - 20 M_{\odot}$). Assuming a Gaussian probability distribution, we conclude that the probability that the IMF is as steep as the Salpeter IMF ($\Gamma = -1.35$) is less than $\sim 10\%$.

Our result supports the hypothesis of a top-heavy IMF in starbursts, especially in combination with other studies of similar clusters (e.g. the Arches cluster).

Appendix A

Photometry list

#	$\Delta RA^{[a]}$ [$''$]	$\Delta DEC^{[a]}$ [$''$]	J [mag]	H [mag]	K_S [mag]	L' [mag]	Spectral ^[b] Type	MDS94 ^[c] (MTT89)	NS03 ^[d]	SB04 ^[e]	Ref. ^[f]
1	0.53	-0.39	7.78	7.70	7.08	6.45	WN6h+abs	H23(B)		10582	
2	-0.23	-0.24	7.98	7.79	7.21	6.75	WN6h+abs	H ^[c9] 30(A1)		10558	[1]
3	1.83	0.18	8.49	8.13	7.81	7.49	WN6h+abs	H18(C)		10635	
4	-0.17	-0.60	9.38	8.95	8.78	8.80	O3 V	H ^[c9] 31(A2)		10559	[1]
5	0.11	-0.26	9.68	9.45	9.31	9.32	O3 III	H ^[c9] 26(A3)		10570	[1]
6	6.20	-9.19	9.94	9.64	9.45	-	O5 III(f)	H22(17)			
7	-2.00	-1.10	9.95	9.51	9.31	9.19	O3 III	H42		10478	
8	-3.67	2.57	10.09	9.64	9.37	8.93	O5.5 III(f)	H39(6/F)		10392	
9	-0.40	3.26	10.16	9.76	9.54	9.34	O5 V	H19(E)		10543	
10	-2.98	-0.78	10.24	9.78	9.54	9.45	O4 V	H ^[c10] 49(D ^[c5])		10422	
11	-1.53	-0.90	10.25	9.84	9.65	9.60	O3 V	H40		10498	
12	1.15	-8.19	10.29	9.67	9.64	9.78	O4 V(f)	H51(23)		10616	
13	-2.95	-1.01	10.30	9.97	9.75	9.65	O5 V	H ^[c10] 50(D ^[c5])		10423	
14	3.52	0.35	10.33	9.92	9.78	9.74	O3 V	H16		10706	
15	-0.63	1.06	10.40	10.02	9.85	9.83	O4 V	25		10534	
16	-3.02	1.60	10.54	10.14	9.93	9.73	O3 V	38		10419	
17	-3.58	-6.51	10.59	10.20	9.94	9.78	O4 V	H62(15 ^[c3])	6N ^[d3]	10396	
18	8.50	-0.13	10.74	10.11	10.13	10.18	O4 V	H9(21 ^[c4])	6K ^[d2]	10895	
19	-7.98	1.62	10.90	10.26	10.25	9.76	O5 V	H61 ^[c1] (10/G)		10207 ^[e1]	
20	2.91	-2.95	10.95	10.52	10.41	10.49	O4 V	20	6G ^[d1]		
21	3.05	3.01	10.98	10.58	10.44	10.33	O4 V	H14		10683	
22	-1.96	-7.15	11.08	10.70	10.47	10.43	O5.5 V	58(15 ^[c3])	6N ^[d3]		
23	1.86	2.24	11.13	10.73	10.57	10.50	O4 V	17			
24	-4.26	-4.24	11.19	10.78	10.52	10.39	O4 V	H60		10363	
25	3.53	10.28	11.20	10.71	10.52	9.97	O4 V	H7(26)		10705	
26	-2.10	-0.75	11.22	10.81	10.64	10.62	O4 V	41			
27	-0.92	-3.32	11.27	10.83	10.67	10.75		46			
28	-2.84	-0.10	11.33	10.92	10.75	10.64	O8 V-III	45			
29	-0.76	0.97	11.37	10.78	10.59	10.71	O4 V	27			
30	-5.41	-2.20	11.37	10.88	10.66	10.45	O4 V	59		10319	
31	-2.40	0.75	11.39	10.98	10.80	10.70	O6.5 V+?	37			
32	-4.29	2.57	11.39	10.94	10.73	10.42	O4 V	43		10361	
33	-3.17	-1.15	11.39	11.10	10.99	10.87	O4 V	52(D ^[c5])			
34	3.97	-2.35	11.52	10.39	9.52	8.31		28	6G ^[d1]		
35	0.98	-2.03	11.55	11.09	10.95	11.10		57			
36	-5.00	-1.16	11.56	11.11	10.86	10.65	O4 V	36			
37	-1.86	0.65	11.66	11.26	11.09	11.02					
38	2.10	7.97	11.67	10.82	10.71	10.45	O4 V	(H7b)10(22 ^[c7])			
39	5.58	-2.11	11.68	11.28	11.16	11.19		68(44 ^[c6])			
40	-1.56	3.85	11.76	11.36	11.13	10.91					
41	9.79	-0.83	11.79	11.27	11.25	11.20		8(21 ^[c4])	6K ^[d2]		
42	-1.25	-2.19	11.81	11.36	11.19	11.26		77			
43	9.82	-6.37	11.83	12.90	13.04	11.43		12(30 ^[c8])			
44	1.06	0.14	11.88	11.59	11.44	11.48					
45	-8.05	1.65	11.97	12.05	12.62	-		H61 ^[c1] (10/G)		10207 ^[e1]	
46	-4.50	5.76	11.98	11.57	11.26	10.80		34			
47	1.02	-0.55	11.99	11.25	10.32	9.14					
48	2.48	-5.59	12.02	11.59	11.43	11.54		70	6M		
49	10.30	-7.35	12.07	11.77	11.67	11.80		13(30 ^[c8])			
50	2.15	6.88	12.10	11.56	11.28	10.99		11(22 ^[c7])			
51	-3.50	2.27	12.10	11.78	11.57	11.33					
52	-4.71	-0.64	12.12	11.65	11.44	11.27		56			
53	-3.79	4.28	12.12	11.71	11.45	11.11		35			
54	2.97	-3.15	12.14	11.66	11.50	11.55		21	6G ^[d1]		
55	11.87	-4.06	12.16	11.58	11.63	11.51		67 ^[c2] (36)			
56	1.86	5.56	12.19	11.82	11.57	11.32					
57	11.76	-3.63	12.19	11.85	11.29	10.30		67 ^[c2] (36)			
58	2.58	3.55	12.20	11.78	11.56	11.42		15			
59	3.12	-8.35	12.21	11.63	11.63	11.85		71			
60	-3.10	-1.31	12.24	11.74	11.61	11.42		53(D ^[c5])			
61	-1.63	3.68	12.28	11.87	11.63	11.42					
62	-2.75	-1.93	12.28	11.88	11.70	11.62		54			
63	5.85	-2.93	12.28	11.86	11.69	11.71		69(44 ^[c6])			
64	0.65	-5.18	12.30	11.89	11.74	11.85					
65	-4.41	-1.06	12.32	11.94	11.70	11.54		55			
66	2.07	-9.93	12.33	12.00	11.94	12.13		72			
67	6.72	2.80	12.38	13.05	11.87	11.62					

#	$\Delta RA^{[a]}$ [$^{\circ}$]	$\Delta DEC^{[a]}$ [$^{\circ}$]	J [mag]	H [mag]	K_S [mag]	L' [mag]	Spectral ^[b] Type	MDS94 ^[c] (MTT89)	NS03 ^[d]	SB04 ^[e]	Ref. ^[f]
68	-0.71	-0.48	12.38	11.67	10.81	9.33					
69	2.30	-0.08	12.40	11.96	11.23	10.04					
70	-2.19	0.47	12.42	12.66	12.48	12.38					
71	-1.24	-2.42	12.43	11.92	11.74	11.82		44			
72	5.33	3.95	12.54	12.12	11.92	11.72		73			
73	2.31	5.25	12.54	12.75	12.48	12.22					
74	-5.83	-4.45	12.55	12.95	12.70	12.45					
75	11.55	-0.93	12.58	11.92	12.39	11.00					
76	-6.58	1.79	12.60	12.15	11.86	11.30					
77	-2.14	-9.15	12.61	12.02	11.92	12.94					
78	-6.29	-9.75	12.65	12.13	12.71	12.76					
79	-0.75	0.76	12.69	12.56	12.28	11.51	O4 V	29	6O		
80	7.42	-3.51	12.74	12.13	12.09	12.20					
81	-3.28	-0.69	12.75	12.37	11.95	10.92					
82	4.37	-1.57	12.78	12.68	12.56	12.50					
83	-0.38	-2.13	12.82	12.36	12.21	12.32					
84	-8.29	2.86	12.86	12.26	12.54	12.08					
85	-3.85	2.88	12.89	12.55	12.16	11.65					
86	-0.39	-8.19	12.89	12.42	11.66	10.35					
87	0.27	5.74	12.90	11.88	10.85	9.19					
88	9.44	3.04	12.95	12.49	12.05	10.34					
89	-3.30	6.03	12.96	12.81	12.38	11.91					
90	-0.04	-2.11	12.98	12.51	12.35	12.49					
91	-0.59	-4.58	12.98	12.53	12.36	12.43					
92	-2.27	-0.08	12.99	12.51	12.35	12.27					
93	-6.33	2.51	13.03	12.91	12.64	12.25					
94	-3.04	9.37	13.07	13.07	13.09	10.94				6J	
95	2.45	-9.33	13.21	13.23	13.02	12.79					
96	-7.76	-7.89	13.23	12.64	12.36	12.13					
97	-3.41	5.40	13.28	12.82	12.71	12.25					
98	-0.49	-6.12	13.29	12.81	12.49	12.42					
99	8.98	3.09	13.30	12.50	12.79	12.61					
100	-3.69	0.73	13.30	12.90	12.65	12.48					
101	7.92	-0.45	13.33	12.98	12.68	12.59					
102	-6.74	-5.69	13.35	12.56	14.21	11.29					
103	3.05	2.88	13.40	12.05	11.13	9.50					
104	6.73	6.26	13.45	12.51	12.43	12.48					
105	9.12	1.00	13.45	12.87	12.62	12.77					
106	-7.25	-7.92	13.48	12.58	12.02	10.64					
107	6.40	5.96	13.50	13.20	12.98	14.29					
108	-2.24	-2.34	13.53	12.78	12.59	12.59					
109	-8.53	-1.49	13.53	13.13	12.56	11.13					
110	-2.61	-6.65	13.55	12.77	12.49	12.38					
111	2.98	-2.72	13.56	13.16	12.98	12.95					
112	0.33	-3.62	13.57	12.53	11.91	11.59					
113	-3.77	0.65	13.62	12.99	12.58	11.96					
114	2.09	-2.07	13.64	12.87	12.72	12.87					
115	1.23	-2.04	13.64	13.28	13.18	13.15					
116	-7.62	7.08	13.68	13.23	12.78	12.74					
117	3.56	-4.81	13.70	13.07	12.38	11.06					
118	1.13	-0.94	13.70	12.79	12.54	12.25					
119	-0.71	2.10	13.70	13.19	13.00	12.95					
120	3.76	0.56	13.71	14.18	14.08	13.70					
121	2.96	-0.67	13.71	12.99	12.69	12.64					
122	-4.76	-0.96	13.77	12.74	11.83	10.35					
123	-2.79	2.21	13.78	12.96	12.35	10.78					
124	-9.19	4.22	13.81	13.55	13.32	12.74					
125	-1.86	3.39	13.82	13.40	13.18	12.90					
126	9.54	4.20	13.86	13.34	13.14	13.44					
127	6.97	0.85	13.88	12.96	12.84	12.70					
128	1.15	9.82	13.89	13.27	12.79	12.63					
129	-6.03	9.27	13.93	15.01	13.92	13.09					
130	5.22	6.60	13.94	13.17	13.12	13.21					
131	12.32	-2.12	13.98	13.39	13.08	13.29					
132	10.05	0.91	14.05	13.65	13.52	13.80					
133	1.81	-6.02	14.06	13.76	13.42	13.14					
134	-5.62	4.22	14.06	13.66	13.32	13.22					
135	-5.76	2.45	14.08	13.56	13.25	12.90					
136	-5.24	-2.54	14.12	13.50	13.18	12.84					
137	1.37	-5.52	14.13	12.88	12.74	12.88					
138	-6.69	1.80	14.16	14.30	14.54	-					
139	3.51	-0.56	14.18	14.38	13.86	13.32					
140	-4.37	12.12	14.19	15.22	13.79	13.36					
141	-3.84	-2.76	14.22	13.90	13.62	12.97					
142	1.25	1.39	14.22	13.49	13.26	13.03					
143	-1.61	-1.42	14.24	14.81	12.87	12.80					
144	-6.03	-10.39	14.31	13.50	13.19	13.24					
145	-1.34	-10.91	14.32	13.37	12.82	12.88					
146	4.06	-2.83	14.38	13.64	13.36	12.99					
147	-6.83	-5.71	14.39	14.62	14.79	-					
148	4.69	3.48	14.40	13.76	13.45	12.93					
149	-8.39	2.87	14.42	14.23	14.84	-					
150	3.74	-7.34	14.45	13.77	13.58	13.40					
151	-2.78	-4.39	14.46	13.96	13.70	13.40					
152	-4.72	6.05	14.49	14.10	13.72	13.13					
153	0.50	-1.39	14.49	13.87	13.72	13.30					
154	1.23	-0.88	14.50	13.95	13.73	13.37					
155	3.49	2.79	14.50	14.10	13.96	13.66					
156	8.84	-8.60	14.53	14.30	14.01	14.09					
157	7.24	7.91	14.53	13.69	13.97	13.92					
158	-2.67	10.39	14.53	14.49	13.90	13.42					
159	-2.59	4.01	14.54	14.69	14.12	13.30					
160	-4.36	-3.96	14.56	14.03	13.71	13.70					
161	-8.21	-3.34	14.56	13.75	13.53	13.04					
162	-1.02	0.02	14.56	13.70	13.43	13.27					
163	-5.92	-4.47	14.57	15.44	15.39	-					
164	2.72	-4.73	14.59	14.25	13.92	13.61					
165	9.24	8.05	14.60	14.28	14.07	13.53					
166	-6.06	5.64	14.61	13.91	13.64	13.23					
167	-2.55	8.23	14.62	13.79	13.59	13.04					
168	-3.46	6.11	14.62	14.31	14.06	13.56					
169	7.81	-8.48	14.63	14.21	13.83	13.62					
170	-9.68	3.60	14.63	13.93	13.63	13.64					
171	-0.06	-10.27	14.65	14.80	14.40	14.23					
172	8.34	4.23	14.65	13.95	13.86	14.07					
173	10.40	-1.83	14.67	14.68	14.43	14.04					
174	1.93	-5.90	14.70	14.31	14.02	13.66					
175	-0.24	1.86	14.70	13.86	13.54	13.12					
176	6.43	-4.20	14.71	13.96	13.49	13.03					
177	-7.26	-6.42	14.71	13.90	13.62	13.53					
178	-10.72	0.81	14.72	13.54	13.25	13.14					
179	5.03	4.13	14.76	13.96	13.71	13.38					

APPENDIX A. PHOTOMETRY LIST

#	$\Delta RA^{[a]}$ [$''$]	$\Delta DEC^{[a]}$ [$''$]	J [mag]	H [mag]	K_S [mag]	L' [mag]	Spectral ^[b] Type	MDS94 ^[c] (MTT89)	NS03 ^[d]	SB04 ^[e]	Ref. ^[f]
180	-2.64	-2.11	14.77	14.03	13.64	13.24					
181	4.12	-4.33	14.78	14.78	13.94	13.61					
182	0.20	0.44	14.78	14.27	14.04	13.57					
183	-5.47	-5.42	14.80	14.40	14.08	13.73					
184	0.87	-4.62	14.84	14.35	13.94	13.43					
185	0.78	-4.06	14.84	14.37	13.93	13.37					
186	-5.82	6.25	14.84	14.21	13.96	13.56					
187	-4.17	-5.15	14.88	14.05	13.62	13.33					
188	-2.38	-1.66	14.88	14.34	14.07	14.01					
189	-1.93	10.03	14.91	14.73	14.54	14.24					
190	-7.51	7.05	14.91	15.04	15.72	-					
191	-11.80	-0.93	14.91	14.15	13.87	13.92					
192	1.36	3.06	14.91	13.96	13.66	13.26					
193	-7.80	-5.42	14.92	14.04	13.76	13.71					
194	3.90	7.44	14.93	13.86	13.76	13.39					
195	2.16	-12.24	14.94	16.54	13.56	13.67					
196	-1.75	-4.84	14.95	14.91	14.77	13.42					
197	-9.76	6.64	14.98	16.41	16.92	-					
198	12.03	0.17	15.02	14.60	14.42	14.59					
199	0.61	-12.82	15.04	14.58	14.28	-					
200	-9.15	-3.56	15.05	14.03	13.50	13.50					
201	-10.89	5.90	15.06	14.93	14.60	14.05					
202	9.64	-4.31	15.06	14.44	14.24	14.03					
203	-6.44	2.52	15.06	15.15	15.64	-					
204	-2.08	9.08	15.07	14.40	14.00	12.48					
205	-9.83	2.76	15.08	14.86	14.25	14.26					
206	0.07	2.31	15.08	14.60	14.41	14.26					
207	-5.29	6.48	15.09	14.53	14.29	13.88					
208	2.36	-2.98	15.10	14.32	13.95	13.52					
209	9.23	-6.76	15.10	14.78	14.39	14.14					
210	-0.86	-0.69	15.13	14.56	14.52	-					
211	-1.70	-2.53	15.13	14.63	14.17	13.41					
212	-1.21	1.78	15.13	14.58	14.41	14.22					
213	1.46	-4.57	15.14	15.25	14.48	13.88					
214	1.65	1.24	15.15	14.69	14.42	14.26					
215	-3.13	8.19	15.15	16.16	14.28	13.62					
216	-3.96	5.85	15.16	14.16	13.83	13.39					
217	-0.30	9.25	15.16	14.98	14.64	14.37					
218	-9.11	-0.36	15.16	14.86	14.56	14.30					
219	-9.69	6.57	15.17	15.08	14.69	14.03					
220	-3.83	-9.70	15.17	14.17	13.69	13.71					
221	-4.38	-0.30	15.18	14.50	14.38	13.79					
222	0.51	-6.21	15.18	14.40	13.99	13.60					
223	7.64	-7.76	15.20	14.61	14.36	14.07					
224	-8.11	-2.49	15.20	14.62	14.48	13.84					
225	-2.53	-3.43	15.21	14.68	14.39	13.84					
226	-0.16	-2.65	15.21	14.57	14.15	13.69					
227	-1.50	-4.39	15.22	15.24	14.77	14.47					
228	-0.68	1.64	15.24	14.81	14.57	13.90					
229	2.25	2.85	15.25	14.15	13.86	13.59					
230	8.33	1.04	15.25	13.96	13.76	13.47					
231	-7.38	0.41	15.26	14.72	14.23	13.44					
232	2.46	0.58	15.27	15.02	14.63	14.28					
233	8.80	8.29	15.27	14.57	13.90	13.84					
234	-0.20	2.11	15.28	14.91	14.51	14.04					
235	8.65	-2.30	15.29	14.71	14.46	14.19					
236	-1.33	4.92	15.29	14.69	14.29	13.73					
237	3.77	4.45	15.30	15.16	14.70	14.27					
238	0.70	6.96	15.31	15.29	14.75	14.37					
239	-7.64	5.60	15.31	14.83	14.64	14.08					
240	-7.80	4.68	15.31	14.90	14.37	14.38					
241	3.72	-0.75	15.32	14.51	14.23	14.11					
242	-5.70	-11.08	15.32	15.02	13.66	13.76					
243	2.67	-11.71	15.35	14.83	14.34	14.12					
244	12.79	0.97	15.36	14.88	14.67	14.84					
245	-3.25	8.73	15.36	14.95	14.65	14.13					
246	-7.87	-5.45	15.37	16.42	15.82	-					
247	-9.85	3.17	15.37	14.38	14.07	13.87					
248	-5.18	0.53	15.39	14.99	14.78	14.06					
249	-1.78	9.00	15.39	14.93	14.69	13.84					
250	-4.63	-2.72	15.40	14.95	14.47	13.63					
251	-8.13	10.08	15.43	15.25	14.65	-					
252	4.09	-1.10	15.44	14.54	14.21	13.82					
253	-1.76	-5.11	15.45	15.06	14.60	14.18					
254	-3.80	7.38	15.47	14.90	14.46	13.90					
255	-7.33	-10.35	15.49	14.79	14.25	14.29					
256	5.63	4.43	15.50	15.00	14.68	13.91					

Photometry and counterparts of 256 JHK_S(L') detected sources brighter than $m_J = 15.5$ (~ 95 % completeness) in the central region $r < 13''$ of the star-forming cluster in NGC 3003.

[a] Source location is shown in an offset from the center of the cluster (RA = 11h15m05.90s, Dec = $-61^\circ 15' 28.4''$ (J2000)).

[b] Spectral type is adopted from a list in Crowther & Dessart (1998) (Tab. 8 therein) which consists of spectra types in their study combined with those in Moffat (1983) and Drissen et al. (1995).

[c] Designated IDs of potential counterparts in HST optical detections by Moffat et al. (1994). A source with prefix H is found to have a X-ray counterpart by Moffat et al. (2002). IDs originated in previous works such as MTT89 (Melnick et al., 1989), and letters were adopted from tables in Moffat et al. (1994). The letters A-F were originated in van den Bos (1928) (G in Walborn (1973)), and the source A was resolved into A1-3 by Hofmann & Weigelt (1986).

[c1] Star 21 and 52 together would correspond to MDS-61 (G/MTT-10).

[c2] Star 73 and 74 together would correspond to MDS-67 (MTT-36).

[c3] Multiple detections. MDS-58 and 62 correspond to MTT-15.

[c4] MDS-8 and 9 correspond to MTT-21.

-
- [c5] MDS-49, 50, 52, and 53 correspond to D.
- [c6] MDS-68 and 69 correspond to MTT-44.
- [c7] MDS-10 and 11 correspond to MTT-22.
- [c8] MDS-12 and 13 correspond to MTT-30.
- [c9] A1, A2, and A3 together consist of a X-ray source within the match of smoothed PSF in Moffat et al. (2002).
- [c10] MDS-49 and 50 together consist of a X-ray source.
- [d] Designated IDs of potential counterparts in a mid-infrared detections by Nürnberger & Stanke (2003). The 11.9 μm sources 6A-F are in the concentrated cluster core.
- [d1] Star 19, 33 and 51 together would correspond to 6G.
- [d2] Star 18 and 43 together would correspond to 6K.
- [d3] Star 17 and 22 together would correspond to 6N.
- [e] IDs in Sung & Bessell (2004) (Tab. 2 therein). Sources brighter than $V = 14$ mag detected in their analysis of the HST/PC1 archival data set.
- [e1] Star 21 and 52 together would correspond to 10207.
- [f] Other references: [1] Hofmann & Weigelt (1986)

Bibliography

- Armitage P. J., Clarke C. J., Palla F. 2003, MNRAS, 342, 1139
- Ascenso, J., Alves, J., Beletsky, Y., Lago, M. T. V. T. 2007, A&A, 466, 137
- Beck, T. L., Simon, M., & Close, L. M. 2003, ApJ, 583, 358
- Balick, B., Boeshaar, G. O., & Gull, T. R. 1980, ApJ, 242, 584
- Baraffe, I., Chabrier, G., Allard, F., & Hauschildt, P. H. 1998, A&A, 337, 403
- Baraffe, I., Chabrier, G., Allard, F., & Hauschildt, P. H. 2002, A&A, 382, 563
- Barlow, R. J., *Asymmetric Systematic Errors*, arXiv:physics/0306168
- Bertelli, G., Bressan, A., Chiosi, C., Fagotto, F., & Nasi, E. 1994, A&AS, 106, 275
- Bessell, M. S., & Brett, J. M. 1988, PASP, 100, 1134
- Binney, J., Tremaine, S. 1987, Galactic Dynamics, Princeton University Press, 514
- Bonatto, Ch., Bica, E., & Girardi, L. 2004, A&A, 415, 571
- Bonnell, I. A., Bate, M. R., Clarke, C. J., Pringle, J. E. 1997, MNRAS, 285, 201
- Bouvier, J., Stauffer, J. R., Martin, E. L., Barrado y Navascues, D., Wallace, B., & Bejar, V. J. S. 1998, A&A, 336, 490
- Brandl, B., Sams, B. J., Bertoldi, F., et al. 1996, ApJ, 466, 254
- Brandl, B., Brandner, W., Eisenhauer, F., Moffat, A. F. J., Palla, F., & Zinnecker, H. 1999, A&A, 352, L69
- Brandner, W., Grebel, E. K., Chu, Y.-H., & Weis, K. 1997, ApJ, 475, L45
- Brandner, W., et al. 2000, AJ, 119, 292
- Briceño, C., Luhman, K. L., Hartmann, L., Stauffer, J. R., & Kirkpatrick, D. 2002, ApJ, 580, 317
- Brown, A. G. A. 1998, ASP Conference Series, 142, ed. G. Gilmore & D. Howell (San Francisco), 45
- Clark, J. S., Negueruela, I., Crowther, P. A., & Goodwin, S. P. 2005, A&A, 434, 949
- Clayton, C. A. 1986, MNRAS, 219, 895

- Crowther, P. A., & Dessart, L. 1998, *MNRAS*, 296, 622
- Crowther, P. A., Lennon, D. J., Walborn, N. R., & Smartt, S. J. 2007, in "Mass loss from stars and the evolution of stellar clusters", *ASP Conf Ser*, Eds. A. De Koter, L.J. Smith & R. Waters
- Chabrier, G. 2003, *PASP*, 115, 763
- Diolaiti, E., Bendinelli, O., Bonaccini, D., Close, L., Currie, D., & Parmeggiani, G. 2000, *A&A*, 147, 335
- Demarque P., Woo J.-H., Kim Y.-C., & Yi S. K. 2004, *ApJS*, 155, 667
- De Pree, C. G., Nysewander, M. C., & Goss, W. M. 1999, *AJ*, 117, 2902
- Drissen, L., Moffat, A. F. J., Walborn, N. R., & Shara, M. M. 1995, *AJ*, 110, 2235
- Duchêne, G., Bouvier, J., & Simon, T. 1999, *A&A*, 343, 831
- Duquennoy, A., & Mayor, M. 1991, *A&A*, 248, 485
- Eisenhauer, F., Quirrenbach, A., Zinnecker, H., & Genzel, R. 1998, *ApJ*, 498, 278
- Elson R. A. W., Fall M. S., & Freeman K. C. 1987, *ApJ*, 323, 54
- Figer, D. F., Kim, S. S., Morris, M., Serabyn, E., Rich, R. M., & McLean, I. S. 1999, *ApJ*, 525, 750
- Figuerêdo, E., Blum, R. D., Daminieli, A., & Conti, P. S. 2002, *AJ*, 124, 2739
- Fischer, D. A., & Marcy, G. W. 1992, *ApJ*, 396, 178
- Frogel, J. A., Persson, S. E., & Aaronson, M. 1977, *ApJ*, 213, 723
- Genzel, R., et al. 2003, *ApJ*, 594, 812
- Girardi, L., Bressan, A., Bertelli, G., & Chiosi, C. 2000, *A&AS*, 141, 371
- Goss, W. M., & Radhakrishnan, V. 1969, *Astrophys. Lett.*, 4, 199
- Grabelsky, D. A., Cohen, R. S., Bronfman, L., & Thaddeus, P. 1988, *ApJ*, 331, 181
- Grebel, E. K. 2004, *ASP Conference Series*, 322, ed. Lamers et al. (San Francisco), 101
- Haisch, K. E., Lada, E. A., Lada, C. J. 2000, *AJ*, 120, 1396
- Haisch, K. E., Lada, E. A., Lada, C. J. 2001a, *ApJ*, 553, 153
- Haisch, K. E., Lada, E. A., Lada, C. J. 2001b, *AJ*, 121, 2065
- Hardy, J. W. 1998, *Adaptive optics for astronomical telescopes* / John W. Hardy, New York : Oxford University Press, 1998 (Oxford series in optical and imaging sciences)
- Hillenbrand, L. A., Strom, S. E., Calvet, N., Merrill, K. M., Gatley, I., Makidon, R. B., Meyer, M. R., & Skrutskie, M. F. 1998, *AJ*, 116, 1816
- Hillenbrand, L. A., & Hartmann, L. W. 1998, *ApJ*, 492, 540

- Hillenbrand, L. A., & Carpenter, J. M. 2000, *ApJ*, 540, 236
- Hillenbrand, L. A., & White, R. J. 2004, *ApJ*, 604, 741
- Hillenbrand, L. A. 2005, in "A Decade of Discovery: Planets Around Other Stars", *SIScI Symp. Ser. 19*, ed. M. Livio, in press, arXiv:astro-ph/0511083
- Hofmann, K.-H., Weigelt, G. 1986, *A&A*, 167, L15
- Hofmann, K.-H., Seggewiss, W., Weigelt, G. 1995, *A&A*, 300, 403
- Hunter, D. A., Shaya, E. J., Holtzman, J. A., Light, R. M., O'Neil, E. J., Jr., & Lynds, R. 1995, *ApJ*, 448, 179
- Hunter, D. A., O'Neil, E. J., Jr., Lynds, R., Shaya, E. J., Groth, E. J., & Holtzman, J. A. 1996, *ApJ*, 459, L27
- Iben, I. 1965, *ApJ*, 141, 993
- Kennicutt, R. C., Jr. 1984, *ApJ*, 287, 116
- Kenyon, S. J., & Hartmann, L. 1995, *ApJS*, 101, 117
- Kenyon, S. J., & Gómez, M. 2001, *AJ*, 121, 2673
- Kerr, F. J. & Lynden-Bell, D. 1986, *MNRAS*, 221, 1023
- Kim, S. S., Figer, D. F., Kudritzki, R. P., & Najarro, F. 2006, *ApJ*, 653, L113
- King, I. 1962, *AJ*, 67, 471
- Kroupa, P. 2001, *MNRAS*, 322, 231
- Kroupa, P. 2002, *Science*, 295, 82
- Köhler, R. 2001, *AJ*, 122, 3325
- Köhler, R., Petr-Gotzens, M. G., McCaughrean, M. J., et al. 2006, *A&A*, 458, 461
- Kouwenhoven, M. B. N., Brown, A. G. A., Zinnecker, H., Kaper, L., & Portegies Zwart, S. F. 2005, *A&A*, 430, 137
- Lada, C. J., & Adams, F. 1992, *ApJ*, 393, 278
- Lada, C. J., Muench, A. A., Haisch, K. E., et al. 2000, *AJ*, 120, 3162
- Lada, C. J. et al. 2006, *AJ*, 131, 1574
- Lada, C. J. 2006, *ApJ*, 640, L63
- Leggett, S. K., et al. 2003, *MNRAS*, 345, 144
- Lejeune, T., & Schaerer, D. 2001, *A&A*, 366, 538
- Liu, W. M., Meyer, M. R., Cotera, A. S., & Young, E. T. 2003, *AJ*, 126, 1665
- Luhman, K. L., Stauffer, J. R., Muench, A. A., Rieke, G. H., Lada, E. A., Bouvier, J., & Lada, C. J. 2003, *ApJ*, 593, 1093

- Mackey, A. D., & Gilmore, G. F. 2003, MNRAS, 338, 85
- Maercker, M., & Burton, M. G. 2005, A&A, 438, 663
- Maercker, M., Burton, M. G., & Wright, C., M. 2006, A&A, 450, 253
- Malkov, O., Zinnecker, H. 2001, MNRAS, 321, 149
- Massey, P., & Hunter, D. A. 1998, ApJ, 493, 180
- Melnick, J., & Grosbøl, P. 1982, A&A, 107, 23
- Melnick, J., Tapia, M., & Terlevich, R. 1989, A&A, 213, 89
- Meyer, M. R., Calvet, N., & Hillenbrand, L. A. 1997, AJ, 114, 288
- Meynet, G., & Maeder, A. 2003, A&A, 404, 975
- Miller G. E., Scalo J. M. 1979, ApJS, 41, 513
- Moffat, A. F. J. 1983, A&A, 124, 273
- Moffat, A. F. J. & Niemela, V. S. 1984, ApJ, 284, 631
- Moffat, A. F. J., Seggewiss, W., & Shara, M. M. 1985, ApJ, 295, 109
- Moffat, A. F. J., Drissen, L., & Shara, M. M. 1994, ApJ, 436, 183
- Moffat, A. F. J., et al. 2002, ApJ, 573, 191
- Moffat, A. F. J., Poitras, V., Marchenko, S. V., Shara, M. M., Zurek, D. R., Bergeron, E., Antokhina, E. A. 2004, AJ, 128, 2854
- Muench, A. A., Lada, E. A., Lada, C. J., Alves J. 2002, ApJ, 573, 366
- Nürnbergger, D. E. A., & Petr-Gotzens, M. G. 2002, A&A, 382, 537
- Nürnbergger, D. E. A., Bronfman, L., Yorke, H. W., & Zinnecker, H. 2002, A&A, 394, 253
- Nürnbergger, D. E. A., & Stanke, T. 2003, A&A, 400, 223
- Nürnbergger, D. E. A. 2003, A&A, 404, 255
- Oliveira, J. M., Jeffries, R. D., van Loon, Th., & Rushton, M. T. 2006, MNRAS, 369, 272
- Padgett, D. L., Strom, S. E., & Ghez, A. 1997, ApJ, 477, 705
- Palla, F., & Stahler, S. W. 1999, ApJ, 525, 772
- Pandey, A. K., Ogura, K., & Sekiguchi, K. 2000, PASJ, 52, 847
- Patience, J., Ghez, A. M., Reid, I. N., Weinberger, A. J., Matthews, K. 1998, AJ, 115, 1972
- Paumard, T., et al. 2006, ApJ, 643, 1011

- Persson, S. E., Murphy, D. C., Krzeminski, W., Roth, M., & Rieke, M. J. 1998, *AJ*, 116, 2475
- Petr-Gotzens, M. G., Coudé du Foresto, V., Beckwith, S. V. W., Richichi, A., & McCaughrean, M. J. 1998, *ApJ*, 500, 825
- Pfalzner, S., Olczak, C., Eckart, A. 2006, *A&A*, 454, 811
- Phelps, R. L., & Janes, K. A. 1993, *AJ*, 106, 1870
- Pinfield, D. J., Hodgkin, S. T., & Jameson, R. F. 1998, *MNRAS*, 299, 955
- Portegies Zwart, S. F., Makino, J., McMillan, S. L. W., & Hut, P. 2002, *ApJ*, 565, 265
- Preibisch, Th., Balega, Y., Hofmann, K.-H., Weigelt, G., Zinnecker, H. 1999, *New Astronomy*, 4, 531
- Preibisch, T., Stanke, T., & Zinnecker, H. 2003, *A&A*, 409, 147
- Prisinzano, L., Micela, G., Sciortino, S., & Favata, F. 2003, *A&A*, 404, 927
- Prosser, C. F., Stauffer, J. R., Hartmann, L., et al. 1994, *ApJ*, 421, 517
- Rabien, S., Davis, R. I., Ott, T., Li, J., Abuter, R., Kellner, S., & Neumann, U. 2004, *Proc. SPIE*, 5490, 981
- Rebull, L. M., et al. 2002, *AJ*, 123, 1528
- Reid, I. N., & Gizis, J. E. 1997, *AJ*, 113, 2246
- Rieke, G. H., & Lebofsky, M. J. 1985, *ApJ*, 288, 618
- Rudolph, A. L., Fich, M., Bell, G. R., Norsen, T., Simpson, J., P., Haas, M. R. & Erickson, E. F 2006, *ApJS*, 162, 346
- Sagar, R., Munari, U., & de Boer, K. S. 2001, *MNRAS*, 327,23
- Sapleter, E. E. 1955, *ApJ*, 121, 161
- Sanner, J., Altmann, M., Brunzendorf, J., & Geffert, M. 2000, *A&A*, 357, 471
- Scalo, J. M. 1986, *Fundamentals of Cosmic Physics*, 11, 1
- Scalo, J. M. 1998, in *ASP Conf. Ser. 142, The Stellar Initial Mass Function (38yh Herstmonceux Conference)*, ed. G. Gilmore & D. Howell (San Francisco: Astron. Soc. Pac.), 201
- Scalo, J. M. 2005, in *IMF@50: The Initial Mass Function 50 Years Later*, ed. E. Corbelli, F. Palla, & H. Zinnecker (Dordrecht: Kluwer), 23
- Schmutz, W., Drissen, L. 1999, *Rev. Mexicana Astron. Astrofis. Ser. Conf.*, 8, 41
- Shatsky, N., & Tokovinin, A. 2002, *A&A*, 382, 92
- Sher, D. 1965, *MNRAS*, 129, 237
- Siess, L., Dufour, E., & Forestini, M. 2000, *A&A*, 358, 593

- Simon, M., Close, L. M., & Beck, T. L. 1999, *AJ*, 117, 1375
- Sirianni, M., Nota, A., De Marchi, G., Leitherer, C., & Clampin, M. 2000, *ApJ*, 533, 203
- Slesnick, C. L., Hillenbrand, L. A., & Massey, P. 2002, *ApJ*, 576, 880
- Stahler, S. W., Shu, F. H., & Taam, R. E. 1980, *ApJ*, 241, 637
- Stahler, S. W. 1983, *ApJ*, 274, 822
- Stolte, A. 2003, PhD thesis “Mass functions and mass segregation in young starburst clusters”, Ruperto-Carola University of Heidelberg, Germany
- Stolte, A., Brandner, W., Brandl, B., Zinnecker, H., & Grebel, E. K. 2004, *AJ*, 128, 765
- Stolte, A., Brandner, W., Grebel, E. K., Lenzen, R., & Lagrange, A.-M. 2005, *ApJ*, 628, L113
- Stolte, A., Brandner, W., Brandl, B., Zinnecker, H., & Grebel, E. K. 2006, *AJ*,
- Sung, H., & Bessell, M. S. 2004, *AJ*, 127, 1014
- Tapia, M., Bohigas, J., Pérez, B., Roth, M., Ruiz, Ma. T. 2001, *RMxAA*, 37, 39
- Tout, C., Livio, M., & Bonnell, I. 1999, *MNRAS*, 310, 360
- Walborn, N. R. 1973, *ApJ*, 182, L21
- Walborn, N. R., Howarth, I. D., Lennon, D. J., et al. 2002, *AJ*, 123, 2754
- van den Bergh, S. 1978, *A&A*, 63, 275
- van den Bos, W. H. 1928, *Bull. Astron. Inst. Netherlands*, 4, 261
- Willing, B. A., Meyer, M. R., Greene, T. P., Mikhail, A., & Carlson, G. 2004, *AJ*, 127, 1131
- Wood, K., Lada, C. J., Bjorkman, J. E., Kenyon, S. J., Whitney, B., Wolff, M. J. 2002, *ApJ*, 567, 1183
- Yi, S., Demarque, P., Kim, Y. -C., Lee, Y.-W., Ree, C. H., Lejeune, T., & Barnes, S. 2001, *ApJS*, 136, 417

List of Figures

4.1	Schematic picture of the influence of the atmospheric turbulence on the resolution of a point source	i
4.2	Schematic picture of the principle of the adaptive optics observations . . .	22
4.3	Schematic showing of the isoplanatic angle	24
4.4	Anisoplanatism observed in the NACO frames	25
5.1	ISAAC K_S -band mosaic of NGC 3603 and NACO K_S -band mosaic of the central starburst cluster	3
5.2	NACO L' -band mosaic of the central starburst cluster	32
6.1	Corrections of the anisoplanatic effect for the NACO photometry	39
6.2	Statistical errors in the photometry based on the NACO 1st and 2nd data sets	42
6.3	Overview of a $26'' \times 26''$ (0.76×0.76 pc) astrometry map of the central cluster in NGC 3603	44
6.4	A close-up $10'' \times 10''$ (0.29×0.29 pc) field of the astrometry map shown in Fig. 6.3	45
7.1	Critical distance curves and the blending maps derived from J -band photometry from the NACO and	
7.2	Completeness fractions	52
7.3	Detection limits in outer regions in the ISAAC field	52
8.1	Color-magnitude diagram of NGC 3603	56
8.2	CMD of the brightest stars	57
8.3	Combined luminosity-mass conversion relation constructed from the best-fit isochrones	61
8.4	CMD of the cluster center with the combined isochrone	63
8.5	Radial variations in the CMD	65
8.6	Radial variations in the CCD	67
8.7	Color-color diagram of the cluster center	68
8.8	$K_S - L'$ vs $J - H$ color-color diagram of the cluster center	72
9.1	Color-cut selection of cluster members from the CMD	78
10.1	Luminosity functions of JHK_S detected stars	82
10.2	Comparison of K_S -band LFs based on three different methods for the field star subtraction	84
10.3	K_S -band luminosity function of NGC 3603	86
10.4	Comparison of our KLF with previous studies	87
11.1	IMF of NGC 3603	91
11.2	Radial variation of the IMF	93
11.3	Comparison of the IMFs from the NACO and ISAAC data	95
12.1	Projected radial mass density profile of NGC 3603	102
13.1	PMS isochrones (PS99) in the $(J - K_S, J)$ CMD	110

13.2	$(J - K_S, J)$ CMD with the candidate isochrones	113
13.3	Individual extinction correction using a smoothed PMS-MS transition isochrone	116
13.4	Effect of the individual extinction on the IMF	117
13.5	Unresolved binary candidates in the CMD	120

List of Tables

4.1	Summary of NGC 3603 observations with VLT NAOS-CONICA	27
6.1	Multi-bands combination of photometry results	38
6.2	Summary of mosaic frame properties	40
11.1	Radial variation of IMF power-law index	94
13.1	Variation of the power-law index due to age	109
13.2	Variation of the power-law index due to distance	111
13.3	Variation of the power-law index by foreground extinction	111
13.4	Variation of the power-law index due to the selection of stellar evolutionary models	114
13.5	Variation of the power-law index by metallicity	114
13.6	Variation of the power-law index by unresolved binary correction	123
13.7	Summary of the error estimates and the combination	124

Table of abbreviations

AO	Adaptive Optics
CCD	Color Color Diagram
CMD	Color Magnitude Diagram
FWHM	Full Width at Half Maximum
IMF	Initial Mass Function
ISM	Interstellar Medium
LF	Luminosity Function
MS	Main Sequence
NACO	NAOS-CONICA
NIR	Near Infrared
ONC	Orion Nebula Cluster
PMS	Pre-Main Sequence
PSF	Point Spread Function

Acknowledgements

I would like to thank first of all Prof. Reinhard Genzel for providing me with the opportunity to work on this fascinating subject as my Ph.D. thesis project.

Then I wish to express my thanks to Frank Eisenhauer for his kind, thorough, and patient direction of my work as a supervisor. All the guidance and suggestions from him as well as discussions with him were essential for this work.

Special thanks to Fabrice Martins for discussions of star formation, as well as for carefully reading substantial part of my thesis and providing me with invaluable comments. I would also appreciate him for being an advocate in my Ph.D. progress meeting.

I also thank Sascha Trippe for writing the German translation of the abstract of this thesis.

I would like to thank Richard Davies for technical advice which helped me a lot in my data analysis and their interpretations.

I also thank Thomas Ott and Sebastian Rabien for performing the NACO observation of NGC 3603 at Paranal in March 2003. I thank Thomas also for his support on computer and networking issues.

I would like to express my sincere thanks to all colleagues in the IR-group and others at MPE. I also thank Francisco Müller-Sanchez, Mario Schweitzer, Sascha Trippe, Fabrice Martins, and Giovanni Cresci for their helps and advice on my work through numerous discussions. The daily tea-time with them, in which our discussions ranged from astrophysics to football, was a fun part of my day. Many non-scientific activities with them such as the "Schnitzel nights" were precious times.

I thank my parents for their love and support throughout my life. And special thanks to my brother for his continuous support in the form of practical advice and strong encouragements to complete my Ph.D. work.

And last but not least, I thank Emi for everything she has given me.